

Solar Wind Dynamics within  
The Atmosphere of Comet 67P/  
Churyumov-Gerasimenko

Etienne Behar

Space technology



SOLAR WIND DYNAMICS WITHIN THE ATMOSPHERE  
OF COMET 67P/CHURYUMOV-GERASIMENKO

ETIENNE BEHAR

*Supervised by* HANS NILSSON

*Oral defence:* 12<sup>th</sup> October 2018

*Opponent:* THOMAS E. CRAVENS

*Examination committee:*

ASTA KATARIINA PELLINEN-WANNBERG

EVA WIRSTRÖM

JAN-ERIK WAHLUND

*Swedish Institute of Space Physics  
Kiruna*

*Luleå University of Technology*



Etienne Behar: Solar wind dynamics within the atmosphere of comet 67P/Churyumov-Gerasimenko, © September 2018

Printed by Luleå University of Technology, Graphic Production 2018

ISSN 1402-1544

ISBN 978-91-7790-156-3 (print)

ISBN 978-91-7790-157-0 (pdf)

Luleå 2018

[www.ltu.se](http://www.ltu.se)





## ABSTRACT

---

In this thesis, we explore the dynamics of the solar wind as it permeates and flows through a tenuous cometary atmosphere, with a focus on the interaction observed at comet 67P/Churyumov–Gerasimenko.

Seven comets had already been visited by nine different probes when the European spacecraft *Rosetta* reached comet Churyumov–Gerasimenko in August 2014. The mission was however the first to orbit its host comet, which it did for a total duration of more than two years, corresponding to a large part of the comet’s orbit around the Sun. This enabled to study how the dynamics of the plasma environment evolved as the comet itself was transformed from one of the smallest obstacles to the solar wind in the Solar System when far away from the Sun, to a well-established magnetosphere at perihelion.

Most of our efforts tackle the early part of this transformation, when the creation of new-born cometary ions starts to induce significant disturbances to the incident flow. During this stage, a kinetic description of the interaction is necessary, as the system of interest cannot be reduced to a hydrodynamic problem. This contrasts with the situation closer to the Sun, where a fluid treatment can be used, at Churyumov–Gerasimenko as well as at previously visited comets.

*Rosetta* was not a mission dedicated to plasma studies, however. It directly translates into a limited spatial coverage of the cometary plasma environment, which by its nature extends over several spatial scales. An approach solely based on the analysis of in-situ data cannot properly address the major questions on the nature and physics of the plasma environment of Churyumov–Gerasimenko. This thesis therefore largely exploits the experimental–analytical–numerical triad of approaches. In Chapters 3 and 4 we propose simple models of the ion dynamics and of the cometary plasma environment, and these are tested against experimental and numerical data. Used together, they give a global description of the solar wind ion dynamics through the cometary atmosphere, that we explore in the 2-dimensional and 3-dimensional cases (Chapter 5). In Chapter 6, we propose a view on the interaction and its fluid aspects when closer to the Sun.

## SAMMANFATTNING

---

I denna avhandling undersöks solvindens dynamik när den flödar genom en tunn kometatmosfär, med fokus på den interaktion som observerats vid kometen 67P/Churyumov-Gerasimenko.

När *Rosetta* nådde fram till komet 67P/Churyumov-Gerasimenko i augusti 2014 hade redan sju olika rymdfarkoster besökt nio olika kometer. *Rosetta* var dock den första missionen som cirklade runt en komet och följde den sedan i dess bana i totalt mer än två år. Detta motsvarade en signifikant del av hela kometens bana runt solen. Detta gjorde det möjligt att studera plasmats dynamiska utveckling under en period när kometen utvecklades från ett av de minsta hindren solvinden möter i solsystemet, när kometen är långt från solen, till en fullt utvecklad magnetosfär nära perihelion.

Avhandlingen behandlar främst den tidiga delen av denna utveckling, när nyligen joniserade molekyler från kometatmosfären börjar ge en signifikant störning i solvindens flöde. Under dessa förhållanden är en kinetisk beskrivning av växelverkan mellan solvinden och kometatmosfären nödvändig. Systemet vi studerar kan inte reduceras till ett hydrodynamiskt problem. Detta till skillnad från situationen när kometen är närmare solen, då växelverkan kan beskrivas med fluidteori, för både Churyumov-Gerasimenko och de tidigare undersökta kometerna.

*Rosetta* var inte en mission främst ägnad åt plasma-studier. Detta medförde begränsad rumslig täckning av de plasma-processer som äger rum, vilka äger rum över flera olika rumsskalor. Att förstå solvindens växleverkan med kometatmosfären enbart med enpunktsmätningar låter sig därför inte göras. I detta arbete används därför en kombination av experimentella data, analytiska beskrivningar och numeriska beräkningar. I kapitel 3 och 4 föreslår vi enkla modeller för att beskriva jondynamiken och kometens plasmamiljö. Dessa testas sedan mot observationer och numeriska modeller. Tillsammans ger de en global beskrivning av solvindens dynamik när den flödar genom kometatmosfären, vilket utforskas i både 2 och 3 dimensioner (kapitel 5). I kapitel 6 utforskar vi interaktionen som sker när kometen är närmare solen, och hur den nu i högre grad kan beskrivas som en fluid.



## PUBLICATIONS

---

### FIRST-AUTHORED

E. Behar, H. Nilsson, G. Stenberg Wieser et al.

“Mass loading at 67P/Churyumov–Gerasimenko: A case study.”  
*Geophysical Research Letters*, 2016 [8]

E. Behar, J. Lindkvist, H. Nilsson et al.

“Mass-loading of the solar wind at 67P/Churyumov–Gerasimenko – Observations and modelling.”  
*Astronomy & Astrophysics*, 2016 [9]

E. Behar, H. Nilsson, M. Alho et al.

“The birth and growth of a solar wind cavity around a comet - Rosetta observations.”  
*Monthly Notices of the Royal Astronomical Society*, 2017 [10]

E. Behar, H. Nilsson, P. Henri et al.

“The root of a comet tail – Rosetta ion observations at comet 67P/Churyumov–Gerasimenko.”  
*Astronomy & Astrophysics*, 2018 [12]

E. Behar, B. Tabone and H. Nilsson

“Dawn–dusk asymmetry induced by the Parker spiral angle in the plasma dynamics around comet 67P/Churyumov–Gerasimenko.”  
*Monthly Notices of the Royal Astronomical Society*, 2018 [7]

E. Behar, B. Tabone, M. Saillenfest et al.

“Solar wind dynamics around a comet – A 2D semi-analytical model.”  
*Astronomy & Astrophysics*, 2018 [11]

## SECOND-AUTHORED WITH SIGNIFICANT CONTRIBUTION

G. Nicolaou, E. Behar et al., “Energy-angle dispersion of accelerated heavy ions at 67P/Churyumov–Gerasimenko: implication in the mass-loading mechanism.”

*Monthly Notices of the Royal Astronomical Society*, 2017 [65]

L. Berčič, E. Behar et al., “Cometary ion dynamics observed in the close vicinity of comet 67P/Churyumov–Gerasimenko during the intermediate activity period.”

*Astronomy & Astrophysics*, 2018 [13]

## CO-AUTHORED

H. Nilsson et al., “Birth of a comet magnetosphere: A spring of water ions.”

*Science*, 2015 [69]

H. Nilsson et al., “Evolution of the ion environment of comet 67P/Churyumov–Gerasimenko.”

*Astronomy & Astrophysics*, 2015 [67]

T. Broiles et al., “Rosetta observations of solar wind interaction with the comet 67P/Churyumov–Gerasimenko.”

*Astronomy & Astrophysics*, 2015 [16]

A. Coates et al., “Ion pickup observed at comet 67P with the Rosetta Plasma Consortium (RPC) particle sensors: similarities with previous observations and AMPTE releases, and effects of increasing activity.”

*Journal of Physics: Conference Series*, 2015 [21]

C. Simon Wedlund et al., “The atmosphere of comet 67P/Churyumov–Gerasimenko diagnosed by charge-exchanged solar wind alpha particles.”

*Astronomy & Astrophysics*, 2016 [81]

N. Edberg et al. “CME impact on comet 67P/Churyumov–Gerasimenko.”

*Monthly Notices of the Royal Astronomical Society*, 2016 [32]

C. Simon Wedlund et al. "Hybrid modelling of cometary plasma environments - I. Impact of photoionisation, charge exchange, and electron ionisation on bow shock and cometopause at 67P/Churyumov-Gerasimenko."

*Astronomy & Astrophysics*, 2017 [82]

H. Nilsson et al., "Evolution of the ion environment of comet 67P during the Rosetta mission as seen by RPC-ICA."

*Astronomy & Astrophysics*, 2017 [70]

O. Witasse et al., "Interplanetary coronal mass ejection observed at STEREO-A, Mars, comet 67P/Churyumov-Gerasimenko, Saturn, and New Horizons en route to Pluto: Comparison of its Forbush decreases at 1.4, 3.1, and 9.9 AU."

*Journal of Geophysical Research*, 2017 [71]

K. Heritier et al., "Vertical structure of the near-surface expanding ionosphere of comet 67P probed by Rosetta."

*Monthly Notices of the Royal Astronomical Society*, 2017 [51]

M. Saillenfest, B. Tabone and E. Behar, "The solar wind dynamics around a comet: the inverse-square-law paradigm."

*Astronomy & Astrophysics*, 2018 [74]

H. Nilsson et al., "Size of a plasma cloud matters. The polarisation electric field of a small-scale comet ionosphere"

*Astronomy & Astrophysics*, 2018 [68]

C. Goetz et al., "Unusually high magnetic fields in the coma of 67P/Churyumov-Gerasimenko during its high activity phase."

*Astronomy & Astrophysics*, 2018 [39]

F. Plaschke et al., "First observations of magnetic holes deep within the coma of a comet"

*Astronomy & Astrophysics*, 2018 [73]

R. Hajra et al., "Cometary plasma response to interplanetary corotating interaction regions during 2016 June - September: a quantitative study by the Rosetta Plasma Consortium"

*Astronomy & Astrophysics*, 2018 [45]

C. Simon Wedlund et al., "Solar wind charge exchange during the Rosetta mission. I. Analytical formulation and cross sections"

*Astronomy & Astrophysics*, 2018 (in preparation) [83]





## ACKNOWLEDGMENTS

---

Here are a few acknowledgments to people who influenced this thesis, through their direct involvement and through their friendship and presence.

Hans, I am grateful for your trust in my work and for your support through these four years.

Benoît et Melaine, sans vous cette thèse serait foncièrement plus fade, je m'estime chanceux d'avoir vécu ça avec vous. Merci pour tout, et on continue!

Pierre, merci de m'avoir gardé motivé, avoir cru à ces différents projets, merci pour tes lumières et pour ton enthousiasme. De même, continuons!

Shahab, thank you for your boundless help on these last months, and for all the exciting discussions.

Maté, Moa, Audrey, oh how lucky have I been to have you around, in and out the Institute!

Merci Laura pour tout ça, pour ton enthousiasme, tes idées et ton aide sur cette thèse.

Stas, I am thankful for the support I received since my first visit at IRF. This is a special place!

To the past and present PhD student squad and the entire IRF staff, I am grateful to you for these memorable four years in such a wonderful place.

À mes enseignants phares, Marie-Bénédicte Flour, merci pour avoir tout démarré il y a 16 ans, Hervé Froissard, Estelle Moraux, Benjamin Cross, Raphaël Bondu, merci pour votre confiance et vos encouragements à travers ma scolarité, vous en avez été les principaux moteurs et je vous en suis profondément reconnaissant.

We rarely take the time to thank the communities of the various open source projects (Linux, Python, matplotlib, scipy, numpy, git, latex and so many more), but without them our work simply cannot be done. We should value this aspect of our activity.

## CONTENTS

---

1	INTRODUCTION	1
1.1	Unique objects	1
1.2	Solar Wind, Comets, and their interaction	2
1.3	Fluid vs. Kinetic comets	4
1.4	Pre- <i>Rosetta</i> in situ investigations	6
1.5	<i>Rosetta</i>	10
2	INSTRUMENT, TOOLS & METHODS	13
2.1	The Ion Composition Analyzer	13
2.2	Instrument coordinate systems, reference frames & units	14
2.2.1	Instrument coordinate systems	14
2.2.2	Units	16
2.2.3	Reference frames	19
2.3	Data	19
2.3.1	Physical values & plasma moments	19
2.3.2	Species selection	22
2.3.3	Upstream solar wind parameters estimation - Method	23
2.3.4	Integrated moments	26
2.4	Numerical model	26
2.4.1	<i>Leo</i> , a light-weighted, simplified, and fast self-consistent hybrid model	26
2.4.2	Hybrid modeling of plasmas	28
3	A GENERALISED GYROMOTION	31
3.1	The generalised Ohm's law	31
3.2	Generalised gyromotion	33
3.3	Solar wind deflection, cometary ion acceleration	37
3.3.1	A case study	37
3.3.2	Dawn-Dusk asymmetry	40
4	SIMPLE MODELS OF THE COMETARY ENVIRONMENT	43
4.1	Parameters	43
4.2	Cometary ion density	44
4.3	Magnetic field pile-up and draping	47
5	SOLAR WIND PROTON DYNAMICS	55
5.1	Semi-analytical solutions	55
5.2	Self-consistent numerical solutions	59
5.3	Discussion	60
5.4	Solar wind speed and deflection	62
5.5	Night-side excursion	69
5.6	Double-beam velocity space distribution functions	70
5.7	3-dimensional case	74
5.7.1	Densities	74
5.7.2	Electric and magnetic fields	79
6	KINETIC VERSUS FLUID COMET	85
6.1	Density and single particle trajectories	85
6.2	Velocity distribution functions	88

7	SUMMARY & CONCLUSIONS	93
7.1	Summary	93
7.2	Conclusions and openings	94
I	APPENDICES	
A	GEOMETRIC FACTOR	99
A.1	The most basic instrument	99
A.2	Continuous energy sweep	101
A.3	Discrete energy sweep	102
A.4	Miscellaneous	103
B	MOMENTS BY INTEGRATION	105
B.1	Density	105
B.2	Bulk velocity	106
B.3	Python implementation	109
C	REPRESENTING A VELOCITY SPACE DISTRIBUTION FUNCTION	111
D	Leo's ALGORITHM	113
	BIBLIOGRAPHY	117
II	PUBLICATIONS	
A	PUBLICATION I	131
B	PUBLICATION II	141
C	PUBLICATION III	153
D	PUBLICATION IV	163
E	PUBLICATION V	177
F	PUBLICATION VI	185



## INTRODUCTION

---

### 1.1 UNIQUE OBJECTS

The sight of a comet passing close to Earth can be an extraordinary spectacle, contrasting with the view of any other celestial objects. Great Comets can stretch over several tens of degrees in the sky. Their appearance is highly variable, and two comets never really look alike. After passing in the night sky, a comet soon disappears and may take decades to come back, or may simply never be seen again. For a combination of these reasons, comets have been one of the longest-lasting puzzles for astronomers.

Understanding the physics of comets was indeed a great challenge, as one particular comet would be visible from Earth only once in a human life time. This intermittency together with their extremely variable appearance made them seemingly unpredictable, and undoubtedly mysterious. Heidarzadeh [49] identifies four periods of cometology. The first to build a complete theory for comets (the material they are made of, the mechanism of their formation, and their motion), was Aristotle [49]. In Aristotle's theory, which prevailed for two millennia, comets are considered to be meteorological phenomena, "sub-lunar exhalations". It is only in 1577 that Tycho Brahe's observations of a non-periodic comet (the Great Comet of 1577) re-evaluated them as astronomical bodies, but their trajectories were still unknown. In Newton's classical mechanics, comets are members of the solar system, with no significant differences with planets or moons, if not for their high ellipticity. It is only after Laplace – and later Whipple – that comets become unique objects, among the smallest and least dense bodies of the solar system. Comets and their mysteries drew attention from a large variety of scientists and philosophers. A succinct list could cite Aristotle, Seneca, Brahe, Galilei, Kepler, Descartes, Newton, Euler, Kant, Hamilton, Herschel, Laplace. These great names may indicate how important comets have been in the evolution of astronomy. Not only have comets been determining for the development of celestial mechanics (providing for instance a proof of Newton's theory through the work of Edmond Halley), they have also been a major key in the development of modern space plasma physics, making the solar wind and its magnetic field visible for us to see from the ground, as discussed later on.

Comets also held a unique place in popular culture. Until Halley finally made comets' behaviour predictable, their apparitions were perceived as dark omens, presaging the death of a king, the start of a war, the outbreak of a plague [18, 72, 77].

*Part of the content of this Chapter is adapted from the appended articles [7–12].*

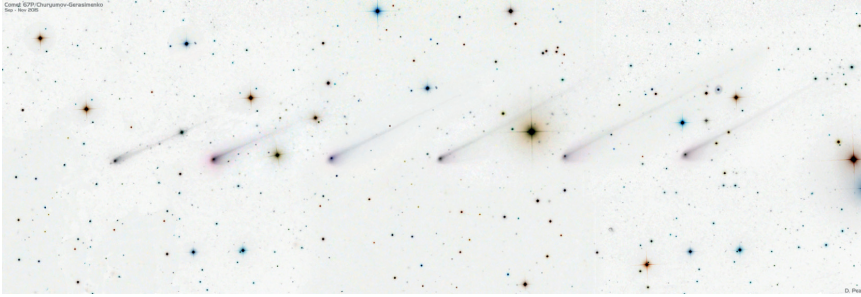


Figure 1.1: Ground-based observations of comet 67P/Churyumov–Gerasimenko from September to November 2015 (Courtesy of Damian Peach, [www.damianpeach.com](http://www.damianpeach.com), inverted here for increased contrast). Only dust tails are visible, as the ion tail was never observed from the ground.

## 1.2 SOLAR WIND, COMETS, AND THEIR INTERACTION

The entire solar system is permeated by a flow of charged particles which is radially and continuously emitted by the Sun: the solar wind. All bodies of the solar system are immersed in and interact with this plasma stream. The rock-in-a-river analogy is an interesting starting point to picture these interactions, as it indeed involves a stream, an obstacle, and the response of the stream during the interaction.

A first limitation of this analogy is the properties of the stream. The solar wind is a supersonic "river", flowing with a speed of 400 km/s in average. Its density is extremely low, with a few particles per cubic centimetres close to Earth, which together with a low thermal speed makes it a collisionless river. This stream is mainly composed of electrons and protons, and is overall neutral. It carries both an electric field and a magnetic field. The presence of charge carriers and fields is the major aspect of this system, in comparison with neutral fluid dynamics. In fluid dynamics, pressure, viscosity and gravity are involved, and in the solar system, the electromagnetic fields must be added to the picture, sometimes dominating its physics.

The second limitation of this analogy is the obstacle itself. By their differences of orbital parameters, of mass, of size, of composition and of electric and magnetic properties, each solar system body interacts in a unique way with the solar wind. In this thesis, we will focus on one special obstacle to the solar wind: a comet.

A comet is composed of a solid nucleus, an atmosphere (referred to as *coma*), and dust and plasma tails. Comets' nuclei are small bodies from hundreds of meters to tens of kilometres large, with no intrinsic magnetic field, and among the darkest objects of the solar system. Composed of ice, dust, small rocks and frozen gases, their estimated averaged density is  $0.6 \text{ g/cm}^3$  [90]: a comet would float on water. They are believed to have formed in the early stage of the formation of the solar system, with little chemical evolution ever since (in opposition with almost all other solar system bodies), which makes them time capsules of this early period of the solar system.

During the first part of the 20<sup>th</sup> century, comets played an important role in the development of space physics. The first suggestion of the existence of a steady stream of charged particles flowing away from the Sun can be attributed to Arthur Eddington in 1910 [30, 33], based on observations of comet Morehouse and the analysis of the shapes of the envelopes seen in the atmosphere and in the ion tail. Later on, a model presented by Ludwig Biermann [14] (1951) describes the tail of comets being dragged by a corpuscular radiation emitted by the Sun. In this description, the momentum is transferred from the wind to the tail by Coulomb collisions. During the same decade, another major model was proposed by Hannes Alfvén [1] (1957) where the magnetic field of the Sun is "frozen" in a similar flow of solar particles. The local addition of a cold and slow cometary ion population corresponds to a significant decrease of the total plasma velocity, and the frozen-in magnetic field piles up and drapes itself around the dense coma. This draping pattern was given as an interpretation of the typical pattern of streamers in a comet tail. Comets have acted as natural solar wind probes before the first in situ measurements and the space exploration era because of their high neutral molecule production rate (with values ranging from  $10^{25}$  to several  $10^{30}$  molecules per second) and their very low gravity: they were the ideal tracers to make the solar wind "visible" from Earth.

From a plasma physics perspective, comets distinguish themselves from other bodies of the solar system by three main aspects, namely the eccentricity of their orbit, the composition of their nuclei, and their low gravity field. Not gravitationally bound to its source, the neutral coma grows and shrinks in size and density following the comets' remoteness from the Sun, which provides the necessary radiation for the sublimation of the various volatiles embedded in their nuclei. The neutral coma is then partially ionised by photoionisation, electron impact or charge exchange processes. From a bare nucleus to a wide and tenuous ionised atmosphere, comets present the most variable obstacle to the solar wind. In turn, the dynamics of the supersonic solar wind around and through a coma doesn't quite lend itself to comparison with the more familiar planetary picture. In this interaction and during most of the comets' orbital period, the solar wind does not meet a conductive ionosphere or a conductive body: the charge carriers inducing a magnetic response to the solar wind are in fact created (ionised) *within* the solar wind, immediately transported away as pick-up ions, and constantly renewed by the ionisation of the neutral coma invisible to the solar wind. Therefore analogies with induced magnetospheres around other unmagnetised bodies are far from trivial.

The properties listed above also result in one of the largest obstacles to the solar wind in the solar system. At comet Halley, the first cometary ions were detected 7.8 million kilometres away from the nucleus by the *Giotto* probe [54], a distance comparable to the day-side extent of the Jovian magnetosphere.

Once created, the new-born ions will be accelerated by the ambient electric and magnetic fields and in the absence of collisions, momen-

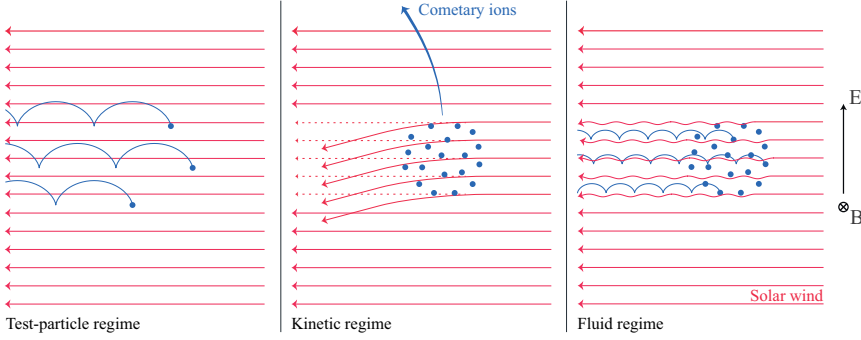


Figure 1.2: Three different simplified cases of mass-loading. In the left panel, the seldom cometary ions behave as test-particles, the solar wind is undisturbed. In the middle panel, the gyroradii are larger than the interaction region, the solar wind is deflected and decelerated. On the right, the ion cloud loading the incident stream is larger than the ion gyroradii, the solar wind is only decelerated.

tum and energy are exchanged through the fields between the solar wind and the partially ionised atmosphere. This phenomenon is known as the *mass-loading* of the solar wind by the new-born ions, as mass is added to the plasma [88], and is the main topic of the present thesis.

### 1.3 FLUID VS. KINETIC COMETS

Since the early works of Biermann and Aflvén, the plasma dynamics of the interaction between the solar wind and a coma has been an active and fascinating topic. Firstly in the perspective of planetary science: understanding the solar system and its various bodies, and their evolution. Secondly, in the perspective of plasma physics. Comets are indeed great plasma laboratories, where one plasma component (the ionised coma) appears *within* another (the solar wind): how do the two plasma components react to one another, and how does the entire system evolve through the parameter space (e.g. upstream solar wind parameters and outgassing rate of cometary neutral molecules)? In this brief introduction, we sketch a very simplified picture, which initiates the work developed in Chapters 3 to 5.

In the absence of gravity, the motion of charged particles in an electric field  $E$  and a magnetic field  $B$  is dictated by the Lorentz force,  $F_L = q(E + \mathbf{v} \times \mathbf{B})$ , with  $q$  the charge of the particle and  $\mathbf{v}$  its velocity. In some cases this motion may be very simple. In the undisturbed solar wind for instance, the effect of the electric field and of the magnetic field on a solar wind ion moving at the average (or bulk) solar wind velocity are cancelling each other, and the overall resulting acceleration on the solar wind particles is null. When considering the simplistic case of a single new-born ion added to the solar wind with no initial velocity, one finds the classical cycloidal motion with the



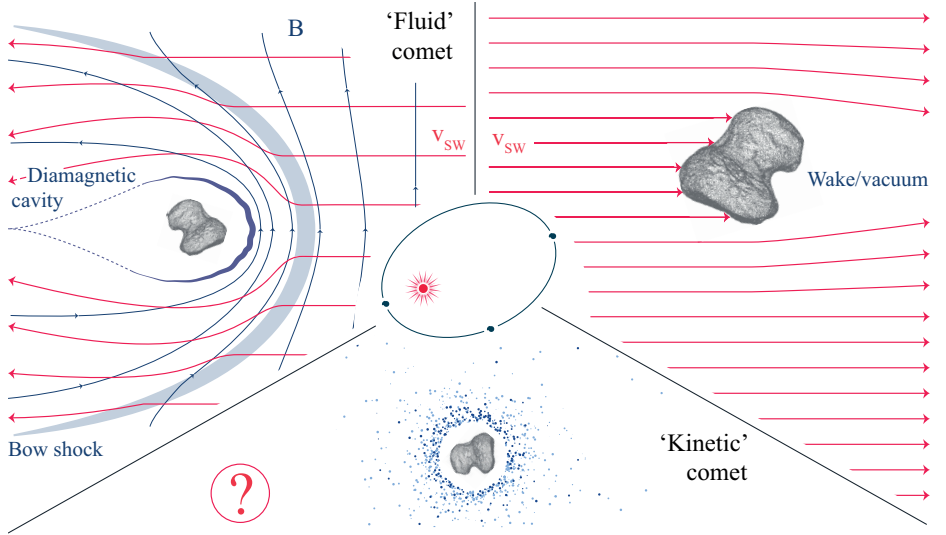


Figure 1.3: Simplified schematic of the evolution of the interaction between the solar wind and a coma, as the distance between the Sun and the nucleus evolves (cf. orbit at the centre of the figure). These sketches do not contain any sense of scale. The question mark indicates the main object of interest for this thesis.

Larmor radius  $\mathcal{R} = m v_{\perp} / (q |\mathbf{B}|)$ , illustrated with the blue trajectories in the left panel of Figure 1.2. In this case, the solar wind and the electric and magnetic fields are left unaffected by the addition of a single ion.

Soon however, as the nucleus draws closer to the Sun, we cannot consider anymore that the solar wind is undisturbed when loaded with these new-born ions, as their density is growing. And this is precisely our starting point, with the following question: what happens to the solar wind and to the cometary ions when we reach the limit of the test-particle description?

Immediately, we have to consider two more schematic situations, also sketched in Figure 1.2. In the first situation (middle panel), the source region of cometary ions is of the same scale or smaller than the gyro-radius. In the second situation (right-hand panel), the source region is much larger than their gyroradius. Both situations present a different case of mass-loading. In the first, the momentum of the cometary ions is mostly vertical (the early phase of the cycloid). In the macroscopic terms of conservation of momentum, the solar wind particles are expected to be deflected from their upstream flow direction, as well as decelerated, losing as much kinetic energy as gained by the cometary ions. We term this picture a “kinetic regime”, and later on a “kinetic comet”. In the second situation, the momentum of both populations is on average horizontal throughout the schematic, the solar wind is on average not deflected but decelerated by the addition of the new-born ion mass. *The motion of the charged particles can be reduced*

to their average (or bulk) motion. We therefore term this picture a “fluid regime”, resulting in a “fluid comet”. Whether or not these simplistic pictures hold any relevancy will be seen in the next chapters. We can already raise the following limitations and questions:

- How can we define and quantify gyroradii in such a case?
- What effects would a non-constant density of cometary ions have on the situation, and precisely on the gyroradii?
- In the kinetic case, what happens when the deflected solar wind meets the undisturbed solar wind?
- In both cases, how complex would the tail (or downstream, or night-side) region really look like?

The second point, the effect of the non-constant cometary ion density, may indicate something important. Intuitively, the closer we are from the nucleus, the denser the coma is. Therefore when the comet is far away from the Sun, the region that will actually be dense enough to significantly disturb the stream of solar particles will be of a limited extent, to then grow in size with decreasing heliocentric distances and increasing neutral outgassing rate. For this reason, we hypothesise that the interaction between the solar wind and the coma will go through the three different regimes: from the test-particle regime, then to the kinetic regime, and finally to the fluid regime, close to the Sun.

Far away from the Sun, at aphelion, the outgassing rate is extremely low, and the undisturbed solar wind impacts the bare surface of the nucleus. The interaction is then similar to the case of an asteroid, and even has similarities with the situation at the Moon. The seldom cometary ions can be described as test-particles. On the other end of the orbit, close to perihelion, previous experimental results given in the next section showed that at about 1 au away from the Sun, active comets and their coma interact with the solar wind in a very fluid manner. This is summarised in Figure 1.3.

Somewhere between aphelion and perihelion, right in-between the test-particle description and the fluid description of the interaction, lies a regime almost unstudied before the last decade. This is the topic of the early interaction between a young tenuous coma and the solar wind, far away from the Sun, and is the main topic of this thesis.

#### 1.4 PRE-*rosetta* IN SITU INVESTIGATIONS

The early theoretical studies of the cometary plasma environment were tackling the features of the comet’s head and tails that were visible from Earth, naturally directing the scientific interest towards strongly outgassing comets close to their perihelion. With a growing interest towards space physics, and increasing space technologies, humans eventually went exploring comets and their environment in situ.

Less than thirty years after Biermann's study, space probes started leaving Earth targeting such active comets, and at Giacobini–Zinner [22] and Halley [44], what had previously been invisible became visible: a whole set of plasma structures came within the reach of scientists [26, 43]. Between 1978 and 1985, six probes that would eventually reach the neighbourhood of a comet were launched, and as of today, ten different spacecraft have visited eight different comets. An overview of these missions is given in Figure 1.4. The last mission to terminate its active phase was the European probe *Rosetta*, which explored comet Churyumov–Gerasimenko. Because of much lower outgassing rates, the kinetic regime of the interaction between the solar wind and the coma was more susceptible to be witnessed by *Giotto* and *Rosetta* at comets Grigg–Skjellerup and Churyumov–Gerasimenko. In fact, at the other comets, the fluid treatment of the interaction was almost systematically and successfully applied by the scientific community. We now gather some important observations made prior to *Rosetta*, and relevant to this thesis.

**Outgassing rates** – At the exception of *Rosetta*, all missions met their host comet between 0.79 and 1.03 au away from the Sun [26]. The reported neutral gas production rates were  $7.5 \times 10^{27} \text{ s}^{-1}$  at Grigg–Skjellerup, between  $2$  and  $4 \times 10^{28} \text{ s}^{-1}$  at comet Giacobini–Zinner,  $3.5 \times 10^{28} \text{ s}^{-1}$  at comet Borrelly, and between  $0.7$  and  $1.3 \times 10^{30} \text{ s}^{-1}$  at comet Halley. For comparison, the neutral gas production rate at Churyumov–Gerasimenko was measured between about  $1 \times 10^{25} \text{ s}^{-1}$  and  $3.5 \times 10^{28} \text{ s}^{-1}$  for heliocentric distances between 4 and 1.24 au, at its perihelion [47].

**Solar wind deceleration and deflection** – We introduced the exchange of momentum and energy that happens between the incident flow and the cometary ions. Clear deceleration was observed at Halley [36, 54, 61, 63], at Grigg–Skjellerup [55], as well as in the coma of comet Borrelly by the *DeepSpace1* probe [94]. As for the exchange of momentum, deflection of the solar wind from the Sun-comet line was also reported at comet Halley [36, 61], and at comet Grigg–Skjellerup [55]. The bulk of the flow is pictured to be deflected around the obstacle, symmetrically [61], as sketched in Figure 1.3, upper left segment. This is fundamentally different than the deflection of the solar wind ions introduced above in the kinetic regime of the interaction (macroscopic deflection of the fluid in the first case versus microscopic deflection of the single particles in the second case).

**Bow shocks & Bow waves** – At comets the solar wind does not meet a blunt, sharp obstacle such as Earth's magnetosphere. In the fluid regime of the interaction, it is gradually decelerated over an extended region by the addition of new-born heavy ions. To that extent, whether a cometary bow shock could form or not in the supersonic solar wind flow was an open question at the time of the first spacecraft encounters with comets. In the work of Biermann, Brosowski, and

Mission	Target	Launch date	Agency	Date peri	$r_{\min}$ (1e3 km)
ICE	21P/Giacobini–Zinner	1978-08-12	NASA/ESA	1985-09-11	7.862
Vega 1	1P/Halley	1984-12-15	USSR	1986-03-06	8.889
Vega 2	1P/Halley	1984-12-21	USSR	1986-03-09	None
Sakigake	1P/Halley	1985-01-07	ISAS	1986-03-11	6990.0
Giotto	1P/Halley	1985-07-02	ESA	1986-03-14	0.605
GiottoExt	26P/Grigg–Skjellerup	1985-07-02	ESA	1992-07-10	0.200
Suisei	1P/Halley	1985-08-19	ISAS	1986-03-08	152.4
SuiseiExt	21P/Giacobini–Zinner	1985-08-19	ISAS	Failure	
Deep Space	107P/Wilson–Harrington	1998-10-24	NASA	Failure	
Deep SpaceExt	19P/Borrelly	1998-10-24	NASA	2001-09-22	2171.0
Stardust	81P/Wild	1999-02-07	NASA	2004-01-02	0.237
StardustExt	9P/Tempel	1999-02-07	NASA	2011-02-15	0.181
CONTOUR	2P/Encke	2002-07-03	NASA	Failure	
CONTOURExt	73P/Schwassmann–Wachmann	2002-07-03	NASA	Failure	
CONTOURExt	6P/d Arrest	2002-07-03	NASA	Failure	
Rosetta	67P/Churyumov–Gerasimenko	2004-03-02	ESA	2014-08-06	0
Philae	67P/Churyumov–Gerasimenko	2004-03-02	ESA	2014-11-12	0
Deep Impact	9P/Tempel	2005-01-12	Nasa	2005-07-04	0
Deep ImpactExt	103P/Hartley	2005-01-12	Nasa	2010-11-04	0.694

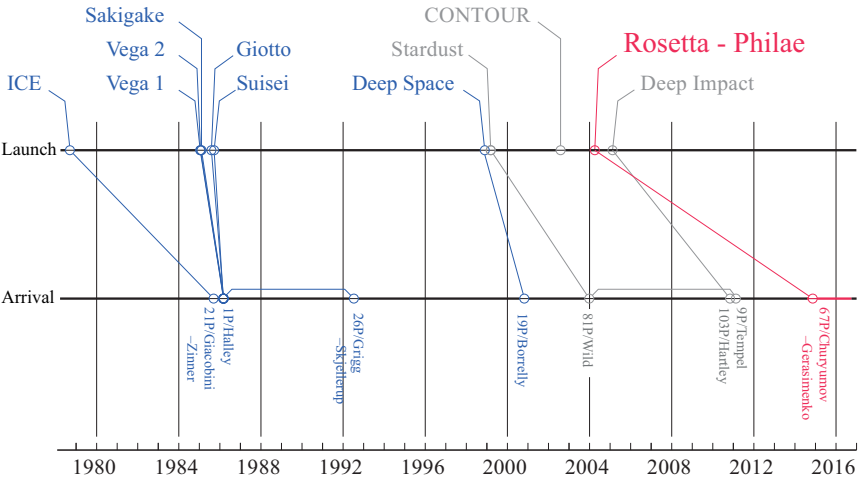


Figure 1.4: Time-line of all cometary missions. Probes with plasma instruments are indicated in blue.

Schmidt [15], a shock was found to appear in the one-dimensional single fluid description of the interaction, as an instability in the flow. This could be only tested two decades later with the exploration of comet Giacobini–Zinner and Halley, where finally experimental confirmation of the existence of a weak cometary bow shock was obtained at comet Halley. At comets Giacobini–Zinner, Grigg–Skjellerup and Borrelly, the term *bow wave* is sometimes suggested instead [26]. The topic of the cometary bow-shock is nicely reviewed by Coates [19], which states that “*cometary bow shocks are probably the most complex in the solar system [...]*”. A broad bow structure is depicted upstream of the nucleus in Figure 1.3 in the fluid case.

**Magnetic field pile-up and draping, diamagnetic cavity** – Downstream of the shock the solar wind keeps being decelerated by the increasing addition of new-born heavy ions. Assuming that the magnetic field is frozen into the total electron fluid, it will pile up (increase of its magnitude) upstream of the nucleus, and drape (deformation of the initially straight magnetic field lines) around the dense coma. Both are represented in Figure 1.3. We indicate once more the seminal work of H. Alfvén [1], where this innovative concept is introduced in a powerful concise, elegant and graphical way. On the experimental side, the clearest results on magnetic field draping were found at comet Giacobini–Zinner [84] and Halley [62]. Close to the nucleus, the magnetic field is the highest, in a heavily loaded plasma flow. Eventually, the radially expanding, partially ionised, and unmagnetised coma is so dense that it repels the magnetic field. A cavity perfectly free of magnetic field is created, the diamagnetic cavity sketched in Figure 1.3, and was observed at comet Halley [62]. A magnetohydrodynamical model of this complex structure is proposed in Cravens, T. E. [23]. A diamagnetic boundary was observed at comet Churyumov–Gerasimenko as well [40, 42]. Before the *Rosetta* exploration of its host comet, a region devoid of solar wind ions was often explicitly or implicitly said to match the diamagnetic cavity (with the exception of the simulation work of Sauer, Bogdanov, and Baumgärtel [76]). We will see in Chapter 5 that the two regions at comet Churyumov–Gerasimenko are well separated.

**Cometary ion dynamics** – In the fluid regime, the cometary ions gyrate in the coma, with a gyroradius smaller than the interaction region. Gyrotropic (phase space) distribution functions can form. First, unstable ring distributions form, which become thickened shell distributions to eventually transform into Maxwellian distributions. The theory and the observations of these gyrotropic distributions are reviewed by Coates [20]. The deceleration of the solar wind can then be tackled by a fluid approach. On large scales, much larger than the scales of the ion gyromotion, the cometary ions are seen accelerated instantaneously at the average plasma velocity, a result of the ideal magnetohydrodynamics [15, 35, 78].

### 1.5 *Rosetta*

After six highly successful and fruitful encounters with two different comets, the need for new cometary missions was obvious, missions which would get closer to the nucleus, and for a much longer time: scientists needed a probe that would rendezvous a comet, and escort it along its orbit. Even more ambitious, the joint NASA–ESA project – the Comet-Rendezvous Asteroid Flyby (CRAF) mission [64] – was designed as a sample return project: the probe would first fly by an asteroid, then escort a comet, land on its nucleus, to eventually bring samples back to Earth. After NASA cancelled the project, ESA went on with the Comet Nucleus Sample Return (CNSR) mission design [79]. An illustration taken from the CNSR *mission and system definition document* (1991) is shown in the upper panel of Figure 1.5, picturing the entire probe landed on the nucleus. The name *Rosetta* was already proposed for the probe. In November 1993, a less ambitious, simplified mission – the International Rosetta Mission, including an orbiter and a small lander – was approved as a Cornerstone Mission in ESA’s Horizons 2000 Science Programme (Figure 1.5, bottom panel). The mission target was initially comet 46P/Wirtanen, however due to rocket issues, the launch had to be delayed and the targeted comet changed. On the 4th of March 2004, the *Rosetta* mission was leaving the ground of French Guyana, onboard an Ariane 5 rocket. The probe was now targeting comet 67P/Churyumov–Gerasimenko, and 10 years were needed to reach and rendezvous with the comet’s nucleus, at 3.65 au from the Sun as the comet was on the inbound half of its orbit. On the 6th of August 2014, *Rosetta* was crossing the 100 km cometocentric distance, and the next day the first cometary ions were detected [69]. The lander *Philae* reached the nucleus’s surface on the 12th of November 2014. Two years later, as the comet was getting further away from the Sun again after its closest approach at 1.24 au (August 2015), the probe could not get enough energy from the Sun and at 3.8 au away from the Sun, the orbiter landed on the nucleus on the 30th of September 2016.

A set of five plasma instruments, the Rosetta Plasma Consortium (RPC) [17] was part of the scientific payload, and probed the plasma environment in the vicinity of the nucleus for more than two years. Data from one instrument in this package, the Ion Composition Analyzer (ICA), are extensively used in the following work. Studies and results from other the RPC sensors are given along the text of the thesis when relevant.



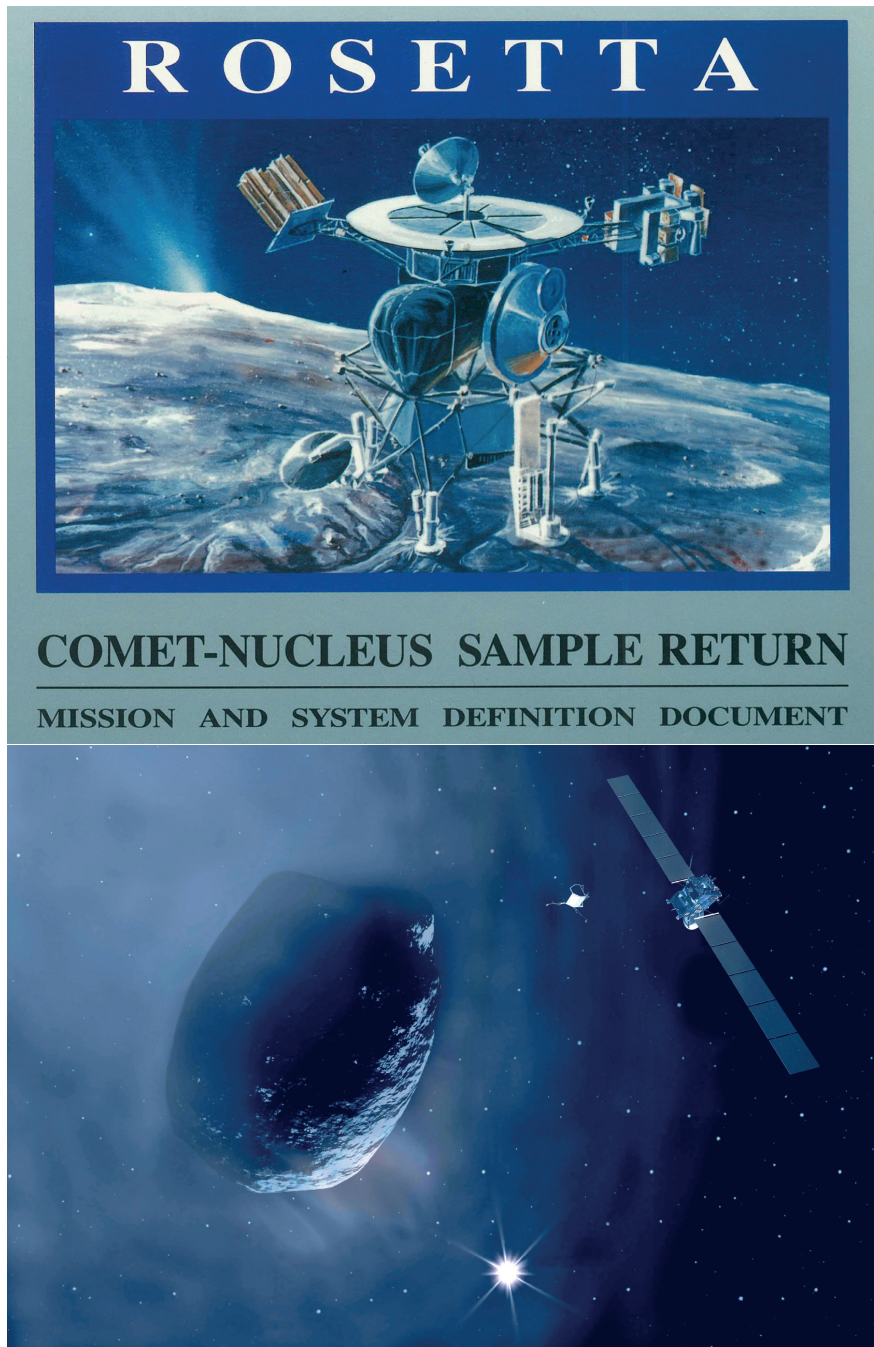


Figure 1.5: Illustrations for the CNSR mission (upper panel) and the Rosetta probe together with the descending Philae lander (lower panel), before the characteristic double-lobe shape of Churyumov-Gerasimenko's nucleus was discovered.





## 2.1 THE ION COMPOSITION ANALYZER

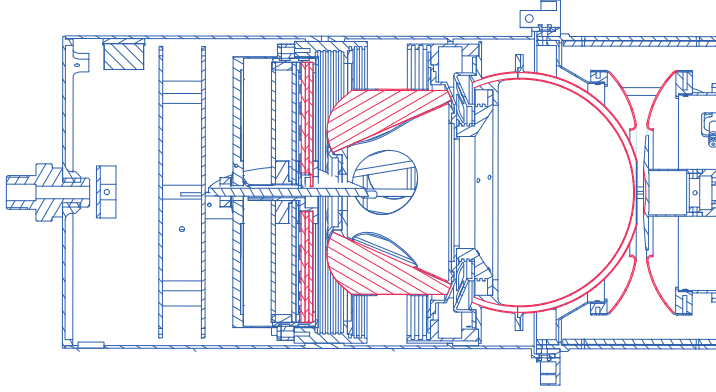


Figure 2.1: Cut of the Ion Composition Analyser (ICA), with the ion optic and the detection plate highlighted in red.

The Ion Composition Analyzer (ICA) is one of the sensors of the Rosetta Plasma Consortium (RPC), and was designed and built by the Swedish Institute of Space Physics in Kiruna. A comprehensive description of this imaging spectrometer is given by Nilsson et al. [66], and here we give a summary of its functioning.

ICA measures phase space (or velocity space) distribution functions of positive ions. It can additionally separate ions of different masses. The energy-per-charge of the detected ions will be noted  $\mathcal{E}$ , and the viewing direction of the instrument is given by two angles, the elevation angle  $\theta$  and the azimuth angle  $\varphi$ . The energy can be set to 96 different values, ranging from a few electron-volts up to 40 keV. The coverage of the angular space is only partial, with  $\theta \in [-45^\circ, 45^\circ]$  (16 steps) and  $\varphi \in [0^\circ, 360^\circ]$  (16 steps).

One can follow the trajectory of an ion in the ion optic of the instrument, as given by the blue curve of Figure 2.2. The first system the ion meets is the elevation angle filter, composed of two plates that can be set at different electric potentials  $U_3$  and  $U_4$  up to several kV. Through the resulting electric field, only positively charged particles coming with the angle  $\theta$  will penetrate the instrument. The energy is then filtered by a toroidal electrostatic analyser: two spherical concentric plates can be set at different electric potentials  $U_1$  and  $U_2$ , and only particles with the adequate energies will follow a circular trajectory, and escape at the output of the analyser (see Figure 2.2). The

next system is an assembly of permanent magnets, which will deflect the trajectory of the ion. The ion will hit the detection plate with a radial distance dependent on its momentum. The heavier elements will be detected closer to the axis of symmetry of the instrument, as indicated on Figure 2.2. Finally, the last value, the azimuth angle  $\varphi$ , is given by the angular position of the ion impact on the detection plate. The impact of the ion with the Micro-Channel Plate (MCP) will produce one or several secondary electrons. The avalanche phenomenon happening in the MCP results in a cloud of electrons hitting an array of electrodes: 16 azimuth electrodes (or azimuth sectors) and 32 radial mass electrodes (or mass channels).

Because the energy-per-charge  $\mathcal{E}$  and the elevation angle  $\theta$  are filtered by electrostatic analysers, their value depends on the setting of the instrument (the values of the four potentials  $U_{1,2,3,4}$  at the moment of the measurement). For a single measurement, all detected ions will have the energy-per-charge  $\mathcal{E}$  and have entered the instrument with the same angle  $\theta$ . However during the same single measurement, all azimuth angles  $\varphi$  and all masses are measured.

The energy dimension  $\mathcal{E}$  is particular for such an instrument, since its measurement (or filtering) does not depend on any other parameters. For this reason, the energy-per-charge of the ions is the most reliable measurement one can get from ICA. This will be illustrated in the next chapters.

In summary, ICA data consist of counts, given over 5 dimensions: time, elevation angle, azimuth angle, energy and mass. Since the integration time  $\tau$  is known, the conversion to count rate is trivial. However we are interested in phase space distribution function values (see Section 2.3). The conversion from counts to phase space distribution function is a sensitive and complex operation, and we give in the next section the various concepts and steps of this conversion. One of the key concept is the Geometric Factor, for which we give a simplified approach in Appendix A.

## 2.2 INSTRUMENT COORDINATE SYSTEMS, REFERENCE FRAMES & UNITS

### 2.2.1 Instrument coordinate systems

Most of the medium energy particle instruments have a "natural" set of variables, which is not the cartesian set  $(v_x, v_y, v_z)$ . Most of them are measuring the energy-per-charge of a particle, and not its speed. They additionally determine the incoming direction using two angles, namely azimuth angle  $\varphi$  and polar angle  $\theta$  (also referred as to elevation angle). We need to change our set of variables from the cartesian system  $(r_x, r_y, r_z, v_x, v_y, v_z) = (\mathbf{r}, \mathbf{v})$  to the instrument natural coordinate system  $(r_x, r_y, r_z, v, \theta, \varphi)$

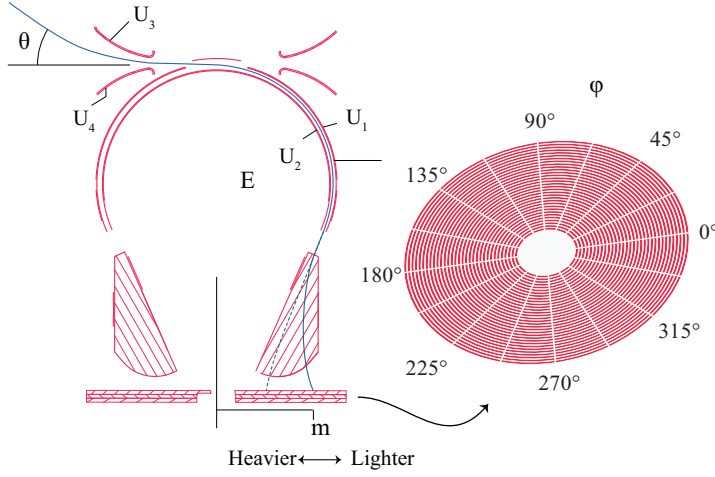
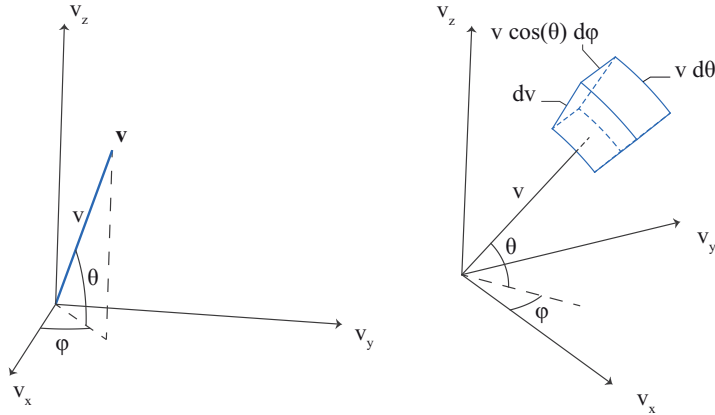


Figure 2.2: Cut through RPC-ICA ion optics & Schematics of the sensor plate.



Note that this is not a classically defined spherical coordinate system, with  $\theta$  being defined from the plane  $(v_x, v_y)$  and not from  $v_z$ .

First, we have:

$$v_x = v \cos(\theta) \cos(\varphi) \quad (2.1)$$

$$v_y = v \cos(\theta) \sin(\varphi) \quad (2.2)$$

$$v_z = v \sin(\theta) \quad (2.3)$$

Our goal is to express the elementary volume element  $dv$  in this new coordinate system, i.e.  $dv(v, \theta, \varphi)$ . In the previous cartesian system, we simply have

$$dv(v_x, v_y, v_z) = dv_x \cdot dv_y \cdot dv_z \quad [\text{m}^3/\text{s}^3]$$

- A small increment  $dv$  along  $v$  simply results in a linear displacement  $dv$  of the point.

- A small increment  $d\theta$  along  $\theta$  will result in the point moving along a small arc of length  $v d\theta$
- A small increment  $d\varphi$  along  $\varphi$  will result in the point moving along a small arc of length  $v \cos(\theta) d\varphi$

Therefore,

$$d\mathbf{v}(v, \theta, \varphi) = v^2 \cos(\theta) dv d\theta d\varphi \quad [\text{m}^3/\text{s}^3]$$

$$dv_x \cdot dv_y \cdot dv_z = v^2 \cos(\theta) dv d\theta d\varphi = v^2 dv d\Omega \quad [\text{m}^3/\text{s}^3] \quad (2.4)$$

$\Omega$  is the solid angle. In the case of RPC-ICA, the numbering of the azimuth anodes, or azimuth sectors, or simply sectors, is given in Figure 2.3. This numbering gives the **viewing direction**: if we get a count with index 4, this particle was coming with an angle  $\varphi$  in the instrument (because of the top hat analyser, this numbering mirrors the physical position of the anodes).

*Important remark* : as defined on the schematics of Figure 2.3,  $\mathbf{v}$  is parallel to the **viewing direction**, not the actual velocity of the particle! This velocity is then  $-\mathbf{v}$ , and this minus sign can be taken into account either in the definition of the angles, or in the final expression of the bulk velocity. The logic here is to stick to the variable we get from the data, and in these variables, we have energy in eV, and two angles that tell us about the viewing direction, and not the velocity direction. Therefore we start deriving the moments with the viewing direction, since it doesn't matter for density and bulk speed.

### 2.2.2 Units

We still need to convert the speed  $v$  (m/s) into a kinetic energy  $E$  (J,  $1 \text{ J} = 1 \text{ kg} \cdot \text{m}^2/\text{s}^2$ ). We introduce the mass  $m$  (kg) of the considered particle.

$$E = \frac{1}{2}mv^2 \quad ; \quad v = \sqrt{\frac{2E}{m}}$$

$$dE = mv dv \quad ; \quad dv = \frac{1}{\sqrt{2mE}} dE$$

From 2.4, the general change of variable from the cartesian system to the natural instrument system is

$$\begin{aligned} dv_x \cdot dv_y \cdot dv_z &= \sqrt{\frac{2E}{m^3}} \cos(\theta) dE d\theta d\varphi \\ &= \sqrt{\frac{2E}{m^3}} dE d\Omega \end{aligned} \quad (2.5)$$

$$[\text{m}^3/\text{s}^3] = [\text{J}^{3/2}/\text{kg}^{3/2}]$$

Electrostatic analysers filter the energy-per-charge of particles, which in space physics are commonly expressed in electron-volt eV, and

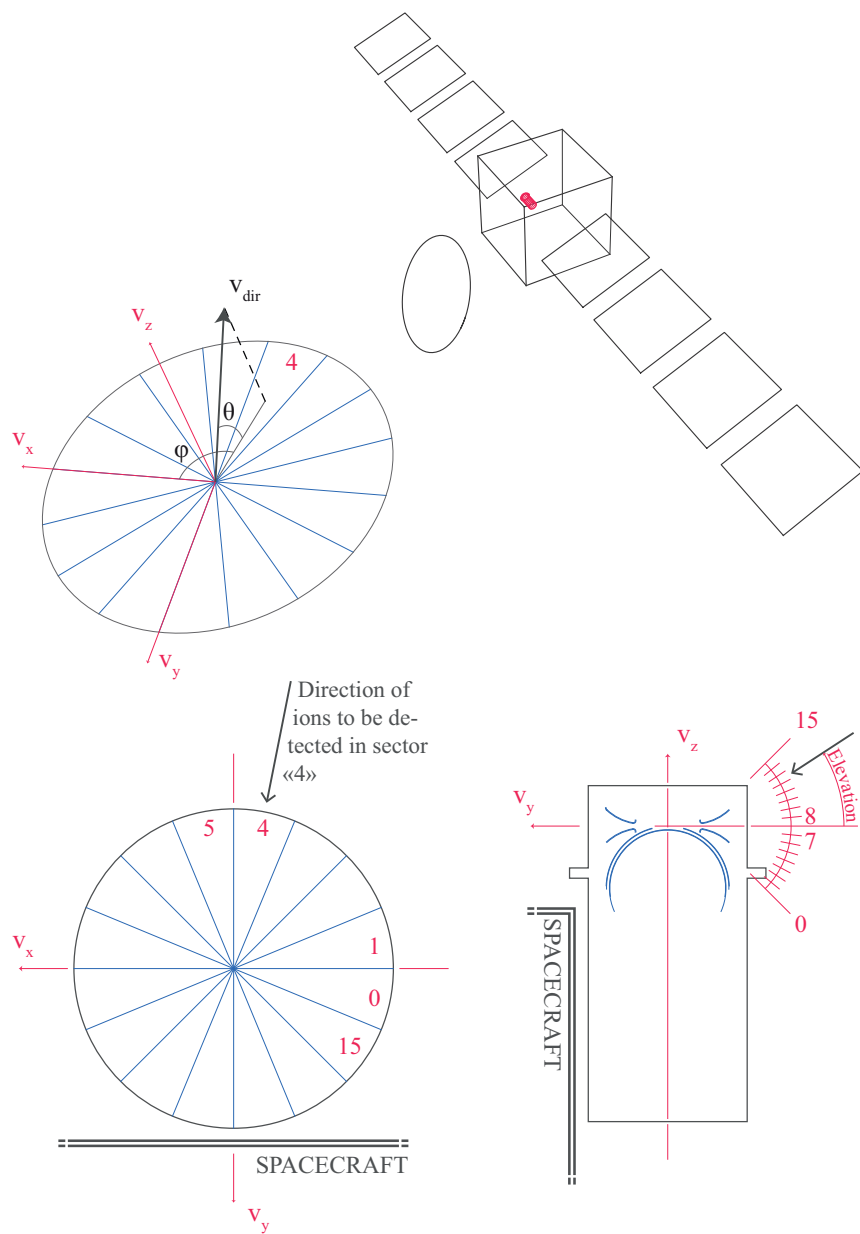


Figure 2.3: Instrument coordinate system of ICA, sector and elevation bin numbering.

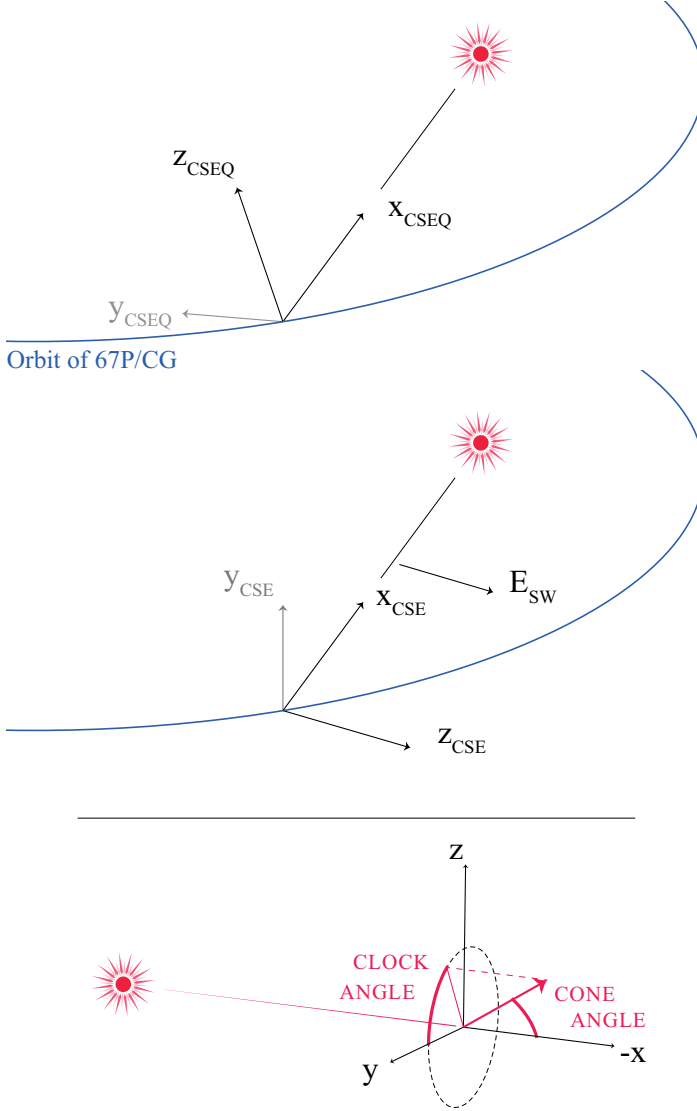


Figure 2.4: Upper panel: CSEQ and CSE reference frames. In the second case, the orientation of the solar wind electric field is arbitrary, and evolves through time. Lower panel: Definitions of the clock angle and the cone angle as used in this thesis.

not in joule J. An additional conversion is thus needed from the instrument energy-per-charge setting  $\mathcal{E}$  (eV/Q) to the total energy of a particle  $E$  (J),  $Q$  being the number of charge for a particle of the considered species:

$$E = e Q \mathcal{E} \quad [\text{J}] \quad (2.6)$$

with the elementary charge  $e = 1.60217662 \cdot 10^{-19}$  in coulombs C.

### 2.2.3 Reference frames

Three reference frames will be used, all centred on the nucleus. The first one is defined using the orbit of the comet around the Sun, and is referred to as the Comet-centred Solar EQUatorial (CSEQ) reference frame: the  $x$ -axis points to the Sun, the  $z$ -axis is perpendicular to the  $x$ -axis and oriented by the Sun's north pole, the  $y$ -axis completes the right-handed triad.

More relevant when it comes to the plasma environment around the comet, the Comet-Sun-Electric field frame, CSE, also has its  $x$ -axis pointing towards the Sun and the  $z$ -axis is along the upstream electric field. However, since defined by unmeasured upstream parameters, this reference frame is not directly available, and one can only give an estimation of the frame orientation.

Yet another reference frame is used, a species-aligned frame. For each scan of the velocity space (every 192 s), a rotation around the Sun-comet line is done in order to cancel the  $v_y$ -component of the bulk velocity of any species of interest. Most of the time, this will be done using protons.

Figure 2.4 defines the cone angle and the clock angle, which can be used for any vector (ion bulk velocity, magnetic field, spacecraft position, etc.) and in any reference frame. Since all frames defined above share the same  $x$ -axis, the cone angle is frame independent.

## 2.3 DATA

### 2.3.1 Physical values & plasma moments

#### 2.3.1.1 Definitions

*Phase space* – The 6-dimensional space  $(r_x, r_y, r_z, v_x, v_y, v_z)$  in which particles with positions  $\mathbf{r} = (r_x, r_y, r_z)$  move with velocities  $\mathbf{v} = (v_x, v_y, v_z)$ .

*Number density* – Number of particles  $N$  in a volume  $d^3r$  at a given time:

$$n(\mathbf{r}) = \frac{N}{d^3r} \quad ; \quad [\text{m}^{-3}] .$$

*Differential directional number flux* –  $j(\mathbf{r}, E, \varphi, \vartheta)$  is the number of particles  $N$  of energy within  $dE$ , crossing a differential area  $dA$  per differential time  $dt$  within a differential solid angle  $d\Omega$ :

$$j(E, \Omega) = \frac{N}{dA \, dt \, dE \, d\Omega} \quad ; \quad [\text{m}^{-2} \text{s}^{-1} \text{sr}^{-1} \text{J}^{-1}] .$$

*Phase space distribution function* – In the phase space  $(\mathbf{r}, \mathbf{v})$  we can define an infinitesimal volume  $dV$  as the 6-dimensional volume as  $dV = dr_x \cdot dr_y \cdot dr_z \cdot dv_x \cdot dv_y \cdot dv_z$ . The phase space distribution function  $f(\mathbf{r}, \mathbf{v})$  gives the number of particles  $N$  enclosed in  $dV$  at a given time:

$$f(\mathbf{r}, \mathbf{v}) = \frac{N}{dV} = \frac{N}{d^3r \, d^3v} \quad ; \quad [\text{s}^3 \text{m}^{-6}] .$$

Differential directional number flux and phase space distribution function can be converted from one to the other as

$$f(\mathbf{r}, \mathbf{v}) = \frac{m^2}{2E} j(E, \Omega) .$$

(2.7)

The proof of 2.7 is given in Annex A.

*Remark* : In this work, the term *velocity space distribution function* is preferably used instead of *phase space distribution function*. Rosetta was a single probe, therefore only one point in physical space was sampled at each time.

### 2.3.1.2 Plasma moments

Based on the continuous description of a plasma given in the previous sub-section, moments of the phase space distribution function can be defined just as for any other continuous function or discrete sets of points. These moments give a quantitative measure of the shape of a distribution, they allow to reduce the amount of information used to describe a plasma at a given time: from a continuous, infinite 6-dimensional distribution function, we get a limited set of values "reducing" the description of the plasma. Usually in experimental space physics, these values are reduced to one scalar (the density), one vector (the bulk velocity) and one tensor (the pressure). The plasma moment of order  $k$  is defined as:

$$\mathbf{M}^k = \int_{\mathbf{v}} \mathbf{v}^k \times f(\mathbf{v}) \, d^3\mathbf{v} . \quad (2.8)$$

For  $k = 0$ , we get the plasma particle density, or number density:

$$n(\mathbf{r}) = \int_{\mathbf{v}} f(\mathbf{v}) \, d^3\mathbf{v} . \quad (2.9)$$



From 2.5, from the cartesian coordinate system to the instrument coordinate system:

$$n(\mathbf{r}) = \int_{-\infty}^{\infty} \int_{-\infty}^{\infty} \int_{-\infty}^{\infty} f(v_x, v_y, v_z) \, dv_x \, dv_y \, dv_z \quad (2.10)$$

$$= \int_E \int_{\varphi} \int_{\theta} f(\mathbf{r}, E, \varphi, \theta) \sqrt{\frac{2E}{m^3}} \cos(\theta) \, dE d\varphi d\theta. \quad (2.11)$$

By discretising the distribution (the instrument samples discretely the distribution), using the Riemann integration and using specificities of the instrument, one can derive the numerical integration of the moments (given in Annex B) and get

$$n(\mathbf{r}) = \frac{2\pi \, 10^4}{16 \, \tau} \sqrt{\frac{m}{2e \, Q}} \cdot \sum_{\mathcal{E}} \sum_{\varphi} \sum_{\theta} \left( \frac{1}{\sqrt{\mathcal{E}^3}} \frac{\cos(\theta)}{G(\mathcal{E})} c(\mathbf{r}, \mathcal{E}, \varphi, \theta) \, \Delta\mathcal{E}(\mathcal{E}) \Delta\theta(\mathcal{E}, \theta) \right) \quad (2.12)$$

[m<sup>-3</sup>]

$k = 1$  corresponds to the flux density, with  $\underline{\mathbf{u}}$  the flow velocity, or bulk velocity.

$$n(\mathbf{r}) \, \underline{\mathbf{u}}(\mathbf{r}) = \int_{\mathbf{v}} \mathbf{v}(\mathbf{r}) f(\mathbf{v}) \, d^3\mathbf{v} \quad (2.13)$$

$$\underline{u_x}(\mathbf{r}) = \frac{2\pi \, 10^4}{16 \, n(\mathbf{r}) \, \tau} \sum_{\mathcal{E}} \sum_{\varphi} \sum_{\theta} \frac{\cos 2(\theta) \cos(\varphi)}{\mathcal{E}} \frac{c(\mathbf{r}, \mathcal{E}, \varphi, \theta)}{G(\mathcal{E}, \varphi, \theta)} \, \Delta\mathcal{E}(\mathcal{E}) \Delta\theta(\mathcal{E}, \theta) \quad (2.14)$$

[m/s]

$$\underline{u_y}(\mathbf{r}) = \frac{2\pi \, 10^4}{16 \, n(\mathbf{r}) \, \tau} \sum_{\mathcal{E}} \sum_{\varphi} \sum_{\theta} \frac{\cos 2(\theta) \sin(\varphi)}{\mathcal{E}} \frac{c(\mathbf{r}, \mathcal{E}, \varphi, \theta)}{G(\mathcal{E}, \varphi, \theta)} \, \Delta\mathcal{E}(\mathcal{E}) \Delta\theta(\mathcal{E}, \theta) \quad (2.15)$$

[m/s]

$$\underline{u_z}(\mathbf{r}) = \frac{2\pi \, 10^4}{16 \, n(\mathbf{r}) \, \tau} \sum_{\mathcal{E}} \sum_{\varphi} \sum_{\theta} \frac{\cos(\theta) \sin(\theta)}{\mathcal{E}} \, \Delta\mathcal{E}(\mathcal{E}) \Delta\theta(\mathcal{E}, \theta) \quad (2.16)$$

[m/s]

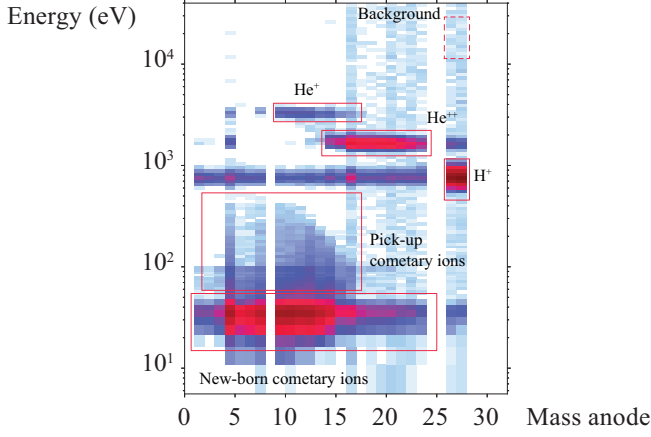


Figure 2.5: Manual species selection using the energy and the mass dimensions of the data, integrated over one day on the 15th December 2014.

### 2.3.1.3 Mean speed

Another speed is also calculated, which in this thesis is generally referred to as *mean speed*. It corresponds to the *distribution function averaged along the radial dimension in the spherical coordinate system*, and can therefore be calculated in a straightforward manner from ICA data based on the energy dimension only. The counts are also initially translated into the physical differential directional number flux  $j(\mathbf{r}, E, \varphi, \vartheta)$ , which is then summed over all dimensions but energy. The average value is taken, and translated into a velocity, knowing the mass and the charge state of the particles:

$$j(\mathcal{E}) = \sum_{\varphi} \sum_{\vartheta} j(\mathbf{r}, E, \varphi, \vartheta) , \quad (2.17)$$

$$\frac{m}{2e Q} u_{\text{mean}}^2 = \frac{\sum_{\mathcal{E}} \mathcal{E} j(\mathcal{E}) \Delta \mathcal{E}(\mathcal{E})}{\sum_{\mathcal{E}} \mathcal{E} \Delta \mathcal{E}(\mathcal{E})} . \quad (2.18)$$

The difference between the *bulk velocity* and the *mean speed* is intuitive. First of all, one is a vector while the other is a scalar. The confusion may appear while using the norm of the bulk velocity, compared to the mean speed. To illustrate the difference, we consider particles evenly distributed along a circle centred on zero in velocity space. One gets the norm of the bulk velocity  $|\mathbf{u}| = 0$ , in other words the centre of the circle. The average speed however is simply the radius of the circle in this frame. The distinction will be made clear when using either of these speeds in the following section.

### 2.3.2 Species selection

RPC-ICA can discriminate ions by their mass, as illustrated in Figure 2.5. The plot shows an energy-mass matrix integrated over one day:

the  $y$ -axis gives the energy-per-charge of the detected counts (96 bins) while the  $x$ -axis represents the mass channel in which the counts were detected. There is no direct translation between one particular mass channel and a physical mass, the physical mass is instead given by the combination of an ion energy and the mass channel it hits.

On the figure, we have identified five populations. First the three solar wind components – the protons  $H^+$ , the alpha particles  $He^{2+}$  and the helium ions<sup>1</sup>  $He^+$ . All the three components have the same speed, and their different mass-per-charge (respectively 1 amu, 2 amu, and 4 amu) result in their separation by a factor 2 in energy-per-charge. Second the cometary ions, either slow (below a few tens of eV, here 60 eV, referred to as new-born ions) or accelerated (referred to as pick-up ions, above 60 eV on that day). The new-born ions were ionised fairly locally. Since the spacecraft is located in the dense inner coma, this local population is also dense (i.e. high count-rates). The pick-up ions were ionised further away, upstream of the measurement point, in a region of the coma less dense, and have been accelerated by the electric and magnetic fields to higher energies.

In the two years of data available from the active mission, it is most of the time possible to separate manually the different populations, as done in Figure 2.5. This method is systematically used for computing moments per species or representing velocity space distribution functions per species. A few issues are to be found however: the cometary pick-up ions can overlap with the spill-over of the solar wind protons, an instrumental artefact seen as the horizontal structure spreading from the proton peak. Similarly, when protons have a lower energy, they can on some occasions overlap with the wide peak of the new-born cometary ions.

Finally, we use an analogy to a signal-to-noise ratio to filter the data, as a daily manual selection blindly selects species, either if present or not in one particular measurement. In Figure 2.5, we materialised with a dashed line a selection of the same mass bins which detect protons, at the high end of the energy range where no particles are expected to be measured (mass lower than 1 amu). This background selection has the same size in energy and mass as the protons (in number of bins). The value estimating the signal-to-noise ratio is then the *difference* of integrated counts for both windows. By experience, protons are indeed observed if this difference is larger than 5 counts, but a higher threshold can be used.

### 2.3.3 Upstream solar wind parameters estimation - Method

As *Rosetta* was deep inside the coma for most of the mission, one needs an estimation of the solar wind parameters *before* it is perturbed

<sup>1</sup> result of the charge exchange between alpha particles and neutral cometary molecules [69, 82]

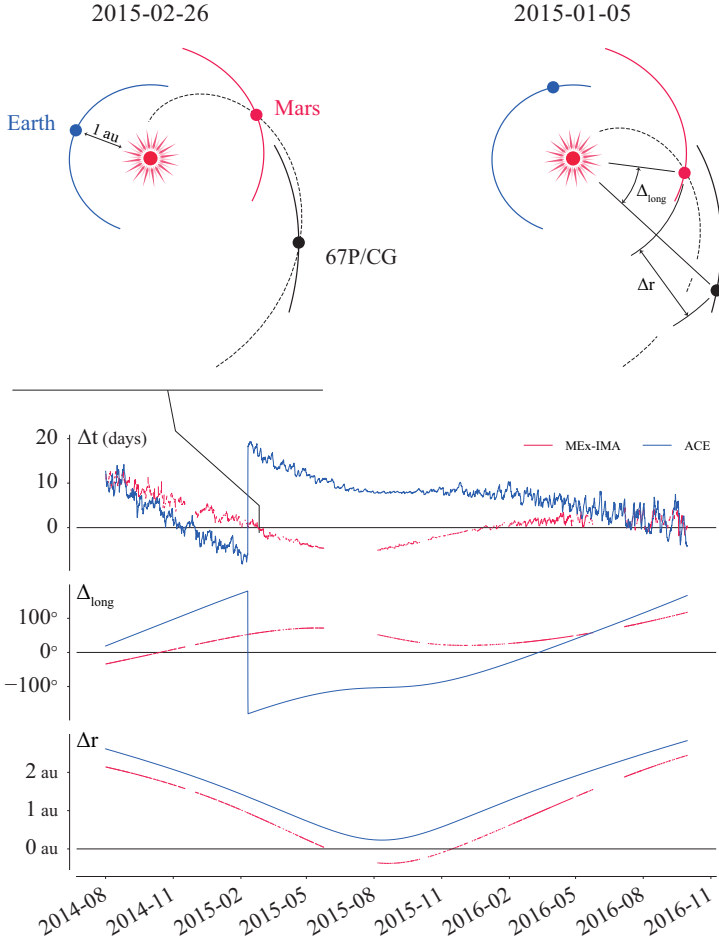


Figure 2.6: Upper-left: one optimum configuration between Mars and 67P/CG lying on the same Parker spiral, on 2015-02-26. Upper-right: a configuration on 2015-01-05, for which measurement at Mars have to be propagated in time according to equation (2.19). Lower panel: time delay, longitudinal shift and radial shift between Earth and 67P/CG (blue) and Mars and 67P/CG (red).

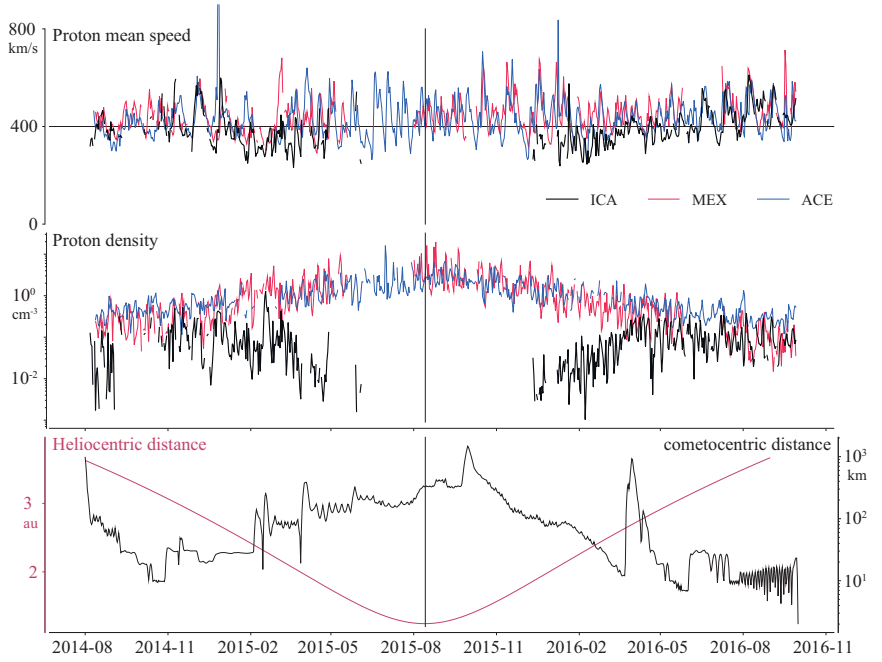


Figure 2.7: Daily averaged solar wind plasma moments measured at 67P/CG (solid black lines), and estimations of the upstream solar wind parameters propagated from Earth (blue) and Mars (red).

by its interaction with the obstacle. To estimate the solar wind speed and density upstream of comet 67P/CG, we use solar wind parameters measured by different missions, either at Earth with the *ACE* and *WIND* probes or at Mars with the *Mars EXpress* mission. In the latter case, the parameters are measured upstream of Mars using the Ion Mass Analyzer (IMA), one of the sensors in the ASPERA-3 instrument package [6] onboard Mars Express. IMA is an ion spectrometer almost identical to RPC-ICA.

As these parameters are sometimes measured a few astronomical units away from comet 67P/CG, one needs to propagate them through time, to get the best estimation just upstream of the coma. We use a simple ballistic propagation, which is simply based on the assumption that along one Parker spiral, the solar wind has the same parameters. The idea is that a source region on the surface of the Sun has produced a stream of particles with the same parameters (density, speed, *etc.*) for some period of time. As the Sun rotates, the particles emitted by this source region are forming a spiral, the well known Parker spiral (see Figure 2.6). In the best case, the measurement point (either Mars or Earth) and the target (67P/CG) are on the same spiral at the same time, as shown in Figure 2.6. However even if this configuration is not met, the spiral necessarily has passed or will pass the

target, and a time delay has to be taken into account: the measurement has to be propagated in time, with the following expression

$$\Delta t = \Delta r / v_{\text{sw}} - T_{\text{Sun}} \Delta_{\text{long}} / (2\pi) , \quad (2.19)$$

in which  $v_{\text{sw}}$  is the solar wind speed measured at either Mars or Earth,  $T_{\text{Sun}}$  is the Sun's rotation period,  $T_{\text{Sun}} = 24.5$  days,  $\Delta_{\text{long}}$  and  $\Delta r$  are the differences in longitude and radius between the two body, as illustrated on Figure 2.6. This expression is fairly straightforward. Between emission of the particles at the Sun and detection at the body, the duration is  $t_{\text{Mars}} = r_{\text{Mars}} / v_{\text{sw}}$  for Mars and  $t_{67\text{P/CG}} = r_{67\text{P/CG}} / v_{\text{sw}}$  for 67P/CG. Therefore absolutely, the solar wind will need  $\Delta r / v_{\text{sw}}$  more time to reach the comet. However, assuming the two bodies lie on the same spiral, the particles detected at Mars and at 67P/CG are most likely not the same, even though emitted by the same source. So a time lag of  $|T_{\text{Sun}} \Delta_{\text{long}} / (2\pi)|$  has to be added or removed to account for the fact that the source had to rotate from one angle to the other. These two components can cancel each other, and the total delay  $\Delta t$  is cancelled, as is the case for the upper-left configuration on Figure 2.6. Note that the delay  $\Delta t$  can be positive as well as negative.

The time series for  $\Delta t_{\text{ACE}}$  and  $\Delta t_{\text{MEX}}$  are given in Figure 2.6. It appears that Mars has been in a better position to provide estimations of solar wind parameters than Earth. First, with a perihelion at 1.24 au, the difference of radius  $\Delta r$  is advantageous for Mars, most of the time. With a longer period of rotation around the Sun, Mars has a rotation speed comparable to 67P/CG around its perihelion, which can be seen in the two consecutive sign flips of the derivative of  $\Delta_{\text{long}}$  in Figure 2.6. The propagated speed and density are given in the next subsection, and we note that we systematically assume the upstream solar wind flows along the Sun-comet line.

#### 2.3.4 Integrated moments

Using ICA data, plasma moments of order 0 and 1 were integrated, as well as the mean speed, according to the method presented in Section 2.3.1.2 and developed in Appendix B. These moments are compared to solar wind parameters estimation upstream of 67P/CG, as presented in Section 2.3.3. The results are given in Figure 2.7.

In this figure, one can already see that a period exists during which protons were not detected, centred on perihelion. This solar wind ion cavity is discussed in Chapter 5. Additionally, the solar wind protons have lost very little kinetic energy, as long as they were observed, close to the nucleus, whereas their density is plummeting rapidly.

### 2.4 NUMERICAL MODEL

#### 2.4.1 Leo, a light-weighted, simplified, and fast self-consistent hybrid model

Numerical models are major scientific tools, as well as a key support for experimental data analysis. For this project, we have implemented

a self-consistent hybrid plasma model, answering to the same need for simplicity which has guided most of the efforts presented in this thesis. To some extent, these simulations are used for direct comparison with the in situ data. But most importantly, they allow to extend the description of the cometary plasma environment given by the one-point measurements, close to the nucleus, to the much larger scales, the "big picture". Often, this is a mandatory check-point in order to conclude anything on the plasma environment of 67P/CG, and more specifically for large spatial scales. However, we will encounter a limitation to this synergy between experimental and numerical approaches, specific to a comet plasma environment. As introduced in the previous chapter, a cometary atmosphere extends over millions of kilometres. And indeed, the important obstacle to the solar wind is primarily this enormous, partially ionised atmosphere, instead of the much less extended ionosphere, as is the case at other unmagnetised bodies. However the small scales close to the nucleus are the ones probed by *Rosetta*, and we will see along the thesis that these small scales reveal fascinating physics. Therefore, in order to be accurate *and* of interest, a simulation has to ideally cover spatial scales from millions of kilometres to tens of kilometres and less. No proper kinetic numerical approach exists for such a problem, as of yet. Some models, in the context of 67P/CG, use refined meshes where details need to be resolved [2, 46, 81]. In this thesis, we use a regular grid, which translates in a limited resolution (down to 50 km) in the innermost coma.

As plainly put by Valentini et al. [91]: *"In many situations, the understanding of the complex plasma dynamics requires to set up a model where the degree of realism can be even rather poor (for example simplified and or reduced geometry, etc.), but it allows one to isolate and study the physical processes underlying the system evolution."* The aim of the model is indeed not the highest degree of realism. Before understanding the effect of higher order phenomena on the interaction (asymmetric neutral outgassing, ion-neutral interactions, etc.), we will see that many relevant aspects of the dynamics emerge from the simplest configuration: a spherically symmetric cloud of newly born ions continuously added to the solar wind. The precise aim is to solve in a self-consistent manner the same simple situations that we try to tackle analytically in the next chapters. Eventually and when the spatial scales allow it, the in situ data have the last word to judge the relevance of the analytical, semi-analytical and numerical approaches.

The new solver was implemented in a very similar manner as the hybrid-FLASH code, developed in Holmström [52, 53] and used in the context of 67P/CG in Behar et al. [9, 11] and Lindkvist et al. [60]. The development of the model was therefore extensively guided by previous results, and largely benefited from the experience in kinetic modelling from Mats Holmström, Jesper Lindkvist, and especially Shahab Fatemi.

Beyond the benefit of implementing a model from scratch (in terms of plasma physics and numerical methods), the solver is entirely de-

signed to run on one CPU-GPU<sup>2</sup> pair, which greatly enhances the performance when compared to parallel codes ran on CPUs. A GPU is a piece of hardware present on all modern computers, tablets and smart phones, which allows for tremendous amounts of parallel calculations (above 5000 parallel threads on current high-performance GPU). An extended comparison between CPU-based and GPU-based hybrid solvers is found in Fatemi et al. [34], which presents the first hybrid solver entirely implemented on a GPU. The reference simulation used along the next chapters is ran on a commercial laptop for a reasonable spatial resolutions (down to 100 km) in about an hour and a half, and using a dedicated high-performance GPU the resolution can be enhanced to 50 km and simulations are completed in about 15 hours.

The code is named *Leo* in reference to Leo Haser and its simple model of a cometary atmosphere density, systematically used in the following work and in the solver. *Leo* is designed to be a simplified, lightweighted, and fast self-consistent solver to study the interaction between the solar wind and a cometary atmosphere. Its high performance allows for simplified, lighter usage and handling of simulations, and enables a larger exploration of the parameter space (physical and numerical).

#### 2.4.2 Hybrid modeling of plasmas

**Governing equations** – In hybrid models, ions are treated as particles, and electrons as a massless, charge-neutralising fluid. In other words, we assume that the plasma is overall quasi-neutral,  $n_e = n_i$ . The trajectory of a particle,  $\mathbf{r}(t)$  and  $\mathbf{v}(t)$ , with charge  $q$  and mass  $m$ , is given by the solution of the equation of motion with the Lorentz force,  $\mathbf{F}$ :

$$\frac{d\mathbf{r}}{dt} = \mathbf{v}, \quad \frac{d\mathbf{v}}{dt} = \frac{\mathbf{F}}{m} = \frac{q}{m} (\mathbf{E} + \mathbf{v} \times \mathbf{B}), \quad (2.20)$$

where  $\mathbf{E} = \mathbf{E}(\mathbf{r}, t)$  is the electric field and  $\mathbf{B} = \mathbf{B}(\mathbf{r}, t)$  is the magnetic field. The particles' motion is integrated in time using a scheme similar to the leap-frog scheme. However, we note that any model solving the motion of particles under the Lorentz force cannot use a symplectic scheme (such as the leap-frog scheme), because the acceleration  $d^2\mathbf{x}/dt^2$  of a particle cannot be written as a function of the position  $\mathbf{x}$ ,  $F(\mathbf{x})$ , but only as a function of both the velocity and the position,  $F(\mathbf{x}, \mathbf{v})$ . A similar situation is met for advancing the magnetic field in time. Therefore for a purely self-consistent solver, the position and the velocity of the particles have to be calculated at each and every half time-step, unlike in the leap-frog scheme.

In this model, the variables that are propagated through time are the particle positions and velocities, and the magnetic field. A major equation which allows to calculate the electric field at any time with no information on the previous time-step is the generalised Ohm's law,



derived from the electron momentum equation, which can be written as

$$\mathbf{E} = \frac{1}{\rho_i} (-\mathbf{J}_i \times \mathbf{B} + \mathbf{J} \times \mathbf{B} - \nabla p_e) + \eta \mathbf{J}, \quad (2.21)$$

where  $\rho_i$  is the ion charge density,  $\mathbf{J}$  is the total current,  $\mathbf{J}_i$  is the ion current,  $p_e$  is the electron pressure, and  $\eta$  is the resistivity. The displacement current  $\partial_t \mathbf{E}$  is neglected from the Ampère-Maxwell's law (corresponding to neglect very high frequencies), which allows us to calculate the total current from the magnetic field as

$$\mathbf{J} = \mu_0^{-1} \nabla \times \mathbf{B}, \quad (2.22)$$

with  $\mu_0 = 4\pi \cdot 10^{-7}$  H/m the vacuum permeability, or magnetic constant. One more equation is needed to describe the pressure of the plasma. We have already assumed that  $n_e = n_i$ . A polytropic energy relation is used to calculate the electron pressure using the ion density. In the simulations we will analyse, an adiabatic index was chosen, corresponding to  $\gamma = 5/3$ . The pressure is then given by

$$p_e = \frac{k_B}{e} \rho_{i,\infty}^{1-\gamma} T_{e,\infty} \rho_i^\gamma, \quad (2.23)$$

with  $k_B$  the Boltzmann constant,  $e$  the elementary charge,  $\rho_{i,\infty}$  and  $T_{e,\infty}$  the ion charge density and electron temperature upstream of the interaction region.

Finally, the Faraday's law allows one to advance the magnetic field in time,

$$\frac{\partial \mathbf{B}}{\partial t} = -\nabla \times \mathbf{E}. \quad (2.24)$$

Because handling grid values is computationally cheaper than handling particles, the magnetic field is advanced in time using sub-cycles (15 in our case).

The algorithm of the solver is graphically represented and discussed in Appendix D.

**The trick of the resistivity** – Equation (2.21) is obtained by first deriving a momentum conservation equation for the electron fluid from the Vlasov equation. In the momentum equation, the term  $\eta \mathbf{J}$  appears and represents the collisional drag between ions and electrons, with the resistivity  $\eta$  (originally a tensor) describes “*short wavelength, high frequency anomalous wave-particle scattering [...], instabilities not explicitly included in the hybrid model*” [93]. This resistive term eventually ends up in the generalised Ohm's law. Since we do not want to simulate such high order processes, the resistivity  $\eta$  should ideally be zero in our model.

However a small value of this term also has the property of damping small numerical scale oscillations which appear because of the finite difference methods classically used in hybrid solvers to compute derivatives. The smaller the cell-size is, the smaller the resistivity is

needed to damp these numerical oscillations. Therefore the higher the resolution we simulate, the more physical the results gets. In particular, we observed that the resistivity has an important impact on detailed aspects of the solar wind ion dynamics analysed in this work. To that extent, the resistivity is both a numerical asset and a physical drawback.

**Set-up of a simplified comet** – In Chapter 4, Section 4.2, we introduce the Haser model of a neutral cometary atmosphere, which provides an analytical expression of the neutral density  $n_0$ . The cometary new-born ions are introduced in the simulation box using the rate

$$q_i(r) = v_i n_0(r). \quad (2.25)$$

with  $v_i$  the ionisation rate of neutral molecules. Every time step, we introduce a spherical cloud of static cometary ions (neglecting their initial speed compared to the speed of the solar wind protons), distributed according to  $n_0$ , which follows a  $r^{-2}$  profile over the simulated spatial scales (see Section 4.2). The motion of these new-born ions is then solved according to the electric and magnetic fields, and the electric and magnetic fields are solved according to the total ion density. The solar wind is composed entirely of protons, we neglect the 5% of heavier alpha particles  $\text{He}^{++}$ .

The simulations are made in the CSE reference frame introduced in Section 2.2.3. The Interplanetary Magnetic Field (IMF) is assumed to be along the  $y_{\text{CSE}}$ -axis (no Parker spiral angle).

The upstream electric field is given by  $\mathbf{E}_\infty = -\mathbf{v}_\infty \times \mathbf{B}_\infty$ , where  $\mathbf{v}_\infty$  is the undisturbed solar wind bulk velocity, and  $\mathbf{B}_\infty$  is the IMF which is initially homogeneous everywhere.

Two different runs are used in the thesis. The first is the reference run, at a heliocentric distance of 2.0 au, and against which the analytical and semi-analytical results are tested. The second corresponds to a heliocentric distance of 1.7 au. Their physical parameters are summarised in the next chapters, in Tables 4.1 and 6.1.

## COLLISIONLESS EXCHANGE OF MOMENTUM: A GENERALISED GYROMOTION

We aim at understanding better how two plasmas interact, react to each other, when being mixed and in the absence of collisions. In such a case, all information is transferred through the electric and magnetic fields. In this chapter, we propose to look at how momentum is transferred between the plasmas for scales shorter than a gyroperiod (see the motivations in Chapter 1), and we illustrate the proposed model with experimental results.

### 3.1 THE GENERALISED OHM'S LAW

Our starting point is the simplified generalised Ohm's law, in which the electron inertia terms and the resistivity/collisions are neglected (see for example Valentini et al. [91] for a derivation). The plasma is weakly magnetised and quasi-neutral. The system is considered to be at steady state:  $\partial_t \cdot \equiv 0$ . The characteristic length, time, and velocity of the system are noted  $\ell$ ,  $t$  and  $u$ .  $\mathbf{E}$  and  $\mathbf{B}$  are the electric and the magnetic fields,  $\mathbf{u}_i$  the average velocity of all charges carried by ions,  $n$  the plasma number density,  $e$  the elementary charge,  $\mathbf{J}$  the electric current and  $p_e$  the electron pressure, considered isotropic here.

*Part of the content of this section is adapted from Behar et al. [11].*

$$\mathbf{E} = \underbrace{-\mathbf{u}_i \times \mathbf{B}}_{\mathbf{E}_u} + \underbrace{\frac{1}{ne} \mathbf{J} \times \mathbf{B}}_{\mathbf{E}_{\text{Hall}}} - \underbrace{\frac{1}{ne} \nabla p_e}_{\mathbf{E}_{\text{ambi}}} . \quad (3.1)$$

The electric field exhibits three distinct components: the motional (or convective) electric field  $\mathbf{E}_u$ , the Hall term  $\mathbf{E}_{\text{Hall}}$  (rising from currents perpendicular to the magnetic fields) and the ambipolar polarisation term  $\mathbf{E}_{\text{ambi}}$  (originating from electron pressure gradients and departure from quasi-neutrality). We are interested in the conditions – if any – for which the Hall and the ambipolar polarisation terms are negligible compared to the motional term, i.e.  $\mathbf{E}_u \gg \mathbf{E}_{\text{Hall}}$  and  $\mathbf{E}_u \gg \mathbf{E}_{\text{ambi}}$ . We are therefore interested in orders of magnitude estimates. The following approximation can be used to estimate orders of magnitude of the derivative of the physical parameter  $f$  with respect to the dimension  $x$ , using the characteristic (or background) value  $f_0$  of that parameter and the characteristic length  $\ell_f$  over which  $f$  changes significantly.

$$\frac{\partial f}{\partial x} \sim \frac{f_0}{\ell_f} \quad (3.2)$$

Note that  $\ell_f$  and  $f_0$  are local values, and may depend on  $x$ . We first consider the Faraday's law, the Ampère's law and the Lorentz force, and their corresponding orders of magnitudes.

$$\begin{aligned}
 \text{Faraday: } \nabla \times \mathbf{E} &= \partial_t \mathbf{B} \Rightarrow E/\ell \sim B/t \\
 &\Rightarrow E \sim uB \\
 \text{Ampère: } \nabla \times \mathbf{B} &= \mu_0 \mathbf{j} \Rightarrow B/\ell \sim \mu_0 j \\
 \text{Lorentz force: } \mathbf{F} &= e(\mathbf{E} + \mathbf{u} \times \mathbf{B}) \Rightarrow m u/t \sim e(E + u B) \\
 &\Rightarrow B t \sim m/e
 \end{aligned} \tag{3.3}$$

This allows one to rewrite the ordering  $\mathbf{E}_u \gg \mathbf{E}_{\text{Hall}}$  as

$$\begin{aligned}
 |\mathbf{u}_i \times \mathbf{B}| &\gg 1/(n e) |\mathbf{j} \times \mathbf{B}| \\
 \Rightarrow \frac{u B n e}{j B} &\gg 1 \\
 \Rightarrow l^2 &\gg \frac{B t}{n e \mu_0} \\
 \Rightarrow l &\gg \frac{c}{\sqrt{\frac{e^2 n}{\epsilon_0 m}}} \\
 \Rightarrow l &\gg d_i .
 \end{aligned} \tag{3.4}$$

In a collisionless non-resistive plasma, the ion inertial length  $d_i$  is the length below which the ions and the electrons decouple. Looking at scales larger than  $d_i$ , the currents perpendicular to the magnetic field are a negligible source of electric field.

For the second ordering  $\mathbf{E}_u \gg \mathbf{E}_{\text{ambi}}$ , one needs to introduce the characteristic length of the pressure gradient  $\ell_P$ .

$$\begin{aligned}
 |\mathbf{u}_i \times \mathbf{B}| &\gg \frac{1}{n e} |\nabla \mathbf{P}_e| \\
 \Rightarrow u B &\gg \frac{P_e}{n e \ell_P} \\
 \Rightarrow \ell_P &\gg \frac{n k_B T_e}{n e u B} \\
 \Rightarrow \ell_P &\gg \frac{r_e v_{\text{the}}}{u} .
 \end{aligned} \tag{3.5}$$

$r_e = m_e u_e / (e B)$  is the electron gyroradius and  $v_{\text{the}} = \sqrt{2 k T_e / m_e}$  the electron thermal speed.

At the scales  $\ell \gg d_i$  and  $\ell_p \gg \frac{r_e v_{\text{the}}}{u}$ , the electric field is reduced to

$$\mathbf{E} = -\underline{\mathbf{u}}_i \times \mathbf{B} . \quad (3.6)$$

### 3.2 GENERALISED GYROMOTION

We are now interested in the general dynamics of the interaction between two collisionless beams of plasma only subject to the Lorentz force, over length scales such that the electric field is given by equation (3.6).

In the context of this work, the subscripts *sw* and *com* are used for parameters and values of respectively the solar wind ion and the cometary ion populations.

The average velocity of all ions in the case of two beams can be reduced to only two terms:

$$\begin{aligned} \underline{\mathbf{u}}_i &= \zeta_{\text{sw}} \underline{\mathbf{u}}_{\text{sw}} + \zeta_{\text{com}} \underline{\mathbf{u}}_{\text{com}} , \\ \zeta_{\text{sw}} &= \frac{n_{\text{sw}} q_{\text{sw}}}{n_{\text{sw}} q_{\text{sw}} + n_{\text{com}} q_{\text{com}}} ; \zeta_{\text{com}} = \frac{n_{\text{com}} q_{\text{com}}}{n_{\text{sw}} q_{\text{sw}} + n_{\text{com}} q_{\text{com}}} . \end{aligned} \quad (3.7)$$

In the absence of any other force than the Lorentz force, the dynamics for a single particle in either of the two populations is described by the following system of ordinary differential equation:

$$\begin{aligned} \dot{\underline{\mathbf{u}}}_{\text{sw}} &= q_{\text{sw}} / m_{\text{sw}} (\mathbf{E} + \underline{\mathbf{u}}_{\text{sw}} \times \mathbf{B}) \\ \dot{\underline{\mathbf{u}}}_{\text{com}} &= q_{\text{com}} / m_{\text{com}} (\mathbf{E} + \underline{\mathbf{u}}_{\text{com}} \times \mathbf{B}) . \end{aligned} \quad (3.8)$$

Considering two initially perfect beams in velocity space, we have  $\underline{\mathbf{u}}_k = \underline{\mathbf{u}}_k$ : all particles of a same population have the same velocity and experience the same force at the same time.

Without loss of generality, we can choose a reference frame in which the magnetic field is along the  $y$ -axis,  $\mathbf{B} = B \hat{\mathbf{y}}$ . With (3.6), (3.7), (3.8), and  $q_{\text{sw}} = q_{\text{com}} = q$ :

$$\begin{aligned} \dot{\underline{\mathbf{u}}}_{\text{com}} &= \frac{q \zeta_{\text{sw}} B}{m_{\text{com}}} (\underline{\mathbf{u}}_{\text{com}} - \underline{\mathbf{u}}_{\text{sw}}) \times \hat{\mathbf{y}} \\ \dot{\underline{\mathbf{u}}}_{\text{sw}} &= -\frac{q \zeta_{\text{com}} B}{m_{\text{sw}}} (\underline{\mathbf{u}}_{\text{com}} - \underline{\mathbf{u}}_{\text{sw}}) \times \hat{\mathbf{y}} . \end{aligned} \quad (3.9)$$

We can already see that the particles are not accelerated along the direction of the magnetic field. An important result is that the velocity of the centre of mass of the two beams defined as

$$\underline{\mathbf{v}}_i = \frac{n_{\text{sw}} m_{\text{sw}}}{n_{\text{sw}} m_{\text{sw}} + n_{\text{com}} m_{\text{com}}} \underline{\mathbf{u}}_{\text{sw}} + \frac{n_{\text{com}} m_{\text{com}}}{n_{\text{sw}} m_{\text{sw}} + n_{\text{com}} m_{\text{com}}} \underline{\mathbf{u}}_{\text{com}} \quad (3.10)$$

is conserved through time,  $\dot{\underline{\mathbf{v}}}_i = \mathbf{0}$ . This holds over spatial scales shorter than  $\ell$  and  $\ell_p$  and if no mass is added. Thus a local inertial

*Part of the content of this section is adapted from Behar, Tabone, and Nilsson [7] and Behar et al. [11].*

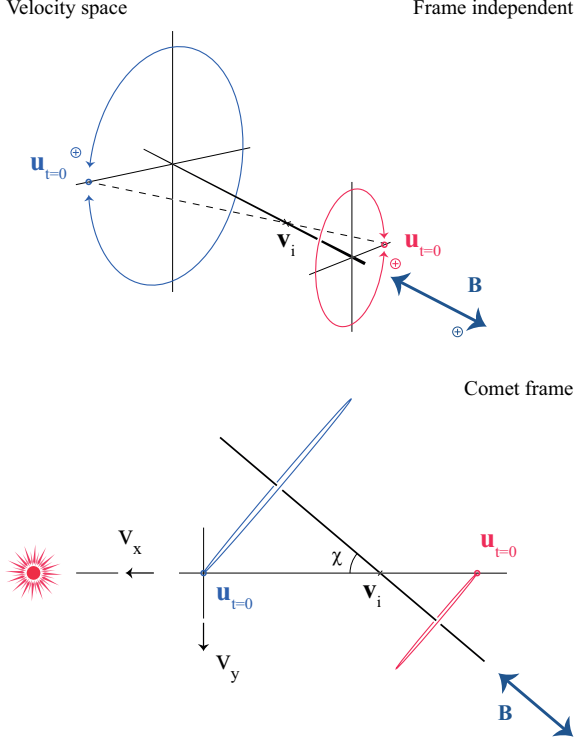


Figure 3.1: Evolution in velocity space of two interacting plasma beams (generalised gyromotion), for two opposite senses of the magnetic field, frame independent (top) and within a chosen frame (bottom). In this frame, the magnetic field lies in the  $(x, y)$ -plane. Applied to the situation at the comet, blue is used for the cometary ions, and red for the solar wind ions.

frame in which  $\mathbf{v}_i = \mathbf{0}$  exists, and is referred to as the 'centre-of-mass reference frame'. In this frame, the magnetic field may very well be along any axis, and the velocities of the two beams become

$$\mathbf{u}_{\text{sw}} = -\frac{n_{\text{com}}m_{\text{com}}}{n_{\text{sw}}m_{\text{sw}}}\mathbf{u}_{\text{com}} \quad (3.11)$$

Rewriting (3.9):

$$\left| \begin{aligned} \dot{\mathbf{u}}_{\text{sw}} &= \frac{qB\tilde{\zeta}_{\text{com}}}{m_{\text{sw}}} \left( 1 + \frac{n_{\text{sw}}m_{\text{sw}}}{n_{\text{com}}m_{\text{com}}} \right) \mathbf{u}_{\text{sw}} \times \hat{\mathbf{y}} \\ \dot{\mathbf{u}}_{\text{com}} &= \frac{qB\tilde{\zeta}_{\text{sw}}}{m_{\text{com}}} \left( 1 + \frac{n_{\text{com}}m_{\text{com}}}{n_{\text{sw}}m_{\text{sw}}} \right) \mathbf{u}_{\text{com}} \times \hat{\mathbf{y}} \end{aligned} \right. \quad (3.12)$$

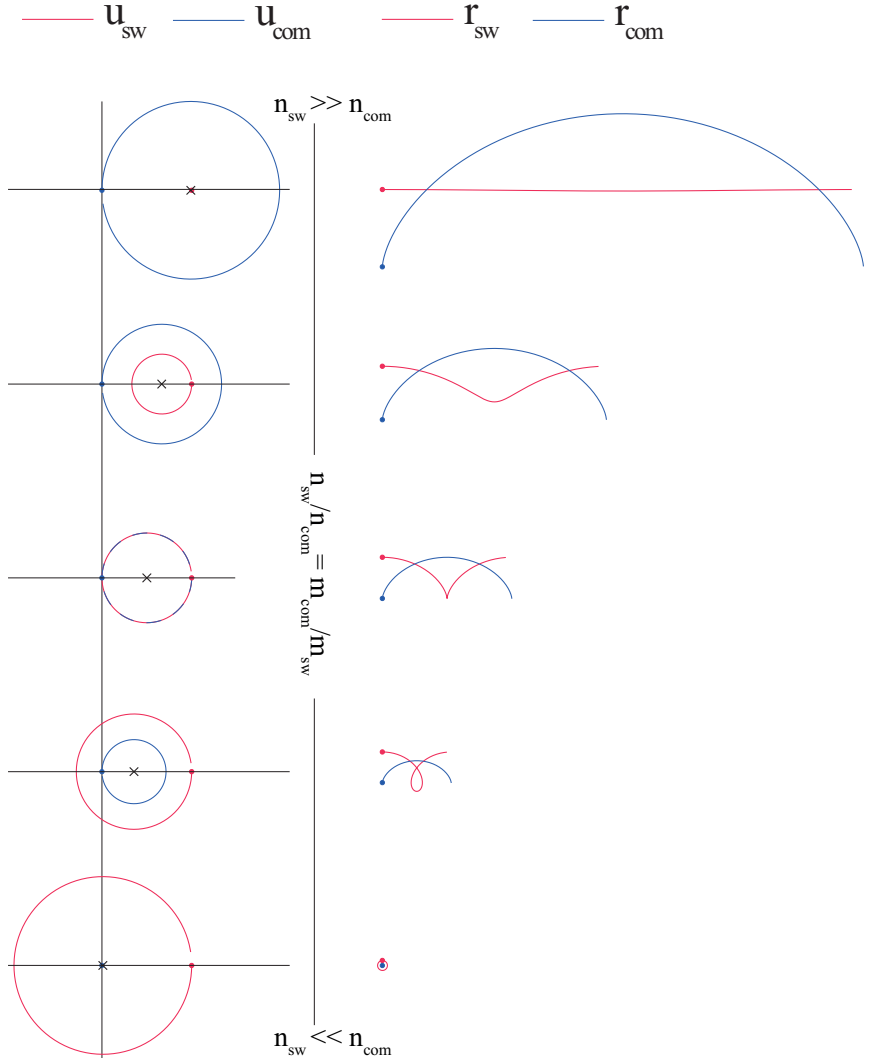


Figure 3.2: Evolution of both populations in velocity (left) and physical (right) space. The first row shows the situation when the solar wind ions dominate, the last row illustrates the opposite.

These equations of motion have the form  $\dot{\mathbf{u}} = \omega \mathbf{u} \times \hat{\mathbf{y}}$ , with the solution:

$$\mathbf{u} = u \begin{pmatrix} \cos(\omega t + \varphi) \\ u_{\parallel} \\ \sin(\omega t + \varphi) \end{pmatrix}. \quad (3.13)$$

The two beams move along circles in velocity space, with one point given by the initial conditions. The planes containing the circles are perpendicular to the magnetic field. In the centre-of-mass reference frame in which the magnetic field is along the  $y$ -axis, the circles are centred on the point  $(0, u_{\parallel}, 0)$ , also given by the initial conditions. This configuration in velocity space is independent of any change of inertial frame, and is illustrated in Figure 3.1. The three components of the velocities are all periodic, thus in physical space the single particle trajectories are helices, 3-dimensional trochoids. If one chooses a reference frame in which one of the velocities is canceled at any point, the more classical cycloid motion appears, with singular stopping points (cusps). If additionally the velocities have the same parallel speed  $u_{\parallel}$  (velocity projected along  $\mathbf{B}$ ), the motion is planar and  $u_{\parallel}$  can be chosen to be 0. The generalised gyrofrequency and gyroradii are:

$$\begin{aligned} \mathcal{R}_{\text{sw}} &= |\mathbf{u}_{\text{sw}}|/\omega, \\ \mathcal{R}_{\text{com}} &= |\mathbf{u}_{\text{com}}|/\omega, \\ \omega &= eB \frac{n_{\text{sw}}m_{\text{sw}} + n_{\text{com}}m_{\text{com}}}{(n_{\text{sw}} + n_{\text{com}})m_{\text{sw}}m_{\text{com}}}. \end{aligned} \quad (3.14)$$

One can also always choose an inertial Cartesian frame in which  $\mathbf{u}_{\text{sw}}$  is along the  $x$ -axis, and  $\mathbf{u}_{\text{com}} = 0$ . Such a frame will be referred to as the comet frame, and is used in the lowest panel of Figure 3.1 and in Figure 3.2.  $\mathbf{v}_i$  is shown with a black cross in the left column (velocity space) of Figure 3.2. Both beams describe circles in velocity space with the same angular speed  $\omega$ . The corresponding motion of the ions in physical space is a trochoid, the most general 2-dimensional gyromotion. In the comet frame, the particles of the population *com* describe a more classical cycloid, as they periodically reach a velocity of  $\mathbf{0}$ .

The dynamics depends greatly on the density ratio. If  $n_{\text{sw}} \gg n_{\text{com}}$ , then  $\mathbf{v}_i \sim \mathbf{u}_{\text{sw}}$  (top-part in Figure 3.2), and the seldom cometary ions behave as test particles in the almost undisturbed flow of the population *sw*, a cycloid with a radius equal to the Larmor radius. As the density ratio  $n_{\text{com}}/n_{\text{sw}}$  increases, particles of the population *com* still describe a cycloid, though the corresponding radius decreases. When the density ratio is equal to the inverse of the mass ratio, both populations move along cycloids of equal radii, as seen in the middle panel of Figure 3.2.



This generalised gyromotion is a 3-dimensional description of such a beam-beam interaction. It is the core of the following sections, the mechanism through which momentum is seen as transferred from one population to the other.

### 3.3 SOLAR WIND DEFLECTION, COMETARY ION ACCELERATION

#### 3.3.1 A case study

We have seen that when two plasma beams interact through an electric and a magnetic field, they *orbit* in velocity space around the magnetic field direction, at a constant distance of their common centre of mass. This corresponds to an anti-correlation of their velocity components: when one accelerates upward, the other accelerates downward, when one accelerates leftward, the other accelerates rightward. This result is fairly intuitive, in terms of conservation of momentum. We can actually test this result against data: we expect to see the solar wind deflected and the cometary ions accelerated, each with opposite accelerations: if the solar wind is deflected towards one direction, the cometary ions should move in the “opposite” direction. More properly, if both populations are in the early phase of this gyromotion, we expect to observe them with clock angles (defined in Section 2.2.3)  $180^\circ$  apart, in any of the frames having its  $x$ -axis pointing to the Sun. The magnetic field clock angle observed at the comet should also be observed fairly close to  $90^\circ$  away from both population clock angles. In the Field-Of-View representation of Figure 3.3, this anti-correlation between solar wind protons and cometary pick-up ions is clearly seen: from one moment to the other, the populations (blue and red) are flowing in opposite “sides” of the Sun’s direction, in orange. Depending on the variable orientation of the upstream magnetic and electric fields, the two flow directions are evolving as well in the instrument’s field of view (instrument-fixed reference frame).<sup>1</sup>

In the same Figure 3.3, the clock angles of the two bulk velocities are given, calculated in the CSEQ reference frame over four days in November 2014, as the comet was at a distance from the Sun of about 2.9 au. The ion measurements are not continuous, either because the instrument was turned off or because the operation mode wouldn’t provide high angular resolution. We also show the clock angle of the observed magnetic field. We find a clear correlation between these three angles, spaced by about  $90^\circ$  over this period, in perfect agreement with the generalised gyromotion. The solar wind proton clock angle is also shifted of  $180^\circ$  (solid red line in the bottom panel), to illustrate its correlation with the cometary pick up ion clock angle.

The same result was found in the statistical approach of Bercic, L. et al. [13], during a period of about a month, starting a month later.

*Part of the content of this section is adapted from Behar et al. [8].*

<sup>1</sup> The attitude of the slowly moving spacecraft introduces only rare and small effects on these FOV maps.

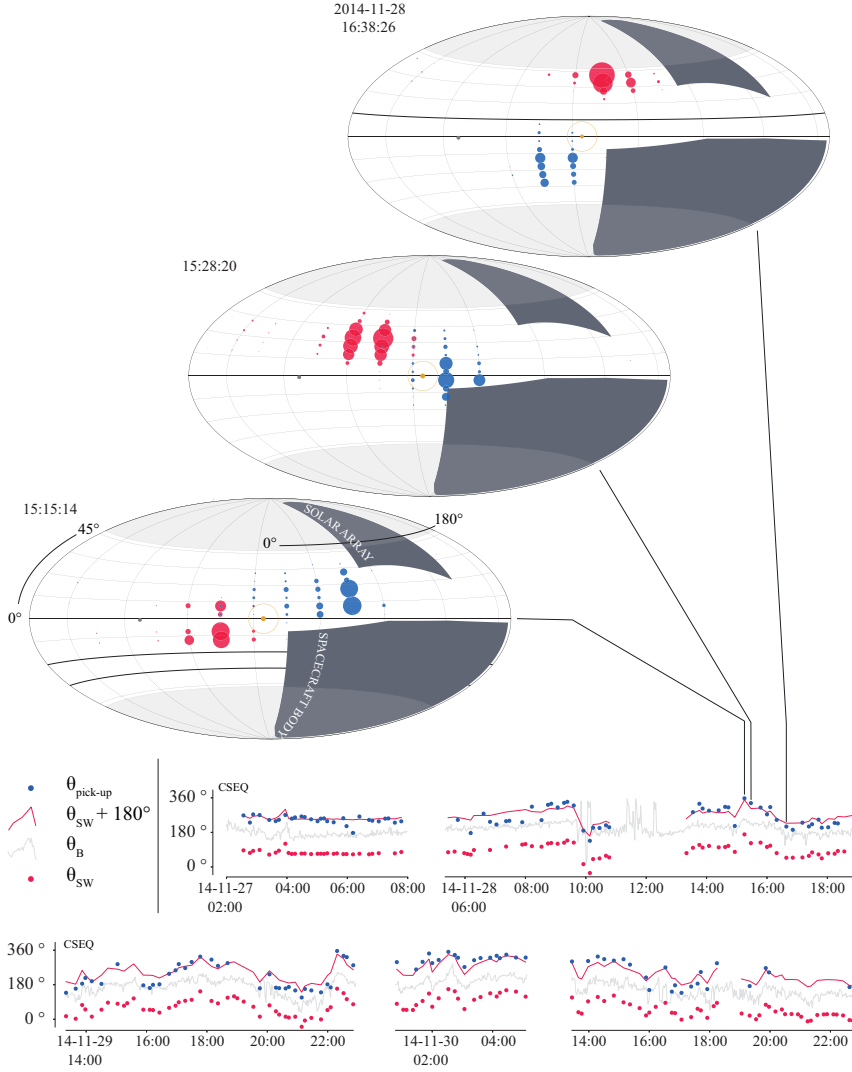


Figure 3.3: Upper panel: Field-Of-View representations, taken at three different times during November 28th. Lower panel: time series of the clock angles of the solar wind proton bulk velocity ( $\theta_{SW}$ , red dots), cometary pick-up ions bulk velocity ( $\theta_{pick-up}$ , blue dots) and magnetic field ( $\theta_B$ , grey solid line) in the CSEQ reference frame. The proton clock angle is also given shifted of  $+180^\circ$  as a red solid line ( $\theta_{SW} + 180^\circ$ ), to illustrate the correlation with the cometary pick-up ion clock angle.

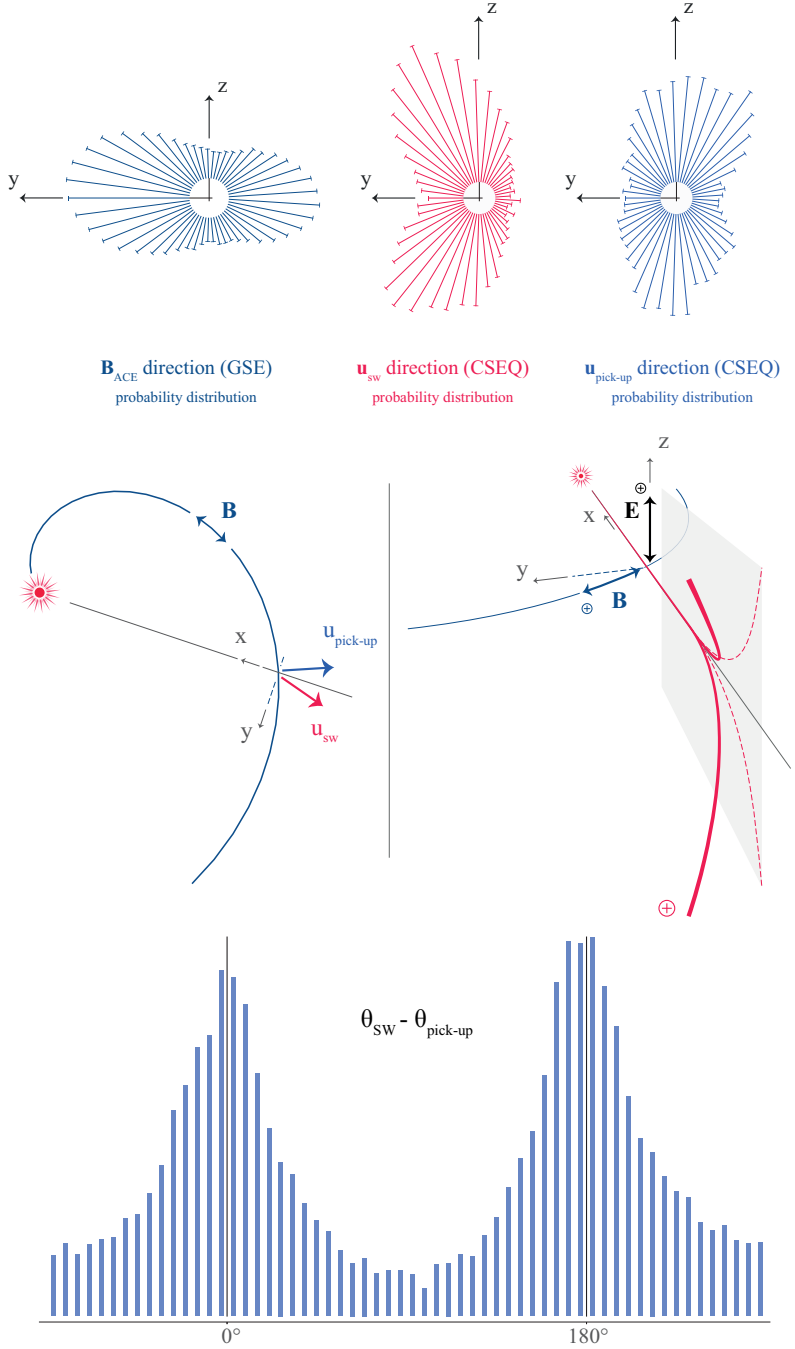


Figure 3.4: Upper panel: Probability distributions of the vector directions projected in the  $(y, z)$ -plane. Middle panel: Schematics of the dynamics, for the solar wind ions (red) and the cometary pick-up ions (blue). No matter the sense of the IMF along the Parker spiral, the solar wind proton velocity will gain a component along the  $+y$ -axis (dusk), while the cometary pick-up ions gain a negative  $-y$ -component (dawn). Lower panel: clock angle difference between the two populations over the entire mission.

Part of the content  
of this section is  
adapted from Behar,  
Tabone, and Nilsson  
[7].

### 3.3.2 Dawn-Dusk asymmetry

Another direct result of the generalised gyromotion can be found in Figure 3.1, bottom panel. When the initial velocities projected along the magnetic field are not equal, the motion of the ions is fully 3-dimensional. We consider the cometary ions initially at rest and at the origin of the velocity space (in the comet reference frame), and the solar wind ions initially flowing along the  $x$ -axis. In this precise frame, the magnetic field has an angle  $\chi$  with the  $x$ -axis, and is within the  $(x, y)$ -plane. The  $v_z$ -component for each species is changing sign every half gyration period. More interestingly, we find that the solar wind beam has a  $v_y$ -component, which is always positive. Conversely, the cometary ions have a  $v_y$ -component always negative. The evolution of the  $v_y$ -component is the same no matter the sense of the magnetic field.

In the comet frame, one can easily derive the velocity of the guiding centres of each population (centres of the two circles), which correspond to the drift of the populations in physical space. In this frame, the cometary ions are drifting perpendicular to the magnetic field, similarly as in the illustration in Coates [20], Figure 2. When the solar wind ions are largely dominating, this tends to the classical  $\mathbf{E} \times \mathbf{B}$ -drift of a test-particle. As the cometary ion density gets larger, the drift speed decreases.

The solar wind ions drift towards the  $+y$ -axis with an angle that depends on the density and mass ratios, which will therefore evolve through the coma, resulting in complex trajectories.

We note however that the problem cannot be reduced to the motion of guiding centres in the case of 67P/CG. Guiding centres are not relevant since ions are only following the early phase of a single gyro-period [10–12]. In other words, ions do not have time to drift.

Using the same data set, we computed the difference of clock angle between the two populations. The initial expectation – based on the case study of Section 3.3.1 – is an angular difference centred on  $180^\circ$ , at 0 order. However, in addition to this peak, a second of comparable magnitude is found centred on  $0^\circ$ , as shown in Figure 3.1. This might either be the result of additional electric field sources (Hall or ambipolar) close to the nucleus and closer to perihelion, or a wrong choice of reference frame: the Sun direction may not be the relevant primary direction, as new born cometary ions are accelerated by an already deflected solar wind (see for example Nicolaou et al. [65]).

The very low complexity of the analysis used for these results, together with the large considered period, highlight how dominant these dynamical aspects are. We now know that on average and for the low-to-medium activity cases, solar wind protons and cometary pick-up ions observed close to the nucleus are flowing in the same plane, also containing the Sun-comet line. On average, the plane

is tilted from the upstream electric field direction. The two populations are flowing either in the same side or in the opposite sides of the Sun-comet line.



## SIMPLE MODELS OF THE COMETARY ENVIRONMENT

We would like to go further than the general drifts and one-point measurement results studied in the previous chapter. We would like to quantify the deflection of the solar wind, over the extended region of interaction. In order to resolve the equation of motion for the solar wind protons in Equation (3.9), we need to express three main parameters, namely the cometary ion density and velocity, and the magnetic field. We remind that the simplified form of the electric field found in the previous chapter is completely given by the magnetic field and the ion dynamics, and does not appear as an independent variable in Equation (3.9).

The aim is not to get detailed and realistic models of these values, to be blindly compared with the data. Instead, we wish to obtain *toy* models, easy to manipulate (analytical or semi-analytical), and that will be representative of one or several major aspects of the ion density, the ion dynamics, and the magnetic field. We are still working in the case of a mildly outgassing nucleus, and are interested in large spatial scales, over which the electric field can be reduced to its motional component.

### 4.1 PARAMETERS

The cometary ions are created by ionisation of the neutral molecules. The latter are created at the centre of the comet at a production rate  $Q$ , and we assume these particles to be water molecules,  $H_2O$ , flowing radially away from the nucleus with the speed  $u_0$ . They are destroyed at a rate  $\nu_d$ , either through ionisation, or photo-dissociation. The cometary ions are created by ionisation of the neutral particles with a rate  $\nu_i$ .

The solar wind is described using its upstream density  $n_\infty$ , together with the norm of the upstream magnetic field  $|\mathbf{B}_\infty|$ . Its angle with the Sun-comet line is assumed to be  $90^\circ$ .

Table 4.1 gives typical values of these various physical quantities together with their evolution with the heliocentric distance  $R$ . At comet Churyumov–Gerasimenko, the creation rate of neutral volatiles  $Q$  was found to be asymmetric around perihelion, with a higher activity after perihelion. A multi-instrument analysis is presented in Hansen et al. [47], resulting in an empirical analytical fit given in Table 1. When necessary, we use the notation  $Q_i$  for the pre-perihelion in-bound leg of the *Rosetta* mission, and  $Q_o$  for the post-perihelion out-bound leg. The drawback of this empirical model is a discontinuity in the value of  $Q$  at perihelion. The value of the destruction rate  $\nu_d$  and the ionisation rate  $\nu_i$  and their dependence on the heliocentric distance is taken from Crovisier [27]. The magnetic field function of

*Part of the content of this chapter is adapted from Behar et al. [11].*

Table 4.1: Nominal parameters and their heliocentric distance evolution.

	1 au	2 au	4 au	Profile
$Q_i$	$2.6 \cdot 10^{28} \text{ s}^{-1}$	$7.5 \cdot 10^{26} \text{ s}^{-1}$	$2.2 \cdot 10^{25} \text{ s}^{-1}$	$\propto R^{-5.10}$
$Q_o$	$1.6 \cdot 10^{29} \text{ s}^{-1}$	$1.1 \cdot 10^{27} \text{ s}^{-1}$	$7.8 \cdot 10^{24} \text{ s}^{-1}$	$\propto R^{-7.15}$
$\nu_i$	$6.5 \cdot 10^{-7} \text{ s}^{-1}$	$1.6 \cdot 10^{-7} \text{ s}^{-1}$	$4.1 \cdot 10^{-8} \text{ s}^{-1}$	$\propto R^{-2}$
$\nu_d$	$1.8 \cdot 10^{-5} \text{ s}^{-1}$	$4.5 \cdot 10^{-6} \text{ s}^{-1}$	$1.1 \cdot 10^{-6} \text{ s}^{-1}$	$\propto R^{-2}$
$n_\infty$	$5.0 \text{ cm}^{-3}$	$1.3 \text{ cm}^{-3}$	$0.3 \text{ cm}^{-3}$	$\propto R^{-2}$
$ \mathbf{B}_\infty $	4.6 nT	2.3 nT	1.2 nT	$\propto (R - \alpha)/R$
$T_e$	$1.48 \cdot 10^5 \text{ K}$	$1.0 \cdot 10^5 \text{ K}$	$0.7 \cdot 10^5 \text{ K}$	$\propto R^{-0.59}$
$T_i$	$7.3 \cdot 10^4 \text{ K}$	$4.9 \cdot 10^4 \text{ K}$	$3.3 \cdot 10^4 \text{ K}$	$\propto R^{-0.57}$
$u_0$	0.7 km/s			
$u_\infty$	400 km/s			

the heliocentric distance can be found in Cravens [25]. The electron temperature radial evolution is taken from Štverák, Trávníček, and Hellinger [87], based on *Helios* data, whereas the proton temperature is taken from Smith, E. J. and Barnes, A. [85] based on *Pioneer 10* and *11* data.

In the following sections and chapters, we use one reference simulation (or reference run) from the self-consistent hybrid model, to test the analytical and semi-analytical results, as well as some aspects of the experimental data. The model simulates the interaction at a heliocentric distance of 2 au, and the parameters are given in Table 4.1.

#### 4.2 COMETARY ION DENSITY

The spatial distribution of the cometary ions is a major ingredient of the model, as it defines what obstacle is presented to the solar wind. Many efforts have been proposed over the decades to model this density, most of the time with a focus on the inner region of the coma (cf. Cravens [24], Galand et al. [37], and Gombosi [43]). Our own effort focuses on the large scales of the coma, and will not account for any detailed ion composition and dynamics in the inner coma, which were one of the nice problems tackled using *Rosetta* data with the studies of Heritier et al. [50, 51]. We keep the model as simple as possible, both for commodity (the model of the density is only a step towards solving the dynamics of the solar wind ions) and with the same motivation to separate the fundamental features from the detailed features, for large scales.



The cometary atmosphere is assumed to have a spherical symmetry. For this exercise, the size of the nucleus is neglected, and so is its mass: the neutral elements, produced at a rate  $Q$  at one point-source, are expanding radially in all directions with a constant speed  $u_0$ . By writing the equation of continuity with source terms on the cometary neutral density  $n_0$ , we get in this spherical symmetry:

$$\frac{1}{r^2} \frac{d(r^2 n_0 u_0)}{dr} = -\nu_d n_0, \quad (4.1)$$

with the following solution established and used by Haser [48]:

$$n_0(r) = \frac{Q}{4\pi u_0 r^2} \cdot e^{-r/R_d} \quad ; \quad R_d = u_0 / \nu_d. \quad (4.2)$$

We see that for radial distances lower than the radius  $R_d$ , the neutral molecule density is barely affected by the destruction term: the density of cometary ions is negligible compared to the neutral density, the plasma is only weakly ionised. This means that despite the ion-ion collisions being absent, the ion-neutral collisions may (and will) take place, leading to an additional ionisation source for the neutral molecules (through charge exchange processes) and to ion-neutral drag. These aspects are neglected in the present work, but not forgotten entirely, and we will come back on these processes in the next sections.

The cometary ions have the initial radial velocity  $u_0$  but will immediately be accelerated by the local electric and magnetic fields, to eventually escape the region of the denser coma. We separate the ionised coma into two different cometary ion components: the new-born cometary ions first, which are the main obstacle to the solar wind, and second the accelerated (or pick-up) cometary ions. The dynamics of the first population is assumed to be trivial: the new-born cometary ions move radially away from the nucleus with the same speed as the neutral molecules. The dynamics of the second however is much more complex, driven by the exchange of energy and momentum that the previous section only approached, so that the pick-up cometary ions leave the system quicker than they would have ballistically. New born ions become pick-up ions with the rate  $\nu_{ml}$ . Accordingly, a destruction term appears in the continuity equation of the new-born cometary ions, on which we now focus:

$$\frac{1}{r^2} \frac{d(r^2 n_{com} u_0)}{dr} = \nu_i n_0 - \nu_{ml} n_{com}. \quad (4.3)$$

With  $R_i = u_0 / \nu_i$  and  $R_{ml} = u_0 / \nu_{ml}$

$$n_{com}(r) = \frac{1}{R_i} \frac{R_d R_{ml}}{R_d - R_{ml}} \left( 1 - e^{-r \left( \frac{1}{R_{ml}} - \frac{1}{R_d} \right)} \right) \cdot n_0(r). \quad (4.4)$$

Three characteristic radii are found in the density profile. In the previous Section 4.1 and through Chapter 5, we find that  $R_{ml} \ll R_d < R_i$ , as the time needed to significantly accelerate new-born cometary ions is orders of magnitude lower than the characteristic time of ionisation

and photo-dissociation of the neutral particles. The profile is then simplified to

$$n_{\text{com}}(r) = \frac{R_{\text{ml}}}{R_{\text{i}}} \frac{Q}{4\pi u_0} \left(1 - e^{-r/R_{\text{ml}}}\right) e^{-r/R_{\text{d}}} \cdot r^{-2} \quad (4.5)$$

For  $r < R_{\text{ml}}$ , *i.e.* before the new born ions are accelerated and neglected,  $n_{\text{com}}(r < R_{\text{ml}})$  is proportional to  $1/r$ , a result observed at comet Churyumov–Gerasimenko in the first  $\sim 200$  km from the nucleus, and discussed by Edberg et al. [31].<sup>1</sup> At the larger scales we are interested in,  $R_{\text{ml}} \ll r \ll R_{\text{d}}$ , the neutral and the ion densities are proportional, while the exponential term of the neutral molecule destruction is still negligible. We get

$$n_{\text{com}}(r) = \frac{R_{\text{ml}}}{R_{\text{i}}} \frac{Q}{4\pi u_0} \cdot r^{-2} \quad [m^{-3}] \quad (4.6)$$

Since a point source of neutral molecules was assumed all along, both density profile expressions contain a singularity at the very centre of the comet, either with the slope  $r^{-1}$  for the first, or  $r^{-2}$  for the second. In anticipation to Chapter 5, we propose an alternative expression of the cometary ion density cancelling this singularity, by adding a constant slope in the inner-most cometary ion density. Inevitably, such a modified profile is not a solution to the continuity equation proposed above, and only inherits from it the  $r^{-2}$  slope at large scales. This flat profile around  $r = 0$  is given by the additional term  $(1 - e^{-r/R_0})$  in the following expression.  $R_0$  is the radial extent of this inner region with constant cometary ion density. Additionally, we replace the radius  $R_{\text{ml}}$  by an arbitrarily chose radius  $R_1$ .

$$n_{\text{com}}(r) = \frac{R_{\text{ml}}}{R_{\text{i}}} \frac{Q}{4\pi u_0} \left(1 - e^{-r/R_0}\right) \left(1 - e^{-r/R_1}\right) e^{-r/R_{\text{d}}} \cdot r^{-2} \quad (4.7)$$

Obviously, the singularity is also avoided if we consider not a point source but a surface source, see for example Heritier et al. [51]. The difference between the profile of Equation (4.5), the simplified one of Equation (4.6), and the "flattened" profile of Equation (4.7) is illustrated in Figure 4.1. Additionally, we extracted the cometary ion density from the reference simulation for identical parameters. The (total) cometary ion density is taken along the Sun-comet line, upstream of the nucleus. The result is given in the upper panel of Figure 4.1 as the

<sup>1</sup> In a very different context, at comet Halley, the similar type of profile was observed by the *Giotto* probe, with a profile following  $r^{-1}$  for cometocentric distances lower than  $10^4$  km and theoretically derived by Cravens [24], and a profile following  $r^{-2}$  for larger heliocentric distances (cf. Balsiger et al. [5]), on each side of the contact surface.

thicker solid red line, which for obvious reasons has a much more limited spatial coverage than the analytical expressions. We find that on average and over the entire simulation box, at distances larger than a few hundreds of kilometres, the density profile follows a slope much steeper than  $r^{-1}$ . A value of  $v_{\text{ml}} = 0.035 \text{ s}^{-1}$ , together with  $R_0 = 40 \text{ km}$  and  $R_1 = 500 \text{ km}$ , gives a great match with the self-consistent density profile.

In these three profiles, we have a steady creation and disappearance of the new-born cometary ions slowly moving with the neutral molecules, and which constitute the bulk mass of the ionised coma, which interacts electromagnetically with the solar wind. The presence of cometary pick-up ions is neglected.

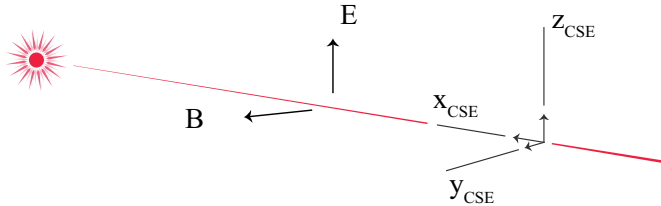
#### 4.3 MAGNETIC FIELD PILE-UP AND DRAPING

Another important term to model in the equation of motion of the protons is the magnetic field  $\mathbf{B}$  within the coma. Considering a magnetic field frozen in the ion fluid (electrons and ions are not decoupled), we first need to express the bulk velocity of that fluid, for which we already have an expression:

$$\mathbf{u}_i = \frac{n_{\text{sw}}}{n_{\text{sw}} + n_{\text{com}}} \mathbf{u}_{\text{sw}} + \frac{n_{\text{com}}}{n_{\text{sw}} + n_{\text{com}}} \mathbf{u}_{\text{com}} .$$

Our goal is to solve  $\mathbf{u}_{\text{sw}}$ , therefore necessarily some more assumptions have to be made in order to simplify the total ion velocity and remove degrees of freedom in the system.

In the Comet-Sun-Electric frame (CSE, defined in Section 2.2.3 and represented once more just below for convenience),  $\mathbf{u}_{\text{com}} \ll \mathbf{u}_{\text{sw}}$ , and based on the cometary ion density profile and the generalised gyromotion, it can be shown that through most of the interaction region,  $\mathbf{u}_i \sim \frac{n_{\text{sw}}}{n_{\text{sw}} + n_{\text{com}}} \mathbf{u}_{\text{sw}}$ .



As  $\mathbf{B}_\infty$  is along the  $y$ -axis (*i.e.* no Parker spiral angle),  $\mathbf{u}_\infty$  along the  $x$ -axis and as the cometary outflow is spherical, the plane  $y = 0$  is a plane of symmetry of the system. Therefore within  $y = 0$ , neither  $\mathbf{v}_i$  nor  $\mathbf{u}_i$  can have a component along  $\hat{\mathbf{y}}$ . But one more simplification is needed to be able to express the magnetic field, and we assume that the total ion velocity remains along the  $x$ -axis. This can be seen as the macroscopic idea that the momentum given to the cometary ions in one direction is balanced by the momentum given to the solar wind

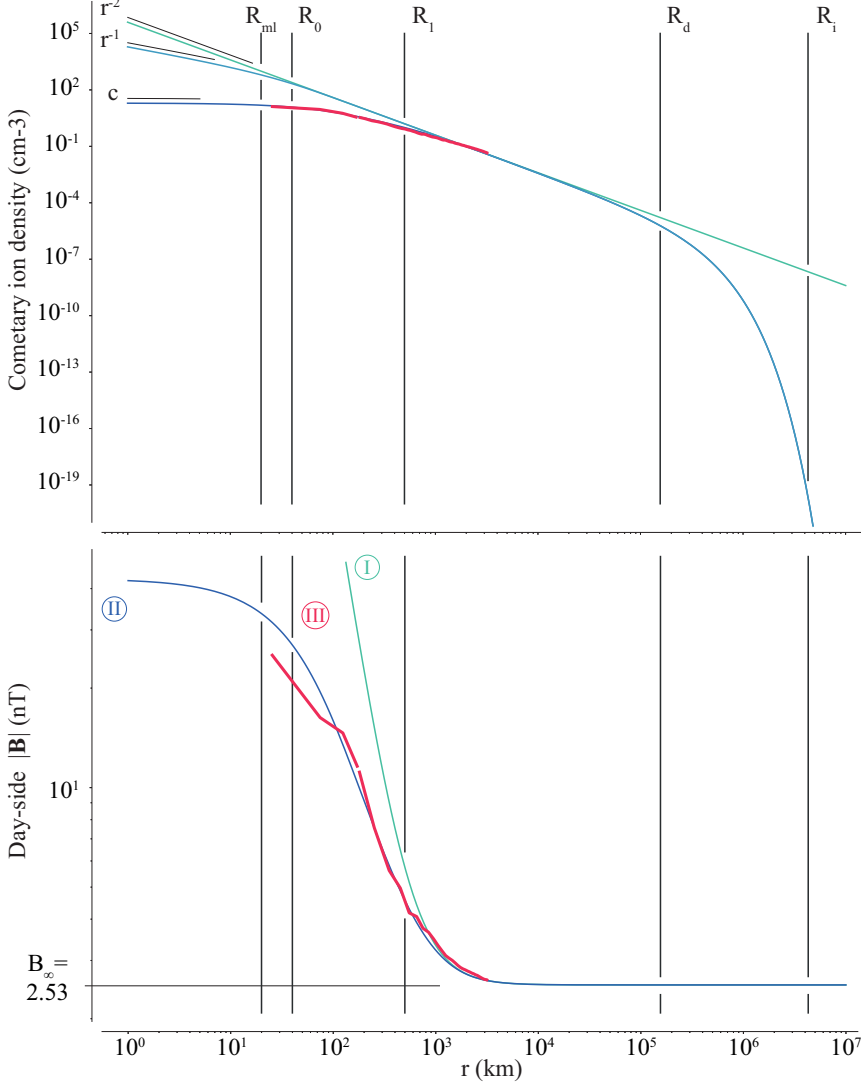


Figure 4.1: Upper panel: Density profiles for equations (4.5), (4.6) and (4.7), as well as from the hybrid reference simulation (red). Lower panel: magnetic field along the day-side comet-Sun line for Equation (4.17) and for the semi-numerical approach (see Section 4.3). The values taken from the hybrid reference simulation are shown as well (red).

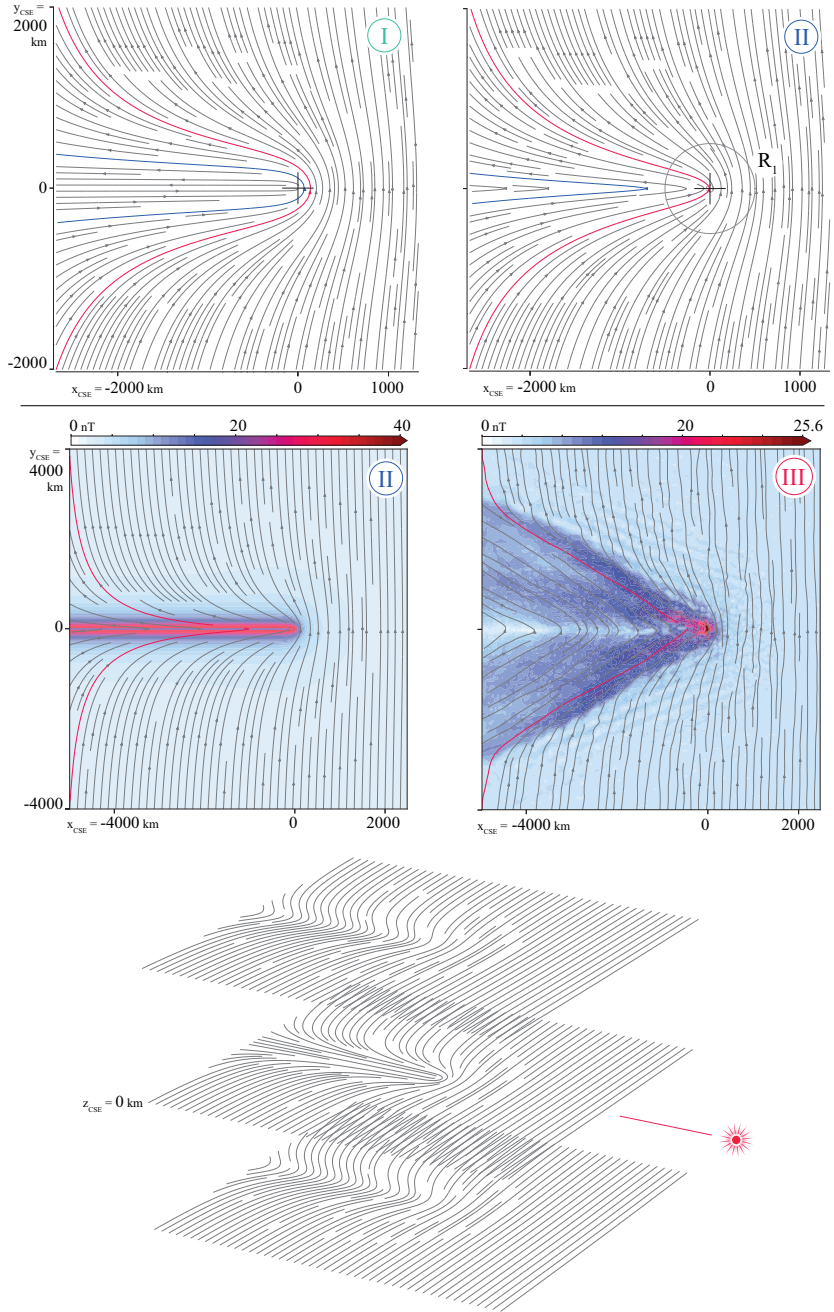


Figure 4.2: Magnetic fields lines in the ( $y_{\text{CSE}} = 0$ )-plane, obtained analytically (upper-left) or numerically (upper-right) using the two different cometary ion density profiles shown in Figure 4.1. The correspondence is given by the coloured numbering. The middle row gives a zoom-out of profile II (left), and a cut through the simulation box of the reference simulation (right). One coloured field line is given in each panel to help the comparison. The last row gives a 3-dimensional representation of profile I.

in the “opposite” direction, over the entire coma. It is admittedly difficult to defend further this necessary assumption locally, everywhere through the coma. We get the following expression:

$$\mathbf{u}_i = \zeta_{\text{sw}} u_\infty \hat{\mathbf{x}} \quad ; \quad \zeta_{\text{sw}} = \frac{n_{\text{sw}}}{n_{\text{sw}} + n_{\text{com}}} . \quad (4.8)$$

From the expression (4.8) of the ion fluid velocity and the expression (3.6) of the electric field, one finds

$$\mathbf{E} = -\mathbf{u}_i \times \mathbf{B} \quad \Rightarrow \quad \begin{cases} E_x = 0 \\ E_y = -\zeta_{\text{sw}} u_\infty B_z \\ E_z = \zeta_{\text{sw}} u_\infty B_y \end{cases} \quad (4.9)$$

The Faraday’s law at steady state gives

$$\nabla \times \mathbf{E} = \mathbf{0} \quad \Rightarrow \quad \begin{cases} \partial_y E_z = \partial_z E_y \\ \partial_x E_z = 0 \\ \partial_x E_y = 0 \end{cases} \quad (4.10)$$

$E_y$  and  $E_z$  do not depend on  $x$  and are therefore given by their up-stream value, namely  $E_{y\infty} = 0$  and  $E_{z\infty} = u_\infty B_\infty$ . In turn

$$\begin{cases} E_y = -\zeta_{\text{sw}} u_\infty B_z = 0 \\ E_z = \zeta_{\text{sw}} u_\infty B_y = u_\infty B_\infty \end{cases} \quad (4.11)$$

$$\begin{cases} B_z = 0 \\ B_y = B_\infty / \zeta_{\text{sw}} = B_\infty \left( 1 + \frac{\alpha}{n_\infty (x^2 + y^2 + z^2)} \right) \end{cases} \quad (4.12)$$

with

$$\alpha = \frac{R_{\text{ml}}}{R_i} \frac{Q}{4\pi u_0 n_\infty} . \quad (4.13)$$

As seen in Equations (4.8) and (4.10), the Faraday’s law cannot give us an information on the last component  $B_x$  of the magnetic field. However, and together with  $B_z = 0$ , another Maxwell’s equation – the so-called magnetic Gauss’s law – gives us

$$\begin{aligned} \nabla \cdot \mathbf{B} &= 0 \\ \Rightarrow \partial_x B_x &= -\partial_y B_y \\ \Rightarrow B_x(x, y, z) + C &= -\int \partial_y B_y \, dx \end{aligned} \quad (4.14)$$

$$\partial_y B_y = \frac{B_\infty \alpha}{n_\infty} \frac{-2y}{(x^2 + y^2 + z^2)^2} . \quad (4.15)$$

Finally

$$B_x + C = \frac{B_\infty \alpha}{n_\infty} y \left( \frac{x}{(y^2 + z^2)(x^2 + y^2 + z^2)} + \frac{\arctan \left( x / \sqrt{y^2 + z^2} \right)}{(y^2 + z^2)^{3/2}} \right) .$$

(4.16)

The constant is given by the upstream condition  $B_x(x \rightarrow \infty) = 0$ . It follows that  $C = \frac{B_\infty \alpha}{n_\infty} y \frac{\pi/2}{(y^2 + z^2)^{3/2}}$ .

$$\begin{cases} B_x = \frac{B_\infty \alpha}{n_\infty} y \left( \frac{x}{(y^2 + z^2)(x^2 + y^2 + z^2)} + \frac{\arctan(x/\sqrt{y^2 + z^2}) - \pi/2}{(y^2 + z^2)^{3/2}} \right) \\ B_y = B_\infty \left( 1 + \frac{\alpha}{n_\infty(x^2 + y^2 + z^2)} \right) \\ B_z = 0 \end{cases} \quad (4.17)$$

A qualitative 3-dimensional representation of this field is given in the lowest part of Figure 4.2, showing the plane ( $z_{\text{CSE}} = 0$ ) containing the point source of the neutral elements through which the magnetic field line cannot be advected, and resulting in a radical draping, discussed shortly after.

We will see in the next chapter that a lot can be done using these simple cometary ion density and magnetic field models, especially in the 2-dimensional case. In order to prepare for the more complex approach done in the last section of Chapter 5 however, we now explore a more complex solutions of the magnetic field.

As previously mentioned, a fundamental limitation of this first model of the magnetic field, given by Equation (4.17) and based on the simplest cometary ion velocity of Equation (4.6), is the general form  $1/r^2$ , appearing in both the strength of the magnetic field (for example in the plane  $y = 0$ ) and in the cometary ion density. The singularity corresponds to a single point in space, at the very centre of the comet, where the electron (or ion) fluid is static. The magnetic field cannot be advected further than this point, which introduces a region just upstream of the singularity where the pile-up of the magnetic field is infinite, an unphysical situation. Further more in the tail region, the magnetic field is purely along the  $x$ -axis, somehow “infinitely draped”, introducing a single current *line*, seen in the upper-left panel of Figure 4.2 showing the magnetic field lines of Equation (4.17), in the plane ( $z_{\text{CSE}} = 0$ ). This is very similar to the seminal picture of the magnetic field draping introduced by Alfvén [1]. Obviously, the resulting magnetic tension would eventually force the advection of the magnetic field through the innermost coma, resulting in a non-static electron fluid. The importance of this aspect in the context of this study (in which we are interested in large spatial scales) is that the influence of a very local and small scale feature (the velocity of the fluid in the innermost coma) extends to large scales in the night-side of the coma, i.e. the tail region, through the magnetic field topology.

A way around this singularity was introduced in the expression of the cometary ion density given in Equation (4.7). We note that such

a constant fluid speed is not far from mimicking the magnetic field advection through a resistive body. However in this case, the complete derivation of the magnetic field cannot be done analytically, and only the  $B_y$  component can be expressed as previously:

$$B_y = B_\infty / \zeta_{sw} = B_\infty \left( 1 + \frac{R_{ml}}{R_i} \frac{Q}{4\pi u_0 n_\infty} (1 - e^{-r/R_0}) (1 - e^{-r/R_1}) r^{-2} \right) \quad (4.18)$$

So we need a trick to get the  $B_x$ -component. We keep the assumption that the total ion fluid flows along the  $x$ -axis, therefore the  $B_z$ -component of the magnetic field remains equal to zero everywhere. From there, we calculate the angle between the magnetic field direction and the  $x$ -axis with a very naive approach. We consider the fluid that has the velocity  $\mathbf{u}_i = \zeta_{sw} u_\infty \hat{\mathbf{x}}$ . If we follow a set of particles that had the same  $x$ - and  $z$ -component far upstream (forming a line perpendicular to the Sun-comet line), they will eventually end up misaligned along the  $x$ -dimension because of the shear of the velocity field. This is precisely what happens to the magnetic field lines, frozen into the electron (or here ion) fluid. We retrieve the angle of the magnetic field at any point in space by integrating numerically the difference of  $x$ -component of two close neighbouring fluid parts. This is indeed almost identical to the last step of the analytical approach proposed above for a simpler (and integrable) expression of the velocity field. With the analytical expression of  $B_y$  and the numerical value of the draping angle, we get the value of the  $B_x$ -component anywhere in the coma.<sup>2</sup>

The amplitude of the magnetic field line along the day-side comet-Sun line is given for all profiles and for the hybrid reference simulation in the lower panel of Figure 4.1, using the exact same parameters as for the density profiles of the upper panel. The magnetic field amplitude resulting from the modified cometary ion density profile (Equation (4.7)) compares very well with the self-consistent result, illustrating the need for a modified density profile: without the arbitrary modifications, both the cometary ion density and the magnetic field amplitude are reaching values orders of magnitude above the self-consistent result.

*Remark:* This is a point discussed by Goetz, C. et al. [41] in their analysis of the magnetic field experimental results over the entire mission. The authors introduce in the context of comet Churyumov-Gerasimenko the model from Galeev, A. A., Cravens, T. E., and Gombosi, T. I. [38], which obtains such an early flattening of the magnetic field in a *shocked flow* by introducing a cooling of the flow, resulting from charge exchange processes between the solar wind and the dense neutral coma. We note however that this cannot be the situation in the case of the reference simulation, which does not account for charge exchange processes, and which does not show any shock

<sup>2</sup> This semi-numerical approach was verified in the case of the simple density profile following  $r^{-2}$ , by comparing the numerical result with the analytical result.



in the incident flow (see Chapter 6). In our case, it is the density profile, changing its slope around a thousand kilometres, which results in a lower magnetic pile-up than analytically found.

We compare in the plane ( $z_{\text{CSE}} = 0$ ) the field lines and the field norm given by the modified expression of the velocity field and the hybrid reference simulation in Figure 4.2, first and second row. The upper-left panel gives the field lines for the simplest profile, and the upper-right to the modified profile. The second row gives the same modified profile in the left panel, zoomed out, and the self-consistent simulation field lines. In the day-side of the coma as well as along the flanks of the draping pattern, no noticeable difference is found between the semi-analytical and the self-consistent field lines. The two models greatly differ in the tail region however, where neither the field lines nor the field norm agree. We will analyse the self-consistent magnetic field in more details in Chapter 5, and we will see that this very regular wake is the result of the particles' feedback on the fields.

A field line is highlighted (pink) in each figure to help the comparison. The singularity present in the simplest profile following  $r^{-2}$  translates into no magnetic field line cutting the Sun-comet line in the night-side: all lines are piled-up upstream of the nucleus. It is only by assuming a non-stagnating fluid in the innermost coma that the field lines are found to intersect the Sun-comet line downstream of the nucleus, as seen in the bottom panels.

In summary, we have a fully analytical 3-dimensional model of the magnetic field, which contains a singularity, and another semi-analytical model without this singularity. The latter is simple, but accounts for the large scale characteristics of the self-consistent picture in most of the interaction region. It has the right qualitative topology (draping) with the right spatial scales, and it has an accurate quantification of the magnetic field pile-up in the day-side of the coma. The dynamics of the solar wind close to the nucleus (and therefore at the spacecraft location) largely reflects its interaction with the upstream coma, therefore it may be more important to capture properly the day-side plasma environment than the night-side region. The main drawback of the simple model is the tail region, in which the field does not decrease significantly, in contrast with the reference simulation.



## GENERALISED GYROMOTION IN A COMETARY ATMOSPHERE, SOLAR WIND PROTON DYNAMICS

Based on the simple models presented in the previous chapter, a lot can be learned about the interaction – and particularly about the solar wind proton dynamics – by focusing on the ( $y_{\text{CSE}} = 0$ ) plane. First, because of the symmetries in the magnetic field and the total ion velocity, the analytical effort on solving Equation (3.9) can be pushed much further. Second, because of the same reasons, we will see that solar wind protons that were initially in this plane remain in this plane. It allows us to illustrate and comprehend better the dynamics, before the 3D analysis proposed in the next Chapter, in which the trajectories of single particles are much more intricate and can't easily be visualised.

### 5.1 SEMI-ANALYTICAL SOLUTIONS

In the plane ( $y = 0$ ), accordingly with the symmetries and assuming the simplified cometary ion density following  $r^{-2}$ , the magnetic field is reduced to

*Part of the content of this section is adapted from Behar et al. [11].*

$$\begin{cases} B_x &= 0 \\ B_y &= B_\infty \left( 1 + \frac{\alpha}{n_\infty(x^2 + y^2 + z^2)} \right) \\ B_z &= 0 \end{cases} \quad (5.1)$$

In the cometary frame and considering the new-born ion population, one can remark that  $u_{\text{com}} \ll u_{\text{sw}}$ . Thus using (3.9), (4.8) and (5.1), we have

$$\begin{aligned} \dot{\mathbf{u}}_{\text{sw}} &= -\frac{e \zeta_{\text{com}} B}{m_{\text{sw}}} \cdot \mathbf{u}_{\text{sw}} \times \hat{\mathbf{y}} \\ &= -\frac{e v_i Q B_\infty}{4\pi m_{\text{sw}} n_{\text{sw}} v_{\text{ml}} u_0} \cdot \frac{1}{r^2} \cdot \mathbf{u}_{\text{sw}} \times \hat{\mathbf{y}} \quad [\text{m/s}] \end{aligned} \quad (5.2)$$

The force experienced by single solar wind protons is therefore of the form

$$\mathbf{F} = \frac{m_{\text{sw}} \eta}{r^2} \mathbf{u}_{\text{sw}} \times \hat{\mathbf{y}}. \quad (5.3)$$

The force is always perpendicular to the protons velocity, with a strength proportional to the inverse of the square distance,  $1/r^2$ . If

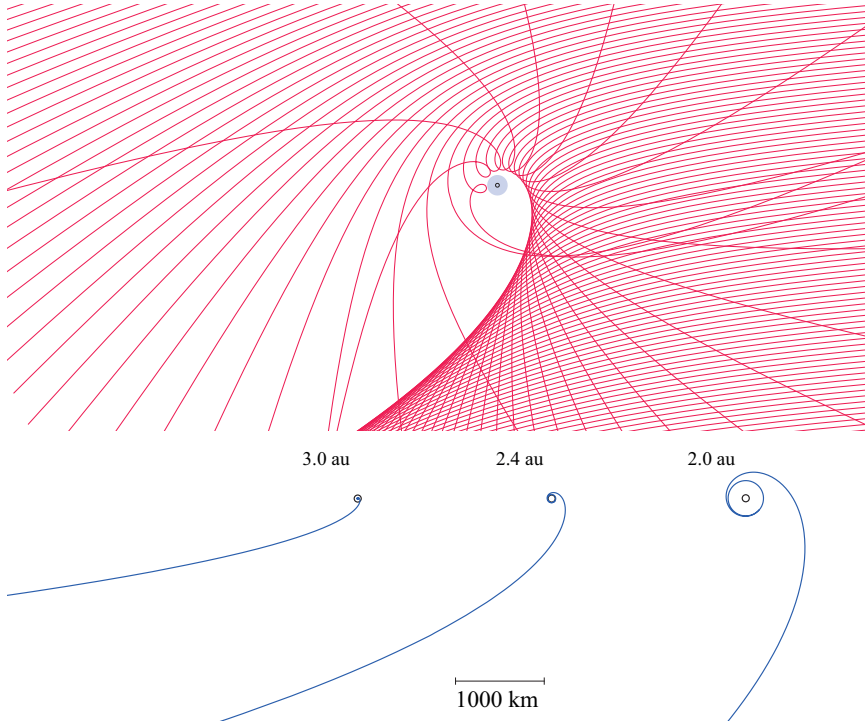


Figure 5.1: Result of the semi-analytical model of the solar wind ion dynamics. Upper panel: Examples of solar proton trajectories, dimensionless, initially flowing from the right to the left. No particle can enter in the central circle. Lower panel: The shape of the caustic created by particles coming from infinity, using the same scale for three different heliocentric distances, as developed by Saillenfest, Tabone, and Behar [74]. Near the origin, the caustic wraps around the cavity.

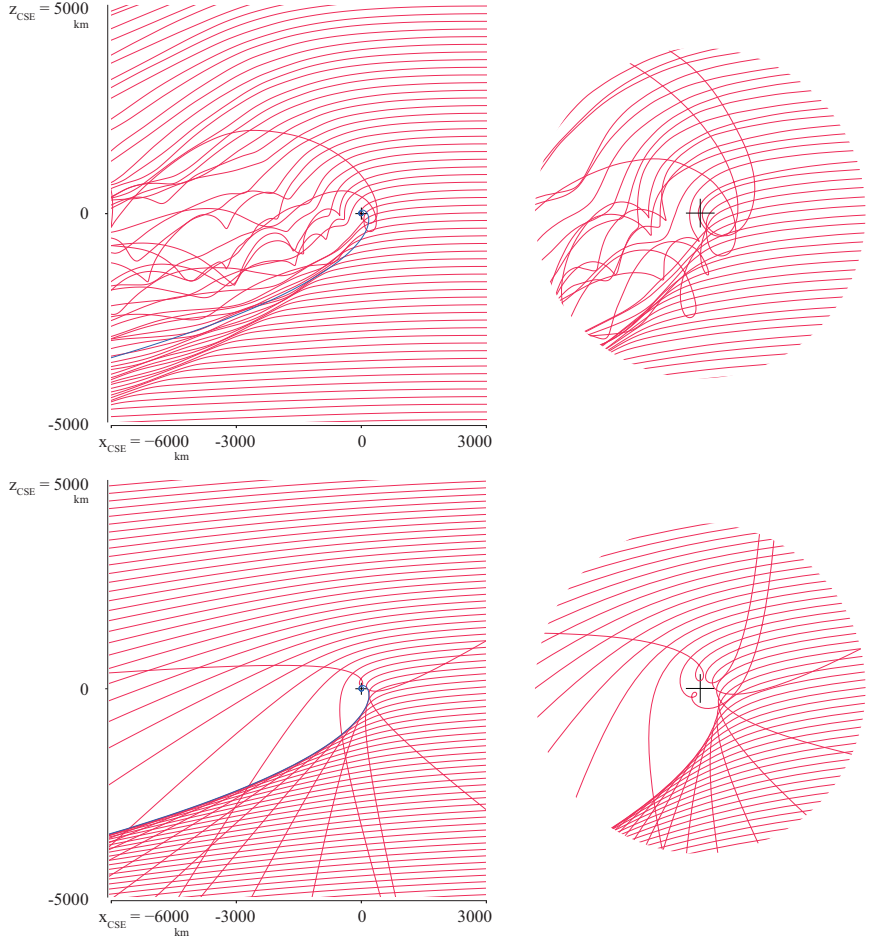


Figure 5.2: Solar wind proton trajectories (red lines) from the reference simulation (upper row) and from the 2-dimensional semi-analytical model (lower row). The theoretical position of the caustic is given by the blue line. Zoom-ins are given in the right column, showing the details of the single particle behaviour after passing the caustic: in both models, a double-beam of protons is found.

their velocity is contained in the plane ( $y_{\text{CSE}} = 0$ ) at any time, they remain in this plane: the dynamics are planar. The equation of motion for protons is then

$$\ddot{\mathbf{r}} = \frac{\eta}{r^2} \dot{\mathbf{r}} \times \hat{\mathbf{y}} \quad ; \quad \eta = \frac{e v_i Q B_\infty}{4\pi v_{\text{ml}} n_{\text{sw}} m_{\text{sw}} u_0} \quad [\text{m}^2/\text{s}] . \quad (5.4)$$

This expression of the acceleration is paramount. In that description, the solar wind protons do not lose kinetic energy, which is in agreement with one of the main observations in the first overview of the averaged proton moments, at the end of Chapter 2. We will shortly come back on this aspect, which is one of the most unfamiliar result of this study, in the context and general knowledge about the solar wind interaction with solar system bodies.

The solar wind protons are purely gyrating, with a gyroradius function of their distance to the nucleus only. It can be seen as the motion of charged particles in an effective magnetic field, always perpendicular to the plane of the motion, with an amplitude proportional to  $r^{-2}$ . This is the core of the model of their dynamics, the reduced form of the solar wind proton interaction with a coma.

Obviously, this  $r^{-2}$  law is inherited from the simplified cometary ion density, but it is only through this simplification that we can access all the way to the particle dynamics. We therefore have to keep in mind that this model is best for large spatial scales.

The dynamical system defined by (5.4) for solar wind protons is integrable. Its solutions are thoroughly studied in Saillenfest, Tabone, and Behar [74], and the resulting trajectories are shown in Figure 5.1. A portion of the incoming flux of particles is temporarily focussed along a very specific curve, defined as the crossing points of infinitely close neighbour trajectories. By analogy to light rays, we call it a “caustic”, resulting in an overdensity of particles. This caustic has a well-defined shape, which is analysed in [74], and plotted in Figure 5.1. A noteworthy property of this system is that the shape of this caustic, and the trajectories in general, are only scaled with the outgassing activity and the heliocentric distance, reason for which the upper panel of Figure 5.1 is dimensionless.

Around the nucleus, a circular region in which no solar wind ion can enter is formed. Its radius is [11, 74]

$$r_{\text{cav}} \sim 0.28 \frac{e v_i Q B_\infty}{4\pi v_{\text{ml}} n_{\text{sw}} m_{\text{sw}} u_0 u_\infty} . \quad (5.5)$$

We will see soon that at comet Churyumov–Gerasimenko, the solar wind was not observed close to the nucleus for a portion of the mission. In Section 5.4, this theoretical value of the solar wind ion cavity will be tested against experimental data.

Finally, we note that a very similar overdensity curve can be observed in the flux of charged particles in the equatorial plane of a magnetic dipole [80, 86].

## 5.2 SELF-CONSISTENT NUMERICAL SOLUTIONS

The solar wind deflection pattern and the corresponding caustic (an over-density structure in the solar wind) can be seen in the results of numerical simulations, in several publications. In the context of comet Churyumov–Gerasimenko, a similar curved over-density in the solar wind can clearly be seen in the results of Hansen et al. [46] (Fig. 5-B), Wiehle et al. [92] (Fig. 3-a), Koenders et al. [58] (Fig. 14-a), Koenders et al. [59] (Fig. 3-b), Behar et al. [9] (Fig. 6), and Deca et al. [28] (Fig. 4-c). Many of these results also show the average deflection of the solar wind, in qualitative agreement with the present model.

Such an asymmetric density structure in the solar particle flow can also be spotted in the simulation of the plasma environment at other solar system bodies. A first example is the solar wind dynamics modelled by Delamere [29] at Pluto (Fig. 4). There, for two neutral production rate cases, the flow is highly asymmetric and develops a similar structure along which proton trajectories intersect. An even more familiar result can be found in Kallio and Jarvinen [57], with the simulation of the solar wind interaction with unmagnetised bodies like Mars or Venus. Figure 3 presents the effect of mass-loading on the solar wind, in a test-run where the body has no physical extent, and new-born ions are created according to a  $1/r^2$  law, with a total production rate of  $10^{26} \text{ s}^{-1}$ . This is virtually the same system as treated here, and therefore the strong agreement between the flow line of Figure 3-b in Kallio and Jarvinen [57] and the proton trajectories modelled here-above is natural.

However, all these results present only the bulk velocity of the flow, with the exception of Delamere [29]. Despite the kinetic nature of these models, the behaviour of the single particles is discarded and lost, and makes it impossible to judge how the particles behave in the structure itself. In Figure 5.2, trajectories of single solar wind protons from the reference simulation are given. They are obtained by launching test-particles in the steady-state fields  $\mathbf{E}$  and  $\mathbf{B}$ . We compare them with the semi-analytical trajectories (bottom panel) using the exact same parameters (Table 4.1) and the value of  $v_{\text{ml}}$  found in the previous comparison with the self-consistent ion density and magnetic field strength,  $v_{\text{ml}} = 0.035 \text{ s}^{-1}$ . The corresponding solar wind proton density is given in Figure 5.3, left panel, normalised to the upstream density.

We find that in most of the region, the deflection of the single particles is well captured by the semi-analytical solutions, and especially

*Part of the content of this section is adapted from Behar et al. [11].*

in the day-side of the coma. A first discrepancy is to be found on the  $+z_{\text{CSE}}$  region (i.e.  $+E$ -hemisphere), where neglecting the pick-up ions result in an underestimated deflection. This point will be clearly illustrated in Chapter 5. The main discrepancy is found in the caustic region. The self-consistent picture shows intersecting trajectories only close to the center of the coma, in a radius of about 1000 km from the nucleus. Further downstream, the trajectories indeed forming an over-density (see next section) but do not intersect. There, the solar wind protons meet a structure in the electric and magnetic field that changes their gyroradius fairly abruptly. The corresponding over-density has a larger opening angle than the theoretical caustic.

In the central region, where the trajectories intersect each other in both the simulation and the semi-analytical model, the phase space distribution function of the solar wind protons presents two beams. We do not discuss the situation for cometocentric distances below 500 km, as with too few cells, one cannot properly resolve the smaller scales in this innermost region, where charge exchange is also expected to play a role. A noteworthy observation is that in the simulation, the finite size of the domain leads to an underestimation of the deflection, as can be seen 3000 km upstream of the nucleus. This is due to an injection of solar wind protons at the inflow boundary with an initial velocity along the  $x$ -axis, whereas in the analytical model, protons have already experienced a significant deflection at this cometocentric distance. This issue is pointed out and quantified in Saillenfest, Tabone, and Behar [74] (*cf.* Sect. 3.2).

### 5.3 DISCUSSION

Before moving on to the experimental results, more can be discussed about this asymmetric structure and its origin. In the theoretical model, it is the geometry of the particle dynamics that creates an over-density in the flow. In this picture, the gyroradius of the solar wind particles is only function of their distance to the nucleus, and evolves very continuously. The resulting over-density does not feedback on the electric and magnetic field in this simplified model. In the self-consistent model however, we find that the solar wind proton gyro-radii are changed more suddenly at the over-density position. It seems like the situation is somewhat the opposite as in the semi-analytical model: a structure in the fields is dictating the solar particle dynamics (at the structure location). It is a highly difficult exercise to try to find cause-and-effects relationships in space plasma physics, and this situation is no different. However we propose the idea that the 0-order structure – the caustic – formed by the particle dynamics is the seed of the asymmetric structure. The theoretical caustic is a perturbation in the flow, in both the plasma pressure (over-density) and the fields (motional electric field and its corresponding feedback on the magnetic field, see Section 5.7). This perturbation will propagate, and if the propagation speed is larger than the flow speed, the theoretical



caustic would grow to form a wider and more open structure, as seen in Figure 5.2.

Bagdonat and Motschmann [4] describe the same structure as one side of an asymmetric Mach cone, formed by the front wave of propagating density and magnetic field disturbances, induced by the obstacle in the incident flow. The theoretical propagation speed of magnetosonic waves is:

$$C_{\text{MS}} = \sqrt{C_{\mathcal{A}}^2 + C_{\text{s}}^2}, \quad (5.6)$$

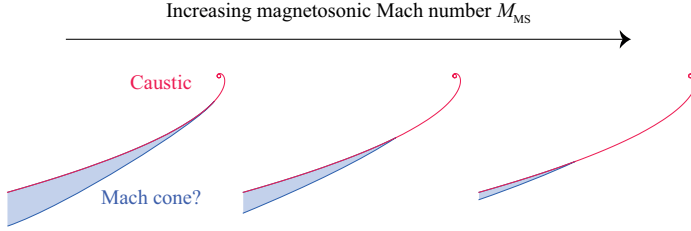
$$C_{\mathcal{A}} = \sqrt{\frac{B_0^2}{\mu_0 m_i n_0}}, \quad (5.7)$$

$$C_{\text{s}} = \sqrt{\frac{\gamma k_{\text{B}}(T_{\text{i}} + T_{\text{e}})}{m_{\text{i}}}}. \quad (5.8)$$

$C_{\mathcal{A}}$  is the Alfvénic speed and  $C_{\text{s}}$  the speed of sound.  $B_0$  and  $n_0$  denotes the background magnetic field and total number density.  $T_{\text{e}}$  is the electron temperature,  $m_{\text{i}}$  the mass of the considered ions,  $\gamma$  the polytropic index,  $k_{\text{B}}$  the Boltzmann constant and  $\mu_0$  the vacuum permeability. In the most general configuration, the magnetosonic waves can propagate in any directions, and three wave modes are found: intermediate, slow and fast modes. In the plane of interest ( $y_{\text{CSE}} = 0$ ) however, the waves are propagating perpendicular to the magnetic field, and only the fast mode is present, with a phase velocity  $v_{\text{f}} = C_{\text{MS}}$  (see Cravens [25], Section 4.8.3). In a supersonic and super-Alfvénic flow, the wave fronts are aligning and form a cone, with the opening half-angle  $\alpha = \sin^{-1}(M_{\text{MS}}^{-1})$ , with  $M_{\text{MS}} = u_0/C_{\text{MS}}$  the magnetosonic Mach number. All these various values are given in Table 5.1, using the parameters of the reference simulation (Table 4.1).

However the term “Mach cone” was chosen by Bagdonat and Motschmann [4] based on a different, simplified simulation, which included a localised, static cloud of cometary ions as obstacle to the solar wind, which indeed generates a Mach cone in its wake. We note that a Mach cone is classically defined in the wake of a blunt obstacle, and not *within* an extended obstacle, as a coma permeated by the solar wind. However the term, which we could find in a cometary context used for the first time by Sauer and Dubinin [75], has been used since, to describe the asymmetric over-density in the interaction between a low activity comet and the solar wind. Could it be that in our situation, at 2 au away from the Sun and for nominal parameters, the over-density is indeed the result of a Mach cone? The source of the initial perturbation is only indirectly the cometary ions: it is the deflected solar wind that “stumbles over itself” and creates an over-density that will tend to propagate. So if indeed the initial caustic is the perturbation, it can be argued that whether or not a Mach cone is formed locally along the caustic depends on the local opening angle of both the caustic and the Mach cone, as sketched below: it may be that on medium spatial scales, the caustic opening angle is simply too large for the Mach cone to develop. And since the caustic does not depend

on the magnetosonic speed, the more supersonic and super-Alfvénic the flow becomes, the more caustic-like the structure gets.



We carefully considered the possibility of the structure being a Mach cone because of how widespread the concept is in the literature, in the same context. However for two reasons that we now propose, it may be that this precise structure, for this precise heliocentric distance, is not a Mach cone.

The first reason is simply that the theoretical Mach cone in the pure solar wind is only  $10^\circ$  wide (half-angle), which is very far from the structure found in the self-consistent case (about  $40 - 45^\circ$ ). Of course, this number does not account for the additional density of the heavier cometary ions, which modifies locally both the speed of sound and the Alfvén speed through the average ion mass, the ion and electron temperatures and the piled-up “background” magnetic field.

To approach this mechanism in a self-consistent manner and without changing the regime of the interaction (in other words the amount of momentum and energy transferred between the two plasmas), we ran the same reference simulation with identical parameters, at the exception of the electron temperature, decreased to 100 K, three orders of magnitude colder than in the reference run. This reduces by three orders of magnitude the plasma pressure in the hybrid model (see Equation (2.23)), reducing considerably the ambipolar electric field which is the only way for acoustic waves to arise in the hybrid equations. The magnetosonic speed is then equal to the Alfvén speed. In summary, the new run cannot contain acoustic waves. Figure 5.3 compares the two resulting solar wind densities, and almost no differences can be found in the structure’s opening angle. It does not rule out entirely the possibility that this structure purely results from magnetic pressure, but the test wouldn’t be as straightforward, and is one task which is not tackled in this thesis.

#### 5.4 EVOLUTION OF THE SOLAR WIND SPEED AND DEFLECTION & THE SOLAR WIND ION CAVITY

*Part of the content  
of this section is  
adapted from Behar  
et al. [10].*

What bridges can be thrown between these results from analytical and numerical models, and in situ data collected close to the nucleus for more than 2 years, as the neutral outgassing was radically evol-

Table 5.1: Values at 2 au for the nominal parameters

$u_0$	$C_s$	$C_A$	$C_{MS}$	
400 km/s	46 km/s	50 km/s	67 km/s	
	$M_s$	$M_A$	$M_{MS}$	$\alpha$
	8.8	8.1	5.9	9.7°

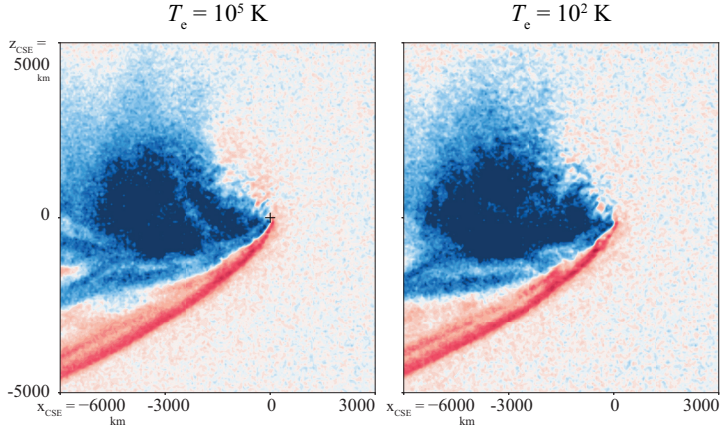


Figure 5.3: Effect of the upstream electron temperature on the solar wind overdensity.

ing? We have learned that the solar wind can be largely deflected without significant loss of kinetic energy, as it gyrates through the coma. We are also able to retrieve the expected solar wind deflection from the semi-analytical model, provided an upstream solar wind speed and a spacecraft position. We can therefore start to look at solar wind particle speed and deflection, either as separate values taken from the integrated bulk velocities (continuous evolution), or combined by looking at the distribution functions (discrete times).

**Methods** – The solar wind proton bulk velocity amplitude (speed) and deflection are shown in Figure 5.4, middle panels. The theoretical deflection estimated by the semi-analytical approach is also given in the upper panel. In the lower panel, the cometocentric distance of the spacecraft is given. We over-plotted on the same line the time when solar wind protons were detected. Most of the detections shown on the figure are based on the daily manual selections, explained in Section 2.3.2, and using a threshold on the signal-to-noise ratio of 4 (the number of counts in the selection window is at least 4 counts higher than the background). For other periods like the fly-by in February 2015, or within and around the solar wind ion cavity (from May 2015 to December 2016, included), we went through each and every full angular scan (192 s) to verify the presence or the absence of solar wind protons in RPC-ICA data. Note that the absence of protons in the data can still be due to Field-Of-View obstructions. This manual selection

at the highest time resolution is necessary, as protons can on some days be seen in only a handful of the thousands of available scans, making them invisible when integrated over the day. It is important to stress out that between April 2015 and December 2016, solar wind protons are rarely seen, if at all, which is not the impression given by this representation.

The estimation of the solar wind proton deflection given by the semi-analytical model is entirely based on the work detailed in Sailenfest, Tabone, and Behar [74]. We provide to the model the spacecraft position as function of time, and the upstream solar wind speed value assuming that the solar wind was not decelerated at all: upstream speed and local speed are the same. We can't possibly know where the spacecraft was in the CSE reference frame, as we can't know precisely the orientation of the upstream electric field. What is given in Figure 5.4 is the value of the deflection if the spacecraft lies in the ( $y_{\text{CSE}} = 0$ )-plane, and for  $y_{\text{CSE}} > 0$ .

**Solar wind deflection** – The solar wind deflection far away from the Sun is just a few degrees large. The data from the earliest period (highlighted in grey in Figure 5.4) suffer from a systematic obstruction of the Sun by the spacecraft body. This obstruction, together with the way it was dealt with on-board (a quarter of the pixels were simply set to zero count), results in moments of poor quality. On the other hand at the end of the mission, the spacecraft was much closer to the nucleus for similar heliocentric distances, and the solar wind deflection then never reaches  $0^\circ$ .

As the nucleus gets closer to the Sun, the deflection reflects the escalating neutral outgassing, and reaches values all the way up to  $180^\circ$ : solar wind protons are sometimes seen flowing back towards the Sun. The variability of the deflection is also increasing with decreasing heliocentric distances. The period of high deflection variability is highlighted in blue in Figure 5.4. In the early period, a clear anti-correlation between solar wind speed and deflection is observed [9].

The deflection given by the semi-analytical model gives very satisfying results. The first aspect is the range of deflection angles, from  $0^\circ$  as the spacecraft approaches the nucleus at high heliocentric distances (earliest dates) up to  $180^\circ$ . An appreciable match is the deflection at large heliocentric distances and at the end of the mission, which never reaches  $0^\circ$ , as seen in the data: the semi-analytical model indeed indicates that despite the very low outgassing activity, the solar wind is effectively deflected (about  $10$  to  $20^\circ$ ) when close enough to the nucleus. Some detailed variations are correlated between experimental data and semi-analytical deflection, first during October and November 2014, when the large upstream solar wind speed variations reflect on its deflection, and second during the remarkable dip in deflection, corresponding to the night-side excursion (March-April 2016, see Section 5.5). The high variability of the solar wind deflection for lower heliocentric distances is also found in the semi-analytical results: according to the model, this variability is to be expected from

the upstream solar wind speed variability, convoluted with the intrinsic dynamics of the system. In other words, a shock is not needed to induce large variability in the deflection.

**Solar wind speed** – The average solar wind proton speed was given in Figure 2.7 as a daily average. In the third panel of Figure 5.4, we now give each and every measurement<sup>1</sup> as a single data point. The agreement with the estimated upstream speed (propagated OMNI data, solid purple line) is still striking, but we now see a tendency of lower speeds in ICA data, for higher heliocentric distances, around the solar wind ion cavity. We should however be very careful with the interpretation of the data during these periods, as the bias introduced by Field-Of-View limitations is strongly affecting the observations for high solar wind deflections. One thing is for sure, for solar wind deflections up to  $90^\circ$ , the particles observed close to the nucleus in the densest coma did not lose a measurable amount of kinetic energy despite their high deflection: momentum is transferred much more efficiently than kinetic energy, as explained by the semi-analytical model of the interaction. *For low-to-medium outgassing activity, the mass-loading mechanism is essentially not decelerating the solar wind.* This is an unfamiliar result in the more general context of the solar wind interaction with solar system bodies.

**Solar wind proton distribution functions** – Typical proton distributions are given in Figure 5.5 to illustrate different heliocentric distances. We find that the distributions remain beam-like until the deflection reaches about  $90^\circ$ . They then spread in partial ring distributions, during the period of high variability of the deflection discussed above. These partial ring distributions are a major discrepancy with the semi-analytical approach, which tells us that only multiple beams can be observed outside the ion cavity. This is a limit of the model at higher activity and close to the nucleus only. These partial rings confirm that the solar wind is gyrating. The example given in the second row from the bottom display a partial ring which is not centred on zero. Accordingly with the generalised gyromotion, the central velocity is that of the electron fluid: a few tens of kilometre per second, with negative  $v_x$  and  $v_z$ , no  $v_y$ . Therefore close to the nucleus and in opposition with one of our main assumptions in the simple model, the electron fluid is not solely moving along the  $x$ -axis. Another way to interpret these partial ring distributions is, the more deflected protons are, the more kinetic energy they lost. This deceleration is still limited, and it is worthwhile to repeat that as seen at comet Churyumov–Gerasimenko, mass-loading is only marginally decelerating the solar wind.

Finally, the deflection of the solar wind is seen to refocus close to the solar wind ion cavity, with values of about  $140\text{--}150^\circ$  (period

<sup>1</sup> Provided high angular resolution and high mass resolution.

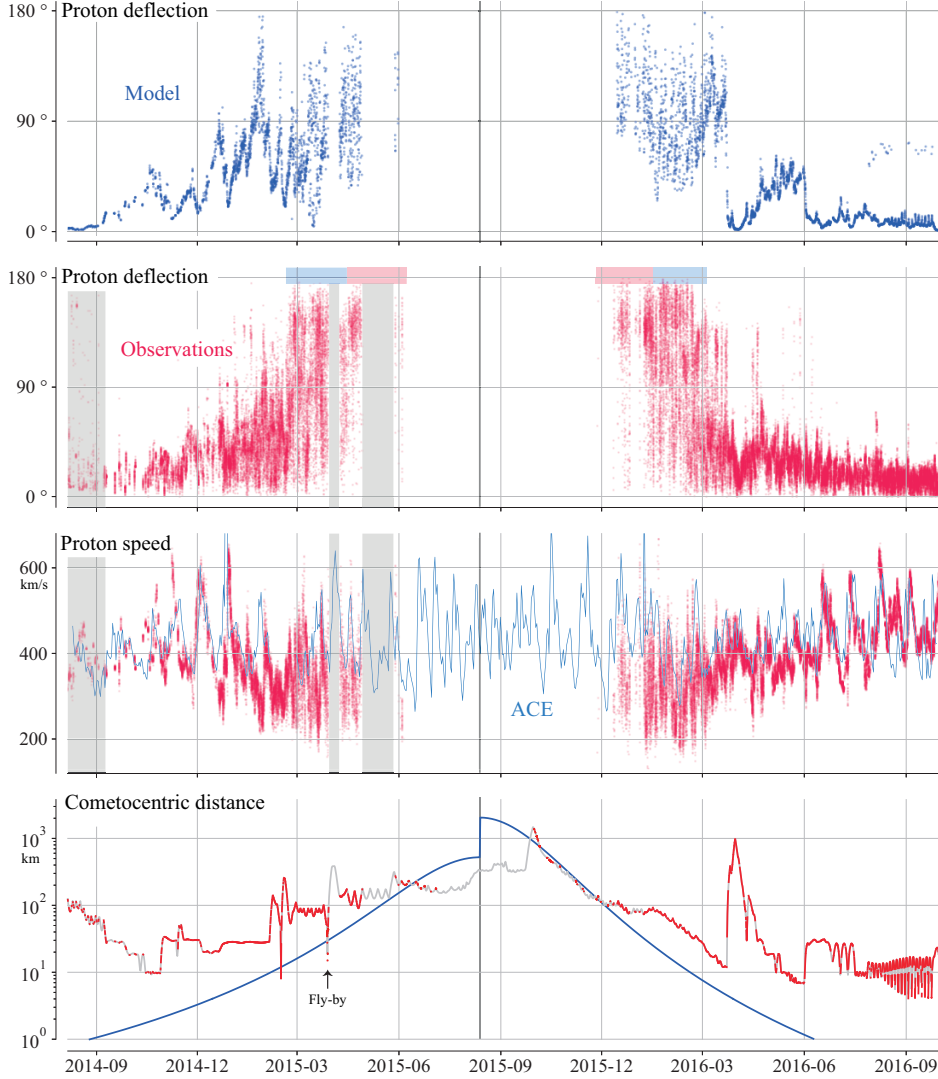


Figure 5.4: Overall-mission solar wind proton parameters. 1<sup>st</sup> and 2<sup>nd</sup> panels from top: modelled deflection and observed deflection. 3<sup>rd</sup> panel from top: proton average speed observed by RPC-ICA (red) and their estimated upstream speed (solid line). Bottom panel: cometocentric distance (grey) and theoretical solar wind ion cavity extent (blue). Proton observations are over plotted in red.

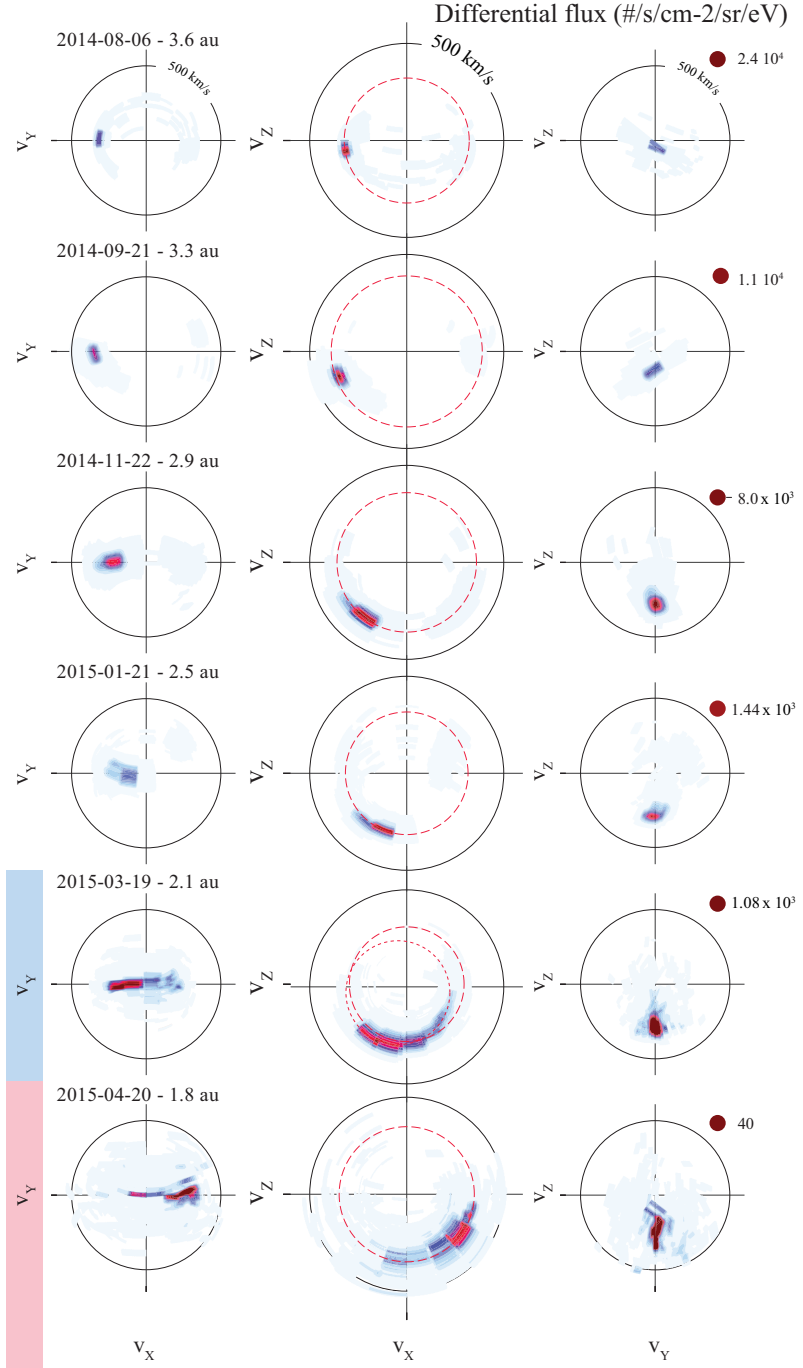


Figure 5.5: Characteristic velocity space distribution functions of solar wind protons observed by ICA, at various outgassing activity levels. A correspondence between the two bottom distributions and the deflection time series of Figure 5.4 (top panels) is given with the left-hand colour tags.

highlighted in blue in the figure), which is illustrated with the last distribution function. In Behar et al. [10], the geometry of the simple model was given as an interpretation of this refocusing, with highly deflected and highly focused proton trajectories at the very top of the caustic, very close to the ion cavity. Recent numerical hybrid simulation results including charge exchange (personal communication with Katharina Ostaszewski) indicates that the situation close to the nucleus at the apparition of the ion cavity might be very different from this picture, with the main population lost through charge exchange (and deflected up to  $90^\circ$ ) and a second population heavily deflected with a more complex dynamics. We indeed observe a severe decrease of the solar wind proton density (Figure 2.7), which is most likely due to charge exchange between solar wind ions and cometary neutral molecules. This important aspect is tackled by Simon Wedlund, C. et al. [81] and Simon Wedlund, C. et al. [83].

**Solar wind ion cavity** – Between June and December 2015, solar wind protons are seen only on seldom measurements, and not at all for the period around perihelion. We have plotted the theoretical extent of the cavity given in Equation (5.5), taking a value  $v_{ml} = 0.06 \text{ s}^{-1}$ , and assuming a constant solar wind speed of 400 km/s for readability. The asymmetry of the neutral outgassing rate can be recognised, resulting in a larger ion cavity after perihelion. The value of  $v_{ml}$ , taken constant throughout the mission, was taken again as a fitting parameter. Numerous aspects of the semi-analytical model make it so that we know for sure the cavity is not circular, that it is not a sharp boundary, and that its extent can only be taken as an order of magnitude estimate. However we find that this order of magnitude is relevant to describe the relative position of this cavity along the mission. In June 2015, the proton observations are becoming extremely rare, and none are observed from July 2015 until the day-side excursion. Admittedly, at these outgassing rates, it is obvious that the model cannot possibly account for the detailed dynamics of the solar wind ions, but still the theoretical extent of the cavity is in the right order of magnitude as the observed cavity. From the end of the day-side excursion until December, the cometocentric distance of the probe is actually following the evolution of the theoretical cavity boundary. This is not completely surprising, as the spacecraft would try to be as close as possible to the nucleus as the outgassing of the nucleus would allow: its position is somewhat correlated to the nucleus activity. Very interestingly, the second fly-by happening in March 2015 crosses the theoretical ion cavity. On that part of the day, only a handful of observations contain solar wind ions, and these observations actually contain a double-beam in the velocity space distribution functions, as presented in Section 5.6. It is important to note however that the attitude of the spacecraft was fairly different than during the rest of the mission, and Field-Of-View effects cannot be ruled out for observations even closer to the nucleus.



## 5.5 NIGHT-SIDE EXCURSION

In the previous sections, we have compared the predictions of the model with experimental data, through a case study or over the entire mission. However until now, these data were mostly taken in the inner coma, close to the nucleus, as the spacecraft was orbiting in the terminator plane. We also know that the semi-analytical model is better at larger scales, and should give a poorer description of the solar wind dynamics close to the nucleus. It is therefore of prime importance to test it against data on larger spatial scales.

The spacecraft went away from the nucleus only twice, at the exception of the rendez-vous phase, far away from the Sun. The first occasion was a day-side excursion, the aim of which was to probe the potential bow-shock that would have had formed upstream of the nucleus. With a maximum distance of about 1500 km from the nucleus, the bow-shock was not observed. The spacecraft remained in a region mostly depopulated of solar wind particles. During the second excursion, the spacecraft explored the night-side of the coma, reaching cometocentric distances of almost a thousand kilometres. During this excursion, one of the main result was the acceleration of the pick-up cometary ions, with speeds correlating with the cometocentric distances. The cometary ion population at low energy (the expanding population as termed in Bercic, L. et al. [13]) was not observed out of the innermost region. The density of the pick-up cometary ions plummets with the cometocentric distance. Both the solar wind ions and the cometary pick-up ions were forming beams in velocity space. The solar wind is not seen losing a detectable amount of kinetic energy.

The main challenge for the analysis of this data set is the absence of information about the spacecraft position in the CSE frame: a rotation of the upstream electric field would imply a shift of hundreds or thousands of kilometres of the spacecraft position, from one instant to the other. We propose an estimate of this position based on the proton flow direction, explained in details in Behar et al. [12]. It is again based on the assumption that in the ( $y = 0$ )-plane of the CSE frame, the dynamics of the particles are planar, and solar wind protons coming from upstream with no  $v_y$ -component will remain in this plane. This assumption neglects the Parker spiral angle inducing the dawn-dusk asymmetry exposed previously. It allows us to estimate when the spacecraft was close to the ( $y = 0$ )-plane. With this information we only consider the data taken close to this plane, for which we luckily have a model. These data are presented in Figure 5.6. The bulk velocity of the cometary pick-up ions and the solar wind protons are given respectively in the upper-left and lower-left panels. The cometary pick-up ions are seen flowing mostly radially away from the nucleus with a speed increasing with the distance to the nucleus.

The protons are flowing more or less perpendicular to the pick-up ions. Their deflection is seen to correlate surprisingly well with the proton trajectories of the semi-analytical model for a parameter  $v_{ml} = 0.01 \text{ s}^{-1}$ , given by the red lines. The agreement is poor close to

*Part of the content of this section is adapted from Behar et al. [12].*

the nucleus and in the lower-left quadrant, confirming the limitations of the model for these regions. In the lower-left quadrant, i.e. the region downstream of the caustic, the trajectories of the protons in the hybrid simulation (Figure 5.2, upper-left panel) were much less ordered, as different protons gyrate with different phases and radii.

Since we have information on the velocity and the density of all populations present in this region, as well as magnetic field measurements, we can compute the motional electric field. The result is given in the upper-right panel of Figure 5.6. The direction of this electric field component is found to match nicely the cometary pick-up ion flow direction in the  $z_{\text{CSE}} > 0$  region. As expected from its definition, the motional electric field becomes stronger further out, as the fast solar wind is dominating. These results prove that in this part of the explored night-side of the coma, the motional electric field is indeed largely dominating. However, as we follow the proton trajectories further in the night-side, the motional electric field and the cometary ion flow direction are becoming mis-aligned. This indicates that additional electric field components are at work. In Figure 5.6, lower-right panel, we indicate the plausible additional electric field components. First, the radial ambipolar electric field, set up by charge separation between fast moving electrons and slower ions, due to pressure gradients of the spherically outflowing atmosphere. Such a field is also discussed based on the cometary ion dynamics in Bercic, L. et al. [13]. It could as well have a tail-ward component due to the region downstream of the caustic, of lower ion density. The second electric field source is the Hall electric field, rising from the magnetic field draping around the coma, which is a source of curl for  $\mathbf{B}$  and resulting in a mostly tail-ward field.

Unfortunately, based on this adjustment of the model, the caustic was not crossed during this excursion. Nothing obvious happens to the solar wind in ICA data.

## 5.6 DOUBLE-BEAM VELOCITY SPACE DISTRIBUTION FUNCTIONS

The principal feature of the semi-analytical model is the presence of a caustic, along which neighbour trajectories intersect, one by one. This implies that close to the caustic, the velocity space distribution function of the solar wind protons should consist of two beams, one corresponding to the incoming flow of particles and one formed by the particles that have just passed the caustic. The latter should be much more deflected, and decelerating, as they flow partly or completely against the electric field (depending on the local angle of the caustic). Such trajectories are found in the self-consistent solutions, close to the nucleus (see Figure 5.2).

A very good candidate for an *in situ* confirmation of this phenomenon is the fly-by operated in March 2015, during which the spacecraft probed cometocentric distances ranging from 50 km down to 15 km (from the centre of the body) in less than a day, increasing the likelihood to probe the right cometocentric distance. And

indeed, during a part of this fly-by in the morning of the 28<sup>th</sup> of March 2015, two clear peaks appear in the energy spectrum, for both the solar wind protons and alpha particles. This is shown in Figure 5.7. The lower energy peak corresponds to much larger deflections of about  $135^\circ$ , as shown in the velocity space distribution function, given in a proton aligned frame for 26 integrated scans (about 83 minutes). These distributions were observed at cometocentric distances between 32 and 42 km. They perfectly match the double beam seen in the models, with two beams contained in one plane, one with lower energy and much more deflected than the other. The alpha particles show the same velocity distributions.

Several other dates present two peaks in the proton energy spectrum, for similar heliocentric distances. However these distributions, because of their total angular width, are challenging for ICA and its large field of view obstructions. Additionally, the fairly static spacecraft position subject to large, random and unknown rotation of the upstream electric field, and the variable solar wind conditions, make it very difficult to identify the position of the spacecraft with regard to the caustic.

In the inner region of comet Grigg-Skjellerup, explored by the *Giotto* spacecraft, two proton beams were observed for a while, around closest approach, and reported by Jones and Coates [56]. Comet Grigg-Skjellerup is already known to be a comet less active than the previously visited nuclei (comet Halley or Giacobini-Zinner for instance), and may present similarities with Churyumov-Gerasimenko. In this precise case, the closest approach occurred in the night-side of the coma at about 100-200 km of the nucleus, on the 10th of July 1992, at a heliocentric distance of 1.01 au. The neutral gas production rate was found to be  $7.5 \cdot 10^{27}$  water molecules per second [55]. This rate is about an order of magnitude higher than what was estimated by Hansen et al. [47] at 2.0 au during the inbound leg, corresponding to the fly-by. Whether or not this much higher rate at Grigg-Skjellerup can result in a caustic would require more simulation work. However, the description of the two beams given by the authors is surprisingly similar to the present observation at Churyumov-Gerasimenko:

*"Within the MPB [Magnetic Pile-up Boundary], we have discovered two beams of protons (Fig. 2). Careful analysis revealed that one beam emanated from close to the -z direction in the CSE system, whereas the other was close to the solar wind direction outside the comet (a beam separation of  $135^\circ$  to  $157.5^\circ$ ). The peak energy of the beams was in the range 0.102- 0.133 keV. [...] The beams' peaks were almost perpendicular to the B-field direction at the time. As the exact geometry of the flyby with respect to the comet's diamagnetic cavity is not known, it is difficult to fit a physical explanation. If the flyby occurred on the nightside of the cavity, we tentatively suggest that the beams may be the signature of dayside reconnection. The beams could also delineate the deflected flow of plasma around the cavity. Also at closest approach, a burst of cold heavy ions peaking at 0.258 keV was detected by Polar 4, emanating close to the Ram direction."* Jones and Coates [56]

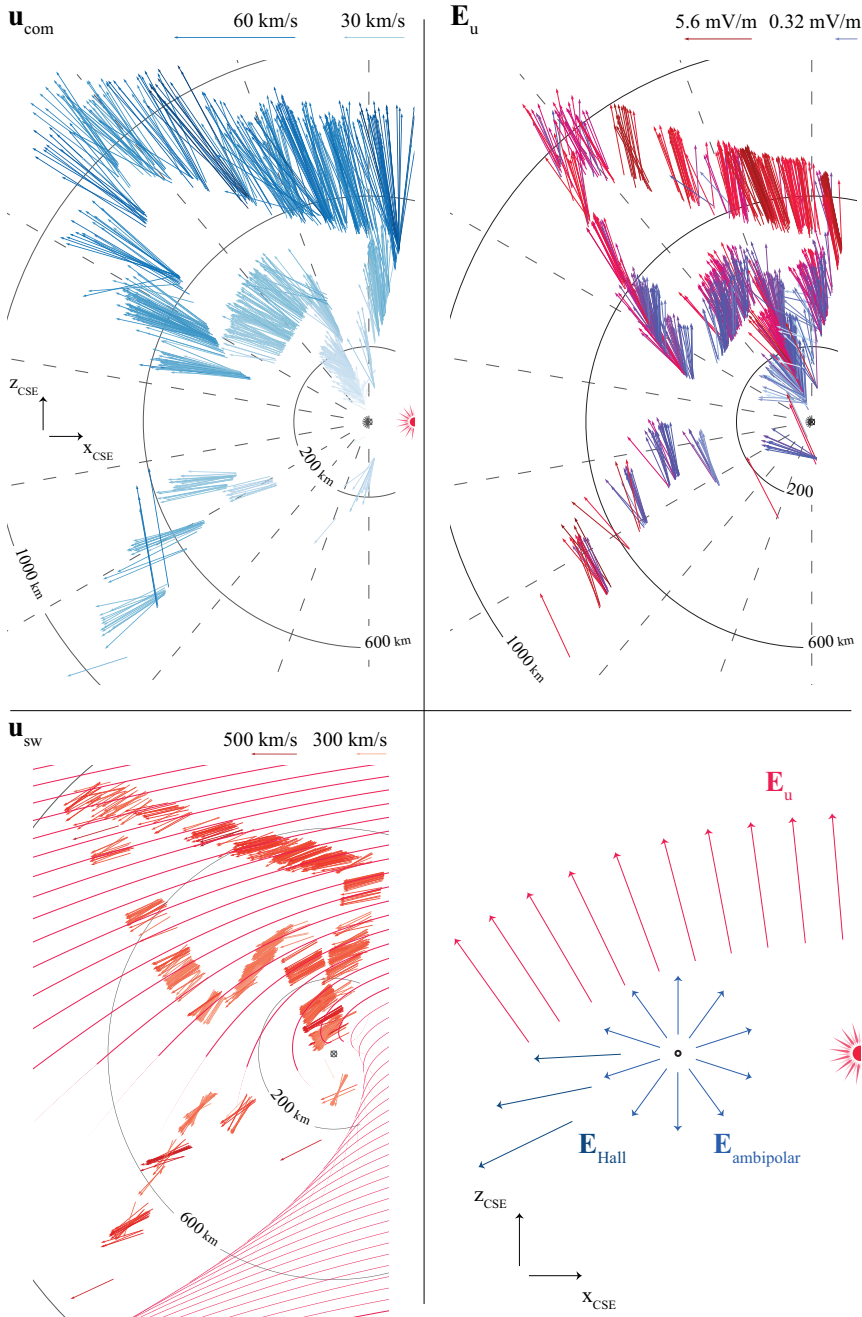


Figure 5.6: Night-side excursion observations. Left column: Cometary ion (top) and solar wind proton (bottom) bulk velocity. The theoretical particle trajectories are given in red. Upper-right: Motional electric field computed with experimental data only. Bottom-right: Schematics of the interpretation, with three different sources of electric field.

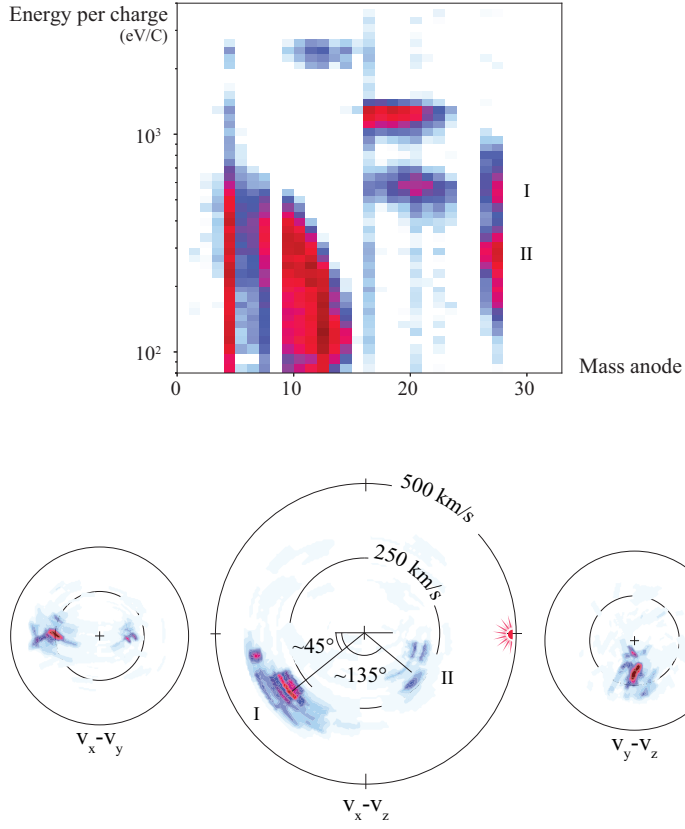


Figure 5.7: Solar wind proton double beam observation during one of the two Rosetta's fly-bys.

Finally, we find in the reference simulation a velocity distribution function almost identical to the observation, and shown in Figure 6.3 of Chapter 6.

## 5.7 3-DIMENSIONAL CASE

### 5.7.1 Densities

We saw in the previous sections how much could be done with the two-dimensional view of the interaction, between semi-analytical approaches, numerical results, and most of all the support of experimental data. Adding a third dimension is the goal of the present section. However due to the lack of information on the spacecraft real position in the CSE frame, as well as the general lack of cometocentric distance coverage, this three-dimensional approach is for now limited to semi-analytical and numerical efforts.

We already have a three-dimensional analytical expression of the magnetic field in the case of the simplest cometary ion density, following  $r^{-2}$ . We also developed a simple numerical method to calculate the magnetic field anywhere in the coma in the case of a modified density profile, as presented in Section 4.3. Additionally, the generalised gyromotion is fully three-dimensional, therefore we have all the elements available to calculate the trajectory of a single solar wind ion through the coma, by numerically integrating its motion.

This time, the single trajectories will not be contained in a plane, and thus they are difficult to visualise. If the physics is not more complex than for the two-dimensional case, the result is more intricate and challenging to represent in terms of single particles. This was also one reason to focus on the two-dimensional case first. Here, we propose to look at the resulting density of solar wind ions instead: the particle motion is integrated in a continuous space, but we map their density over a three-dimensional grid, using *Leo's* methods. Since the regime in the simple model is assumed to be at perfectly steady state, and the dynamics of one particle does not depend on other particles, we can continuously launch particles from upstream of the coma, map them over the grid, enhancing the statistics and the resolution of the picture. Again, this numerical approach is verified against the analytical results in the ( $y = 0$ )-plane, for the simplest  $r^{-2}$  profile.

In Figures 5.8 and 5.9, we give the density found in the reference simulation. In Figure 5.8 are shown density cuts in the ( $y_{\text{CSE}} = 0$ )-plane (upper row, plane containing the upstream electric field) and ( $z_{\text{CSE}} = 0$ )-plane (lower row, plane containing the upstream magnetic field). The density of the protons (left column) is normalised to the upstream density, whereas the cometary ion density (right column) is expressed in physical units. In the left panel, one can easily recognise the asymmetric over-density, along which density is almost ten times higher than upstream. The particle trajectories given in Figure 5.2, upper panel, correspond to the exact same situation. As already seen in Chapter 4, Figure 4.1, the cometary ions show densities over

$100 \text{ cm}^{-3}$ , close to the nucleus. In the upper-left quadrant ( $x_{\text{CSE}} < 0$ ,  $z_{\text{CSE}} > 0$ ), higher densities of about  $0.1 \text{ cm}^{-3}$  and less are found where the pick-up ions start their gyration. The early phase of a cycloid for a single particle in the undisturbed solar wind is given by the dashed red line, and agrees well with the cometary ion plume (or early tail). However only a fraction of the cometary ions follow this cycloidal motion. The larger densities are found downstream of the nucleus, where cometary ions actually experience a strong anti-sunward acceleration. We will come back on the electric field result in a few paragraphs. A striking feature of the cometary ion density in this precise plane are the fan-like structures found on the flanks of the solar wind ion over-density (see next paragraph). Overall, the cometary ions are the densest where solar wind ions are the least dense, and vice-versa, as can be seen even more clearly in the ( $z_{\text{CSE}} = 0$ )-plane (bottom-right panel).

Figure 5.9 shows a “tomographic” view of both population densities (solar wind protons in the lower row, cometary ions in the upper row), in slices perpendicular to the Sun-comet line, for various values of  $x_{\text{CSE}}$ . This is where we really enter the third dimension, and we realise that the over-density actually has partially circular profiles, open on the top ( $+z$  in CSE frame). Within the over-density, a tear-drop shaped solar wind ion cavity extends along the  $+z_{\text{CSE}}$ -semi-axis. Intuitively, it is very tempting to interpret the tear-drop shape as a result of the pick-up ion channel escaping the dense coma. As for the circular shape of the caustic, a Mach cone would seem a perfect candidate. The density of the cometary ions is also given in the upper row of the same figure. With no surprise, the highest densities are found at the centre, and the pick up ions escape through the tail region with a limited gyroradius. In the slices at  $x_{\text{CSE}} = -2000 \text{ km}$  and  $x_{\text{CSE}} = -4000 \text{ km}$ , one can recognise the shape of the solar wind over-density, resulting in almost no cometary ions. As observed previously and overall, the solar wind proton density and the cometary ion density are somewhat inverted, with the higher cometary ion density found in the vertically oriented solar wind ion cavity. A vertical structuring of the coma is seen on its flanks, corresponding to these fan-like structures found in the ( $z_{\text{CSE}} = 0$ )-plane. The same structures are found in other hybrid models, and are specifically addressed by Koenders et al. [58] in the context of comet Churyumov–Gerasimenko, where these spatial oscillations are described as the interference pattern of low frequency waves triggered by cometary ion cross-field currents, only to be found in the  $+E$ -hemisphere. This topic as well as the detailed analysis of the cometary ion dynamics in the self-consistent model are not tackled in this thesis. We note here that a regular grid – providing relatively high resolution everywhere in the domain – is



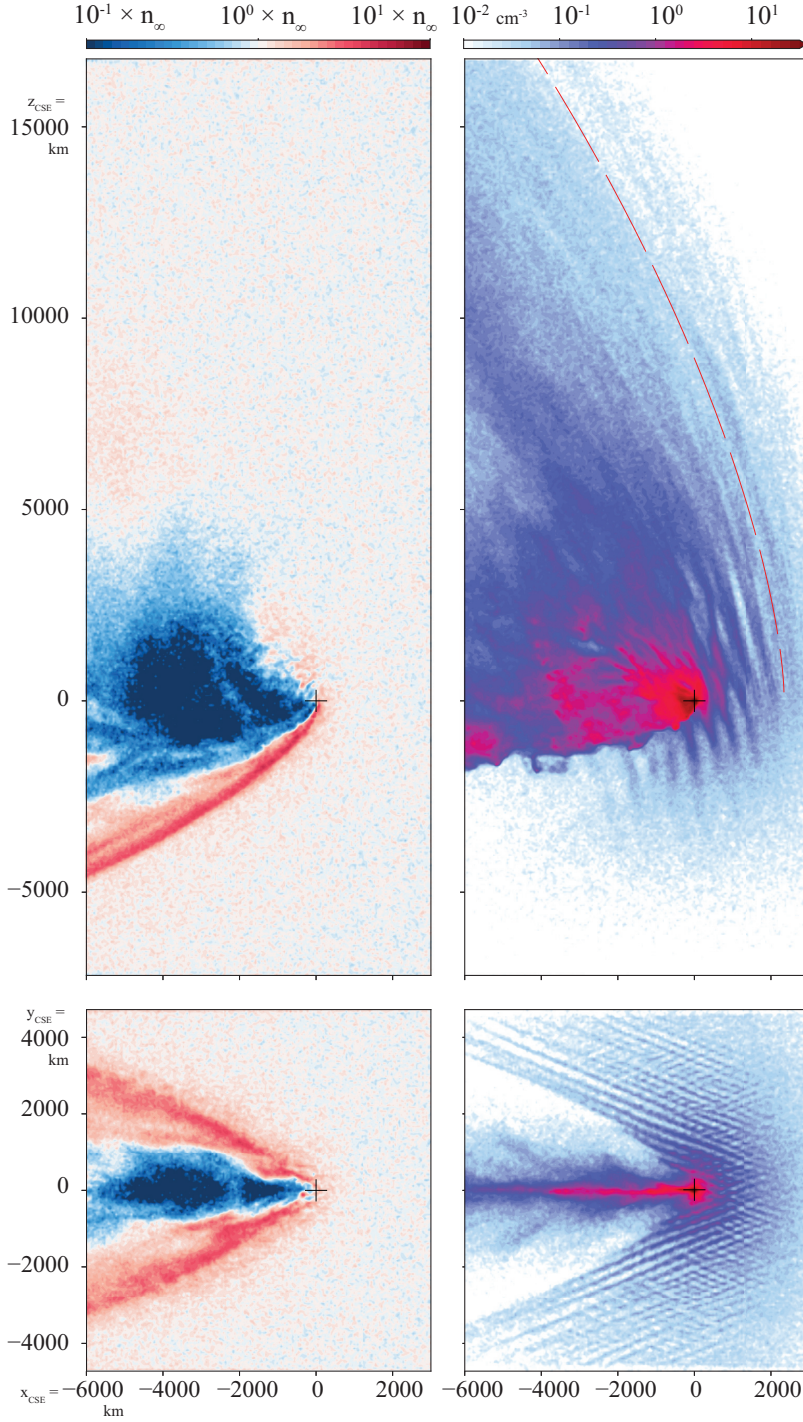


Figure 5.8: Density cuts of the solar wind protons (left column) and the cometary ions (right column), taken from the reference simulation ( $R = 2.0 \text{ au}$ ). The proton density is normalised to its upstream value,  $n_{\infty} = 1.25 \text{ cm}^{-3}$ .



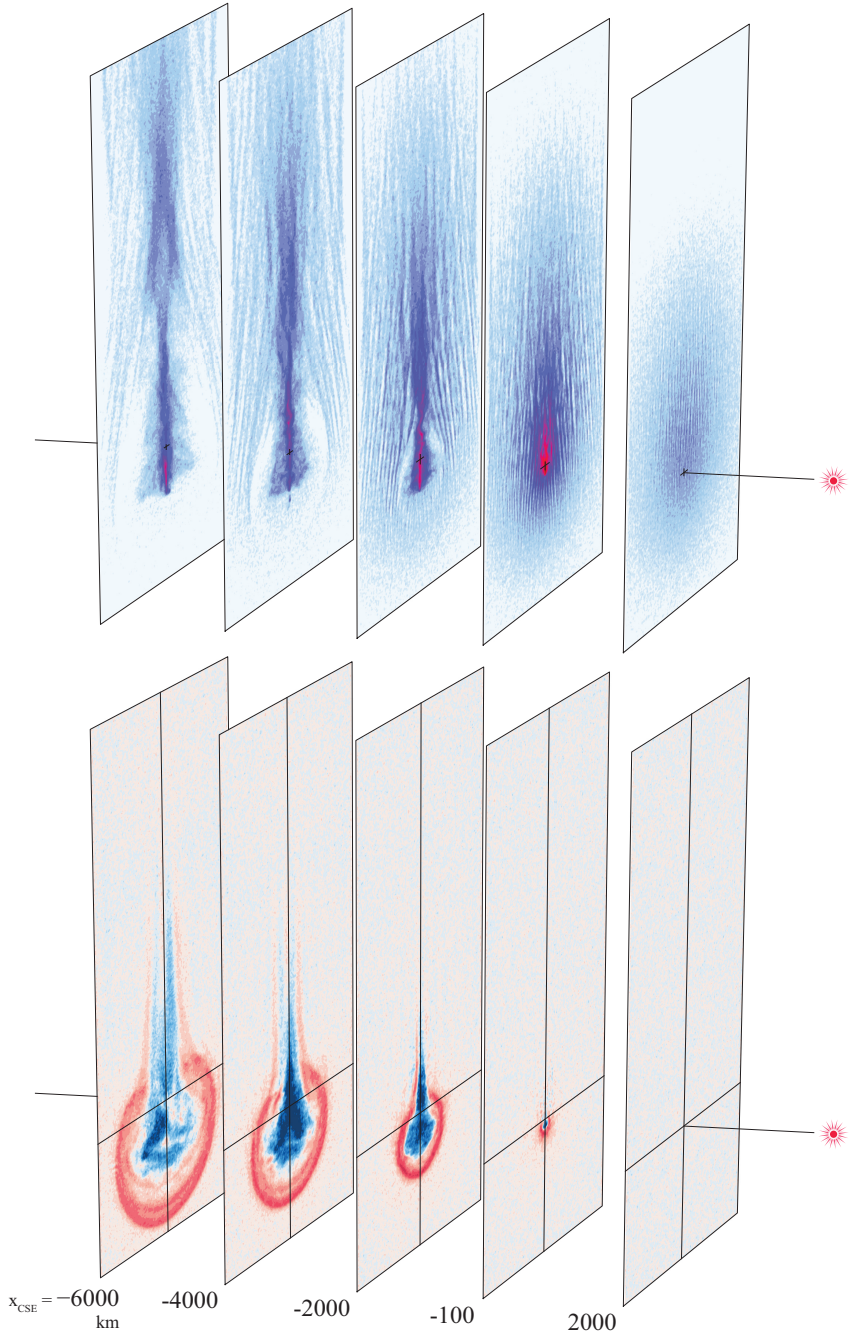


Figure 5.9: Density cuts perpendicular to the Sun-comet line, for the solar wind protons (lower row) and the cometary ions (upper row), taken from the reference simulation ( $R = 2.0$  au). The proton density is normalised to its upstream value,  $n_{\infty} = 1.25 \text{ cm}^{-3}$ .

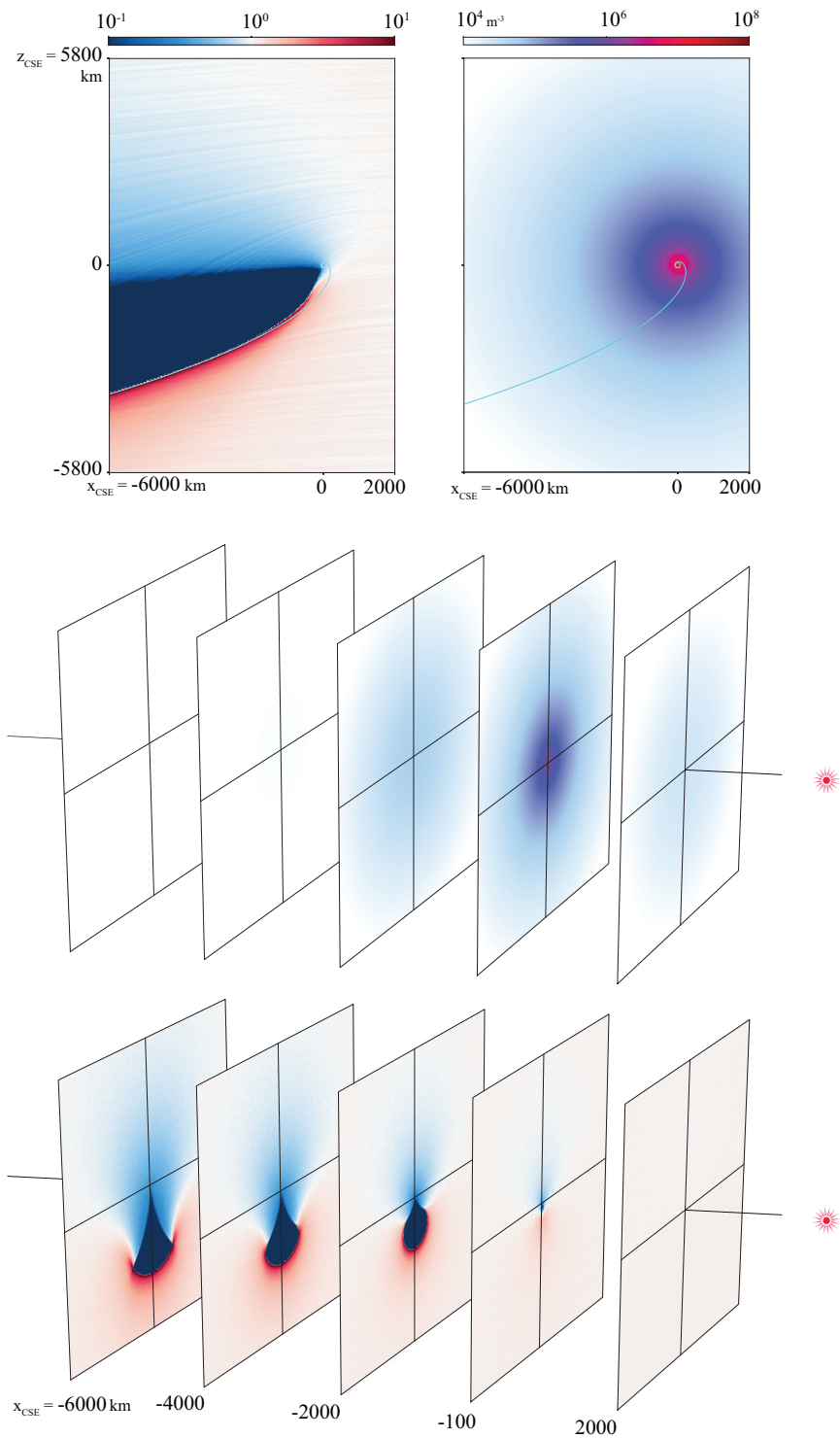


Figure 5.10: Same representation as in Figure 5.9, but taken from the semi-analytical model.

a great advantage when it comes to these structures, which form also far away from the nucleus. The refined meshes would not resolve them a large cometocentric distances due to too large cell size there.

We now look at the result of the three-dimensional semi-analytical approach, analysing the densities the exact same way, in Figure 5.10. The three-dimensional caustic of the semi-analytical model presents partially circular density profiles in the solar wind, and a tear-drop shaped cavity extending along the  $+z_{\text{CSE}}$ -semi-axis, with a general decrease of the solar wind ion density in the  $+z_{\text{CSE}}$  tail region. The increase and decrease of density, relative to the upstream flow, are almost equivalent with the simulation result of Figures 5.8 and 5.9.

Neither cometary pick-up ions nor a Mach cone are needed to reproduce a fairly accurate picture of the self-consistent view, and especially the partially circular shape of the over-density and the tear drop shaped solar wind ion cavity. These two aspects are the results of the single particle trajectories in a draped and piled-up magnetic field, just as described in the 2-dimensional case. What we learn from the 2D to the 3D case is the effect of the draping on the dynamics, effect that we isolated from higher order mechanisms included in the self-consistent model. Finally, since the situation in the  $(y = 0)$ -plane is the same as analysed in the previous chapter, the three-dimensional semi-analytical result also benefit from the support of the experimental results.

The simple model however shows a shift towards  $-z_{\text{CSE}}$  of the entire structure, and the solar wind over-density does not tend to close itself at  $z_{\text{CSE}} > 0$ . An obvious discrepancy in the models is the absence of feedback from the caustic on the plasma environment. For instance, in the simple model and unsurprisingly, the cometary ion density is not reflecting the presence of the solar wind over-density. It is also spherically symmetric, and densities at  $x = 2000$  km are equal to the densities at  $x = -2000$  km, whereas the self-consistent picture shows a denser cometary ion tail.

### 5.7.2 Electric and magnetic fields

In Figure 5.11, we give with the same tomographic representation the amplitude of the magnetic (upper row) and electric (lower row) fields from the reference simulation, to find out more about the discrepancies between simple and self-consistent models. The highest magnetic fields are found at the centre, with an enhancement of more than an order of magnitude from the upstream (also seen in Figure 4.1, along

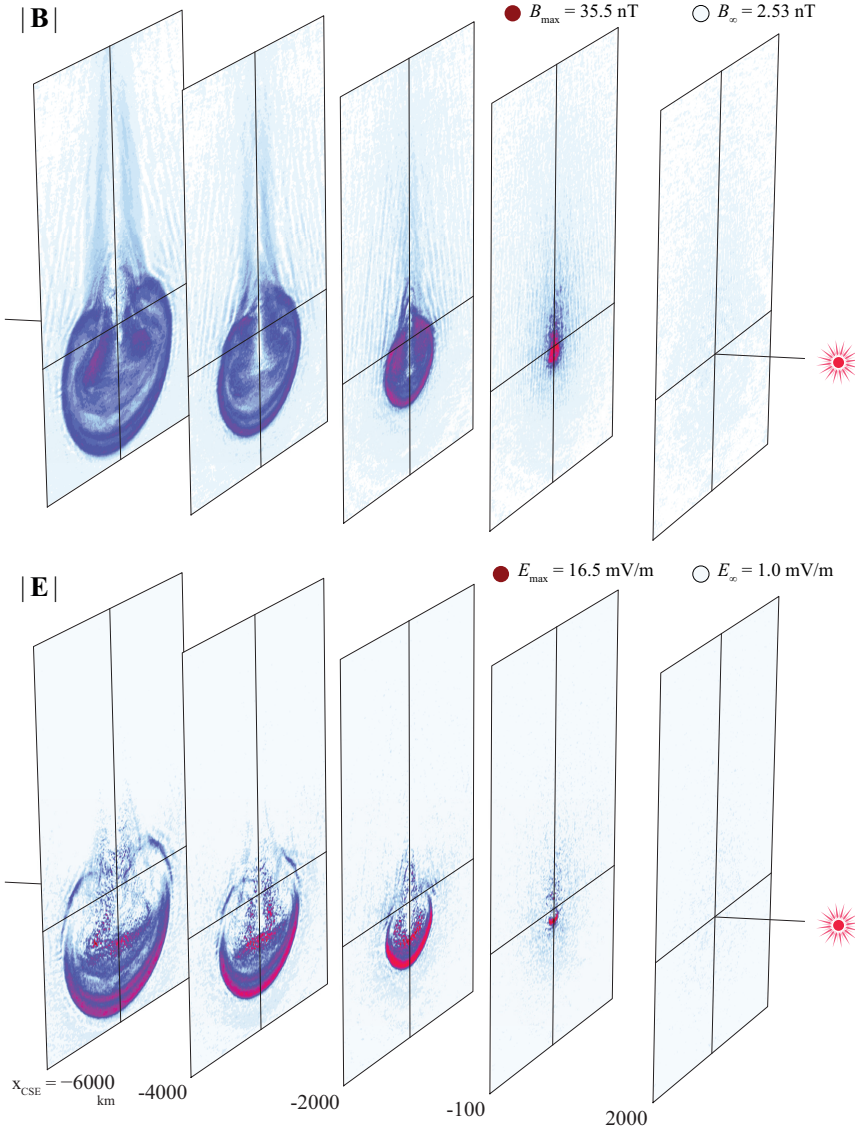


Figure 5.11: Tomographic representation of the magnetic and (total) electric fields, taken from the reference simulation ( $R = 2.0 \text{ au}$ ).

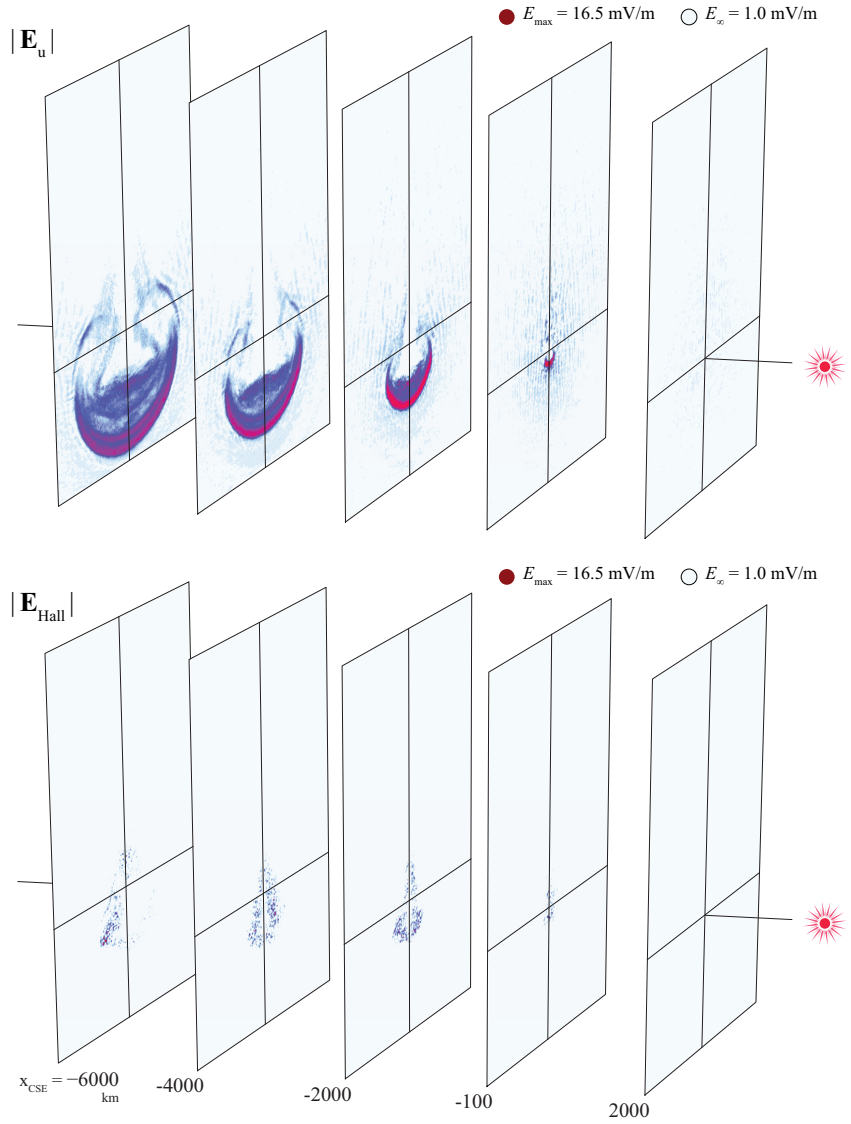


Figure 5.12: Decomposition of the total electric field into its motional component (upper row) and Hall component (lower row)

the day-side Sun-comet line). This corresponds to the classical magnetic field pile-up due to the deceleration of the overall plasma speed. However, we also find that both field amplitudes show a topography very similar with the proton density, with the typical partial ring profiles. This is precisely the feedback of the particles on the fields, the one that the simple model does not account for. To diagnose further the electric field, we divide it into its motional component and its Hall component, as shown in Equation (3.1). The first row of Figure 5.12 shows the norm of the motional component of the electric field,  $|\mathbf{E}_u| = |-\mathbf{u}_i \times \mathbf{B}|$ . We find that this component precisely reflects the proton over-density, with almost identical increase and decrease from upstream to downstream. The second row gives the amplitude of the Hall electric field,  $|\mathbf{E}_{\text{Hall}}| = 1/ne |\mathbf{j} \times \mathbf{B}| = 1/ne\mu_0 |(\nabla \times \mathbf{B}) \times \mathbf{B}|$ . The signature of the over-density is invisible in this component. The Hall electric field depends on the total current, which itself is given by the curl of the magnetic field (assuming a negligible displacement current in the Ampère-Maxwell law) and the total charge density. We find that the higher values of the Hall electric field in this case are due to the low densities, and not to the curl of the magnetic field (not shown). This also verifies that in most of the interaction region the motional electric field is indeed largely dominating.

Finally, the right column of Figure 5.13 gives the electric field lines, in the ( $y_{\text{CSE}} = 0$ )-plane (lower panel) and the plane ( $x_{\text{CSE}} = -4000$  km), which corresponds to the second to last cut in the tomographic views. The cometary ion density is given in the left column. As discussed in the 2-dimensional view of the tail excursion, the solar wind deflection results in a tilted motional electric field in the tail region, just as sketched in Figure 5.6 in the 2-dimensional case: as the solar wind dictates the bulk velocity of the plasma, the electric field – dominated by its motional component – is overall perpendicular to deflected the solar wind, and therefore misaligned with the  $z_{\text{CSE}}$ -axis. The same holds in the 3-dimensional case, and the deflection of the solar wind sideways (previous subsection) results in a motional electric field directed inward, towards the ( $y_{\text{CSE}} = 0$ )-plane. This corresponds to a focusing force on the slow cometary ions, which mostly follow the electric field before gaining speed (the magnetic field has little influence on the early cometary ion tail): the resulting cometary ion plume is a very thin structure. The effect will be found to be even stronger closer to the Sun (see next chapter).



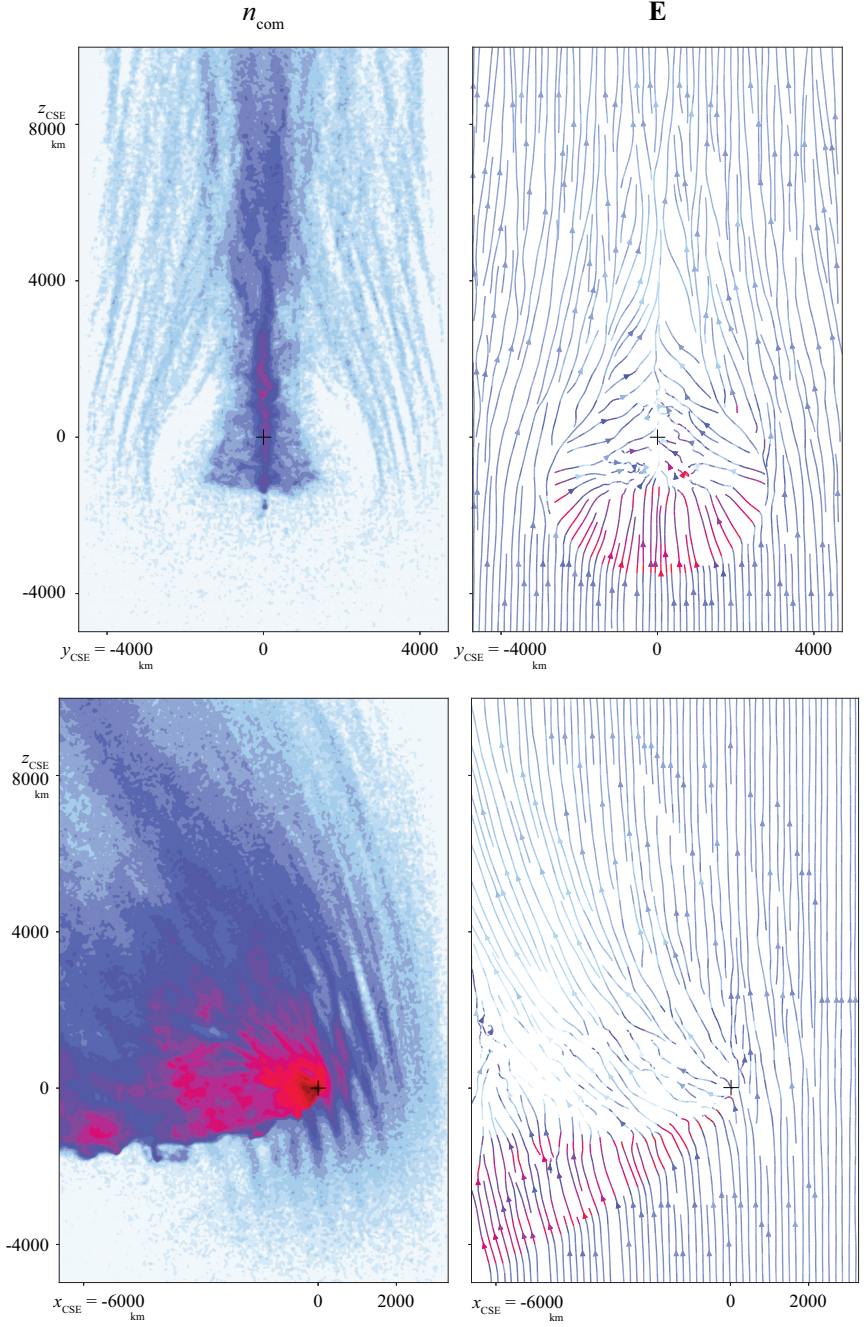


Figure 5.13: Cometary ion density (left column) and electric field lines (right column). The field lines are colour-coded with the field norm. The slow cometary ions are focused by the electric field into a thin structure.





## KINETIC VERSUS FLUID COMET

We have seen in the previous chapters different illustrations of the kinetic nature of the regime of the interaction, at 2 au from the Sun. We now propose a short excursion towards the fluid aspect of this interaction, when the comet is closer to the Sun. We use a second self-consistent simulation of the interaction when the comet is 1.7 au away from the Sun, in addition to the reference run, to try to capture the moment when the highly asymmetric plasma environment at large heliocentric distance starts its transformation towards a classical “fluid” comet, which as sketched in Figure 1.3 is axisymmetric with respect to the Sun-comet line.

### 6.1 DENSITY AND SINGLE PARTICLE TRAJECTORIES

The parameters of the new simulation are summarised in Table 6.1, and a 3-dimensional view of the solar wind proton and cometary ion densities is given in Figures 6.1 and 6.2 to illustrate the simulation result. In Figures 6.3 (2 au) and 6.4 (1.7 au), we give in the upper-left panel the solar wind proton density normalised with the upstream density, in the plane ( $y_{\text{CSE}} = 0$ ). The upper-right panels provide single particle trajectories, as previously done in Figure 5.2. We already discussed extensively the solar wind picture in the 2 au case. 0.3 au closer to the Sun, the most noticeable difference is that a similar over-density of solar wind protons is found, but this time with a branch in the  $+z_{\text{CSE}}$  region. The structure is however not perfectly symmetric, and the  $-z_{\text{CSE}}$  branch is curved, much like the over-density at larger heliocentric distance. In contrast with the earlier structure, we find several parallel over-densities, that were termed by Bagdonat and Motschmann [4] as *multiple Mach cones*. These concentric layers are also seen in the cuts of Figure 6.2. The nucleus (at the centre of the black cross) is now almost within a region in which almost no solar wind ions enter. This solar wind ion cavity extend in the tail region, most likely much farther than the simulation domain. The cometary ions are now accelerated mostly anti-sunward, with the highest densities found along the night-side Sun-comet line. As previously, the cometary ion and the solar wind ion densities are strongly anti-correlated. Figure 6.2 shows how the entire structure tends to close itself and become symmetric with respect to the Sun-comet line. The presence of cometary pick-up ion in the  $+E$ -hemisphere still results in an additional asymmetric structure in the solar wind density. The fan-like structures in the cometary ions are still present, only

Table 6.1: Parameters of the simulation – 1.7 au.

$R$	$Q$	$v_i$	$v_d$
1.7 au	$1.7 \cdot 10^{27} \text{ s}^{-1}$	$2.3 \cdot 10^{-7} \text{ s}^{-1}$	$6.2 \cdot 10^{-6} \text{ s}^{-1}$
$n_\infty$	$ \mathbf{B}_\infty $	$u_0$	$u_\infty$
$1.7 \text{ cm}^{-3}$	2.8 nT	$700 \text{ m} \cdot \text{s}^{-1}$	$400 \text{ km} \cdot \text{s}^{-1}$

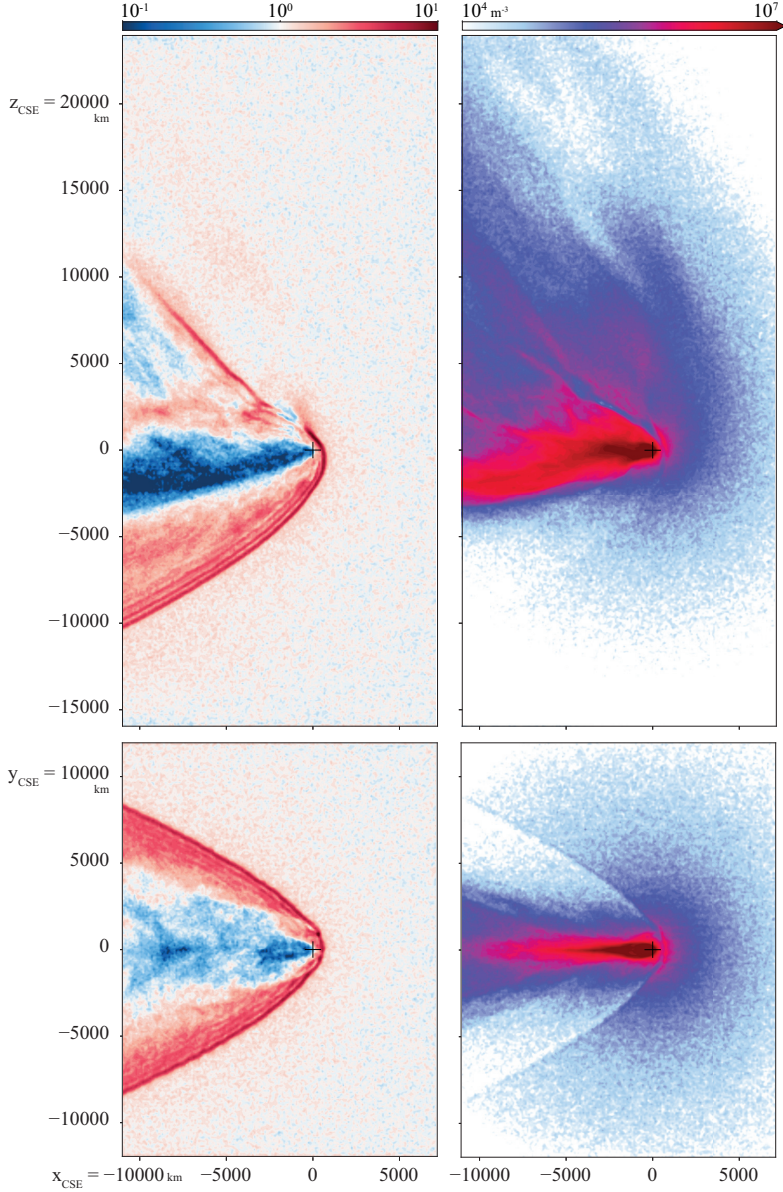


Figure 6.1: Density cuts of solar wind protons (left, normalised to the upstream value  $n_\infty = 1.7 \text{ cm}^{-3}$ ) and cometary ions (right) from the self-consistent simulation at 1.7 au

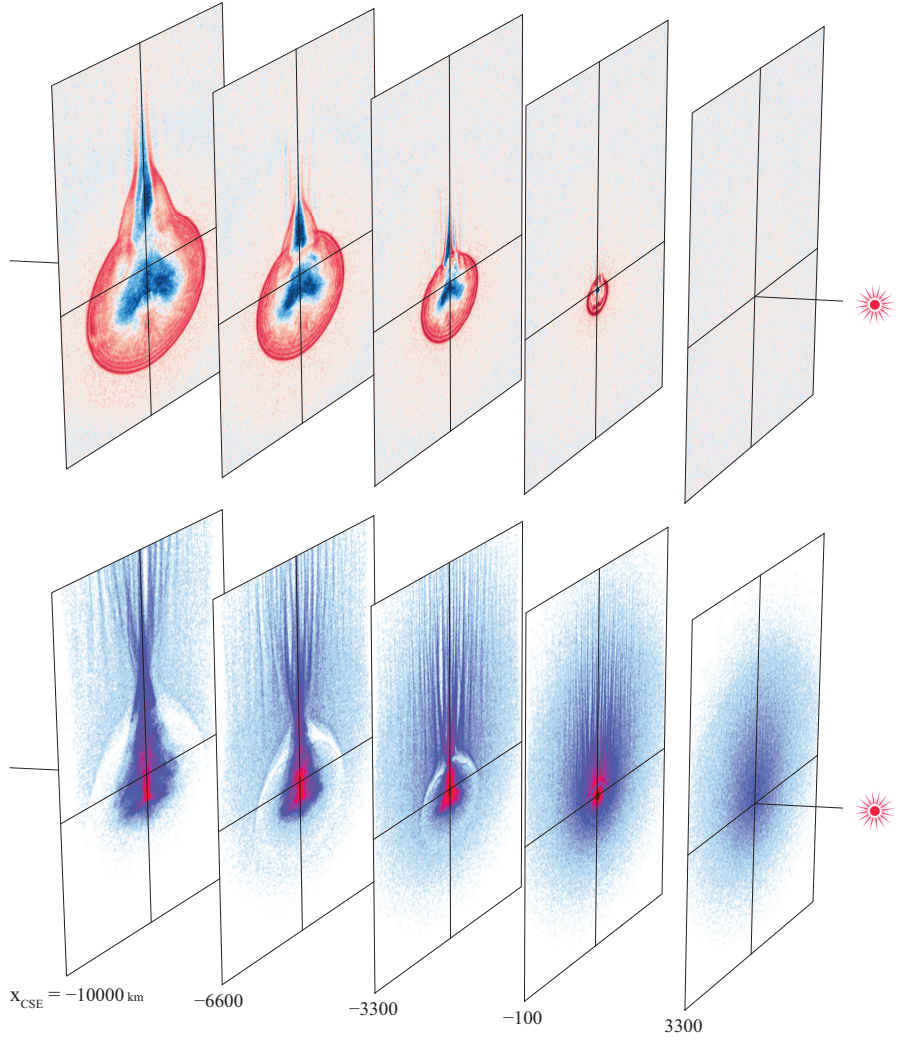


Figure 6.2: Density cuts perpendicular to the Sun-comet line, of solar wind protons (up, normalised to the upstream value  $n_{\infty} = 1.7 \text{ cm}^{-3}$ ) and cometary ions (down) from the self-consistent simulation at 1.7 au

in this hemisphere. The same focusing phenomenon happens, even more pronounced than previously. Overall, the picture tends to be more familiar with the situation at other solar system bodies, with for example the parabolic-like structure in the solar wind in the lower-left panel of Figure 6.1. On this point, one of the main interests of these figures is to show that the interaction between the two population is in no way limited to this young magnetosphere, where the solar wind density and the electric and magnetic fields are strongly increased. Indeed, upstream of this structure, the cometary ion density is high, higher than the incoming solar wind: already a lot of momentum is exchanged there.

We now go further than the partial information the density provides, and look at the single particle trajectories. As discussed previously, the solar wind proton gyroradius in the 2 au case is overall larger or comparable to the size of the simulation domain, upstream and downstream the caustic. In the 1.7 au case, the picture is very similar upstream of the structure, where the solar wind is mass-loaded and deflected continuously, with extremely large gyroradii. However, these radii are abruptly shrunk when the ions reach the structure. Downstream of the structure, the protons form cycloids with radii between 100 and 1000 kilometres. We note that inevitably, these cycloids are not all contained in the ( $y_{\text{CSE}} = 0$ )-plane, and some of them can reach large  $y$ -values: this seemingly 2-dimensional picture is a projection. Because the gyroradius is fairly constant behind the structure, the cusps of all the cycloids are aligned, forming the characteristic layers of higher densities, where the bulk velocity is decreased.

In the comprehensive doctoral thesis of Bagdonat [3], the formation of multiple Mach cones in fairly different conditions (outgassing rate and solar wind parameters) is discussed, in terms of the ion dynamics and in terms of non-linear MHD wave theory, and similar results were found.

## 6.2 VELOCITY DISTRIBUTION FUNCTIONS

We can still go beyond the single particle trajectories, by reconstructing the velocity space distribution functions at various locations. Particle-In-Cell models classically use a few tens of particles per cell: the velocity distribution function at one precise location is approximated by a few tens of particles, a fundamental limitation of this method. In order to better resolve the functions, we use the Liouville's theorem, which states that the distribution function is constant along the trajectories of the system, namely in our case the particle trajectories (in phase space). If we measure the value of the distribution function (number of particles per infinitesimal volume of phase space) anywhere along the trajectory  $(x(t), y(t), z(t), v_x(t), v_y(t), v_z(t))$  of one precise particle, we always get the same number. Using this fact, one can reconstruct the velocity distribution function at any point in physical space. We first launch particles from this point with all possible velocities, and integrate their motion *back in time*, to see what was

their trajectory far away from the interaction region, i.e. in the undisturbed solar wind where their distribution function is known (we use a simple maxwellian distribution). With this method, we can reconstruct the velocity distribution function with the desired resolution: the more particles are launched, the better resolved the distribution is. For each distribution in Figure 6.3 and 6.4, 27 million particles were used. The location where distribution functions are reconstructed are chosen in the ( $y_{\text{CSE}} = 0$ )-plane, in regions where the solar wind is seemingly largely disturbed.

We have to stress out the obvious limitation of this method. The reconstructed distributions are the real distributions only in the case of a perfectly steady system, i.e. a system in which the electric and the magnetic field are time independent, at least for the time it takes for the solar wind ions to go across the system. This is rarely the case in the interactions between solar system bodies and the solar wind, but some interactions are more “suitable” than others. In our case, the 2 au situation reaches a state in which no major changes happen, and the fields are fairly time independent. In the 1.7 au case, some features are dynamical, typically the  $+z_{\text{CSE}}$  branch of the solar wind structure. The reconstructed velocity space distribution functions are only estimations of the real functions. Somewhat, they are an instantaneous view of the fields’ properties, which becomes a physical distribution function only if the system is steady long enough for solar particles to follow the whole solutions (trajectories) of the system. Obviously, this limitation is also shared with the single test-particle trajectories used in Figures 5.2, 6.3 and 6.4.

A lot of information can be found in these distribution functions, and we only tackle a part of it here. The main observation in the 2.0 au case is that in all the locations we looked at, the main beam of the solar wind remains, with negligible deceleration, and still concentrating most of the density. This main beam, close to the upstream speed of 400 km/s, is deflected in the ( $x_{\text{CSE}}, z_{\text{CSE}}$ )-plane, towards negative  $z_{\text{CSE}}$  values, exactly as discussed and illustrated in the previous chapters. In all distributions but distribution *ii*, secondary structures of lower density appear. The most noticeable one is a second beam in distribution *i*, also contained in the ( $x_{\text{CSE}}, z_{\text{CSE}}$ )-plane, which shows a lower speed, a lower density, and a much larger deflection, larger than  $90^\circ$ . The distribution function is reconstructed about a hundred kilometres from the nucleus, slightly day-side, exactly similar to the fly-by during which a double proton beam was observed, at 1.99 au from the Sun. The reconstructed distribution and the observed distribution (Figure 5.7) look almost identical. However we note that the solar wind ions building this distribution have flown through the inner-most region, which has a limited resolution in the hybrid simulation, and where the physics may very well be more complex (ambipolar electric field and charge exchange processes are the most



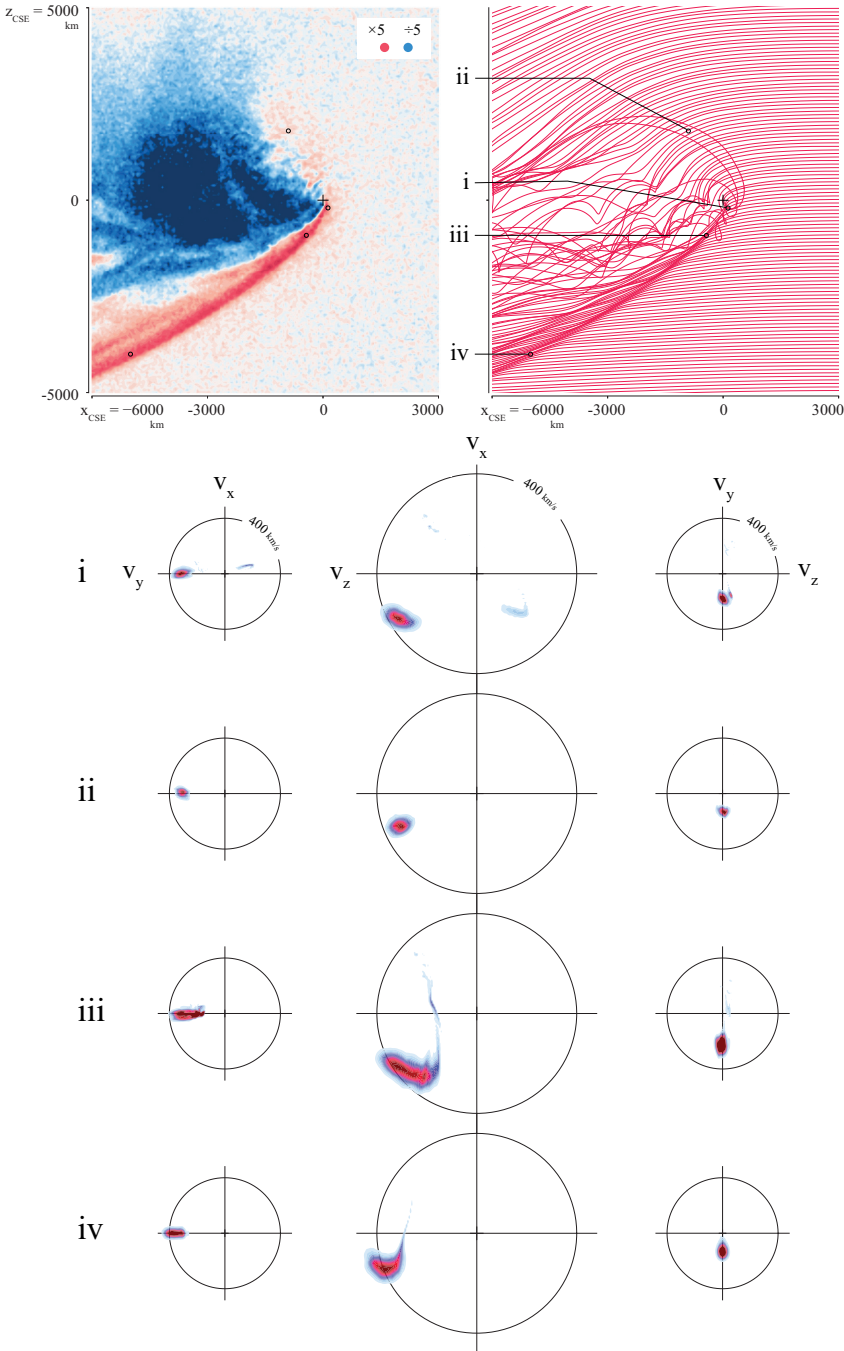


Figure 6.3: Solar wind proton density (upper-left) and trajectories (upper-right) from the reference run. Lower rows: velocity space distribution function reconstructed using a backward-Liouville method, at four different locations indicated in the upper-row.

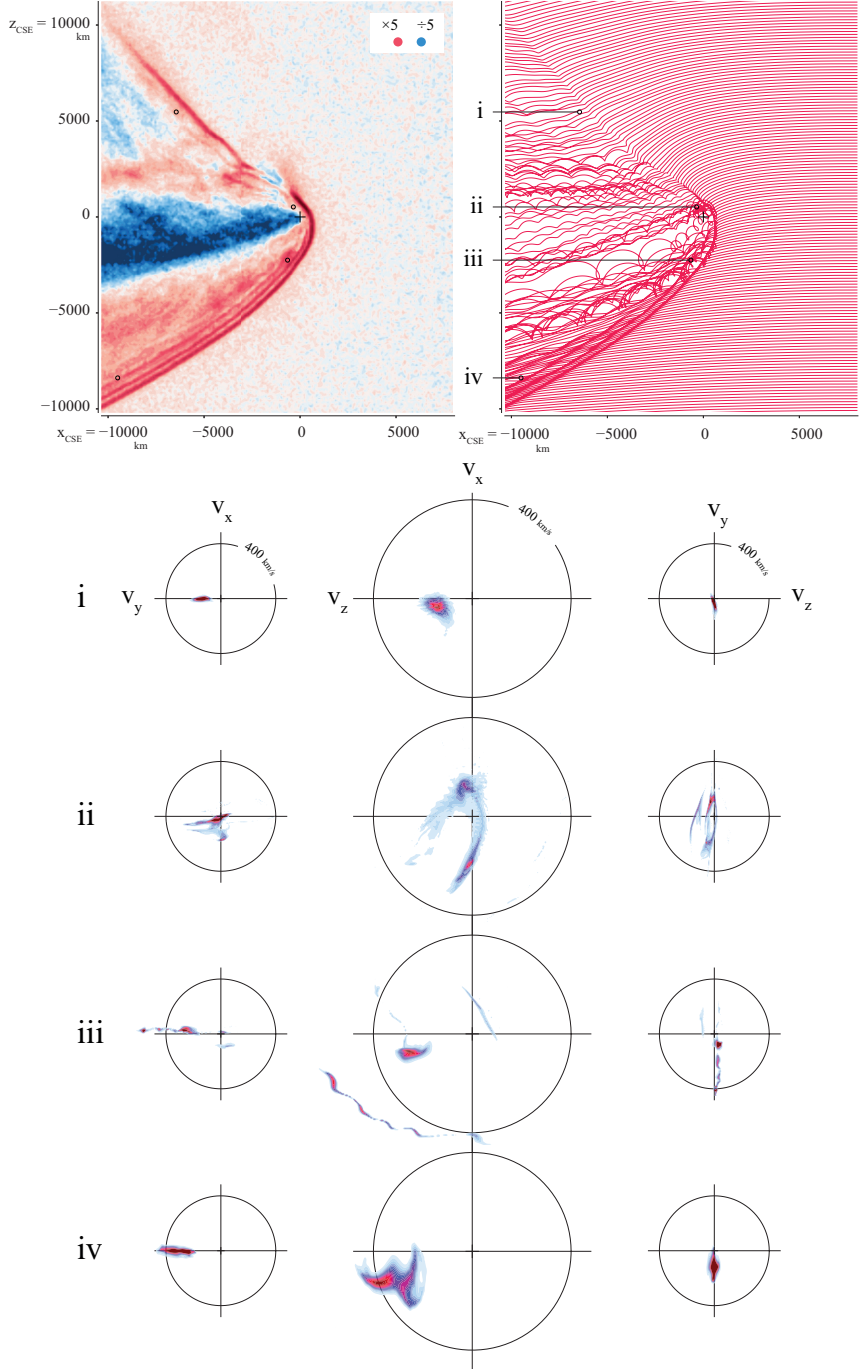


Figure 6.4: Same as Figure 6.3 for the 1.7 au case.

obvious candidates). The similarity between the distributions may in this case point at the limited effect of these higher level physical processes.

Looking now at the situation 1.7 au away from the Sun, the picture is completely transformed. Whereas previously the main beam of the solar wind was surviving the interaction at no energy cost and some limited deflection, we now observe that within the structure, the solar wind proton beam is profoundly transfigured. Distributions *i* and *ii* are taken in the  $+z_{\text{CSE}}$  region, and they show a severely decelerated flow. The situation in the  $-z_{\text{CSE}}$  region is different. We find sharp and clear structuring of the distribution functions, manifestly due to the ordered gyration of the solar ions downstream the structure. Distribution *iii* shows significant acceleration of a complete branch. This difference between the  $-z_{\text{CSE}}$  and the  $+z_{\text{CSE}}$  regions couldn't be spotted even in the single particle trajectories. By analogy with comet Halley's magnetosphere, we term this region of somewhat heated and somehow decelerated flow a *cometosheath* [89]. However in the 1.7 au case, we have seen that the system is not yet symmetric, and that different regions of the sheath contain differently behaving plasmas.

We note that we yet couldn't find partial ring distribution functions of solar wind protons, centred on the origin and contained in the  $(x_{\text{CSE}}, z_{\text{CSE}})$ -plane, as often observed in situ, discussed in Section 5.4 and shown in Figure 5.5. This is a major missing bridge between the numerical and the experimental data. Additionally, it appears that in the experimental data, the solar wind distribution function is transformed from a deflected beam to a partial ring at a heliocentric distance larger than 2 au. Once more, we note that *Rosetta* was probing very low cometocentric distances, not accessible to these simulations.



## SUMMARY & CONCLUSIONS

---

### 7.1 SUMMARY

We have first proposed a simple model of the exchange of momentum between two plasma beams, a generalised gyromotion. This kinetic description allows us to go to the much smaller scales of the interaction of one plasma loaded by another. We have illustrated the signature of this exchange of momentum in the experimental in situ results, on the relative dynamics of the solar wind and the pick-up cometary ions.

Simple models of the cometary ion density and of the magnetic field, together with the modelled exchange of momentum, lead us to a global model of the solar wind ion dynamics. One of the main aspects of this model is the very limited deceleration of the solar particle stream, in perfect agreement with *Rosetta* observations, and in contrast with the classical view of the interaction at comets with higher outgassing rates. The solar wind deflection was quantified over the mission and successfully compared to in situ results. One of the model's features is a solar wind ion cavity, the scale of which appeared to correlate nicely with the observations. The modelled proton trajectories were successfully tested against data from one of *Rosetta*'s excursions, over an extended region of the coma. Double-beam distribution functions of solar wind protons are found in the model as well as in the self-consistent simulations and the in situ data, a phenomenon which may have been observed at comet *Krigg-Skjellerup* as well.

When comparing the simple 3-dimensional model with a self-consistent model, we find a causality between the particle dynamics and the field properties. The initial addition of new-born cometary ions leads to an amplified and deformed magnetic field. The peculiar dynamics of the incoming solar ions within this field leads to a density structure. All these first steps are found in the simple model and in the self-consistent model. The density structure then triggers a response from the fields, only seen in the self-consistent picture. We conclude that contrary to what was thought until now, the very seed of a young cometary magnetosphere is not a Mach cone, but the geometric characteristics of the stream.

This fields' feedback triggered by the flow geometry forms a first discontinuity in the system, which later on at lower heliocentric distances will separate two distinct regions, characterised by the ion velocity space distribution functions, upstream and downstream of the structure.

## 7.2 CONCLUSIONS AND OPENINGS

Fundamentally, the cometary ion density, which for large scales, day-side of the coma and down to 2 au from the Sun, can be approximated by a  $r^{-2}$  law, implies a spatial gradual evolution of the interaction over a gigantic region, interaction which is indeed fundamentally kinetic. Therefore, the fluid case naively depicted in the introduction (Figure 1.2) cannot possibly exist without the creation of a boundary, a discontinuity. *The continuity of the plasma environment has to be broken in order to get gyroradii smaller than the interaction region.* The seed of this discontinuity is the caustic, which from a purely geometric aspect of the flow in a simplified and continuous environment introduces the first seminal structure, in the particle density. Somewhat, the solar wind stumbles over itself. This structure in turn induces a response from the magnetic field, and combined together the ion density and the magnetic field result in a modified electric field.

Between 2.0 au and 1.7 au in the numerical results, the nature of the simulated interaction between the solar wind and the ionised coma is transformed. At 2.0 au, despite structures already appearing in the solar wind density, together with some “exotic” single particle behaviour, the incident flow as a whole is only slightly disturbed, the solar wind ion beam survives the interaction. At 1.7 au, the early over-density has now evolved into a structure of different nature, which sharply separates an upstream kinetic region from a downstream fluid region, with properties similar to a magnetosheath. Without looking at the kinetic level of the data (experimental or numerical), this fundamental aspect is missed. Figure 7.1 summarises and reduces these pictures in two different schematics, for the 2.0 au and the 1.7 au cases.

We willingly avoid the term “shock”, and its hydrodynamic connotation. Our entire description is based on the kinetic properties of the system, and mixing these kinetic properties with macroscopic fluid concepts could only mislead us and lead to severe short-cuts. As introduced in the first Chapter, cometary bow-shocks or bow waves are a difficult and somewhat elusive topic. A complete – and exciting – study is needed to compare properly the fluid analysis and the kinetic analysis. For instance, what is the value of the magnetosonic Mach number at the structure? Where does the solar wind, when treated as a fluid, become subsonic? We can already note that the solar wind boundary introduced in this thesis in the 1.7 au case is a sharp boundary separating two different regions, in contrast with the general fluid description of a thick, weak bow shock observed and modelled in higher outgassing activity cases.

The subsequent studies in the continuation of this work could focus on two main problems. The first would be to find the numerical tools and new ways of analysing the experimental data (single-instrument as well as multi-instrument) to diagnose what really happens close to the nucleus, at the probe, when the proton density plummets. In other words, what are the detailed mechanisms playing a role in the

opening of the solar wind ion cavity? This would require a better physics for the electrons on the numerical side (fully kinetic models for instance) and a better spatial resolution to resolve the ambipolar electric field set by the pressure gradients within the inner coma, as well as a realistic modelling of the ion-neutral interactions acting upon the incident flow.

The second topic of great – and somewhat of more fundamental – interest is the general comparison between the kinetic and the fluid descriptions of the interaction, unifying and building bridges between the previous descriptions at higher outgassing activity and the kinetic theory built in the context of 67P/Churyumov–Gerasimenko. This comet definitely provides us with a unique laboratory, right at the interface of the two plasma physics scales, a situation which cannot easily be found elsewhere in nature.

Solar wind structures  
 $R = 2$  au

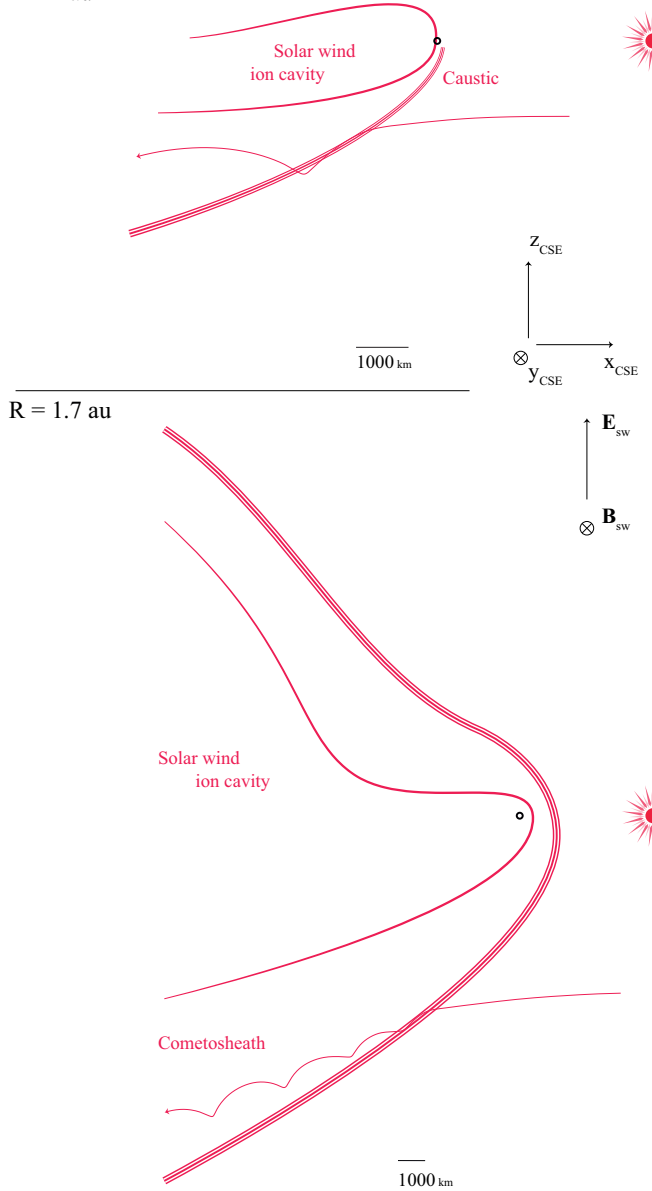


Figure 7.1: Summary schematics of the solar wind structures within a partially ionised cometary atmosphere. The first row pictures the interaction when the regime is fully kinetic, whereas the lower schematic shows the interaction happening closer to Sun, with two well-separated regions in which the interaction is either kinetic in nature (upstream) or fluid (downstream of the structure).

Part I

APPENDICES



## GEOMETRIC FACTOR

---

### A.1 THE MOST BASIC INSTRUMENT

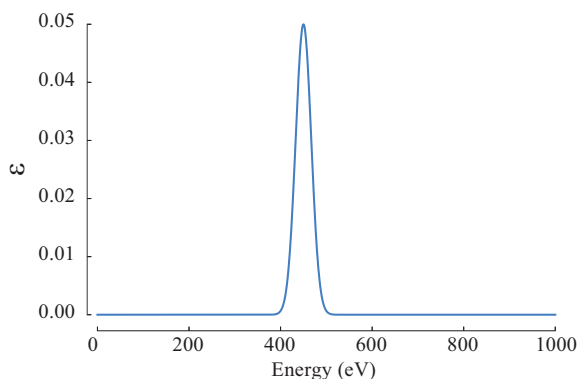
We first consider a simplified and hypothetical particle instrument. Contrary to most of particle instruments, this simplified one is not sweeping through energy and angles, i.e. our simplified instrument is sampling one single point of the velocity space. To further simplify the problem, we only consider the energy dimension  $E$  and ignore all other dimensions (energy is an arbitrary choice).

We integrate for a time  $\tau$ , and the instrument provide one scalar  $c$  (#), which is immediately translated into count rates  $r$  :

$$r(t) = c(t)/\tau \quad (\#/s) .$$

If this instrument is meant to measure particles with energy  $E_0$ , it would ideally tell us "in  $\tau$  seconds,  $c$  particles with energy  $E_0$  eV where detected". But such an ideal <sup>1</sup> instrument cannot exist, since any real instrument necessarily has a broad response  $\varepsilon(E)$ , as defined and illustrated below:

$$\varepsilon(E) = out(E)/in(E) .$$



$in(E)$  is the real, physical rate of incoming particles, and  $out(E)$  is the detected count rate. So this instrument, if illuminated with a flat signal of 100 #/s and integrating for 1 s, would detect 5 counts at its central response  $E_0 = 450$  eV. Note that this gaussian shaped

---

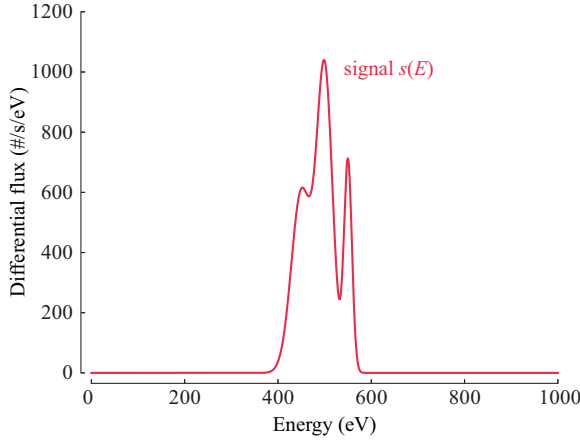
<sup>1</sup> Ideal is not the right word. In this context, we consider that the signal to be measured is a continuous function of energy, which is an approximation. Since we consider particles, the signal is a discrete function of energy, and such an "ideal" instrument (with a dirac as its response) would most likely detect nothing at all.

instrument response is another simplification (but considering a more general response would not add a lot to the thinking).

An important value is the area  $G$  below this response, which is a major product from calibration:

$$G = \int_{-\infty}^{+\infty} \varepsilon(E) dE \quad (\text{eV}) . \quad (\text{A.1})$$

Let's now consider a "scientific signal" with the energy profile (or spectrum) given below, constant through time.



The ideal instrument would provide the value of the signal  $s(E)$  at its central response  $E_0$ , i.e.  $s(E_0) = s(450)$ . It would tell us "at 450 eV, the signal is 613 particles per second". But what does the real instrument provide us with?

For some time integration  $\tau$ , the real instrument will give us one scalar  $c$  (#) which correspond to

$$c = \tau \int_{-\infty}^{+\infty} \varepsilon(E) \cdot s(E) dE$$

$$\Rightarrow r = \int_{-\infty}^{+\infty} \varepsilon(E) \cdot s(E) dE \quad [\#/s] .$$

And this last expression is extremely important: this is the *only* value we can get from our instrument, the product of the signal with the instrument response, integrated over energy.

A value which is systematically used with particle instruments is the differential flux  $j$  (a scalar value). It is defined as

$$j = \frac{r}{G} = \frac{\int_{-\infty}^{+\infty} \varepsilon(E) \cdot s(E) dE}{\int_{-\infty}^{+\infty} \varepsilon(E) dE} \quad [\#/s/\text{eV}] . \quad (\text{A.2})$$

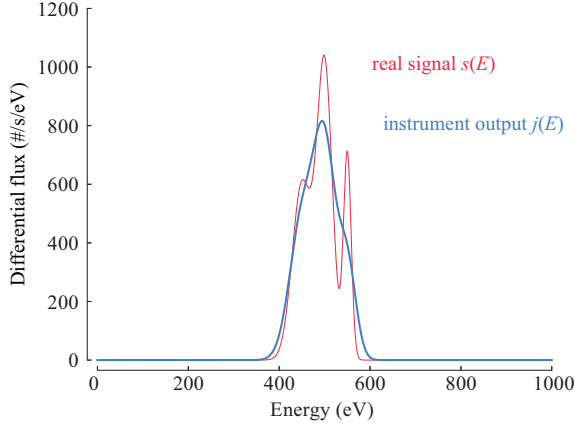
But  $j$  is still different than  $s(450)$  ! In our example,  $s(450 \text{ eV}) = 613$ , and  $j$  is 549.6 #/s/eV. (For a flat signal of 100 #/s however,  $j$  would be 100 #/s/eV.)

So we understand that fundamentally, a particle instrument cannot provide an exact information about a signal, no matter the quality of the calibration.



## A.2 CONTINUOUS ENERGY SWEEP

Let's imagine that we can now tune the central response  $E_0$  of our simplified instrument, in order to scan through the spectrum. We assume (wrongly) that the response keeps the same shape as  $E_0$  sweeps through energy. For one value of  $E_0$  (one position of the response along energy) we get one value for  $j$ . So we get a series of differential flux  $j(E)$ . What does it look like in our ideal example, compared to the real signal?



We see that some times the instrument under-estimates the real signal, sometimes it over-estimates it. Of course, in this continuous description of the signal, the narrower the instrument response would be, the closer to the real signal the instrument output would get.

However, we may not be only interested in reconstituting the signal  $s(E)$ . If we are after the density (moment of the 0th order), defined as the area below  $s(E)$ <sup>2</sup>, this effect of over/under-estimation might tend to cancel itself. The differential flux  $j$ , now function of energy, is:

$$j(E) = \frac{r(E)}{G(E)} = \frac{\int_e \varepsilon_E(e) \times s(e) de}{\int_e \varepsilon_E(e) de} \quad [\#/s/eV]. \quad (\text{A.3})$$

The density is:

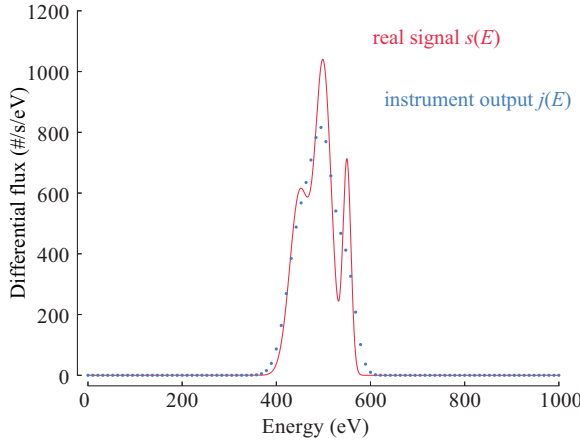
$$n = \int_E j(E) dE = \int_E \frac{r(E)}{G(E)} dE \quad [\text{cm}^{-3}]. \quad (\text{A.4})$$

The instrument is better at estimating the density than at reconstructing the real signal. In this precise example, since the instrument response shape is considered to be independent of the energy, we actually define the instrument output  $j(E)$  as the convolution between the instrument response  $\varepsilon(E)$  and the signal  $s(E)$ , divided by  $G$  (also energy independent). Therefore, in this precise example only, the density given by the instrument is the real density.

<sup>2</sup> This is not the proper definition of the density, which would require to transform the differential flux  $j$  into the velocity distribution function  $f$ , see below.

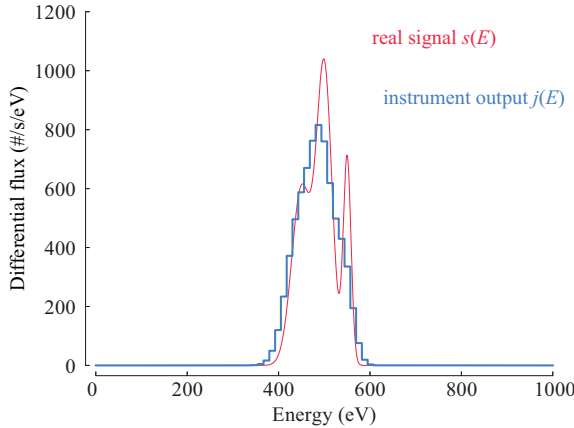
## A.3 DISCRETE ENERGY SWEEP

One step further toward reality: for telemetry (data volume) and time resolution considerations, the instrument cannot sweep its response continuously to get a perfect resolution. We have to limit ourselves to a finite number of energy settings, 96 in the example below. We get a rougher estimation of the signal:



Each point of the instrument output  $j(E)$  is given by equation A.3.

It is now quite challenging to discern the three components of the real signal. What about density? To estimate the density, most of the time the rectangle method is used to integrate the instrument output  $j(E)$  (Riemann integral):



Equation A.4 becomes:

$$n = \sum_E \left( \frac{\int_{-\infty}^{+\infty} \varepsilon_E(e) \times s(e) \, de}{\int_{-\infty}^{+\infty} \varepsilon_E(e) \, de} \times \Delta E(E) \right) = \sum_E \left( \frac{r(E)}{G(E)} \times \Delta E(E) \right) . \quad (\text{A.5})$$

And in our case, considering an instrument response and an energy step independent of the energy:

$$n = \Delta E / G \times \sum_E r(E) .$$

The exact same thinking can be applied for other dimensions, and the expressions of the integrated moments are given in Chapter 2 and developed in Appendix B in the case of ICA.

#### A.4 MISCELLANEOUS

Term	Definition	Unit
Phase distribution function $f(\mathbf{r}, \mathbf{v})$	Number of particles $N$ within differential phase volume $d^3r d^3v$ , i.e. $f(\mathbf{r}, \mathbf{v}) = \frac{N}{d^3r d^3v}$	$\text{s}^3 \text{m}^{-6}$
Number density $n(\mathbf{r})$	Number of particles $N$ in a volume $d^3r$ , i.e. $n(\mathbf{r}) = \frac{N}{d^3r}$	$\text{m}^{-3}$
Differential directional number flux $j(\mathbf{r}, E, \varphi, \vartheta)$	Number of particles $N$ of energy within $dE$ , crossing a differential area $dA$ per differential time $dt$ within a differential solid angle $d\Omega$ , i.e. $j(E, \Omega) = \frac{N}{dA dt dE d\Omega}$	$\text{m}^{-2} \text{s}^{-1} \text{sr}^{-1} \text{J}^{-1}$

Table A.1: Definitions and descriptions of the three main physical values used in this work

Proof of equation 2.7:

By definition:

$$f(\mathbf{r}, \mathbf{v}) = \frac{N}{d^3r d^3v}$$

$$j(E, \Omega) = \frac{N}{dA dt dE d\Omega}$$

One can always rotate  $(\hat{x}, \hat{y}, \hat{z})$  so  $\hat{z}$  is aligned with  $\mathbf{v}$ . This way,  $dx dy = dA$  and  $dz = v dt$ . Therefore:

$$d^3r = dx dy dz = v dA dt = \sqrt{\frac{2E}{m}} dA dt$$

From 2.5:

$$d^3v = \sqrt{\frac{2E}{m^3}} dE d\Omega$$

So we write  $f(\mathbf{r}, \mathbf{v})$  as:

$$f(\mathbf{r}, \mathbf{v}) = \frac{N}{dA dt dE d\Omega} \frac{m^2}{2E}$$

$$f(\mathbf{r}, \mathbf{v}) = \frac{m^2}{2E} j(E, \Omega)$$

## MOMENTS BY INTEGRATION

We consider now the distribution function  $f(\mathbf{r}, \mathbf{v})$  of one ion population. Macroscopic properties of this population (density, velocity, temperature, etc.) can be described by the following family of integrals:

$$\mathbf{M}^k = \int_{\mathbf{v}} \mathbf{v}^k \times f(\mathbf{v}) \, d^3\mathbf{v} \quad (\text{B.1})$$

$\mathbf{M}^k$  is the moment of order  $k$ .  $k = 0$  corresponds to the number density  $n(\mathbf{r})$ ,  $k = 1$  will give the bulk velocity of the population,  $k = 2$  gives the pressure tensor.

## B.1 DENSITY

We get for  $k = 0$ :

$$n(\mathbf{r}) = \int_{\mathbf{v}} f(\mathbf{v}) \, d^3\mathbf{v}$$

From 2.5, in the instrument reference frame:

$$n(\mathbf{r}) = \int_E \int_{\varphi} \int_{\theta} f(\mathbf{r}, E, \varphi, \theta) \sqrt{\frac{2E}{m^3}} \cos(\theta) \, dE d\varphi d\theta \quad (\text{B.2})$$

$\mathbf{r}$  is the spacecraft position,  $E$  the total energy of a particle in joule J,  $m$  its total mass in kilogram kg,  $\varphi$  and  $\theta$  the azimuth and polar angles in the instrument coordinate system, in radian.

Using the rectangle method exactly as we did in Appendix A, we get the estimation of the density by integration:

$$n(\mathbf{r}) = \sum_E \sum_{\varphi} \sum_{\theta} f(\mathbf{r}, E, \varphi, \theta) \sqrt{\frac{2E}{m^3}} \cos(\theta) \, \Delta E \Delta \varphi \Delta \theta \quad (\text{B.3})$$

Using 2.7:

$$n(\mathbf{r}) = \sum_E \sum_{\varphi} \sum_{\theta} \frac{m^2}{2E} j(\mathbf{r}, E, \varphi, \theta) \sqrt{\frac{2E}{m^3}} \cos(\theta) \, \Delta E \Delta \varphi \Delta \theta \quad (\text{B.4})$$

$$= \sum_E \sum_{\varphi} \sum_{\theta} \sqrt{\frac{m}{2E}} \cos(\theta) j(\mathbf{r}, E, \varphi, \theta) \, \Delta E \Delta \varphi \Delta \theta \quad [\text{m}^{-3}] \quad (\text{B.5})$$

We now use the geometric factor  $G$ , making the next steps "calibration-specific" (*i.e.* dependent on the definition of  $G$ ). A factor  $10^{-4}$  appears

in order to convert  $G$  to  $m^2$ , as the one factor used for ICA is given in  $\text{cm}^{-2}$ .

$$n(\mathbf{r}) = 10^4 \sum_E \sum_\varphi \sum_\theta \sqrt{\frac{m}{2E}} \cos(\theta) \frac{c(\mathbf{r}, E, \varphi, \theta)}{\tau G(E, \varphi, \theta) E} \Delta E \Delta \varphi \Delta \theta \quad (\text{B.6})$$

$$= 10^4 \sum_E \sum_\varphi \sum_\theta \sqrt{\frac{m}{2E^3}} \frac{\cos(\theta)}{\tau} \frac{c(\mathbf{r}, E, \varphi, \theta)}{G(E, \varphi, \theta)} \Delta E \Delta \varphi \Delta \theta \quad [\text{m}^{-3}] \quad (\text{B.7})$$

Using 2.6,  $E = e Q \mathcal{E}$ , and  $\Delta E = e Q \Delta \mathcal{E}$ . We get:

$$n(\mathbf{r}) = 10^4 \sum_{\mathcal{E}} \sum_\varphi \sum_\theta \sqrt{\frac{m}{2e Q \mathcal{E}^3}} \frac{\cos(\theta)}{\tau} \frac{c(\mathbf{r}, \mathcal{E}, \varphi, \theta)}{G(\mathcal{E}, \varphi, \theta)} \Delta \mathcal{E} \Delta \varphi \Delta \theta \quad (\text{B.8})$$

The rest of the derivation is calibration and instrument dependent. For ICA,  $G(\mathcal{E}, \varphi, \theta) = G(\mathcal{E})$  and  $\Delta \varphi$  can be extracted for the general sum:

$$n(\mathbf{r}) = \frac{10^4}{\tau} \sqrt{\frac{m}{2e Q}} \Delta \varphi \cdot \sum_{\mathcal{E}} \left( \frac{1}{\sqrt{\mathcal{E}^3}} \frac{\Delta \mathcal{E}(\mathcal{E})}{G(\mathcal{E})} \sum_\theta \left( \cos(\theta) \Delta \theta(\mathcal{E}, \theta) \sum_\varphi (c(\mathbf{r}, \mathcal{E}, \varphi, \theta)) \right) \right) \quad (\text{B.9})$$

Note that for ICA,  $\Delta \varphi = \frac{2\pi}{16}$ . But for clarity of the expression, all these factorisations are not desirable:

$$n(\mathbf{r}) = \frac{2\pi 10^4}{16 \tau} \sqrt{\frac{m}{2e Q}} \sum_{\mathcal{E}} \sum_\varphi \sum_\theta \left( \frac{1}{\sqrt{\mathcal{E}^3}} \frac{\cos(\theta)}{G(\mathcal{E})} c(\mathbf{r}, \mathcal{E}, \varphi, \theta) \Delta \mathcal{E}(\mathcal{E}) \Delta \theta(\mathcal{E}, \theta) \right) \quad (\text{B.10})$$

## B.2 BULK VELOCITY

We get for  $k = 1$ :

$$n(\mathbf{r}) \underline{\mathbf{u}}(\mathbf{r}) = \int_{\mathbf{v}} \mathbf{v}(\mathbf{r}) f(\mathbf{v}) d^3 \mathbf{v}$$

From 2.5, in the instrument reference frame:

$$n(\mathbf{r}) \underline{\mathbf{u}}(\mathbf{r}) = \int_E \int_\varphi \int_\theta \mathbf{v}(\mathbf{r}) f(\mathbf{r}, E, \varphi, \theta) \sqrt{\frac{2E}{m^3}} \cos(\theta) dE d\varphi d\theta \quad (\text{B.11})$$

$\mathbf{r}$  is the spacecraft position,  $E$  the total energy of a particle in joule J,  $m$  its total mass in kilogram kg,  $\varphi$  and  $\theta$  the azimuth and polar angles in the instrument coordinate system, in radian.

We are now working with a vectorial expression. In order to express this vector, we need to choose 3 directions, orthogonal to each-other, and project this expression along each one of these direction. A good choice is the initial cartesian system  $(v_x, v_y, v_z)$ , with the change of variable given in Section 2.2. We project B.11 along the directions  $\hat{v}_x$ ,  $\hat{v}_y$ , and  $\hat{v}_z$ .

$$n(\mathbf{r}) u_x(\mathbf{r}) = \int_E \int_\varphi \int_\theta v_x(\mathbf{r}) f(\mathbf{r}, E, \varphi, \theta) \sqrt{\frac{2E}{m^3}} \cos(\theta) dE d\varphi d\theta \quad (\text{B.12})$$

Using the rectangle method, with  $v_x = v \cos(\theta) \cos(\varphi)$  and  $v = \sqrt{\frac{2E}{m}}$ :

$$n(\mathbf{r}) u_x(\mathbf{r}) = \sum_E \sum_\varphi \sum_\theta \sqrt{\frac{2E}{m}} \cos(\theta) \cos(\varphi) f(\mathbf{r}, E, \varphi, \theta) \sqrt{\frac{2E}{m^3}} \cos(\theta) \Delta E \Delta \varphi \Delta \theta \quad (\text{B.13})$$

$$= \sum_E \sum_\varphi \sum_\theta \frac{2E}{m^2} \cos^2(\theta) \cos(\varphi) f(\mathbf{r}, E, \varphi, \theta) \Delta E \Delta \varphi \Delta \theta \quad (\text{B.14})$$

Using 2.7:

$$n(\mathbf{r}) u_x(\mathbf{r}) = \sum_E \sum_\varphi \sum_\theta \frac{2E}{m^2} \cos^2(\theta) \cos(\varphi) \frac{m^2}{2E} j(\mathbf{r}, E, \varphi, \theta) \Delta E \Delta \varphi \Delta \theta \quad (\text{B.15})$$

$$= \sum_E \sum_\varphi \sum_\theta \cos^2(\theta) \cos(\varphi) j(\mathbf{r}, E, \varphi, \theta) \Delta E \Delta \varphi \Delta \theta \quad (\text{B.16})$$

$$= 10^4 \sum_E \sum_\varphi \sum_\theta \cos^2(\theta) \cos(\varphi) \frac{c(\mathbf{r}, E, \varphi, \theta)}{\tau G(E, \varphi, \theta) E} \Delta E \Delta \varphi \Delta \theta \quad (\text{B.17})$$

$$= 10^4 \sum_E \sum_\varphi \sum_\theta \frac{\cos^2(\theta) \cos(\varphi)}{\tau E} \frac{c(\mathbf{r}, E, \varphi, \theta)}{G(E, \varphi, \theta)} \Delta E \Delta \varphi \Delta \theta \quad [\text{m}^{-3}] \quad (\text{B.18})$$

Using 2.6,  $E = e Q \mathcal{E}$ , and  $\Delta E = e Q \Delta \mathcal{E}$ . We get:

$$n(\mathbf{r}) u_x(\mathbf{r}) = 10^4 \sum_{\mathcal{E}} \sum_\varphi \sum_\theta \frac{\cos^2(\theta) \cos(\varphi)}{\tau \mathcal{E}} \frac{c(\mathbf{r}, \mathcal{E}, \varphi, \theta)}{G(\mathcal{E}, \varphi, \theta)} \Delta \mathcal{E} \Delta \varphi \Delta \theta \quad (\text{B.19})$$

The rest of the derivation, as previously for the density, is calibration- and instrument dependent.

$$n(\mathbf{r}) u_x(\mathbf{r}) = \frac{2\pi}{16 \tau} 10^4 \sum_{\mathcal{E}} \sum_\varphi \sum_\theta \frac{\cos^2(\theta) \cos(\varphi)}{\mathcal{E}} \frac{c(\mathbf{r}, \mathcal{E}, \varphi, \theta)}{G(\mathcal{E}, \varphi, \theta)} \Delta \mathcal{E}(\mathcal{E}) \Delta \theta(\mathcal{E}, \theta) \quad [\text{s}^{-1} \text{m}^{-2}] \quad (\text{B.20})$$

With an almost identical derivation, we get:

$$u_x(\mathbf{r}) = \frac{2\pi 10^4}{16 n(\mathbf{r}) \tau} \sum_{\mathcal{E}} \sum_{\varphi} \sum_{\theta} \frac{\cos^2(\theta) \cos(\varphi)}{\mathcal{E}} \frac{c(\mathbf{r}, \mathcal{E}, \varphi, \theta)}{G(\mathcal{E}, \varphi, \theta)} \Delta \mathcal{E}(\mathcal{E}) \Delta \theta(\mathcal{E}, \theta) \quad (\text{B.21})$$

$$u_y(\mathbf{r}) = \frac{2\pi 10^4}{16 n(\mathbf{r}) \tau} \sum_{\mathcal{E}} \sum_{\varphi} \sum_{\theta} \frac{\cos^2(\theta) \sin(\varphi)}{\mathcal{E}} \frac{c(\mathbf{r}, \mathcal{E}, \varphi, \theta)}{G(\mathcal{E}, \varphi, \theta)} \Delta \mathcal{E}(\mathcal{E}) \Delta \theta(\mathcal{E}, \theta) \quad (\text{B.22})$$

$$u_z(\mathbf{r}) = \frac{2\pi 10^4}{16 n(\mathbf{r}) \tau} \sum_{\mathcal{E}} \sum_{\varphi} \sum_{\theta} \frac{\cos(\theta) \sin(\theta)}{\mathcal{E}} \Delta \mathcal{E}(\mathcal{E}) \Delta \theta(\mathcal{E}, \theta) \quad (\text{B.23})$$



## B.3 PYTHON IMPLEMENTATION

```

import numpy as np

def moments(specAll, E, el, Q=1, m=1):
    # Integration of moments, for k=0 (density) and k=1 (
    # velocity).
    # specAll.shape=nbScanx16elx16azx96Ex32 in COUNTS
    # el elevation table in RADIANT
    # az azimuth table in RADIANT
    # Q number of charge of the considered species
    # m its mass in amu.

    DEl = el[1:]-el[:-1]
    ## Delta Elevation (rad)
    DEl = np.vstack((DEl,np.nanmean(DEl, axis=0))) ## 16x96,
    RADIANT.
    DE = E[1:]-E[:-1] ## Delta Energy (
    eV)
    DE = np.append(DE,DE[-1]) ## 96, eV.

    M = 1.660538e-27 ## kg
    e = 1.60217e-19 ## C
    tau = .1209 ## s

    GF = scipy.io.loadmat(Rc().get('ica', 'ICAGFFFile'))
    if sw == 10: GF = GF['mGH'][0][8][2]
    else: GF = GF['mGH'][0][sw-1][2]
    GF[GF==0] = np.nan

    j = 1e4*specAll/( tau * GF[None,None,None,:] * E[None,
    None,None,:])
    ## j.shape : nbScan, 16el, 16az, 96, #/s/m-2/sr/eV

    #-----
    # Order 0 , density.
    density = np.cos(el[None,:,None,:]) * j * E[None,None,None
    ,:]*-.5
    ## density.shape : nbScan,16el,16az,96
    density = np.nansum( density * DEl[None,:,None,:] * DE[
    None,None,None,:] \
    , axis=(1,2,3)) #
    # Integration
    !
    density *= (2*np.pi/16) * np.sqrt(m*M/(2*e*Q)) ## m^-3
    density[density==0] = np.nan

    #-----
    # Order 1 , velocity.
    v = np.zeros((3,density.size,16,16,96))
    v[0] = np.cos(el[None,:,None,:])**2 * np.cos(az[None,None
    ,:,None]) * j
    v[1] = np.cos(el[None,:,None,:])**2 * np.sin(az[None,None
    ,:,None]) * j

```

```

v[2] = np.cos(el[None,:,None,:]) * np.sin(el[None,:,
None,:]) * j
# v.shape: 3, nbScan, 16el, 16az, 96

v = (2*np.pi/16) * \
    np.nansum( v * DEl[None,None,:,None,:] * DE[None,
None,None,None,:] , axis=(2,3,4)) \
    /density[None,:]      ## Integration! m/s

v *= -1 ## From viewing direction to actual particle
velocity!

return density, v

```

## REPRESENTING A VELOCITY SPACE DISTRIBUTION FUNCTION

---

We give here a short description of the procedure to reconstruct, time integrate and represent velocity space distribution functions. The starting point is the data, which are given in the natural spherical coordinate system of the instrument. On the other hand, the usual coordinate system for plotting libraries is cartesian. The translation of a set of coordinates from one to the other is straightforward, but the handling of a 3-dimensional "pixel" is an abundant source of errors (personal experience). Another complication arises from the integration of several measurements. Depending on the time, the orientation of the instrument in a given reference frame may change of any value. The width of the pixel in terms of energy and elevation is also time-dependent. One very simple technics can overcome all these difficulties and errors, at the coast of computation time.

A first possible way to proceed would be to rotate the data themselves from the instrument reference frame to the frame of interest, and once in that frame, project and bin the data over an arbitrarily defined 3-dimensional grid. However, this binning process is precisely the source of all issues. An example of these issues is the fact that an instrument pixel has a logarithmic energy width: for low energies, the instrument-pixel will be contained in one plot-pixel, but for high energies, the instrument-pixel will spread over several plot-pixels.

To obtain the representation in Figure C.1, which integrates 50 different full angular scans and given in a proton aligned reference frame (see Chapter 5), a set of  $400 \times 400 \times 400$  cartesian coordinates was defined. We can consider these coordinates as "nodes" (in opposition to "pixels") in velocity space. These nodes were rotated from the frame of interest (the frame of the plot) to the instrument frame, for each scan. We then evaluated to which instrument-bin each node belongs, and we copy the value of the phase space distribution function given by this precise instrument-bin. Several nodes may belong to the same instrument-bin, and one instrument bin may be left unsampled, which are not physical issues, but resolution details. Ideally, the density of the cartesian nodes may be chosen so that each instrument-bin is sampled by at least one node. To reduce the size of this high-resolution array, which contains many redundant informations, we apply a contour treatment using about twenty levels.

The cost of this technics is computation time: many information are redundant, and all nodes do not end up in the instrument coverage. However the technics provide a final result which shows all instrumental features, and no artefact can be possibly found. The technics apply to the most general change of reference frame (rotation and translation).

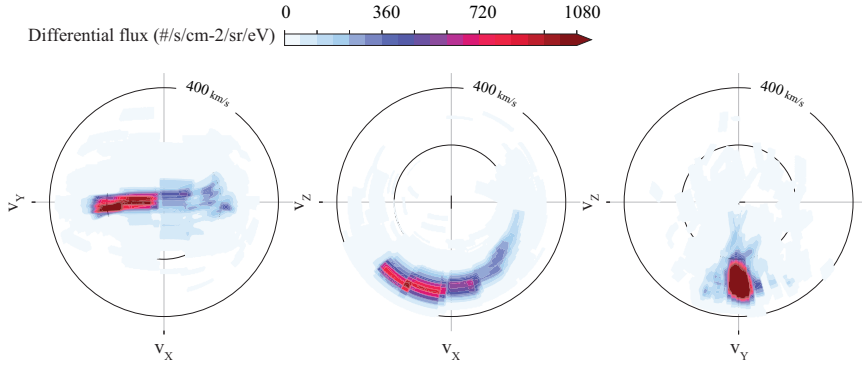


Figure C.1: Solar wind proton velocity distribution function, 50 scans integrated on 2015-03-19.

## LEO'S ALGORITHM

We first summarise the main aspects of the solver. *Leo* uses a Particle-In-Cell method: it manipulates particles in *continuous* phase space, whereas the fields are stored *discretely* in physical space, at the nodes of a grid. In the implementation of the model, only the nodes of the regular grids are considered, and there is actually no concept of cell (similarly as described in Appendix C).

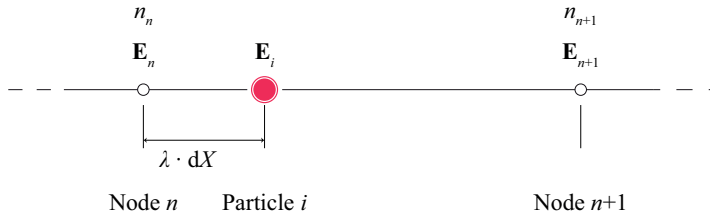
The volume of the domain of the reference simulation used throughout the thesis is  $2.3 \cdot 10^{21} \text{ m}^3$ , corresponding to  $2.9 \cdot 10^{27}$  solar wind protons (for a total mass of 4.7 kg!). It is technically impossible to simulate that amount of particles, therefore one particle in memory represents a cluster of many physical particles (about  $10^{19}$  particles in the reference simulation), which are considered to have the same evolution in phase space. These *macro particles* thus have a numerical weight  $w$ , which allows one to translate the amount of macro particles neighbouring a node to a physical density.

Particles and fields are interpolated linearly from one to the other *in the same way*, illustrated below in the one-dimensional case. We consider one particle with index  $i$  and numerical weight  $w_i$ , in-between the nodes  $n$  and  $n+1$ . When mapping the particles to the fields – the number density  $n$  for instance – the number density at the neighbouring nodes will be incremented as

$$n_n \leftarrow n_n + (1 - \lambda) \cdot w_i \quad (\text{D.1})$$

$$n_{n+1} \leftarrow n_{n+1} + \lambda \cdot w_i \quad (\text{D.2})$$

with  $\lambda \in [0, 1]$  the distance from the left neighbouring node, relative to the node-spacing  $dX$ .



In the same way, considering for the example the electric field  $x$ -component, the field at the particle position is calculated as

$$E_{x,i} \leftarrow (1 - \lambda) \cdot E_{x,n} + \lambda \cdot E_{x,n+1} \quad (\text{D.3})$$

The generalisation to the three-dimensional case (for a cartesian grid) is trivial: one particle will be mapped to eight nodes, and the fields' value at the particle's position will be a sum of height weighted fields.

Here is the algorithm used in the solver (adapted from [52]).

**Step 0** – The particles are pushed half a time step forward using  $\mathbf{v}_n$ .

**Step 1** – The particles are mapped on the grid to obtain the charge density and the current.

**Step 2** – The magnetic field is advanced in time using the Faraday's law. At each sub-step, the electric field is estimated using the magnetic field at the sub-step and the density and current at  $n$ .

**Step 3** – The particles are pushed another half time step forward using  $\mathbf{v}_n$ . Note: this is strictly equivalent as pushing the particle a full time step from  $n - 1/2$ , as represented on the schematics.

**Step 4** – The particles are mapped on the grid to obtain the density at  $n + 1/2$ .

**Step 5** – The electric field at  $n + 1/2$  is estimated using the density at  $n + 1/2$  and the current at  $n$ .

**Step 6** – The particles' velocities are pushed half a time step using the estimated electric field.

**Step 7** – The particles are mapped on the grid to obtain the current at  $n + 1/2$ .

**Step 8** – The electric field at  $n + 1/2$  computed once again using the new current.

**Step 9** – The velocities are brought back to  $n$  using the (stored) previously estimated electric field.

**Step 10** – The velocities are pushed one time step ahead using the Boris scheme.

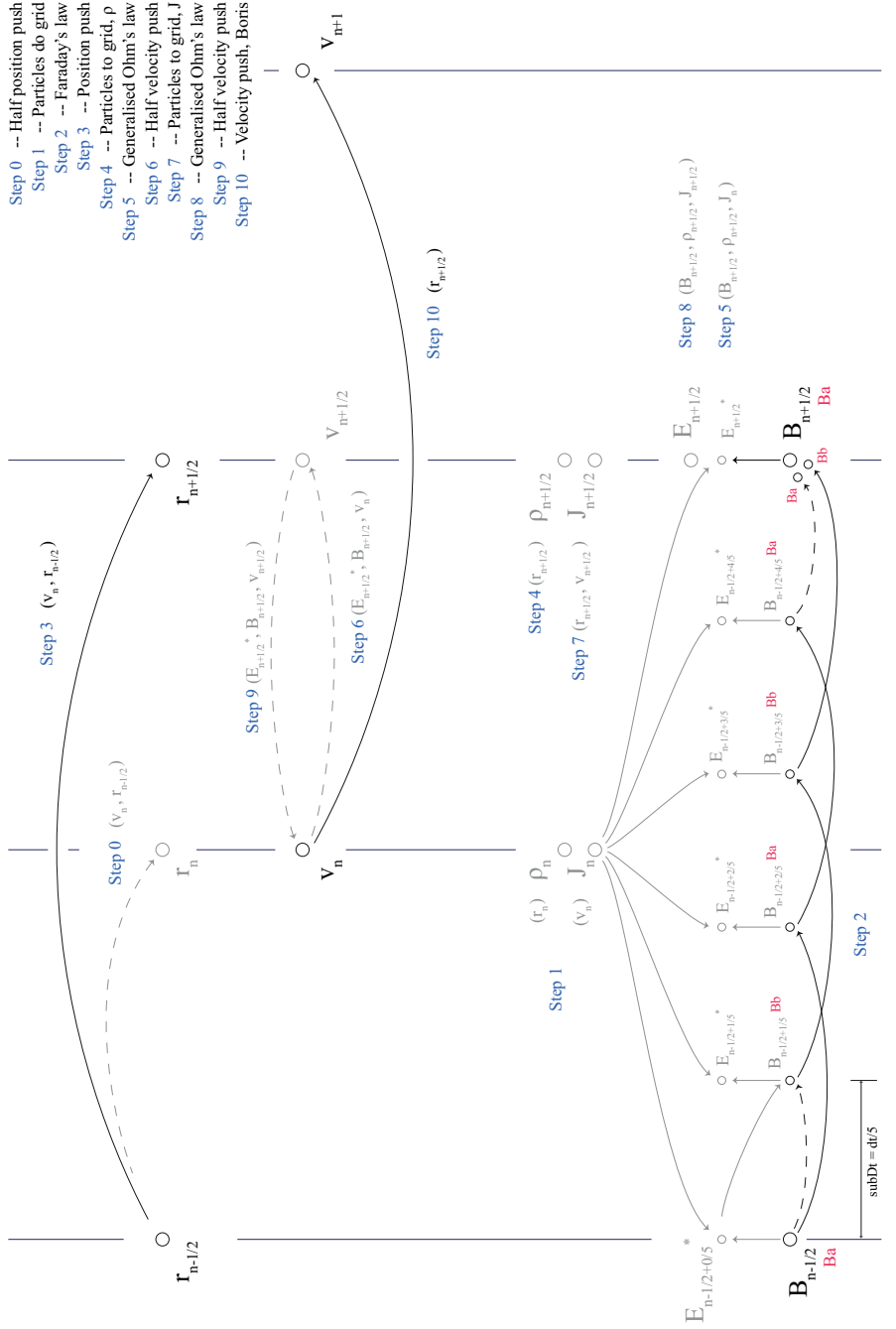


Figure D.1: Algorithm of the hybrid solver.





## BIBLIOGRAPHY

---

- [1] H. Alfven. "On the theory of comet tails." In: *Tellus IX* (1957), p. 92.
- [2] T. Bagdonat and U. Motschmann. "3D Hybrid Simulation Code Using Curvilinear Coordinates." In: *Journal of Computational Physics* 183 (2002).
- [3] Thorsten Bagdonat. *Hybrid Simulation of Weak Comets*. 2005.
- [4] Thorsten Bagdonat and Uwe Motschmann. "From a Weak to a Strong Comet – 3d Global Hybrid Simulation Studies." In: *Earth, Moon, and Planets* 90.1 (2002), pp. 305–321. ISSN: 1573-0794. DOI: [10.1023/A:1021578232282](https://doi.org/10.1023/A:1021578232282). URL: <https://doi.org/10.1023/A:1021578232282>.
- [5] H. Balsiger et al. "Ion composition and dynamics at comet Halley." In: *Nature* 321 (May 1986), 330 EP –. URL: <http://dx.doi.org/10.1038/321330a0>.
- [6] S. Barabash et al. "The Analyzer of Space Plasmas and Energetic Atoms (ASPERA-3) for the Mars Express Mission." In: *Space Science Reviews* 126.1 (2006), pp. 113–164. ISSN: 1572-9672. DOI: [10.1007/s11214-006-9124-8](http://dx.doi.org/10.1007/s11214-006-9124-8). URL: <http://dx.doi.org/10.1007/s11214-006-9124-8>.
- [7] E Behar, B Tabone, and H Nilsson. "Dawn–dusk asymmetry induced by the Parker spiral angle in the plasma dynamics around comet 67P/Churyumov–Gerasimenko." In: *Monthly Notices of the Royal Astronomical Society* 478.2 (2018), pp. 1570–1575. DOI: [10.1093/mnras/sty1111](https://doi.org/10.1093/mnras/sty1111). eprint: [oup/backfile/content\\_public/journal/mnras/478/2/10.1093\\_mnras\\_sty1111/2/sty1111.pdf](http://oup/backfile/content_public/journal/mnras/478/2/10.1093_mnras_sty1111/2/sty1111.pdf). URL: <http://dx.doi.org/10.1093/mnras/sty1111>.
- [8] E. Behar, H. Nilsson, G. Stenberg Wieser, Z. Nemeth, T. W. Broiles, and I. Richter. "Mass loading at 67P/Churyumov-Gerasimenko: A case study." In: *Geophysical Research Letters* 43.4 (2016). 2015GL067436, pp. 1411–1418. ISSN: 1944-8007. DOI: [10.1002/2015GL067436](https://doi.org/10.1002/2015GL067436). URL: <http://dx.doi.org/10.1002/2015GL067436>.
- [9] E. Behar, J. Lindkvist, H. Nilsson, M. Holmström, G. Stenberg-Wieser, R. Ramstad, and C. Götz. "Mass-loading of the solar wind at 67P/Churyumov-Gerasimenko - Observations and modelling." In: *Astronomy & Astrophysics* 596 (2016), A42. DOI: [10.1051/0004-6361/201628797](https://doi.org/10.1051/0004-6361/201628797). URL: <https://doi.org/10.1051/0004-6361/201628797>.
- [10] E. Behar, H. Nilsson, M. Alho, C. Goetz, and B. Tsurutani. "The birth and growth of a solar wind cavity around a comet - Rosetta observations." In: *Monthly Notices of the Royal Astronomical Society* 469.Suppl2 (2017), S396–S403.

- [11] E. Behar, B. Tabone, M. Saillenfest, P. Henri, J. Deca, J. Lindkvist, M. Holmström, and H. Nilsson. "Solar wind dynamics around a comet - A 2D semi-analytical model." In: *Astronomy & Astrophysics* (2018). DOI: [10.1051/0004-6361/201832736](https://doi.org/10.1051/0004-6361/201832736).
- [12] E. Behar, H. Nilsson, P. Henri, L. Bercic, G. Nicolaou, G. Stenberg Wieser, M. Wieser, B. Tabone, M. Saillenfest, and C. Goetz. "The root of a comet tail – Rosetta ion observations at comet 67P/Churyumov-Gerasimenko." In: *Astronomy & Astrophysics* (2018). DOI: [doi.org/10.1051/0004-6361/201832842](https://doi.org/10.1051/0004-6361/201832842).
- [13] Bercic, L., Behar, E., Nilsson, H., Nicolaou, G., Wieser, G. Stenberg, Wieser, M., and Goetz, C. "Cometary ion dynamics observed in the close vicinity of comet 67P/Churyumov-Gerasimenko during the intermediate activity period." In: *A&A* 613 (2018), A57. DOI: [10.1051/0004-6361/201732082](https://doi.org/10.1051/0004-6361/201732082). URL: <https://doi.org/10.1051/0004-6361/201732082>.
- [14] L. Biermann. "Kometenschweife under solar Korpuskularstrahlung." In: *Zeitschrift für Astrophysik* 29 (1951), p. 274.
- [15] L. Biermann, B. Brosowski, and H. U. Schmidt. "The interaction of the solar wind with a comet." In: *Solar Physics* 1.2 (1967), pp. 254–284. ISSN: 1573-093X. DOI: [10.1007/BF00150860](https://dx.doi.org/10.1007/BF00150860). URL: <http://dx.doi.org/10.1007/BF00150860>.
- [16] T. W. Broiles, J. L. Burch, G. Clark, C. Koenders, E. Behar, R. Goldstein, S. A. Fuselier, K. E. Mandt, P. Mokashi, and M. Samara. "Rosetta observations of solar wind interaction with the comet 67P/Churyumov-Gerasimenko." In: *Astronomy & Astrophysics* 583 (2015), A21. DOI: [10.1051/0004-6361/201526046](https://dx.doi.org/10.1051/0004-6361/201526046). URL: <http://dx.doi.org/10.1051/0004-6361/201526046>.
- [17] C. Carr et al. "RPC: The Rosetta Plasma Consortium." In: *Space Science Reviews* 128.1 (2007), pp. 629–647. ISSN: 1572-9672. DOI: [10.1007/s11214-006-9136-4](https://doi.org/10.1007/s11214-006-9136-4). URL: <https://doi.org/10.1007/s11214-006-9136-4>.
- [18] Marilina Cesario. *Nine medieval comet sightings that signalled death and destruction*. 2018. URL: <https://www.britac.ac.uk/blog/nine-medieval-comet-sightings-signalled-death-and-destruction>.
- [19] A.J. Coates. "Heavy ion effects on cometary shocks." In: *Advances in Space Research* 15.8 (1995). Proceedings of the D2.1 Symposium of COSPAR Scientific Commission D, pp. 403 – 413. ISSN: 0273-1177. DOI: [https://doi.org/10.1016/0273-1177\(94\)00125-K](https://doi.org/10.1016/0273-1177(94)00125-K). URL: <http://www.sciencedirect.com/science/article/pii/027311779400125K>.
- [20] A.J. Coates. "Ion pickup at comets." In: *Advances in Space Research* 33.11 (2004). Comparative Magnetospheres, pp. 1977 – 1988. ISSN: 0273-1177. DOI: <https://doi.org/10.1016/j.asr.2003.06.029>. URL: <http://www.sciencedirect.com/science/article/pii/S0273117704000213>.

- [21] A.J. Coates, J.L. Burch, R. Goldstein, H. Nilsson, G. Stenberg Wieser, E. Behar, and the RPC team. "Ion pickup observed at comet 67P with the Rosetta Plasma Consortium (RPC) particle sensors: similarities with previous observations and AMPTE releases, and effects of increasing activity." In: *Journal of Physics: Conference Series* 642.1 (2015), p. 012005. URL: <http://stacks.iop.org/1742-6596/642/i=1/a=012005>.
- [22] S. W. H. Cowley. "ICE observations of Comet Giacobini-Zinner." In: *Philosophical Transactions of the Royal Society of London A: Mathematical, Physical and Engineering Sciences* 323.1572 (1987), pp. 405–420. ISSN: 0080-4614. DOI: 10.1098/rsta.1987.0095. eprint: <http://rsta.royalsocietypublishing.org/content/323/1572/405.full.pdf>. URL: <http://rsta.royalsocietypublishing.org/content/323/1572/405>.
- [23] Cravens, T. E. "A magnetohydrodynamical model of the inner coma of comet Halley." In: *Journal of Geophysical Research: Space Physics* 94.A11 (1989), pp. 15025–15040. DOI: 10.1029/JA094iA11p15025. eprint: <https://agupubs.onlinelibrary.wiley.com/doi/pdf/10.1029/JA094iA11p15025>. URL: <https://agupubs.onlinelibrary.wiley.com/doi/abs/10.1029/JA094iA11p15025>.
- [24] T.E. Cravens. "Theory and observations of cometary ionospheres." In: *Advances in Space Research* 7.12 (1987). Proceedings of the Topical Meeting of the COSPAR Interdisciplinary Scientific Commission C(Meeting C3), Workshop III and Symposium 8 of the COSPAR Twenty-sixth Plenary Meeting, pp. 147–158. ISSN: 0273-1177. DOI: [https://doi.org/10.1016/0273-1177\(87\)90212-2](https://doi.org/10.1016/0273-1177(87)90212-2). URL: <http://www.sciencedirect.com/science/article/pii/S0273117787902122>.
- [25] T.E. Cravens. *Physics of Solar System Plasmas*. Cambridge Atmospheric and Space Science Series. Cambridge, 2004.
- [26] T.E. Cravens and T.I. Gombosi. "Cometary magnetospheres: a tutorial." In: *Advances in Space Research* 33.11 (2004). Comparative Magnetospheres, pp. 1968–1976. ISSN: 0273-1177. DOI: <http://dx.doi.org/10.1016/j.asr.2003.07.053>. URL: <http://www.sciencedirect.com/science/article/pii/S0273117704000201>.
- [27] J. Crovisier. "The photodissociation of water in cometary atmospheres." In: *Astronomy & Astrophysics* 213 (1989), pp. 459–464.
- [28] Jan Deca, Andrey Divin, Pierre Henri, Anders Eriksson, Stefano Markidis, Vyacheslav Olshevsky, and Mihály Horányi. "Electron and Ion Dynamics of the Solar Wind Interaction with a Weakly Outgassing Comet." In: *Phys. Rev. Lett.* 118 (20 2017), p. 205101. DOI: 10.1103/PhysRevLett.118.205101. URL: <https://link.aps.org/doi/10.1103/PhysRevLett.118.205101>.
- [29] P. A. Delamere. "Hybrid code simulations of the solar wind interaction with Pluto." In: *Journal of Geophysical Research: Space Physics* 114.A3 (2009). A03220, n/a–n/a. ISSN: 2156-2202. DOI:

- 10.1029/2008JA013756. URL: <http://dx.doi.org/10.1029/2008JA013756>.
- [30] Ian T Durham. "RETHINKING THE HISTORY OF SOLAR WIND STUDIES: EDDINGTON'S ANALYSIS OF COMET MOREHOUSE." In: *Notes and Records* 60.3 (2006), pp. 261–270. ISSN: 0035-9149. DOI: [10.1098/rsnr.2006.0149](https://doi.org/10.1098/rsnr.2006.0149).
- [31] N. J. T. Edberg et al. "Spatial distribution of low-energy plasma around comet 67P/CG from Rosetta measurements." In: *Geophysical Research Letters* 42.11 (2015). 2015GL064233, pp. 4263–4269. ISSN: 1944-8007. DOI: [10.1002/2015GL064233](https://doi.org/10.1002/2015GL064233). URL: <http://dx.doi.org/10.1002/2015GL064233>.
- [32] Niklas J. T. Edberg et al. "CME impact on comet 67P/Churyumov-Gerasimenko." In: *Monthly Notices of the Royal Astronomical Society* 462.Suppl1 (2016), S45. DOI: [10.1093/mnras/stw2112](https://doi.org/10.1093/mnras/stw2112). eprint: [/oup/backfile/content\\_public/journal/mnras/462/suppl\\_1/10.1093\\_mnras\\_stw2112/2/stw2112.pdf](http://oup/backfile/content_public/journal/mnras/462/suppl_1/10.1093_mnras_stw2112/2/stw2112.pdf). URL: [+http://dx.doi.org/10.1093/mnras/stw2112](http://dx.doi.org/10.1093/mnras/stw2112).
- [33] A. S. Eddington. "The Envelopes of Comet Morehouse (1908 c)." In: *Monthly Notices of the Royal Astronomical Society* 70.5 (1910), pp. 442–458. DOI: [10.1093/mnras/70.5.442](https://doi.org/10.1093/mnras/70.5.442). eprint: [/oup/backfile/content\\_public/journal/mnras/70/5/10.1093\\_mnras\\_70.5.442/2/mnras70-0442.pdf](http://oup/backfile/content_public/journal/mnras/70/5/10.1093_mnras_70.5.442/2/mnras70-0442.pdf). URL: [+http://dx.doi.org/10.1093/mnras/70.5.442](http://dx.doi.org/10.1093/mnras/70.5.442).
- [34] Shahab Fatemi, Andrew R. Poppe, Gregory T. Delory, and William M. Farrell. "AMITIS: A 3D GPU-Based Hybrid-PIC Model for Space and Plasma Physics." In: *Journal of Physics: Conference Series* 837.1 (2017), p. 012017. URL: <http://stacks.iop.org/1742-6596/837/i=1/a=012017>.
- [35] K. R. Flammer and D. A. Mendis. "A note on the mass-loaded MHD flow of the solar wind towards a cometary nucleus." In: *Astrophysics and Space Science* 182.1 (1991), pp. 155–162. ISSN: 1572-946X. DOI: [10.1007/BF00646450](https://doi.org/10.1007/BF00646450). URL: <https://doi.org/10.1007/BF00646450>.
- [36] V. Formisano, E. Amata, M. B. Cattaneo, P. Torrente, and A. Johnstone. "Plasma flow inside Comet P/Halley." In: *Astronomy & Astrophysics* 238 (Nov. 1990), pp. 401–412.
- [37] M. Galand et al. "Ionospheric plasma of comet 67P probed by Rosetta at 3 au from the Sun." In: *Monthly Notices of the Royal Astronomical Society* 462.Suppl1 (2016), S331–S351. DOI: [10.1093/mnras/stw2891](https://doi.org/10.1093/mnras/stw2891). eprint: [/oup/backfile/content\\_public/journal/mnras/462/suppl\\_1/10.1093\\_mnras\\_stw2891/3/stw2891.pdf](http://oup/backfile/content_public/journal/mnras/462/suppl_1/10.1093_mnras_stw2891/3/stw2891.pdf). URL: <http://dx.doi.org/10.1093/mnras/stw2891>.
- [38] Galeev, A. A., Cravens, T. E., and Gombosi, T. I. "Solar wind stagnation near comets." In: *Astrophysical Journal* 289 (1985), p. 807.

- [39] Goetz, C. "Unusually high magnetic fields in the coma of 67P/Churyumov-Gerasimenko during its high activity phase." In: *Astronomy & Astrophysics* (2018).
- [40] Goetz, C. et al. "First detection of a diamagnetic cavity at comet 67P/Churyumov-Gerasimenko." In: *Astronomy & Astrophysics* 588 (2016), A24. DOI: [10.1051/0004-6361/201527728](https://doi.org/10.1051/0004-6361/201527728). URL: <https://doi.org/10.1051/0004-6361/201527728>.
- [41] Goetz, C., Volwerk, M., Richter, I., and Glassmeier, K.-H. "Evolution of the magnetic field at comet 67P/Churyumov-Gerasimenko." In: *Monthly Notices of the Royal Astronomical Society* (2017).
- [42] C. Goetz et al. "Structure and evolution of the diamagnetic cavity at comet 67P/Churyumov-Gerasimenko." In: *Monthly Notices of the Royal Astronomical Society* 462.Suppl1 (2016), S459. DOI: [10.1093/mnras/stw3148](https://doi.org/10.1093/mnras/stw3148). eprint: [/oup/backfile/content\\_public/journal/mnras/462/suppl\\_1/10.1093\\_mnras\\_stw3148/3/stw3148.pdf](http://oup/backfile/content_public/journal/mnras/462/suppl_1/10.1093_mnras_stw3148/3/stw3148.pdf). URL: [+http://dx.doi.org/10.1093/mnras/stw3148](http://dx.doi.org/10.1093/mnras/stw3148).
- [43] Tamas I. Gombosi. "Physics of Cometary Magnetospheres." In: *Magnetotails in the Solar System*. John Wiley & Sons, Inc, 2015, pp. 169–188. ISBN: 9781118842324. DOI: [10.1002/9781118842324.ch10](https://doi.org/10.1002/9781118842324.ch10). URL: <http://dx.doi.org/10.1002/9781118842324.ch10>.
- [44] M. Grewing, F. Praderie, and Rüdeger Reinhard, eds. *Exploration of Halley's Comet*. Vol. 10.1007/978-3-642-82971-0. Springer, 1988.
- [45] Hajra, R. "Cometary plasma response to interplanetary corotating interaction regions during 2016 June - September: a quantitative study by the Rosetta Plasma Consortium." In: *Astronomy & Astrophysics* (2018).
- [46] K. C. Hansen, T. Bagdonat, U. Motschmann, C. Alexander, M. R. Combi, T. E. Cravens, T. I. Gombosi, Y.-D. Jia, and I. P. Robertson. "The Plasma Environment of Comet 67P/Churyumov-Gerasimenko Throughout the Rosetta Main Mission." In: *Space Science Reviews* 128.1 (2007), pp. 133–166. ISSN: 1572-9672. DOI: [10.1007/s11214-006-9142-6](https://doi.org/10.1007/s11214-006-9142-6). URL: <http://dx.doi.org/10.1007/s11214-006-9142-6>.
- [47] Kenneth C. Hansen et al. "Evolution of water production of 67P/Churyumov-Gerasimenko: an empirical model and a multi-instrument study." In: *Monthly Notices of the Royal Astronomical Society* 462.Suppl1 (2016), S491–S506. DOI: [10.1093/mnras/stw2413](https://doi.org/10.1093/mnras/stw2413). eprint: [/oup/backfile/content\\_public/journal/mnras/462/suppl\\_1/10.1093\\_mnras\\_stw2413/3/stw2413.pdf](http://oup/backfile/content_public/journal/mnras/462/suppl_1/10.1093_mnras_stw2413/3/stw2413.pdf). URL: [+http://dx.doi.org/10.1093/mnras/stw2413](http://dx.doi.org/10.1093/mnras/stw2413).
- [48] L. Haser. "Distribution d'intensité dans la tête d'une comète." In: *Bulletin de la Classe des Sciences de l'Académie Royale de Belgique* 43 (1957), pp. 740–750.

- [49] T. Heidarzadeh. *A History of Physical Theories of Comets, From Aristotle to Whipple*. Archimedes: New Studies in the History and Philosophy of Science and Technology. Springer, 2008. ISBN: 978-1-4020-8323-5. DOI: [10.1007/978-1-4020-8323-5](https://doi.org/10.1007/978-1-4020-8323-5).
- [50] K. L. Heritier et al. "Ion composition at comet 67P near perihelion: Rosetta observations and model-based interpretation." In: *Monthly Notices of the Royal Astronomical Society* 469.Suppl2 (2017), S427–S442. DOI: [10.1093/mnras/stx1912](https://doi.org/10.1093/mnras/stx1912). eprint: [oup/backfile/content\\_public/journal/mnras/469/suppl\\_2/10.1093.mnras\\_stx1912/1/stx1912.pdf](http://oup/backfile/content_public/journal/mnras/469/suppl_2/10.1093.mnras_stx1912/1/stx1912.pdf). URL: <http://dx.doi.org/10.1093/mnras/stx1912>.
- [51] K. L. Heritier et al. "Vertical structure of the near-surface expanding ionosphere of comet 67P probed by Rosetta." In: *Monthly Notices of the Royal Astronomical Society* 469.Suppl2 (2017), S118–S129. DOI: [10.1093/mnras/stx1459](https://doi.org/10.1093/mnras/stx1459). eprint: [oup/backfile/content\\_public/journal/mnras/469/suppl\\_2/10.1093.mnras\\_stx1459/2/stx1459.pdf](http://oup/backfile/content_public/journal/mnras/469/suppl_2/10.1093.mnras_stx1459/2/stx1459.pdf). URL: <http://dx.doi.org/10.1093/mnras/stx1459>.
- [52] M. Holmström. "Hybrid Modeling of Plasmas." In: *Numerical Mathematics and Advanced Applications 2009: Proceedings of ENU-MATH 2009, the 8th European Conference on Numerical Mathematics and Advanced Applications, Uppsala, July 2009*. Ed. by Gunnilla Kreiss, Per Lötstedt, Axel Målqvist, and Maya Neytcheva. Berlin, Heidelberg: Springer Berlin Heidelberg, 2010, pp. 451–458. ISBN: 978-3-642-11795-4. DOI: [10.1007/978-3-642-11795-4\\_48](https://doi.org/10.1007/978-3-642-11795-4_48). URL: [http://dx.doi.org/10.1007/978-3-642-11795-4\\_48](http://dx.doi.org/10.1007/978-3-642-11795-4_48).
- [53] M. Holmström. "Handling Vacuum Regions in a Hybrid Plasma Solver." In: *ASP Conference series* 474 (2013), pp. 202–207.
- [54] A. Johnstone et al. "Ion flow at comet Halley." In: *Nature* 321.6067s (May 1986), pp. 344–347. URL: <http://dx.doi.org/10.1038/321344a0>.
- [55] A. Johnstone, A. J. Coates, D. E. Huddleston, K. Jockers, B. Wilken, H. Borg, C. Gurgiolo, J. D. Winningham, and E. Amata. "Observations of the Solar Wind and Cometary Ions during the Encounter Between Giotto and Comet Grigg-Skjellerup." In: *Astronomy & Astrophysics* 273 (1993).
- [56] G.H. Jones and A.J. Coates. "Observations of structures within the Grigg-Skjellerup cometsheath." In: *Advances in Space Research* 20.2 (1997). Planetary Ionospheres and Magnetospheres, pp. 271–274. ISSN: 0273-1177. DOI: [http://dx.doi.org/10.1016/S0273-1177\(97\)00545-0](http://dx.doi.org/10.1016/S0273-1177(97)00545-0). URL: <http://www.sciencedirect.com/science/article/pii/S0273117797005450>.
- [57] E. Kallio and R. Jarvinen. "Kinetic effects on ion escape at Mars and Venus: Hybrid modeling studies." In: *Earth, Planets and Space* 64.2 (2012), p. 11. ISSN: 1880-5981. DOI: [10.5047/eps.2011.08.014](https://doi.org/10.5047/eps.2011.08.014). URL: <https://doi.org/10.5047/eps.2011.08.014>.

- [58] C. Koenders, C. Perschke, C. Goetz, I. Richter, U. Motschmann, and K. H. Glassmeier. "Low-frequency waves at comet 67P/Churyumov-Gerasimenko - Observations compared to numerical simulations." In: *Astronomy & Astrophysics* 594 (2016), A66. DOI: [10.1051/0004-6361/201628803](https://doi.org/10.1051/0004-6361/201628803). URL: <https://doi.org/10.1051/0004-6361/201628803>.
- [59] C. Koenders, C. Goetz, I. Richter, U. Motschmann, and K.-H. Glassmeier. "Magnetic field pile-up and draping at intermediately active comets: results from comet 67P/Churyumov-Gerasimenko at 2.0 AU." In: *Monthly Notices of the Royal Astronomical Society* 462.Suppl1 (2016), S235. DOI: [10.1093/mnras/stw2480](https://doi.org/10.1093/mnras/stw2480). eprint: [http://oup/backfile/Content\\_public/Journal/mnras/462/Suppl\\_1/10.1093\\_mnras\\_stw2480/2/stw2480.pdf](http://oup/backfile/Content_public/Journal/mnras/462/Suppl_1/10.1093_mnras_stw2480/2/stw2480.pdf). URL: [+http://dx.doi.org/10.1093/mnras/stw2480](http://dx.doi.org/10.1093/mnras/stw2480).
- [60] J. Lindkvist, M. Hamrin, H. Gunell, H. Nilsson, C. Simon Wedlund, E. Kallio, I. Mann, T. Pitkänen, and T. Karlsson. "Energy conversion in cometary atmospheres: Hybrid modeling of 67P/Churyumov-Gerasimenko." In: *Astronomy & Astrophysics* (2018). DOI: [10.1051/0004-6361/201732353](https://doi.org/10.1051/0004-6361/201732353).
- [61] T. Mukai, W. Miyake, T. Terasawa, M. Kitayama, and K. Hirao. "Plasma observation by Suisei of solar-wind interaction with comet Halley." In: *Nature* 321 (May 1986), 299 EP -. URL: <http://dx.doi.org/10.1038/321299a0>.
- [62] F. M. Neubauer et al. "First results from the Giotto magnetometer experiment at comet Halley." In: *Nature* 321.6067s (May 1986), pp. 352–355. URL: <http://dx.doi.org/10.1038/321352a0>.
- [63] M. Neugebauer. "Spacecraft observations of the interaction of active comets with the solar wind." In: *Reviews of Geophysics* 28.2 (1990), pp. 231–252. ISSN: 1944-9208. DOI: [10.1029/RG028i002p00231](https://doi.org/10.1029/RG028i002p00231). URL: <http://dx.doi.org/10.1029/RG028i002p00231>.
- [64] M. Neugebauer and R.F. Draper. "The comet rendezvous asteroid flyby mission." In: *Advances in Space Research* 7.12 (1987). Proceedings of the Topical Meeting of the COSPAR Interdisciplinary Scientific Commission C(Meeting C3), Workshop III and Symposium 8 of the COSPAR Twenty-sixth Plenary Meeting, pp. 201 –204. ISSN: 0273-1177. DOI: [https://doi.org/10.1016/0273-1177\(87\)90218-3](https://doi.org/10.1016/0273-1177(87)90218-3). URL: <http://www.sciencedirect.com/science/article/pii/0273117787902183>.
- [65] G. Nicolaou, E. Behar, H. Nilsson, M. Wieser, M. Yamauchi, L. Bercic, and G. Stenberg Wieser. "Energy-angle dispersion of accelerated heavy ions at 67P/Churyumov-Gerasimenko: implication in the mass-loading mechanism." In: *Monthly Notices of the Royal Astronomical Society* 469.Suppl2 (2017), S339–S345. DOI: [10.1093/mnras/stx1621](https://doi.org/10.1093/mnras/stx1621). eprint: [http://oup/backfile/content\\_public/journal/mnras/469/suppl\\_2/10.1093\\_mnras\\_stx1621/1/stx1621.pdf](http://oup/backfile/content_public/journal/mnras/469/suppl_2/10.1093_mnras_stx1621/1/stx1621.pdf). URL: [+http://dx.doi.org/10.1093/mnras/stx1621](http://dx.doi.org/10.1093/mnras/stx1621).



- [66] H. Nilsson et al. "RPC-ICA: The Ion Composition Analyzer of the Rosetta Plasma Consortium." In: *Space Science Reviews* 128.1 (2007), pp. 671–695. ISSN: 1572-9672. DOI: [10.1007/s11214-006-9031-z](https://doi.org/10.1007/s11214-006-9031-z). URL: <http://dx.doi.org/10.1007/s11214-006-9031-z>.
- [67] H. Nilsson et al. "Evolution of the ion environment of comet 67P/Churyumov-Gerasimenko." In: *Astronomy & Astrophysics* 583 (2015), A20. DOI: [10.1051/0004-6361/201526142](https://doi.org/10.1051/0004-6361/201526142). URL: <http://dx.doi.org/10.1051/0004-6361/201526142>.
- [68] H. Nilsson, H. Gunell, T. Karlsson, N. Brenning, P. Henri, C. Goetz, A. I. Eriksson, E. Behar, G. Stenberg Wieser, and R. Slapak. "Small is different - The polarisation electric field of a small scale comet ionosphere." In: *Astronomy & Astrophysics* (2018).
- [69] Hans Nilsson et al. "Birth of a comet magnetosphere: A spring of water ions." In: *Science* 347.6220 (2015). DOI: [10.1126/science.aaa0571](https://doi.org/10.1126/science.aaa0571). eprint: <http://www.sciencemag.org/content/347/6220/aaa0571.full.pdf>. URL: <http://www.sciencemag.org/content/347/6220/aaa0571.abstract>.
- [70] Hans Nilsson et al. "Evolution of the ion environment of comet 67P during the Rosetta mission as seen by RPC-ICA." In: *Monthly Notices of the Royal Astronomical Society* 469.Supp2 (2017), S252–S261. DOI: [10.1093/mnras/stx1491](https://doi.org/10.1093/mnras/stx1491). eprint: [oup/backfile/content\\_public/journal/mnras/469/suppl\\_2/10.1093/mnras/stx1491/1/stx1491.pdf](http://oup/backfile/content_public/journal/mnras/469/suppl_2/10.1093/mnras/stx1491/1/stx1491.pdf). URL: [+http://dx.doi.org/10.1093/mnras/stx1491](http://dx.doi.org/10.1093/mnras/stx1491).
- [71] Witasse O. et al. "Interplanetary coronal mass ejection observed at STEREO-A, Mars, comet 67P/Churyumov-Gerasimenko, Saturn, and New Horizons en route to Pluto: Comparison of its Forbush decreases at 1.4, 3.1, and 9.9 AU." In: *Journal of Geophysical Research: Space Physics* 122.8 (), pp. 7865–7890. DOI: [10.1002/2017JA023884](https://doi.org/10.1002/2017JA023884). eprint: <https://agupubs.onlinelibrary.wiley.com/doi/pdf/10.1002/2017JA023884>. URL: <https://agupubs.onlinelibrary.wiley.com/doi/abs/10.1002/2017JA023884>.
- [72] S. P. Papamarinopoulos. "A Comet during the Trojan War?" In: *Science and Technology in Homeric Epics*. Ed. by S. A. Paipetis. Dordrecht: Springer Netherlands, 2008, pp. 341–356. ISBN: 978-1-4020-8784-4. DOI: [10.1007/978-1-4020-8784-4\\_26](https://doi.org/10.1007/978-1-4020-8784-4_26). URL: [https://doi.org/10.1007/978-1-4020-8784-4\\_26](https://doi.org/10.1007/978-1-4020-8784-4_26).
- [73] Plaschke, F. "First observations of magnetic holes deep within the coma of a comet." In: *Astronomy & Astrophysics* (2018).
- [74] M. Saillenfest, B. Tabone, and E. Behar. "The solar wind dynamics around a comet: the inverse-square-law paradigm." In: *Astronomy & Astrophysics* (2018). DOI: [10.1051/0004-6361/201832742](https://doi.org/10.1051/0004-6361/201832742).



- [75] K. Sauer and E. Dubinin. "Cometosheath Structures and Tail Rays: Outcome of bi-ion Fluid Simulations." In: *Earth, Moon, and Planets* 77.3 (1997), pp. 271–278. ISSN: 1573-0794. DOI: [10.1023/A:1006241906247](https://doi.org/10.1023/A:1006241906247). URL: <https://doi.org/10.1023/A:1006241906247>.
- [76] Konard Sauer, Alexander Bogdanov, and Klaus Baumgärtel. "Evidence of an ion composition boundary (protonopause) in bi-ion fluid simulations of solar wind mass loading." In: *Geophysical Research Letters* 21.20 (1994), pp. 2255–2258. DOI: [10.1029/94GL01691](http://dx.doi.org/10.1029/94GL01691). URL: <http://dx.doi.org/10.1029/94GL01691>.
- [77] Sara Schechner. *Comets, Popular Culture, and the Birth of Modern Cosmology*. Princeton University Press, 1999. ISBN: 9780691009254.
- [78] H. U. Schmidt, R. Wegmann, and F. M. Neubauer. "MHD modeling applied to Giotto encounter with comet P/Grigg-Skjellerup." In: *Journal of Geophysical Research: Space Physics* 98.A12 (1993), pp. 21009–21016. ISSN: 2156-2202. DOI: [10.1029/93JA03014](http://dx.doi.org/10.1029/93JA03014). URL: <http://dx.doi.org/10.1029/93JA03014>.
- [79] G.H. Schwehm. "Rosetta — Comet Nucleus Sample Return." In: *Advances in Space Research* 9.6 (1989), pp. 185–190. ISSN: 0273-1177. DOI: [https://doi.org/10.1016/0273-1177\(89\)90228-7](http://www.sciencedirect.com/science/article/pii/0273117789902287). URL: <http://www.sciencedirect.com/science/article/pii/0273117789902287>.
- [80] I. F. Shaikhislamov, V. G. Posukh, A. V. Melekhov, Y. P. Zakharov, E. L. Boyarintsev, and A. G. Ponomarenko. "West-east asymmetry of a mini-magnetosphere induced by Hall effects." In: *Plasma Physics and Controlled Fusion* 57 (July 2015), p. 075007.
- [81] Simon Wedlund, C., Kallio, E., Alho, M., Nilsson, H., Stenberg Wieser, G., Gunell, H., Behar, E., Pusa, J., and Gronoff, G. "The atmosphere of comet 67P/Churyumov-Gerasimenko diagnosed by charge-exchanged solar wind alpha particles." In: *Astronomy & Astrophysics* 587 (2016), A154. DOI: [10.1051/0004-6361/201527532](http://dx.doi.org/10.1051/0004-6361/201527532). URL: <http://dx.doi.org/10.1051/0004-6361/201527532>.
- [82] Simon Wedlund, C., Alho, M., Gronoff, G., Kallio, E., Gunell, H., Nilsson, H., Lindkvist, J., Behar, E., Stenberg Wieser, G., and Miloch, W. J. "Hybrid modelling of cometary plasma environments - I. Impact of photoionisation, charge exchange, and electron ionisation on bow shock and cometopause at 67P/Churyumov-Gerasimenko." In: *Astronomy & Astrophysics* 604 (2017), A73. DOI: [10.1051/0004-6361/201730514](https://doi.org/10.1051/0004-6361/201730514). URL: <https://doi.org/10.1051/0004-6361/201730514>.
- [83] Simon Wedlund, C. et al. "Solar wind charge exchange at comets. Analytical formulation and application to comet 67P during the Rosetta mission." In: *Astronomy & Astrophysics* (2018 (in preparation)).

- [84] J. A. Slavin, E. J. Smith, B. T. Tsurutani, G. L. Siscoe, D. E. Jones, and D. A. Mendis. "Giacobini-Zinner magnetotail: ICE magnetic field observations." In: *Geophysical Research Letters* 13.3 (1986), pp. 283–286. ISSN: 1944-8007. DOI: [10.1029/GL013i003p00283](https://doi.org/10.1029/GL013i003p00283). URL: <http://dx.doi.org/10.1029/GL013i003p00283>.
- [85] Smith, E. J. and Barnes, A. "Spatial dependences in the distant solar wind: Pioneers 10 and 11." In: *Nasa Conf. Publication NASA CP2280, solar wind* 5. 1983.
- [86] C. Störmer. "Periodische Elektronenbahnen im Felde eines Elementarmagneten und ihre Anwendung auf Brüches Modelversuche und auf Eschenhagens Elementarwellen des Erdmagnetismus." In: *Zeitschrift für Astrophysik* 1 (1930), p. 237.
- [87] Štěpán Štverák, Pavel M. Trávníček, and Petr Hellinger. "Electron energetics in the expanding solar wind via Helios observations." In: *Journal of Geophysical Research: Space Physics* 120.10 (), pp. 8177–8193. DOI: [10.1002/2015JA021368](https://doi.org/10.1002/2015JA021368). eprint: <https://agupubs.onlinelibrary.wiley.com/doi/pdf/10.1002/2015JA021368>. URL: <https://agupubs.onlinelibrary.wiley.com/doi/abs/10.1002/2015JA021368>.
- [88] Károly Szegő et al. "Physics of Mass Loaded Plasmas." In: *Space Science Reviews* 94.3 (2000), pp. 429–671. ISSN: 1572-9672. DOI: [10.1023/A:1026568530975](https://doi.org/10.1023/A:1026568530975). URL: <http://dx.doi.org/10.1023/A:1026568530975>.
- [89] M. Tatralay, T.I. Gombosi, D.L. De Zeeuw, M.I. Verigin, A.P. Remizov, I. Apathy, and T. Szemerey. "Plasma flow in the cometosheath of comet Halley." In: *Advances in Space Research* 20.2 (1997). Planetary Ionospheres and Magnetospheres, pp. 275 – 278. ISSN: 0273-1177. DOI: [https://doi.org/10.1016/S0273-1177\(97\)00546-2](https://doi.org/10.1016/S0273-1177(97)00546-2). URL: <http://www.sciencedirect.com/science/article/pii/S0273117797005462>.
- [90] M. G. G. T. Taylor, N. Altobelli, B. J. Buratti, and M. Choukroun. "The Rosetta mission orbiter science overview: the comet phase." In: *Philosophical Transactions of the Royal Society of London A: Mathematical, Physical and Engineering Sciences* 375.2097 (2017). ISSN: 1364-503X. DOI: [10.1098/rsta.2016.0262](https://doi.org/10.1098/rsta.2016.0262). eprint: <http://rsta.royalsocietypublishing.org/content/375/2097/20160262.full.pdf>. URL: <http://rsta.royalsocietypublishing.org/content/375/2097/20160262>.
- [91] F. Valentini, P. Trávníček, F. Califano, P. Hellinger, and A. Mangeney. "A hybrid-Vlasov model based on the current advance method for the simulation of collisionless magnetized plasma." In: *Journal of Computational Physics* 225.1 (2007), pp. 753 –770. ISSN: 0021-9991. DOI: <https://doi.org/10.1016/j.jcp.2007.01.001>. URL: <http://www.sciencedirect.com/science/article/pii/S0021999107000022>.

- [92] S. Wiehle, U. Motschmann, N. Gortsas, K.-H. Glassmeier, J. Müller, and C. Koenders. "Simulation of cometary jets in interaction with the solar wind." In: *Advances in Space Research* 48.6 (2011), pp. 1108 –1113. ISSN: 0273-1177. DOI: <https://doi.org/10.1016/j.asr.2011.05.024>. URL: <http://www.sciencedirect.com/science/article/pii/S0273117711003632>.
- [93] D. Winske and N. Omidi. *Hybrid codes: Methods and applications*. 1991.
- [94] D.T Young et al. "Solar wind interactions with Comet 19P/Borrelly." In: *Icarus* 167.1 (2004). Special Issue on DS1/Comet Borrelly, pp. 80 –88. ISSN: 0019-1035. DOI: <http://dx.doi.org/10.1016/j.icarus.2003.09.011>. URL: <http://www.sciencedirect.com/science/article/pii/S0019103503002811>.



Part II

PUBLICATIONS



A

PUBLICATION I

---







## RESEARCH LETTER

10.1002/2015GL067436

## Key Points:

- Prime role of the SW electric field in the cometary ion dynamics, through mass loading, at 2.88 AU
- The cometary ion flow direction has a main antisunward component
- We find an indication for an antisunward polarization electric field developing in the coma

## Correspondence to:

E. Behar,  
etienne.behar@irf.se

## Citation:

Behar, E., H. Nilsson, G. Stenberg Wieser, Z. Nemeth, T. W. Broiles, and I. Richter (2016), Mass loading at 67P/Churyumov-Gerasimenko: A case study, *Geophys. Res. Lett.*, 43, doi:10.1002/2015GL067436.

Received 14 DEC 2015

Accepted 28 JAN 2016

Accepted article online 30 JAN 2016

## Mass loading at 67P/Churyumov-Gerasimenko: A case study

E. Behar<sup>1,2</sup>, H. Nilsson<sup>1,2</sup>, G. Stenberg Wieser<sup>1</sup>, Z. Nemeth<sup>3</sup>, T. W. Broiles<sup>4</sup>, and I. Richter<sup>5</sup>
<sup>1</sup>Swedish Institute of Space Physics, Kiruna, Sweden, <sup>2</sup>Department of Computer Science, Electrical and Space Engineering, Luleå University of Technology, Kiruna, Sweden, <sup>3</sup>Wigner Research Centre for Physics, Budapest, Hungary, <sup>4</sup>Space Science and Engineering Division, Southwest Research Institute, San Antonio, Texas, USA, <sup>5</sup>Institute for Geophysics and Extraterrestrial Physics, Technische Universität Braunschweig, Braunschweig, Germany

**Abstract** We study the dynamics of the interaction between the solar wind ions and a partially ionized atmosphere around a comet, at a distance of 2.88 AU from the Sun during a period of low nucleus activity. Comparing particle data and magnetic field data for a case study, we highlight the prime role of the solar wind electric field in the cometary ion dynamics. Cometary ion and solar wind proton flow directions evolve in a correlated manner, as expected from the theory of mass loading. We find that the main component of the accelerated cometary ion flow direction is along the antisunward direction and not along the convective electric field direction. This is interpreted as the effect of an antisunward polarization electric field adding up to the solar wind convective electric field.

## 1. Introduction

The phenomenon of mass loading is common in space plasmas. Newly charged material added to the fast solar wind flow is accelerated by the Lorentz force. The newly added material gains energy and momentum from the solar wind. Solar wind ions experience an equal but opposite net force, thus balancing the total momentum of the system. The thin atmosphere permeated by the solar wind around a comet is one of the most evident cases where mass loading is expected to control the dynamics of the plasma environment [Szegő *et al.*, 2000, section 4.1]. In situ investigations of the solar wind interaction with a cometary plasma were made possible by different missions prior to Rosetta: ICE at P/Giacobini-Zinner in 1985, Giotto, Vega 1 and 2, Susei, Sakigake at P/Halley in 1986, and Giotto at P/Grigg-Skjellerup in 1992 are some examples. However, all those measurements were performed during single flybys, at about 1 AU away from the Sun, and bow shocks were observed at each flyby, indicating a high nucleus activity [cf. Neugebauer, 1990; Coates, 1997].

The Rosetta mission [Glassmeier *et al.*, 2007a] has provided a unique opportunity to continuously observe mass loading in a cometary environment over longer time scales and during varying nucleus activity. The Rosetta spacecraft reached comet 67P/Churyumov-Gerasimenko (67P/CG) in early August 2014. First results from the plasma measurements made at 67P/CG describe how the cometary environment evolves from a thin coma where only low fluxes of low-energy ions are observed, to the point when the effect on the solar wind flow becomes significant [Nilsson *et al.*, 2015b, 2015a; Goldstein *et al.*, 2015]. During these early observations no plasma boundaries had yet formed between the solar wind and the comet atmosphere; i.e., there was no bow shock or ionopause. The scale size of the interaction observed at comet 67P/CG was small, initial observations of water ions were made only when the spacecraft got closer to the nucleus than 100 km distance. The solar wind-atmosphere interaction at a low-activity comet may thus have similarities to artificial comets formed through barium and lithium ion releases from the Active Magnetospheric Particle Tracer Explorers (AMPTE) spacecraft [Haerendel *et al.*, 1986; Rodgers *et al.*, 1986; Coates *et al.*, 1986, 2015].

For a low-activity comet the solar wind is undisturbed before permeating the coma, and no other acceleration process has to be taken into account to study the solar wind-atmosphere interaction. We expect to observe the simplest mass loading phenomenon: newly charged mass is simply added to the undisturbed solar wind flow. This interaction has been previously addressed by Broiles *et al.* [2015], using data from another particle instrument within the Rosetta Plasma Consortium (RPC), RPC ion and electron sensor [Burch *et al.*, 2007]. They reported that the solar wind near the comet was deflected by a Lorentz force opposite to that experienced by cometary pickup ions. They also found that this deflection was not well ordered by the spacecraft position relative to the comet and was well correlated with large changes in the observed magnetic field.

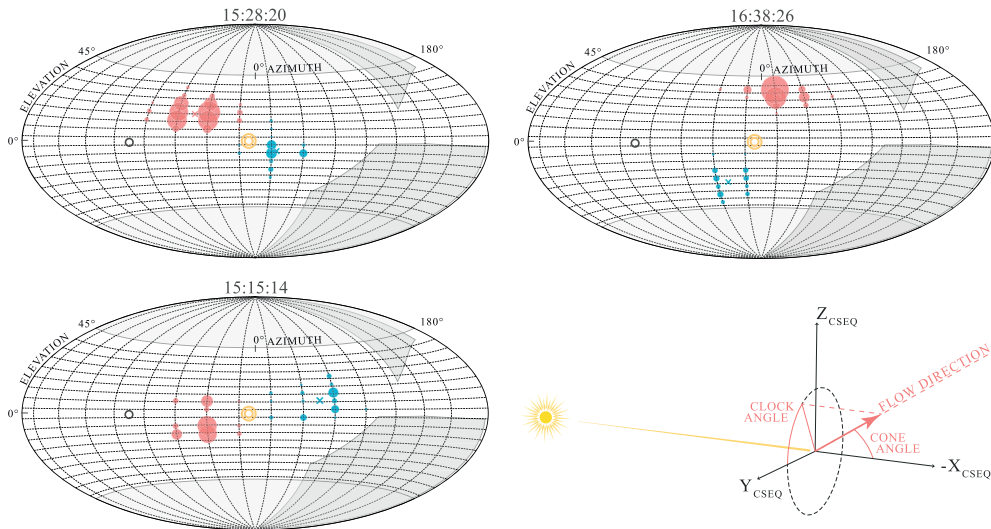


**Figure 1.** Three examples of  $\text{H}_2\text{O}^+$  and  $\text{H}^+$  flows pictured in the instrument FOV at precise times during the 28 November. Depending on the time, the two flows are coming from completely different directions (the spacecraft attitude is unchanged during this period), but always with a  $180^\circ$  difference in clock angle as defined in the bottom right illustration. It represents the spherical coordinate system used for this study. All vectors are normalized,  $\mathbf{v}_{\text{norm.}} = \frac{\mathbf{v}}{|\mathbf{v}|}$ .

We present a case study that provides new details about the dynamics of this interaction between the solar wind and the coma, based on ion and magnetic field data from 28 November 2014.

## 2. Instrument Description

The ion composition analyzer, part of the Rosetta Plasma Consortium (RPC-ICA), is an ion spectrometer aimed to study the interaction between the solar wind and positive cometary ions at comet 67P/CG [Nilsson *et al.*, 2007]. The instrument resolves energy and mass per charge of the incoming ions. The energy spans from 10 eV up to 40 keV. The instrument field of view is  $360^\circ \times 90^\circ$  (azimuth  $\times$  elevation, illustrated in Figure 1), with a resolution of  $22.5^\circ \times 5.0^\circ$ . For this data set, a full angular scan was produced every 192 s. The elevation angle of the incoming positive ions is determined by an electrostatic acceptance angle filter at the entrance of the instrument, and the azimuth angle is measured by the means of 16 anodes, part of the detection system marking the end of an ion path in the instrument. Thus, the two angles are subject to different constraints, limits, and resolutions.

The magnetometer (RPC-MAG) [Glassmeier *et al.*, 2007b] measures the three components of the magnetic field vector in the range from DC up to 10 Hz. The measurement range is  $\pm 16,384$  nT with a resolution of 31 pT. RPC-MAG is mounted on a 1.5 m long boom in order to minimize the impact of the spacecraft-generated disturbance fields. The magnetometer is affected by a systematic bias field from the spacecraft, which cannot be fully characterized as the spacecraft fields are changing related to the operation status. In this work, we take this into account by considering and propagating a  $\pm 3$  nT uncertainty on each magnetic field component in the spacecraft reference frame.

## 3. The Case

In order to diagnose the dynamics of the interaction between the solar wind and the coma, we considered data sets with a clear and constant water ion signal, simultaneously with a clear solar wind signal. The chosen data set turned out to be the clearest in terms of dynamics, mainly because of large variations in the upstream magnetic field direction.

**Table 1.** Conditions and Estimations of  $\text{H}_2\text{O}^+$  Gyroradius

	Data	Undisturbed Solar Wind
$B$	[12, 20] nT	1 nT
$V_{\text{H}^+}$	380 km/s	400 km/s
$E_{\text{estim}}$	[4.0, 4.6] V/km	3.7 V/km
$R_{\text{gyro}}$	[2600, 5900] km	-

The following case study is based on particle and magnetic field data collected at 2.88 AU on 28 November 2014. The spacecraft was then flying a terminator orbit 30 km away from the center of the nucleus, with a mean speed over the day of 0.15 m/s relative to the comet. This very low speed allows us to neglect any aberration angle concerning the cometary ions.

Moreover, an aberration of  $1.01^\circ$  is obtained for a 400 km/s fast solar wind. Our angular resolution is larger than this angle, so we neglect this aberration angle as well.

To study the dynamics of the interaction, we focus on two species: solar wind protons  $\text{H}^+$  and cometary water ions  $\text{H}_2\text{O}^+$ , the most abundant species in the solar wind and the ionized atmosphere, respectively [Nilsson *et al.*, 2015a]. A large flux of accelerated water ions is observed during the chosen day, and we consider the energy range [70 eV, 330 eV], with a peak value at 100 eV. The upper bound is set higher than the most energetic water ions observed. The lower bound isolates these accelerated water ions from the cold water ion population reported by Nilsson *et al.* [2015b]: this population is affected by the spacecraft potential in terms of direction and therefore is not physically relevant for our study. Protons are observed in the energy range [350 eV, 1200 eV].

The average magnetic field magnitude is  $14 \text{ nT} \pm 5.2 \text{ nT}$  over the 14 h of the data set. The speed of the observed protons is stable, with a value of 380 km/s for a peak at 750 eV and a standard deviation  $\sigma = 20 \text{ km/s}$ .

As a first approximation, we assume that the solar wind electric field is given by  $\mathbf{E} = -\mathbf{v}_{\text{H}^+} \times \mathbf{B}$ . Integrating the movement of a test particle with a velocity  $\mathbf{v}_{\text{test}}$ , only subject to the Lorentz force  $\mathbf{F} = q(\mathbf{E} + \mathbf{v}_{\text{test}} \times \mathbf{B})$ , we estimate that the most energetic cometary ions observed ( $\sim 300 \text{ eV}$ ) were accelerated during less than 3 s, over a distance of about 40 km. With this approximation, the minimum gyroradius is 2600 km, which means that the  $\text{H}_2\text{O}^+$  we observe are on the very early phase of the gyromotion, i.e., flowing along the local electric field. For this reason, we expect that the observed accelerated water ion flow gives us the direction of the local electric field. These numbers are summarized in Table 1.

To complete the description of the environment during the measurement, we estimate the density profile of the coma using the Haser model [Haser, 1957]. In this model, the neutral density falls off following  $\sim 1/r^2$ , with  $r$  the distance to the nucleus. At 100 km away from the nucleus, the densities would be an order of magnitude lower than the one met along the 30 km terminator orbit.

## 4. Method

To study the dynamics of the interaction between the solar wind and the comet atmosphere, we aim to express the flow directions of  $\text{H}^+$  and  $\text{H}_2\text{O}^+$  in the body-Centered Solar Equatorial (CSEQ) frame. To achieve that, we first collect the observed counts for the two ion populations, which are well separated in both energy and mass. We then compute full angular distributions for each species every 192 s.

To clearly visualize the two flows and their dynamics, we produce a sequence of pictures as seen with the instrument field of view (FOV). Three of the pictures composing the sequence are given in Figure 1; the full sequence can be seen at <http://irf.se/~etienne/mediaFOV.html>. To that extent, the instrument is used as a camera. The produced sequence also helps us assess that the restricted field of view of the instrument does not impact our results.

We calculate the direction of the bulk velocity for both species, then express the two flow directions (unit vectors) in the CSEQ reference frame. The  $x_{\text{CSEQ}}$  axis is along the Sun-comet line, pointing to the Sun. The  $z_{\text{CSEQ}}$  axis is parallel to and oriented by the Sun's north pole direction, orthogonal to the  $+x$  axis. The  $y_{\text{CSEQ}}$  completes the right-handed reference frame. We compute the angle of each flow direction from the Sun-comet line and refer to this angle as the cone angle. We complement it with the clock angle expressed in the  $(y_{\text{CSEQ}}, z_{\text{CSEQ}})$  plane. It is the angle of the projected flow direction in this plane, from the  $y_{\text{CSEQ}}$  axis and positive toward  $z_{\text{CSEQ}}$ , as shown in Figure 1, bottom right illustration. Both angles form a spherical coordinate system, and all vectors are normalized in this study,  $\mathbf{v}_{\text{norm.}} = \frac{\mathbf{v}}{|\mathbf{v}|}$ . The magnetic field is also expressed in this coordinate system.

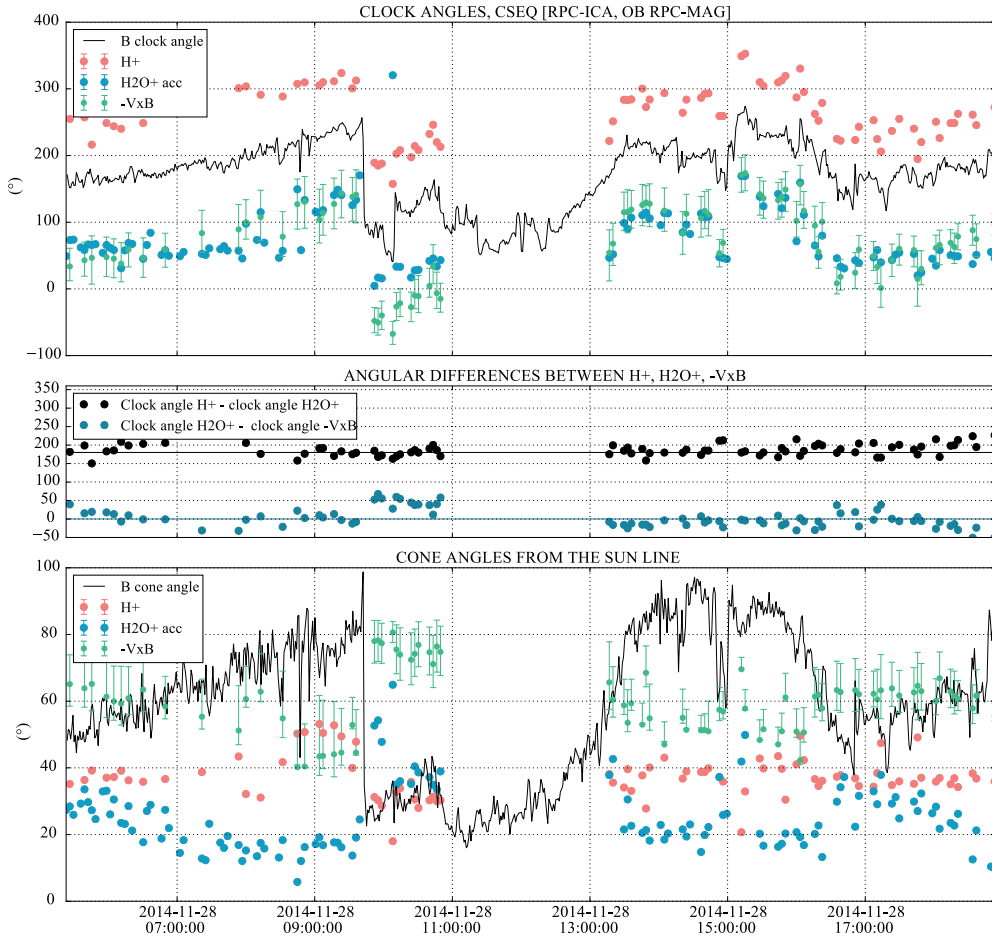


**Figure 2.** (top) Clock and (bottom) cone angle time series, for the H<sup>+</sup> (red) and H<sub>2</sub>O<sup>+</sup> (blue) flow directions, and for the magnetic field direction (solid black line). (middle) The difference between the two flow clock angles is given, with the two solid lines indicating  $y = 180^\circ$  and  $y = 0^\circ$ . Finally, the  $-\mathbf{v}_{H^+} \times \mathbf{B}$  direction is given in green, and its angular difference with cometary ion flow is given in Figure 2 (middle) in terms of clock angle. Between 11:00 and 13:00, no particle data are available.

## 5. Results and Discussion

If mass loading is the only mechanism in the interaction between the solar wind and the coma, we expect to see cometary ions accelerated along the local electric field direction and solar wind protons deflected with an opposite clock angle, as a result of momentum conservation. The dynamics takes place in the plane that includes both flow directions and the comet-Sun line. As the direction of the solar wind electric field varies, both flows are expected to follow the field rotation,  $180^\circ$  away from each other in terms of clock angle. We thus verify with only one coordinate if the two ion populations flow in the same plane or not. The cone angle quantifies the antisunward component in this plane. It gives the amount of solar wind proton deflection and the antisunward component of the cometary ion velocity.

### 5.1. Clock Angle, Momentum Conservation

In Figure 2 (top), clock angles for  $H^+$  (red dots),  $H_2O^+$  (blue dots), and  $\mathbf{B}$  (black line) are given. All three clock angles show variations over a span of about  $200^\circ$ . Despite these large variations, the difference between proton and cometary ion flow directions remains around  $180^\circ$  and is given in Figure 2 (middle). The mean value of this angular difference is  $187^\circ$ , and its standard deviation is  $18^\circ$ . The proton flow clock angle is more correlated to the magnetic field clock angle than the cometary ion flow is. The variations thus mainly originate from the cometary ion flow direction, which is most of the time less regular, or beam like (cf. Figure 1, bottom left FOV picture: there are two peak values instead of one). An energy dependence in the water ion flow direction could explain these variations and will be the topic of a more advanced study focused on the cometary ion population.

The two observed flows have very different directions. Thus, the two populations,  $H^+$  and  $H_2O^+$ , have been flowing along different paths in the coma. Observing this  $180^\circ$  difference ensures us that the magnetic and electric fields have, respectively, very similar directions along these two different paths. As the upstream electric field direction varies, the two paths also move inside the coma, but the angular difference remains the same. This also confirms that the flow directions of both populations remain in the same plane, containing the comet-Sun line.

The direction of the deflection does not seem to be influenced by the position of the nucleus; the flow may be deflected away just as well as toward the nucleus. There is no indication of the ion population flowing around the nucleus. This is because the size of the nucleus is much smaller than the gyroradii of solar wind ions. To be able to flow around an obstacle, the particles of the flow must have sufficient time and space to interact several times inside a boundary layer. The interactions inside the boundary layer mediate the effect which “pushes away” the flow in a conventional situation. There is no such layer in the case of the newborn cometary magnetosphere. The flow only experiences electromagnetic forces due to the mass loading; it feels the much larger inner coma that way, but it simply cannot feel the nucleus. Solar wind ions are bombarding the surface of the nucleus instead of flowing around it. In this regard this early stage of the interaction is very different from later stages.

The dynamics is clearly driven by the solar wind electric and magnetic fields. The nearly constant difference in clock angle between  $H_2O^+$  and  $H^+$  and the correlation with magnetic field clock angles emphasize the role of mass loading as the main mechanism controlling the dynamics of this plasma environment.

### 5.2. Cone Angle

The cone angles of  $H^+$ ,  $H_2O^+$ , and  $\mathbf{B}$  are given in Figure 2 (bottom). An anticorrelation between the  $H_2O^+$  flow direction and the magnetic field can be seen: when the magnetic field cone angle decreases (i.e., the magnetic field is more parallel to the Sun-comet line), the  $H_2O^+$  cone angle increases, and vice versa.

Concerning the proton flow, the cone angle seems to be correlated with the magnetic field cone angle in the first half of the data set. Around 9:40, a sudden and large decrease is observed in both angles. This correlation has an immediate interpretation.  $B_\perp$  is the component of the magnetic field orthogonal to the proton flow. The larger  $B_\perp$  is (for the same  $B$  amplitude), the larger  $\mathbf{E} = -\mathbf{v}_{H^+} \times \mathbf{B}$  is. The acceleration of newborn ions is then larger, and as a direct consequence the deflection of the protons is also larger. The correlation is not clearly observed after 12:00.

On average,  $H_2O^+$  flow direction is  $20^\circ$  away from the Sun-comet line, and a  $40^\circ$  solar wind proton deflection is observed, as illustrated in Figure 3.

### 5.3. Electric Field

The generalized Ohm’s law can be written as follows:

$$\mathbf{E} = \mathbf{E}_{\text{motional}} + \mathbf{E}_{\text{other}}$$

As previously introduced, we approximate the direction of the motional field by  $\mathbf{E}_{\text{motional}} = -\mathbf{v}_{H^+} \times \mathbf{B}$ , computing together particle data and magnetic field data. For two earlier cases (data from 21 September 2014—cf. Nilsson *et al.* [2015a]—and 16 November 2014), the  $H_2O^+$  ions are flowing along  $-\mathbf{v}_{H^+} \times \mathbf{B}$ .  $\mathbf{E} = \mathbf{E}_{\text{motional}} = -\mathbf{v}_{H^+} \times \mathbf{B}$  was then a good description of the local electric field. These data sets correspond to a lower activity and larger distances to the nucleus, resulting in a lighter mass loading of the solar wind. In the extreme case where only few cometary ions are picked up, the solar wind is almost undisturbed by the interaction, and those few pickup ions are first accelerated along the convective electric field given by  $\mathbf{E} = -\mathbf{v}_{H^+} \times \mathbf{B}$ .

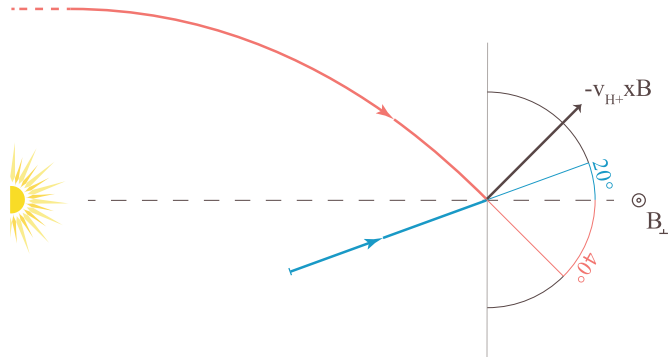


**Figure 3.** Illustration of the observation: the solar wind protons (red line) are gradually deflected by the coma, reaching a  $40^\circ$  angle from the comet-Sun line in average, measured in the terminator plane. The main component of the cometary ion flow is along the comet-Sun line. The dynamics takes place in a plane, containing the comet-Sun line and rotating around it.

The case studied here corresponds to a more significant mass loading of the solar wind and reveals a new configuration of the electric and magnetic fields inside the coma. The result for the comparison between the  $-\mathbf{v}_{H^+} \times \mathbf{B}$  direction and the  $H_2O^+$  flow direction is given in Figure 2, using the same spherical coordinate system previously introduced. In terms of clock angle (Figure 2, top), the two series are overlapping nicely. Their angular difference, given in Figure 2 (middle), is centered around the solid black line at  $0^\circ$ . We note that between 09:45 and 11:00, after the sudden decrease in the magnetic field cone angle, this difference is centered around  $\sim 45^\circ$ . This may indicate that a further specific study of this quasi-parallel regime is needed.

The cone angles give us a more complex picture of the dynamics.  $-\mathbf{v}_{H^+} \times \mathbf{B}$  and  $H_2O^+$  flow cone angles seem to correlate with each other, but with an angular difference of about  $30^\circ$ . So it appears that with the activity increasing,  $\mathbf{E} = -\mathbf{v}_{H^+} \times \mathbf{B}$  does not hold anymore. Two possibilities can explain the discrepancy:

1. In the description of the motional electric field  $\mathbf{E}_{\text{motional}} = -\mathbf{v} \times \mathbf{B}$ ,  $\mathbf{v}_{H^+}$  is not a good proxy anymore. Electron and proton flows do not have the same direction anymore.
2.  $\mathbf{E}_{\text{other}}$  became comparable to  $\mathbf{E}_{\text{motional}}$ .

Both possibilities can be directly put in relation with the increasing cometary ion density, and it seems reasonable to say that both are playing a role. The magnetic field is enhanced (with an average value of 14 nT, compared to the  $\sim 1$  nT expected in the undisturbed solar wind at this heliocentric distance), while the solar wind protons are not significantly slowed down (the observed proton flow speed is 380 km/s). This implies that the electron fluid is significantly slowed down. There is no obvious reason why this should lead to an antisunward electric field. Therefore, we do not explore this first possibility and confine the discussion to the possibility of another electric field developing in the coma when densities are higher, resulting in an antisunward acceleration of picked up cometary ions.

The cometary atmosphere provides a constant and distributed source of ions and electrons. The electrons are picked up and swept downstream ( $\mathbf{E} \times \mathbf{B}$  drift), whereas the newborn ions are moving along the local electric field direction. Charge separation occurs because of the scale size of the interaction region being much smaller than the gyroradius of newborn water ions. Whatever electric fields arise from this must in the end have the net effect of reducing this separation. The new net polarization field is in the plane ( $\mathbf{v}_{H_2O^+}, \mathbf{v} = \mathbf{E} \times \mathbf{B}$ ) and therefore cannot have any influence on the clock angle of the  $H_2O^+$  and  $H^+$  ion flow directions. It has, however, a large influence on their cone angle, as seen in the observation presented in the previous subsection.

If we now consider the solar wind, we expect that ions and electrons will also react differently to the obstacle on some scale. As previously mentioned, observations show no significant slowing down of the solar

wind, while we see a significant increase in the magnetic field as compared to the undisturbed solar wind. That implies decoupling between electrons and protons, which could lead to a Hall current or even charge separation.

To get the full picture of this interaction and its dynamics, one would need to add the two components discussed above. The situation becomes very complex, and we believe that numerical simulations are needed to describe the interaction. We observe a mainly antisunward cometary ion flow, implying a mainly antisunward  $E_{\text{other}}$ . This is consistent with the mechanism discussed in the first paragraph.

Haerendel et al. [1986] depict such an antisunward electric field in the context of the AMPTE artificial comet, introducing it with the same argument of charge separation. This work was based on magnetic field data and particle measurements made by a similar 3-D plasma instrument [cf. Rodgers et al., 1986; Coates et al., 1986]. This topic is also widely reviewed by Szegő et al. [2000]. However, the AMPTE releases concerned transient phenomena, whereas Rosetta investigates the evolution of a continuous and time-varying source of neutral particles.

## 6. Conclusion

Despite a limited angular resolution and uncertainties on the magnetic field components, the obvious correlations and anticorrelations presented in this study provide a detailed description of the interaction between the solar wind and the cometary atmosphere, during a period of low nucleus activity. The plasma environment dynamics pictured in this work does not depend on the nucleus position: when the solar wind magnetic field direction changes, the two flow directions evolve accordingly, regardless of the nucleus position; i.e., the ions do not flow around the nucleus. This is in agreement with earlier results [cf. Broiles et al., 2015]. Both ion populations—from the solar wind and from the coma—flow with clock angles  $180^\circ$  apart from each other: the dynamics of the interaction takes place in a single plane that contains and rotates around the comet-Sun line.

Measured at 30 km away from the nucleus and at a distance of 2.88 AU from the Sun, the solar wind protons reach deflections higher than  $50^\circ$ . Even in the absence of plasma boundaries, the solar wind is already substantially disturbed, and the magnetic field is not coupled to the solar wind ions anymore, contrary to what is observed at greater distances to the Sun.

The comet ions are accelerated with a dominating antisunward component. We suggest that the difference of motion between the cometary ions and electrons, together with the limited scale size of the coma, smaller than the cometary ion gyroradius, results in a mainly antisunward new contribution to the electric field.

## Acknowledgments

The work on RPC-ICA, as well as this PhD project, is founded by the Swedish National Space Board. The work on RPC-MAG was financially supported by the German Ministerium für Wirtschaft und Energie and the Deutsches Zentrum für Luft- und Raumfahrt under contract 50QP 1401. Without the tremendous work of the Rosetta Science Ground Segment (RSGS), Rosetta Mission Operation Control (RMOC), and all instrument team planners, this study would be impossible. Sharing data within RPC is made possible by the web-based interface AMDA, developed and made available for RPC use by Centre de Données de la Physique des Plasmas (CDPP). This efficient interface has been of a great use for this work. The SPICE toolkit from NASA's Navigation and Ancillary Information Facility (NAIF) [Acton, 1996] is heavily used in this study and made accessible through python by the SpicePy wrapper.

## References

- Acton, C. H. (1996), Ancillary data services of NASA's navigation and ancillary information facility, *Planet. Space Sci.*, 44, 65–70.
- Broiles, T. W., J. L. Burch, G. B. Clark, C. Koenders, E. Behar, R. Goldstein, S. A. Fuselier, K. E. Mandt, P. Mokashi, and M. Samara (2015), Rosetta observations of solar wind interaction with the comet 67P/Churyumov-Gerasimenko, *Astron. Astrophys.*, 583, A21.
- Burch, J. L., R. Goldstein, T. E. Cravens, W. C. Gibson, R. N. Lundin, C. J. Pollock, J. D. Winningham, and D. T. Young (2007), RPC-IES: The ion and electron sensor of the Rosetta Plasma Consortium, *Space Sci. Rev.*, 128, 697–712.
- Coates, A. J. (1997), Ionosphere and magnetospheres of comets, *Adv. Space Res.*, 20, 255–266.
- Coates, A. J., A. D. Johnstone, M. P. Smith, and D. J. Rodgers (1986), AMPTE/UKS ion experiment observations of lithium releases in the solar wind, *J. Geophys. Res.*, 91(A2), 1311–1319.
- Coates, A. J., J. L. Burch, R. Goldstein, H. Nilsson, G. Stenberg Wieser, E. Behar, and the RPC team (2015), Ion pickup observed at comet 67P with the Rosetta Plasma Consortium (RPC) particle sensors: Similarities with previous observations and AMPTE releases, and effects of increasing activity, *J. Phys.*, 642, 12005.
- Glassmeier, K. H., H. Boehnhardt, D. Koschny, E. Kürtz, and I. Richter (2007a), The Rosetta mission: Flying towards the origin of the solar system, *Space Sci. Rev.*, 128(1–4), 1–21.
- Glassmeier, K. H., I. Richter, A. Diedrich, G. Musmann, U. Auster, U. Motschmann, and A. Balogh (2007b), RPC-MAG—The fluxgate magnetometer in the ROSETTA Plasma Consortium, *Space Sci. Rev.*, 128, 649–670.
- Goldstein, R., et al. (2015), The Rosetta ion and electron sensor (IES) measurement of the development of pickup ions from comet 67P/Churyumov-Gerasimenko, *Geophys. Res. Lett.*, 42(9), 3093–3099.
- Haerendel, G., G. Paschmann, W. Baumjohann, and C. W. Carlson (1986), Dynamics of the AMPTE artificial comet, *Nature*, 320, 720–723.
- Haser, L. (1957), Distribution d'intensité dans la tête d'une comète, *Bull. Acad. R. Belgique, Classes des Sciences*, 43, 740–750.
- Neugebauer, M. (1990), Spacecraft observations of the interaction of active comets with the solar wind, *Rev. Geophys.*, 28, 231–252, doi:10.1029/RG028i002p00231.

- Nilsson, H., et al. (2007), RPC-ICA: The ion composition analyzer of the Rosetta Plasma Consortium, *Space Sci. Rev.*, 128(1–4), 671–695.
- Nilsson, H., et al. (2015a), Birth of a comet magnetosphere: A spring of water ions, *Science*, 347, 6220.
- Nilsson, H., G. Stenberg-Wieser, and E. Behar (2015b), Evolution of the ion environment of comet 67P/Churyumov-Gerasimenko—Observations between 3.6 and 2.2 AU, *Astron. Astrophys.*, 538, A20, doi:10.1051/0004-6361/201526142.
- Rodgers, D. J., A. J. Coates, A. D. Johnstone, M. P. Smith, D. A. Bryant, D. S. Hall, and C. P. Chaloner (1986), UKS plasma measurements near the AMPTE artificial comet, *Nature*, 320, 712–716.
- Szegő, K., et al. (2000), Physics of mass loaded plasmas, *Space Sci. Rev.*, 94, 429–671.



B

PUBLICATION II

---



# Mass-loading of the solar wind at 67P/Churyumov-Gerasimenko

## Observations and modelling

E. Behar<sup>1,2</sup>, J. Lindkvist<sup>1,3</sup>, H. Nilsson<sup>1,2</sup>, M. Holmström<sup>1</sup>, G. Stenberg-Wieser<sup>1</sup>, R. Ramstad<sup>1,3</sup>, and C. Götz<sup>4</sup>

<sup>1</sup> Swedish Institute of Space Physics, 981 28 Kiruna, Sweden  
e-mail: [etienne.behar@irf.se](mailto:etienne.behar@irf.se)

<sup>2</sup> Luleå University of Technology, Department of Computer Science, Electrical and Space Engineering, 981 28 Kiruna, Sweden

<sup>3</sup> Umeå University, Department of Physics, 90187 Umeå, Sweden

<sup>4</sup> Technische Universität Braunschweig, Institute for Geophysics and Extraterrestrial Physics, 38106 Braunschweig, Germany

Received 26 April 2016 / Accepted 12 September 2016

### ABSTRACT

**Context.** The first long-term in-situ observation of the plasma environment in the vicinity of a comet, as provided by the European Rosetta spacecraft.

**Aims.** Here we offer characterisation of the solar wind flow near 67P/Churyumov-Gerasimenko (67P) and its long term evolution during low nucleus activity. We also aim to quantify and interpret the deflection and deceleration of the flow expected from ionization of neutral cometary particles within the undisturbed solar wind.

**Methods.** We have analysed in situ ion and magnetic field data and combined this with hybrid modeling of the interaction between the solar wind and the comet atmosphere.

**Results.** The solar wind deflection is increasing with decreasing heliocentric distances, and exhibits very little deceleration. This is seen both in observations and in modeled solar wind protons. According to our model, energy and momentum are transferred from the solar wind to the coma in a single region, centered on the nucleus, with a size in the order of 1000 km. This interaction affects, over larger scales, the downstream modeled solar wind flow. The energy gained by the cometary ions is a small fraction of the energy available in the solar wind.

**Conclusions.** The deflection of the solar wind is the strongest and clearest signature of the mass-loading for a small, low-activity comet, whereas there is little deceleration of the solar wind.

**Key words.** comets: general – comets: individual: 67P/Churyumov-Gerasimenko – plasmas – methods: observational – methods: numerical – space vehicles: instruments

## 1. Introduction

Comets show large changes in their appearance as their distance from the Sun varies. Closer to the Sun, volatile materials on the comet nucleus start to sublimate, forming a neutral cloud that becomes partially ionized by solar UV radiation and charge exchange processes. When the comet activity evolves, the complexity of its interaction with the solar wind also changes. At large distances from the Sun the solar wind directly impacts the surface of an atmosphereless nucleus in an asteroid-like interaction, while at smaller heliospheric distances the solar wind permeates a thin, partially ionized, unstructured coma. When the comet activity is even higher (or the comet is closer to the Sun), the coma is much denser and plasma boundaries form, creating a cometary magnetosphere (Szegő et al. 2000, Sect. 4.1; Koenders et al. 2015).

In situ investigations of the interaction between active comets and the solar wind started in the mid-80s with the International Cometary Explorer (ICE) visiting P/Giacobini-Zinner in 1985, and *Giotto*, Vega-1 and -2, Suisei and Sakigake examining P/Halley in 1986. *Giotto* went on to probe P/Grigg-Skjellerup in 1992. Although these missions provided valuable information about the structure of a cometary magnetosphere and its interaction with the solar wind at a given time, the fly-by nature of these missions did not enable the study of the

evolution of this interaction as the heliocentric distance changes. The Rosetta spacecraft spends most of its time close to the nucleus of comet 67P/Churyumov-Gerasimenko (67P), scanning the cometary environment out to a maximum of 1500 km only. However, Rosetta has stayed in the vicinity of 67P for two years giving us the unique opportunity to monitor and study in situ how the interaction evolves as the comet transforms from an almost atmosphereless object into an active nucleus (Glassmeier et al. 2007a).

The Rosetta spacecraft completed its long voyage to comet 67P in early August 2014 and recorded the first traces of cometary ions upon rendezvous. The first results from the plasma measurements made at 67P describe the early phase of the comet's transformation. The first observations of cometary water ions and solar wind deflection were reported by Nilsson et al. (2015b), with the subsequent enhancement of comet water ion fluxes around comet 67P down to a heliocentric distance of 2 au described in Nilsson et al. (2015a). The local cold ion environment and its relation to the outgassing from the nucleus is described in Goldstein et al. (2015) and Edberg et al. (2015). First reports on the magnetic field environment showed strong wave activity in the vicinity of the comet (Richter et al. 2015).

At low activity, the solar wind is lightly mass-loaded with freshly ionized cometary particles. As these new-born ions are accelerated by the solar wind electric field, energy and

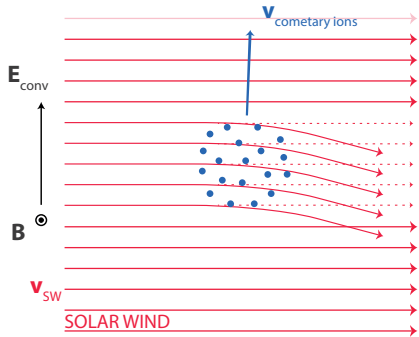


**Fig. 1.** A simplistic view of light mass-loading: energy and momentum are transferred from the solar wind (red streamlines) to the cometary ions (blue dots) in a pick up process. Conservation of energy and momentum leads to a deceleration and deflection of the local solar wind.

momentum are transferred from the solar wind to the coma. Considering the complete system (i.e. the entire coma), the solar wind loses the energy gained by the cometary ions (often referred to as “pick up” ions, as they are picked up by the solar wind).

The most basic expectations are illustrated in Fig. 1: the solar wind flow is deflected from the comet-sun line and slowed down, as new born cometary ions are accelerated. The gyroradius of the new born ions is much larger than the ion source, so these ions move essentially along the solar wind electric field within the ion source region. The newly created electrons on the other hand have a gyro-radius smaller than the source region, and can be expected to  $E \times B$  drift. This might lead to charge separation and, in turn, to new dynamical effects (Nilsson et al. 2015a; Behar et al. 2016). Coates et al. (2015) have discussed how such a situation near a low activity comet with a small coma may be more similar to barium release experiments than to higher activity comets.

The first observations at comet 67P indeed showed solar wind deflection and water ion acceleration approximately orthogonal to the solar wind flow direction (Nilsson et al. 2015b). The plasma dynamics of solar wind deflection at 67P at low activity were further studied in Broiles et al. (2015) and Behar et al. (2016). In these two studies, it was shown how the solar wind deflection direction and the direction of the acceleration of newborn cometary ions are both correlated with the local magnetic field direction, consistent with the transfer of momentum described here-above.

Once the comet activity has increased above the very low level of the initial observations, the cometary ion flow direction has a main anti-sunward component (Nilsson et al. 2015a; Behar et al. 2016). Behar et al. (2016) discuss this in terms of a polarisation electric field developing in the coma as electrons and ions respond differently to the solar wind electric field on scales below the ion gyroradius.

We limit our study of the evolution of the interaction to the solar wind protons. This population reflects the interaction with the cometary ions experienced all along its trajectory through the coma. We expect the solar wind protons to exhibit both deflection and deceleration and we compare our expectations to the measured deflection and speed. In addition to the ion measurements, we consider the local magnetic field, which is highlighted

as one of the major drivers in the solar wind-comet interaction by Broiles et al. (2015) and Behar et al. (2016).

The in situ data recorded onboard Rosetta represent a single-point probe of the whole system, with little spatial coverage over time. Energy and momentum are transferred, via the electromagnetic field, over a larger volume. In order to get a large-scale view, we use a hybrid model of the coma-solar wind interaction. This model provides a global picture of the interaction, allowing us to get an estimate of the size of the region involved in energy and momentum transfer.

Considering the simplicity of our theoretical approach, we choose to define and use a fairly simple model as well, involving only the major components in the system. Cometary water ions are added to the solar wind flow through ionization of an isotropic neutral outflow. The model thus does not have a solid obstacle for the solar wind, nor does it have gravity or momentum transfer by collisions. By proceeding in this manner, we hope to isolate and identify the main drivers of the plasma dynamics at a comet, at low activity.

We focus the study on the early period of the Rosetta mission, from the arrival at the nucleus (3.6 au) to a chosen distance of 2.2 au from the Sun. Closer to the Sun, a larger mass-loading of the solar wind results in a different dynamical regime in which, based on preliminary observations, either more radical or new effects occur. To mark this separation, we refer in this study to the phenomenon of light mass-loading, in opposition with a heavier mass-loading regime occurring later on.

## 2. Method

### 2.1. Instrument description

Particle data used in this work were produced by the Ion Composition Analyzer, part of the Rosetta Plasma Consortium (RPC-ICA). This instrument is an ion mass-energy spectrometer aimed at studying the interaction between the solar wind and positive cometary ions at comet 67P (Nilsson et al. 2007). RPC-ICA data consist of count rates given in five dimensions, namely time, energy per charge, mass per charge, and incoming direction (two angles). Full energy scans are produced every 12 s and full angular scans are produced every 192 s. The energy spans from 10 eV up to 40 keV in 96 steps with a resolution  $\frac{\delta E}{E} = 0.07$ . The instrument field of view is  $360^\circ \times 90^\circ$  (azimuth  $\times$  elevation), with a resolution of  $22.5^\circ \times 5.0^\circ$ . Mass is determined through a position detection system with 32 anodes, which we will refer to as mass channels. The radial position of ions on the detector plate is a function of both mass and energy.

The magnetometer (RPC-MAG, Glassmeier et al. 2007b) measures the three components of the magnetic field vector, with a frequency of 20 vectors per second. The measurement range is  $\pm 16\,384$  nT with an accuracy of 31 pT. RPC-MAG is mounted on a 1.5 m long boom in order to minimise the impact of spacecraft-generated disturbance fields.

In this work, the magnetic field amplitude was averaged over 10 h of data.

### 2.2. Particle data analysis

In order to characterise the protons detected by the instrument, the very first step was to identify and separate them from the rest of the observed ions. On the left panel of Fig. 2, counts integrated over one day are given as function of mass channel and energy, and different species are identified on this energy-mass matrix. The strongest signal was acquired for protons, and over

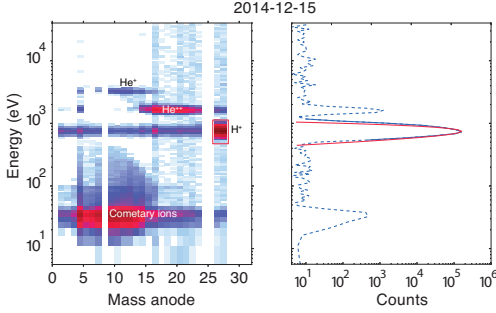


**Fig. 2.** One example of an energy-mass matrix (*left panel*) and the corresponding proton fit (*right panel*).

90% of proton counts were detected in mass channels 26 and 27 (surrounded by dead mass channels). During the period covered by the study, protons were always separated from other species in the energy dimension, at the daily time scale. In the left panel of Fig. 2, protons (the lightest particles) form the rightmost population, at highest mass channels. At about twice the energy and shifted to the left  $\text{He}^{2+}$  particles are found, followed by  $\text{He}^+$  particles at about four times the proton energy and further to the left (lower mass channels). Cometary ions are found in the lower left corner, corresponding to lower energy and higher mass.

We have manually selected the proton energy, one selection per day. This selection was then used for all full angular scans (of 192 s) during each day. The selection window which identifies proton counts and rules out the rest of the counts is defined for one day in energy-mass space, as follows: only mass channels 26 and 27 were considered, and we use an energy interval manually selected. This resulted in the red rectangle window over-plotted on the left panel (Fig. 2).

To determine the average direction of the proton flow, we computed full angular distributions (azimuth-elevation) with all counts in the selection window included. We calculated the direction of the bulk velocity in the body-Centered Solar EQuatorial (CSEQ) reference frame. The  $x_{\text{CSEQ}}$  axis is along the sun-comet line, pointing to the Sun. We computed the solar wind deflection as the angle between  $-x_{\text{CSEQ}}$  and the flow direction. The same method is presented with more details in Behar et al. (2016).

This resulted in one series of deflection angles per day. The time resolution is 192 s. Later on, we calculated the median of each series. In Sect. 3 we work with the time series of median deflection values, one median value per day.

On the right panel of Fig. 2, a normal distribution (solid red line) is fitted to the selected protons (solid blue line), along the energy dimension. In this example, the distribution is integrated over one day. To capture fast variations of the proton energy distribution, the fit parameters were calculated at the full angular scan time resolution (192 s). We collected the central energy value, the height and the Full Width at Half Maximum (FWHM). This resulted in a time series of fit parameters, one series per day. The time resolution was 192 s. Later on, we also calculate the median of each daily series, and work in Sect. 3 with a series of median fit parameters.

### 2.3. Model

To model the interaction between the comet 67P and the solar wind plasma, we used a self-consistent hybrid plasma model where we included a production of cometary ions. In the hybrid approximation, ions are treated as particles, and electrons as a massless fluid. Below we present the governing equations for the solver and the comet model. See Holmström (2010, 2013) for more information about the solver.

The trajectory of a particle,  $\mathbf{r}(t)$  and  $\mathbf{v}(t)$ , with charge  $q$  and mass  $m$ , is given by the solution of the equation of motion with the Lorentz force,  $\mathbf{F}$ :

$$\frac{d\mathbf{r}}{dt} = \mathbf{v}, \quad \frac{d\mathbf{v}}{dt} = \frac{\mathbf{F}}{m} = \frac{q}{m} (\mathbf{E}' + \mathbf{v} \times \mathbf{B}), \quad (1)$$

with  $\mathbf{E}' = \mathbf{E} - \eta \mathbf{J}$  to conserve momentum since electrons are massless (Bagdonat & Motschmann 2002), where  $\mathbf{E} = \mathbf{E}(\mathbf{r}, t)$  is the electric field,  $\mathbf{B} = \mathbf{B}(\mathbf{r}, t)$  is the magnetic field, and  $\mathbf{J} = \mu_0^{-1} \nabla \times \mathbf{B}$  is the current density.

The electric field is not unknown, and is calculated by

$$\mathbf{E} = \frac{1}{\rho_i} (-\mathbf{J}_i \times \mathbf{B} + \mathbf{J} \times \mathbf{B} - \nabla p_e) + \eta \mathbf{J}, \quad (2)$$

where  $\rho_i$  is the ion charge density,  $\mathbf{J}_i$  is the ion current density,  $p_e$  is the electron pressure, and  $\eta$  is the resistivity.

The gradient of the electron pressure is calculated by imposing quasi-neutrality and a polytropic index,  $\gamma_e$ . In this study we chose an adiabatic index, corresponding to  $\gamma_e = 5/3$ .

Faraday's law is used to advance the magnetic field in time,

$$\frac{\partial \mathbf{B}}{\partial t} = -\nabla \times \mathbf{E}. \quad (3)$$

In vacuum regions, that are defined by the number density of ions being less than a given value,  $n < n_{\min}$ , we set  $1/\rho_i = 0$  in Eq. (2), and Faraday's law is reduced to solving the magnetic diffusion equation,

$$\frac{\partial \mathbf{B}}{\partial t} = \frac{\eta}{\mu_0} \nabla^2 \mathbf{B}. \quad (4)$$

A constraint on the time step has been inferred since the field cannot diffuse more than one cell per timestep,

$$\Delta t < \frac{\mu_0 (\Delta x)^2}{2\eta}, \quad (5)$$

where  $\Delta t$  is the time step and  $\Delta x$  is the cell size. The time step is for moving the particles (ions). The electromagnetic fields can be updated more frequently (subcycled) since it is usually computationally cheaper to update the fields compared to moving all the particles.

For a comet, when neglecting gravity and assuming a constant outflow velocity, the total flux of non-collisional water vapor will be constant through any spherical shell around the nucleus at distance  $r$ . This is called the Haser model (Haser 1957), and is described below to a first order approximation that neglects neutral bi-products once created.

The number density of water vapor,  $n$ , as a function of the distance,  $r$ , from the comet nucleus is

$$n_{\text{H}_2\text{O}}(r) = \frac{Q}{4\pi r^2 u}, \quad (6)$$

where  $Q$  is the production rate of water vapor, and  $u$  is the mean velocity of water vapor in the radial direction. However, if one

accounts for losses (mainly due to photodissociation), the flux will decrease exponentially with time,  $t = r/u$ , as the molecules move outwards from the nucleus, and one gets

$$n_{\text{H}_2\text{O}}(r) = \frac{Q}{4\pi r^2 u} \exp\left(-\frac{v_d r}{u}\right), \quad (7)$$

where  $v_d$  is the photodestruction rate of water vapor.

The water vapor ionizes with a certain ionization rate,  $v_i$ , and creates water ions,  $\text{H}_2\text{O}^+$ . The water ion production rate as a function of distance becomes

$$q_i(r) = v_i n_{\text{H}_2\text{O}}(r), \quad (8)$$

where, in the implementation, the number density of water,  $n_{\text{H}_2\text{O}}$ , is taken at the center of each grid cell for each time step, generating the prescribed amount of ions at random positions in that cell.

Note that neglecting the neutral bi-products of water once they are created will barely change the density of neutral water if the mean-free-path due to photodissociation,  $u/v_d$ , is much larger than the size of the simulation domain, which is true for all cases studied in this paper. Other models used by, for example, Hansen et al. (2007), Koenders et al. (2015), have similar first order approximations that instead neglect the creation of neutral bi-products.

### 2.3.1. Coordinate system and simulation box

The coordinate system we use in the hybrid model is a body-centered coordinate system. It is centered in the middle of 67P.

The  $x$ -axis is pointing towards the Sun, with solar wind flowing in the  $-x$  direction, making it the same  $x$  coordinate as in the CSEQ reference frame, which is the only coordinate addressed in the observations. The  $z$ -axis is pointing in the direction of the ambient convective electric field, and the  $y$ -axis completes the right-handed system. We assume that the IMF has a Parker spiral configuration, that is the IMF lies in the  $xy$ -plane.

The convective electric field is given by  $\mathbf{E}_0 = -\mathbf{v}_0 \times \mathbf{B}_0$ , where  $\mathbf{v}_0$  is the undisturbed solar wind bulk velocity, and  $\mathbf{B}_0$  is the IMF which is initially homogeneous everywhere.

The simulation domain is given by  $|x| < 6 \times 10^3$  km,  $|y| < 12 \times 10^3$  km,  $|z| < 18 \times 10^3$  km, with a cellsize  $\Delta x = 125$  km.

### 2.3.2. Model and simulation parameters

We set the plasma resistivity to  $\eta_p = 1.6 \times 10^4$  Ohm m, to dampen numerical oscillations. We assume a vacuum resistivity of  $\eta_v = 2.5 \times 10^5$  Ohm m, which is used when solving the diffusion equation of Faraday's law (Eq. (4)) for regions of a number density less than the arbitrarily chosen  $n_{\min} = n_0/16$ , where  $n_0$  is the ambient solar wind proton number density. To summarize:

$$\eta = \begin{cases} \eta_v, & \text{for } n < n_{\min}, \\ \eta_p, & \text{otherwise.} \end{cases} \quad (9)$$

The electromagnetic fields were updated 20 times for each time step,  $\Delta t = 3.5 \times 10^{-2}$ . The simulations were run for a total of 120 s to reach steady-state.

The water production rate of a comet changes with distance from the sun. We used  $Q = 1.14 \times 10^{29} \cdot R^{-7.06} [\text{s}^{-1}]$ , where  $R$  is the distance to the sun in au (Simon Wedlund et al. 2016). The neutral expansion velocity is observed to be relatively constant around  $u = 0.7 \text{ km s}^{-1}$  (Simon Wedlund et al. 2016), so we used that value.

**Table 1.** Solar wind conditions used in the model.

Case	$R$ [au]	$n_0$ [ $\text{cm}^{-3}$ ]	$v_0$ [ $\text{km s}^{-1}$ ]	$B_0$ [nT]	$\chi$ [ $^\circ$ ]
1	3.6	0.385	400	1.4	74
2	3.25	0.45	400	1.6	73
3	3.05	0.55	400	1.7	72
4	2.7	0.7	400	2.0	70
5	2.35	0.9	400	2.3	67
6	2.0	1.25	400	2.8	63

**Table 2.** Cometary parameters used in the model.

Case	$R$ [au]	$u$ [ $\text{km s}^{-1}$ ]	$Q$ [ $\text{s}^{-1}$ ]	$v_i$ [ $\text{s}^{-1}$ ]	$v_d$ [ $\text{s}^{-1}$ ]
1	3.6	0.7	$1.3 \times 10^{25}$	$5.0 \times 10^{-8}$	$1.4 \times 10^{-6}$
2	3.25	0.7	$2.8 \times 10^{25}$	$6.2 \times 10^{-8}$	$1.7 \times 10^{-6}$
3	3.05	0.7	$4.3 \times 10^{25}$	$7.0 \times 10^{-8}$	$1.9 \times 10^{-6}$
4	2.7	0.7	$1.0 \times 10^{26}$	$8.9 \times 10^{-8}$	$2.4 \times 10^{-6}$
5	2.35	0.7	$2.7 \times 10^{26}$	$1.2 \times 10^{-7}$	$3.2 \times 10^{-6}$
6	2.0	0.7	$8.5 \times 10^{26}$	$1.6 \times 10^{-7}$	$4.5 \times 10^{-6}$

Water ions are produced in the simulation according to Eq. (8). We used scaled values,  $1/R^2$  with heliocentric distances, for photoionization and photodestruction from Crovisier (1989), where a mean value was taken between active and quiet Sun conditions. At 1 au this gives a photoionization rate of  $v_i = 6.5 \times 10^{-7} \text{ s}^{-1}$  and a photodestruction rate of  $v_d = 1.78 \times 10^{-5} \text{ s}^{-1}$  (Crovisier 1989).

In the model we used typical solar wind conditions at 1 au from Cravens (2004) scaled to the heliocentric distances of 67P. The undisturbed solar wind plasma parameters at 1 au are a bulk velocity of  $v_0 = 400 \text{ km s}^{-1}$  in  $-\hat{x}$  (neglecting aberration), a number density of protons being  $n_0 = 5 \text{ cm}^{-3}$ , and a temperature of ions and electrons being constant at  $T_i = 0.5 \times 10^5 \text{ K}$  and  $T_e = 1 \times 10^5 \text{ K}$ , respectively. The interplanetary magnetic field (IMF) has a magnitude of 7 nT with a Parker spiral angle of  $\chi = 45^\circ$ .

To model the evolution of the solar wind interaction with the comet as the comet approaches the Sun, we chose six different heliocentric distances ranging from when Rosetta arrived at the comet at around  $R = 3.6 \text{ au}$ , to  $R = 2.0 \text{ au}$ . Six cases are summarized in Tables 1 and 2, that can be compared with similar cases modeled by Hansen et al. (2007).

## 3. Results

The evolution of the angle between the proton flow direction and the comet-sun line is given in Fig. 3 (top panel) for both the model and the observations. We assume the upstream solar wind is flowing radially from the Sun, and the presented proton deflection angle is then the deflection relative to this assumed initial radial flow.

Broiles et al. (2015) and Behar et al. (2016) previously reported a significant deflection of the solar wind for precise cases, and we now consider a much larger time scale. The observed deflection increases smoothly with decreasing heliocentric distances, reaching a median daily value in the range of  $30$  to  $90^\circ$ . The model displays the same trend, with a non-linear increase reaching a value of  $40^\circ$ .

One would expect the first observed deflection values in the time series to be very close to  $0^\circ$ , since the mass-loading at the time is extremely light. This is seen in the model results, but

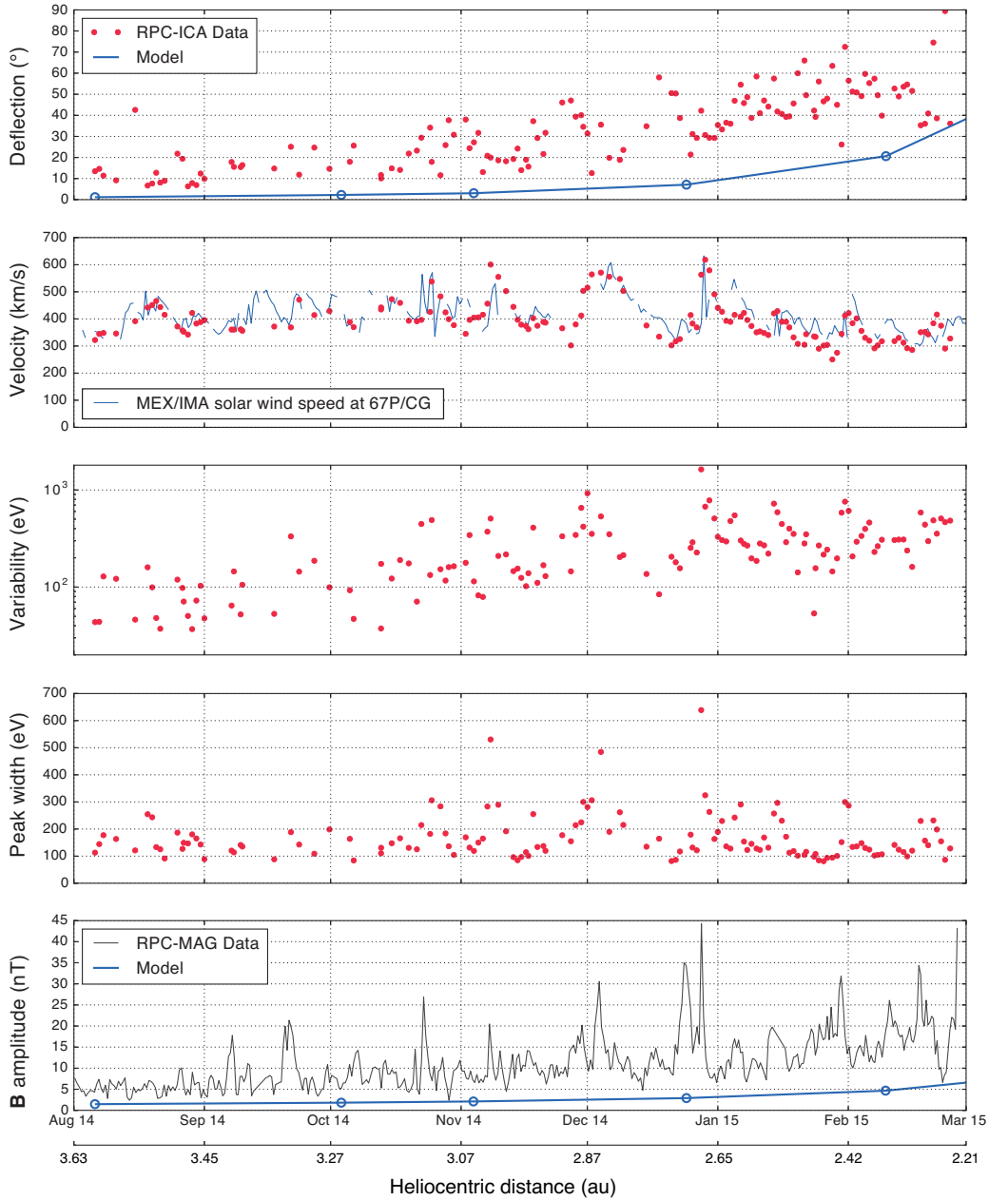


**Fig. 3.** Time series for: deflection angle (*first panel*), speed (*second panel*), energy distribution width (*third panel*), peak centre variability (*fourth panel*) and magnetic field amplitude (*last panel*). RPC-ICA data are given by red dots – every dot is a daily median. Peak width and peak central value are given by the fit parameters. RPC-MAG magnetic field amplitude is averaged over 10 h. Blue lines are either results from the hybrid model (*first and last panels*) or results from the MEX solar wind speed propagation (*second panel from top*).

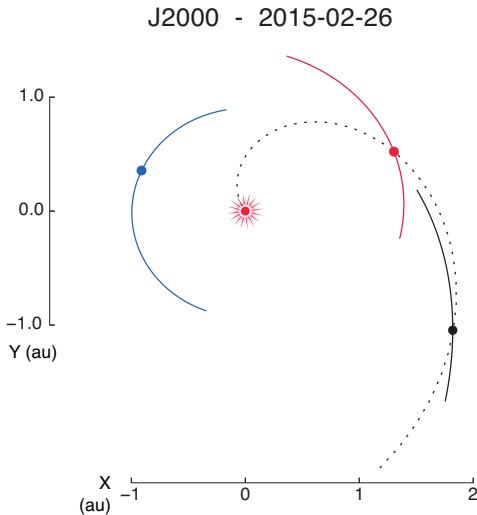


**Fig. 4.** Position of Earth (blue), Mars (red), and 67P (black) in J2000 coordinate system during 2015-02-26, with part of their orbits. The Parker spiral intersecting Mars for that day is also intersecting 67P (dotted).

the deflection is larger in the observations. A closer look at the observed data reveals that the Sun, as seen in the instrument field of view, was just a few degrees away from the spacecraft body. This partial obstruction of the solar wind flow and the way the instrument software handles it (onboard computation) should have a significant influence on the computed deflection, until around mid-September 2014.

By comparing panels 1 and 2 of Fig. 3, one can see that the variability in deflection is anti-correlated with the measured proton velocity.

To estimate the upstream solar wind speed at 67P, we used solar wind speed measured by the Ion Mass Analyzer (IMA), which is one of the sensors in the ASPERA-3 instrument package (Barabash et al. 2006) onboard Mars Express. IMA is an ion spectrometer almost identical to RPC-ICA. We propagated the speed from Mars to 67P, with the assumption that solar wind conditions are identical along a Parker spiral, and remain unchanged over time. We calculate the delay for the Parker spiral to get from one body to the other. Thus delays can be positive as well as negative.

Over the period of the study, the propagation delay started at a high value of 12 days, meaning that what is measured at Mars at one time will be a good estimation at 67P 12 days later. This delay becomes shorter than 4 days after December, to end up at values around 0: the Parker spiral intersects both bodies simultaneously, as shown in Fig. 4. In other words, this propagated speed should be more reliable when getting closer to the end of the period.

The propagated solar wind speed is shown as a blue line in the second panel from the top in Fig. 3. Propagating large variations in the speed results in large time periods not being covered (gaps in the blue line): the propagation delay is a function of the solar wind speed, and two different events measured at Mars

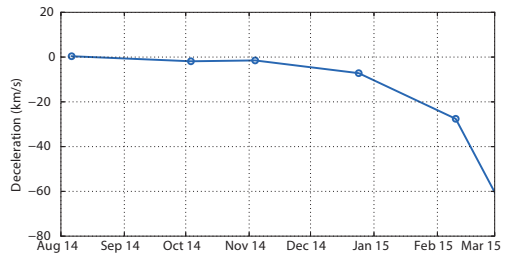


**Fig. 5.** Deceleration seen in the model between a point upstream and the nucleus. The maximum deceleration is  $60 \text{ km s}^{-1}$  at 2.2 au.

at two different times can arrive at the same time at the comet, or even in the opposite order of occurrence.

We get a very good agreement between the estimated upstream speed and the speed measured inside the coma. RPC-ICA data time coverage gets better with time during this period. Thus after January, we have better statistics, and more reliable solar wind upstream speed (as pointed out above). The average deceleration after January is about  $-40 \text{ km s}^{-1}$  from estimated upstream speed to the point of measurement, but no clear trend can be discerned. The uncertainty on this deceleration estimation is rather large, extremely difficult to quantify, and does not allow us to judge whether or not deceleration is systematically observed during the later period. Some features measured at Mars and propagated to the comet are in fact not observed at the comet. Even though the expected delay taken into account when propagating the observations from Mars to the comet is small during the second half of the time period, the absolute distance between the two bodies is never less than 1.7 au. We make the assumption that solar wind conditions are identical along a Parker spiral, but it is obvious that the larger the distance between the two bodies, the worse this assumption gets.

The hybrid model shows a constant deceleration over the period, with a maximum deceleration of  $60 \text{ km s}^{-1}$  at 2.2 au (cf. Fig. 5). This is consistent with the range estimated from the data for the deceleration.

It appears that with decreasing heliocentric distances, the variability of the proton speed (or energy) at the 192 s resolution increases, as seen in the 4th panel of Fig. 3. The variability is given as the difference between the 5th and 95th centiles of the proton peak central values (in energy) observed during one day. At the beginning of our period of study, this variability is about 50 to 100 eV (100 to  $140 \text{ km s}^{-1}$ ). It reaches values of several hundreds to a thousand electron-volts at the end of this period. By comparing panels 2 and 4 of Fig. 3 one can see that the variability of the proton speed in the coma correlates with the upstream proton speed.

The FWHM of the fitted proton spectra, (Fig. 3, 3rd panel) doesn't appear to correlate with heliocentric distance, but correlates with the upstream proton velocity.

In the last panel of Fig. 3, the magnetic field amplitude increases with time and decreasing heliocentric distance, from  $5 \text{ nT} \pm 2 \text{ nT}$  to around  $20 \text{ nT}$ . The peaks in the magnetic field amplitude correlate well with peaks in the proton speed. The model (solid blue line in the same panel) also results in a similar relative increase, from 1.5 to 6.6 nT, though the magnetic field magnitude is lower. The model shows a less dramatic increase compared to the observations.



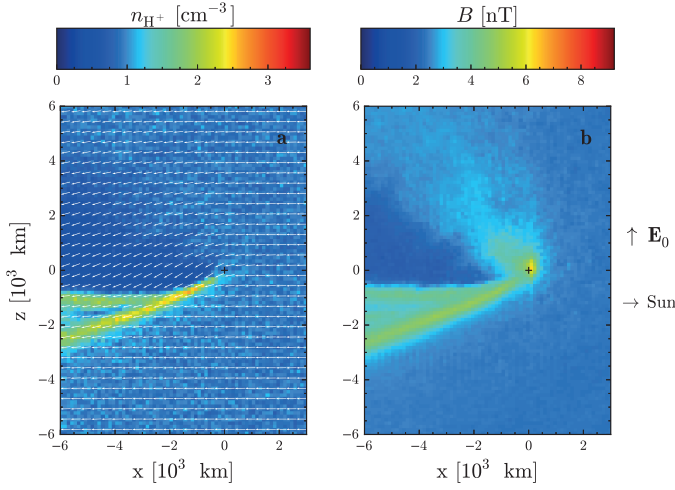


**Fig. 6.** Number density of solar wind protons together with their bulk velocity as a vector field **a**), and the magnetic field magnitude **b**). Cuts through  $y = 0$  for the comet at 2.35 au, case five. The ambient solar wind number density is  $0.9 \text{ cm}^{-3}$ , and the ambient magnetic field is  $2.3 \text{ nT}$  with a Parker spiral angle of  $67^\circ$ . The location of the comet is marked by black cross-hairs.

Finally, the morphology of the interaction when the comet was at 2.35 au can be seen in the hybrid model results in Fig. 6.

#### 4. Discussion

The solar wind observed inside the coma, close to the nucleus, is a good tracer of the interaction between the solar wind and the coma. The spacecraft altitude did not change significantly during the investigated time period; the spacecraft spent 90% of the time below 100 km in altitude. Thus the variations we observe are to a large extent temporal, and not spatial, and the evolution of the proton flow parameters directly reflects the time evolution of the plasma environment. We expect the solar wind to be deflected and slowed down. Both the deflection and the deceleration should increase with increasing comet activity, or a decreasing heliocentric distance. Significant and increasing deflection is observed during the whole period of study, and data from the later part is consistent with deceleration, but we cannot observe a clear trend in this deceleration.

##### Coma evolution

All of the aspects of the protons we have been studying over this period present detectable changes that can be correlated with either the heliocentric distance or the upstream solar wind velocity. The decreasing heliocentric distance gives the main trend in the evolution of the deflection, the magnetic field amplitude, the energy variability and, in the model, the deceleration. The variability around this main trend seems to be associated with the upstream proton velocity: the proton peak width together with the proton energy variability present the best correlation with the upstream speed, but an anti-correlation with deflection is also seen for intermediate heliocentric distances. The main peaks in the measured magnetic field amplitude are also aligned with peaks in upstream velocity.

With the resolution we get after data analysis, no physical aspect other than the heliocentric distance and the upstream solar wind speed is needed to describe the evolution of the deflection and the energy distribution of the solar wind protons.

##### A near-orthogonal force on the protons

Even though we noted that the degree of deceleration of the protons was difficult to assess from our data, we can clearly state that the protons are largely deflected, but not significantly slowed down. Thus the force applied on the observed protons must be near-orthogonal to their velocity, all along their trajectory to the instrument. The observed protons have not lost a significant amount of energy.

##### An unbalanced Lorentz force

During the investigated time period from August 2014 to March 2015, the magnetic field amplitude  $|B|$  measured at the spacecraft increased to average values of approximately 20 nT. We therefore have an augmentation of  $|B|$  following the comet activity escalation, but also an augmentation of  $|B|$  along a proton trajectory, from upstream of the coma to the measurement point. In the undisturbed solar wind, the magnetic force  $q\mathbf{v}_{H^+} \times \mathbf{B}$  and the electric force  $q\mathbf{E}$  are cancelling each other, the Lorentz force  $\mathbf{F} = q(\mathbf{E} + \mathbf{v}_{H^+} \times \mathbf{B})$  is balanced and null.

It is of great interest to put this increase of  $|B|$  in opposition with the rather small deceleration of the solar wind. Without an opportune new configuration of the local electric field in both amplitude and direction, the Lorentz force applied on the protons is not equal to zero anymore. The solar wind protons are perturbed by this increase in  $|B|$  along their trajectory. A significant part of their motion can now be seen as gyrating rather than a true bulk drift. The fact that the magnetic field is enhanced without a corresponding deceleration of the protons indicates that the protons are no longer coupled to the magnetic field, or a significant part of their energy is now in a gyromotion, with a reduced bulk drift.

##### Transfer of momentum and energy – the larger picture

We observe a force applied on the solar wind protons in the coma, a force mainly orthogonal to their bulk velocity. This force is therefore efficient in changing their momentum, but acts less efficiently on their energy, that is, their speed. Both momentum

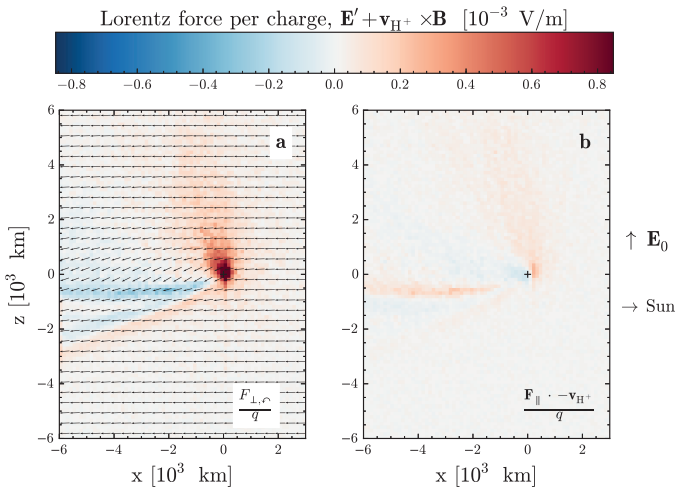


**Fig. 7.** Lorentz force per charge acting on the bulk of the solar wind protons of a cut through  $y = 0$  for the comet at 2.35 au, case 5. The solar wind proton bulk velocity is given as a vector field **a**). The force acting perpendicular to the solar wind bulk velocity,  $\mathbf{v}_{H^+}$ , deflects the solar wind protons **a**), where a positive value is taken as counter-clockwise gyration by convention. The force parallel to the solar wind bulk velocity changes the solar wind speed **b**), where a positive value results in a deceleration. The ambient convective electric field is 0.85 V/km. The location of the comet nucleus is marked by black cross-hairs.

and energy are transferred to the water ions through electromagnetic fields. Haerendel (1982) and Brenning et al. (1991) for example, in the context of barium releases, depict a momentum transfer along Alfvén waves propagating from the cloud (artificial coma).

So the previous observation raises the question about the actual shape of the regions where energy and momentum exchange takes place. In particular, these regions are not necessarily identical.

Since we only have a one-point measurement to assess the situation, we must turn to the modeled interaction to see the larger picture.

In the hybrid model, we can separate the Lorentz force,  $\mathbf{F} = q(\mathbf{E}' + \mathbf{v}_{H^+} \times \mathbf{B})$  into two components: the force acting parallel to the solar wind proton bulk flow,  $\mathbf{F}_{\parallel} = \hat{\mathbf{v}}_{H^+} (\mathbf{F} \cdot \hat{\mathbf{v}}_{H^+})$ , and the force acting perpendicular to the flow,  $\mathbf{F}_{\perp} = \mathbf{F} - \mathbf{F}_{\parallel}$ . The perpendicular component acts to make the bulk of the solar wind deflect, while the parallel component acts to change the solar wind speed.

Hybrid model results for the comet located at 2.35 au, case 5, show that the Lorentz force,  $\mathbf{F}$ , is primarily making the bulk of the solar wind protons gyrate and thus deflect towards the direction opposite of the convective electric field ( $-\hat{\mathbf{z}}$ ). The perpendicular force,  $\mathbf{F}_{\perp}$ , deflects the protons in a counter-clockwise manner in the  $xz$  plane, seen in Fig. 7a, where the bulk velocity of the solar wind protons are given as a vector field.

The parallel force,  $\mathbf{F}_{\parallel}$ , which is slowing the solar wind down, is much weaker (see Fig. 7b, where a positive value corresponds to deceleration). This is in agreement with the in-situ observations.

The regions of deflection (perpendicular force) and deceleration (parallel force) are of comparable sizes and shape, but with different strengths. It is interesting to note that the gyroradius of a pick up ion in the undisturbed solar wind is  $3 \times 10^3$  km, which is much larger than the interaction region of about  $10^3$  km. The interaction region leading to deflection and deceleration of the solar wind protons corresponds to the region where the newly ionized water is accelerating along the convective electric field,  $\mathbf{E}_0$ .

## 5. Conclusion

As the heliocentric distance decreases from 3.6 to 2.2 au, the observed solar wind is increasingly deflected, up to  $90^\circ$ . The modeled interaction results in the same evolution of the deflection angle, with a lower maximum value than observed.

In contrast with this strong deflection, the observed solar wind is not significantly slowed down, with an estimated deceleration of  $40 \text{ km s}^{-1}$  at heliocentric distances between 2.65 and 2.2 au. The modeled deceleration is consistent with the observations.

The strong proton deflection is the most obvious signature of mass-loading at a small comet, while little deceleration is observed. This may also have important implications for other objects where the interaction region is small compared to the gyro radii of pick up ions. The interplanetary magnetic field at the orbit of Pluto is very small and the pick up ion gyro radius correspondingly large, in the order of 1 million km. If there is significant mass-loading of the solar wind due to an extended atmosphere upstream of the bow shock at Pluto, this interaction is likely similar to that of a small scale comet. The New Horizons spacecraft observed very little deceleration of the solar wind at its flyby of Pluto (Bagenal et al. 2016; McComas et al. 2016), while no clear data on solar wind deflection has been published. McComas et al. (2016) reported a clear pressure-related plasma boundary forming between the ionosphere and the solar wind at Pluto, so in this respect Pluto behaves similarly to other unmagnetised planets such as Mars and Venus.

As contrast to the single-point limitation of the measurements, the model enables us to describe the complete picture of the interaction. In the model, the region where energy is transferred and the region where momentum is transferred are close to identical. The force acting on the solar wind protons has a main component orthogonal to their bulk velocity. This confirms and completes the picture we get from the observations, in which solar wind protons are seen as almost gyrating.

The region where momentum and energy are transferred from the solar wind to the coma is centered on the nucleus, with a dimension in the order of  $10^3$  km. But this localized interaction

has significant effects on the downstream solar wind flow over much larger spatial scales. The solar wind is in fact seen piling up in the  $(-z, -x)$  quadrant, a region where neither momentum nor energy are significantly transferred. This happens where the deflected solar wind intersects the nearly undisturbed solar wind.

**Acknowledgements.** This research was conducted using resources provided by the Swedish National Infrastructure for Computing (SNIC) at the High Performance Computing Center North (HPC2N), Umeå University, Sweden. The software used in this work was in part developed by the DOE NNSA-ASC OASCR Flash Center at the University of Chicago. The hybrid solver is part of the openly available FLASH code and can be downloaded from <http://flash.uchicago.edu/>. The simulation results are available from the corresponding author on request. This work was supported by the Swedish National Space Board (SNSB) through grants 108/12, 112/13, 96/15 and 94/11. We acknowledge the staff of CDDP and IC for the use of AMDA and the RPC Quicklook database (provided by a collaboration between the Centre de Données de la Physique des Plasmas (CDPP) supported by CNRS, CNES, Observatoire de Paris and Université Paul Sabatier, Toulouse and Imperial College London, supported by the UK Science and Technology Facilities Council). We are indebted to the whole Rosetta mission team, Science Ground Segment and Rosetta Mission Operation Control for their hard work making this mission possible.

## References

- Bagdonat, T., & Motschmann, U. 2002, *J. Comput. Phys.*, **183**
- Bagenal, F., Horányi, M., McComas, D. J., et al. 2016, *Science*, **351**, 9045
- Barabash, S., Lundin, R., Andersson, H., et al. 2006, *Space Sci. Rev.*, **126**, 113
- Behar, E., Nilsson, H., Stenberg Wieser, G., et al. 2016, *Geophys. Res. Lett.*, **43**, 1411
- Brenning, N., Kelley, M. C., Providakes, J., Stenbaek-Nielsen, H. C., & Swenson, C. 1991, *J. Geophys. Res.: Space Phys.*, **96**, 9735
- Broiles, T. W., Burch, J. L., Clark, G., et al. 2015, *A&A*, **583**, A21
- Coates, A., Burch, J., Goldstein, R., et al. 2015, *J. Phys.: Conf. Ser.*, **642**, 012005
- Cravens, T. 2004, *Physics of Solar System Plasmas*, Cambridge Atmospheric and Space Science Series (Cambridge)
- Crovisier, J. 1989, *A&A*, **213**, 459
- Edberg, N. J. T., Eriksson, A. I., Odelstad, E., et al. 2015, *Geophys. Res. Lett.*, **42**, 4263
- Glassmeier, K.-H., Boehnhardt, H., Koschny, D., Kührt, E., & Richter, I. 2007a, *Space Sci. Rev.*, **128**, 1
- Glassmeier, K.-H., Richter, I., Diedrich, A., et al. 2007b, *Space Sci. Rev.*, **128**, 649
- Goldstein, R., Burch, J. L., Mokashi, P., et al. 2015, *Geophys. Res. Lett.*, **42**, 3093
- Haerendel, G. 1982, *Z. Naturforschung A*, **37**
- Hansen, K. C., Bagdonat, T., Motschmann, U., et al. 2007, *Space Sci. Rev.*, **128**, 133
- Haser, L. 1957, *Bull. Classe Sci. Académie Roy. Belgique*, **43**, 740
- Holmström, M. 2010, in *Numerical Mathematics and Advanced Applications 2009: Proc. ENUMATH 2009, the 8th European Conference on Numerical Mathematics and Advanced Applications*, Uppsala, July, eds. G. Kreiss, P. Lötstedt, A. Målqvist, & M. Neytcheva (Berlin, Heidelberg: Springer Berlin), 451
- Holmström, M. 2013, *ASP Conf. Ser.*, **474**, 202
- Koenders, C., Glassmeier, K.-H., Richter, I., Ranocha, H., & Motschmann, U. 2015, *Planet. Space Sci.*, **105**, 101
- McComas, D. J., Elliott, H. A., Weidner, S., et al. 2016, *J. Geophys. Res.: Space Phys.*, **121**, 4232
- Nilsson, H., Lundin, R., Lundin, K., et al. 2007, *Space Sci. Rev.*, **128**, 671
- Nilsson, H., Stenberg Wieser, G., Behar, E., et al. 2015a, *A&A*, **583**, A20
- Nilsson, H., Stenberg Wieser, G., Behar, E., et al. 2015b, *Science*, **347**, 0571
- Richter, I., Koenders, C., Auster, H.-U., et al. 2015, *Ann. Geophys.*, **33**, 1031
- Simon Wedlund, C., Kallio, E., Alho, M., et al. 2016, *A&A*, **587**, A154
- Szegö, K., Glassmeier, K.-H., Bingham, R., et al. 2000, *Space Sci. Rev.*, **94**, 429



C

PUBLICATION III

---





# The birth and growth of a solar wind cavity around a comet – *Rosetta* observations

E. Behar,<sup>1,2★</sup> H. Nilsson,<sup>1,2★</sup> M. Alho,<sup>3</sup> C. Goetz<sup>4</sup> and B. Tsurutani<sup>5</sup>

<sup>1</sup>Swedish Institute of Space Physics, Kiruna, SE-981 28, Sweden

<sup>2</sup>Luleå University of Technology, Department of Computer Science, Electrical and Space Engineering, Kiruna, SE-981 28, Sweden

<sup>3</sup>Aalto University, School of Electrical Engineering, Department of Electronics and Nanoengineering, PO Box 15500, FI-00076 Aalto, Finland

<sup>4</sup>Technische Universität Braunschweig, Institute for Geophysics and Extraterrestrial Physics, Mendelssohnstraße 3, D-38106 Braunschweig, Germany

<sup>5</sup>Jet Propulsion Laboratory, California Institute of Technology, 4800 Oak Grove Drive, Pasadena, CA 91109, USA

Accepted 2017 July 20. Received 2017 July 18; in original form 2017 March 28

## ABSTRACT

The Rosetta mission provided detailed observations of the growth of a cavity in the solar wind around comet 67P/Churyumov–Gerasimenko. As the comet approached the Sun, the plasma of cometary origin grew enough in density and size to present an obstacle to the solar wind. Our results demonstrate how the initial slight perturbations of the solar wind prefigure the formation of a solar wind cavity, with a particular interest placed on the discontinuity (solar wind cavity boundary) passing over the spacecraft. The slowing down and heating of the solar wind can be followed and understood in terms of single particle motion. We propose a simple geometric illustration that accounts for the observations, and shows how a cometary magnetosphere is seeded from the gradual steepening of an initially slight solar wind perturbation. A perspective is given concerning the difference between the diamagnetic cavity and the solar wind cavity.

**Key words:** acceleration of particles – plasmas – methods: data analysis – techniques: imaging spectroscopy – comets: individual: 67P/Churyumov–Gerasimenko.

## 1 INTRODUCTION

Different collisionless plasma regions do not mix easily. When two plasma components meet, structures form, such as collisionless shocks and cavities in stellar and interstellar winds (Marcowith et al. 2016). Since the early days of the space age, space missions have made possible the *in situ* study of the interaction between the solar wind and various bodies in the Solar system. Since then, our understanding of such interactions has gained in precision, with comprehensive studies conducted at planets, moons and small bodies. Comets were no exception in this large-scale investigation, with the encounter in 1985 between the International Cometary Explorer (launched as ISEE-3, see for example Smith et al. 1986) and comet 21P/Giacobini–Zinner paving the way for subsequent successful cometary missions.

From a plasma physics perspective, comets distinguish themselves from other bodies of the Solar system by three main aspects, namely the eccentricity of their orbit, the composition of their nuclei and their low gravity field. Not gravitationally bound to its source, the cometary atmosphere (coma) grows and shrinks in size and density following the comets’ remoteness from the Sun, which provides the necessary radiation for the sublimation of the various volatiles embedded in their nuclei. From a bare nucleus to a wide and tenuous

ionized atmosphere, comets present the most changeable obstacle to the solar wind. In turn, the dynamics of the supersonic solar wind around and through a coma doesn’t quite lend itself to comparison with the more familiar planetary picture. In this interaction and during most of the comets’ orbital period, the solar wind does not meet a conductive ionosphere or a conductive body: The charge carriers inducing a magnetic response to the solar wind are in fact created (ionized) *within* the solar wind, immediately transported away as pick-up ions, and constantly renewed by the ionization of the neutral coma invisible to the solar wind. Therefore, analogies with induced magnetospheres around other unmagnetized bodies are far from trivial.

One unique phenomenon arises in this interaction: the formation of a void in a plasma stream. Unlike previous missions where spacecraft passed far from their target nuclei, at heliocentric distances of around 1 au, the European *Rosetta* spacecraft has escorted the comet 67P/Churyumov–Gerasimenko (67P/CG) for two years, along an orbit arc including perihelion, and spanning over heliocentric distances between 1.2 and 4.8 au. In addition to this large heliocentric distance range, the probe remained closely bound to the nucleus, spending around 80 per cent of its active mission closer than 200 km to the body centre (60 per cent closer than 100 km). Through Rosetta plasma data, we witness the growth of a solar wind cavity, from initial disturbances of the stream to an established volume devoid of solar wind ions. Later on, as the comet magnetosphere develops, the magnetic field itself is repelled in the vicinity of the nucleus,

\* E-mail: etienne.bihar@irf.se (EB); hans.nilsson@irf.se (HN)

forming the diamagnetic cavities reported by Goetz et al. (2016) at 67P/CG, and earlier by Neubauer et al. (1986) at Comet Halley. *Rosetta* was in fact only the second spacecraft to reach and probe the diamagnetic cavity – or field-free region – together with Giotto (with the exception made of the AMPTE mission, in the context of an artificial comet, see for example Haerendel et al. 1986). In previous descriptions of the Halley-type cometary plasma environment (see for example the comprehensive review of Neugebauer 1990), the diamagnetic cavity surface is defined as the ionopause, or contact surface, and is not distinguishable from the surface of the region free of solar wind ions, referred in this work as the solar wind cavity. One of the seminal models of the interaction between the solar wind and a coma for a high activity comet close to the Sun (Biermann, Brosowski & Schmidt 1967) also describes such a single boundary, separating a region devoid of magnetic field and solar wind ions from the rest of the cometsheath (in which the shocked solar wind ions and cometary ions are mixed). In the environment of 67P/CG, the total plasma density in both types of cavities is still high, and the plasma there is almost purely composed of cometary ions, as shown by Nilsson et al. (2017). Using *Rosetta* observations, it turns out that at 67P/CG, the solar wind cavity and the diamagnetic cavity are two overlapping but well-separated regions. These differences are shown in the next sections.

In the following study, we look at the solar wind dynamics prefiguring the formation of the solar wind cavity, and depict the discontinuity slowly passing over the spacecraft. After perihelion passage, as the comet draws away from the Sun, the same discontinuity will cross the spacecraft position once more as the cavity shrinks. Contrary to other spacecraft observations obtained during fast passages through boundaries around planets, *Rosetta* remained close to the nucleus, and plasma structures evolved and moved over the spacecraft, which provide a very high time resolution picture, at the expense of spatial resolution.

The study of Behar et al. (2016a) showed that the interaction changed in character as mass loading increased, prompting the authors to limit their study to an initial regime of light mass loading. We extend our study here to also include the medium-to-heavy mass-loading regime. Light mass loading was already described in Broiles et al. (2015) and Behar et al. (2016a,b). The basic expectations for such a regime are deflection and deceleration of the solar wind, which loses the momentum and the energy gained by the new born cometary ions, themselves accelerated by the convective electric field. But the results from measurements and simulations show that deflection clearly happens, whereas deceleration is very low: The solar wind is interpreted as gyrating in a disturbed magnetic field, with little energy loss (Behar et al. 2016a). Clear deceleration was observed at 1P/Halley (Johnstone et al. 1986; Formisano et al. 1990; Neugebauer 1990), at 26P/Grigg–Skjellerup (Johnstone et al. 1993), as well as in the coma of comet 19P/Borrelly by the DeepSpace1 probe (Young et al. 2004), and deflection of the solar wind from the comet–Sun line was also reported by Formisano et al. (1990) at comet 1P/Halley, and at 26P/Grigg–Skjellerup by Johnstone et al. (1993).

This study is the first to address the regime of heavy mass loading, during which the deflection of the solar wind surpasses 90°, and when the distribution of the solar wind cannot be considered unidirectional anymore, at the point of observation.

## 2 INSTRUMENT AND METHODS

The data set used in this study was produced by the Ion Composition Analyzer (ICA), a positive ion spectrometer part of the *Rosetta*

Plasma Consortium (RPC). RPC-ICA (Nilsson et al. 2007) measures three-dimensional distribution functions of positive ions in the plasma environment of 67P/CG during the entire *Rosetta* active mission. The instrument detects particles with energy ranging from 10 eV to 40 keV, with a field of view 90° × 360°. A complete angular scan is produced in 192 s, with an angular resolution of 5° × 22.5°. The instrument mass resolution enables one to distinguish solar wind protons and solar wind alpha particles from each other, and from the rest of the detected particles. Because of technical issues, together with various unsuitable instrument modes that ran during the mission, this study doesn't have a complete time coverage of the 787 d of mission.

The solar wind ions were manually selected through the whole set at a daily level, using (energy, mass) selection windows. We refer to Behar et al. (2016a), where the exact same method is used and illustrated in details. After isolating the two groups of solar wind ions, namely protons H<sup>+</sup> and alpha particles He<sup>++</sup>, plasma moments are computed by integrating the measured distributions. Velocity appears in the moment of the order of unity, the density flux, and is expressed as

$$\bar{v}(\mathbf{r}) = \frac{1}{n(\mathbf{r})} \int_{\mathbf{v}} \mathbf{v}(\mathbf{r}) f(\mathbf{v}) d^3v \quad (1)$$

with  $\mathbf{r}$  is the physical position (i.e. the spacecraft position) and  $\mathbf{v}$  is the position in velocity space.  $\bar{v}(\mathbf{r})$  is no more no less than the centre of mass of the same distribution. We refer to  $\bar{v}$  as bulk velocity.

We compute a second value,  $|\bar{v}|$ , which directly corresponds to the mean energy of the particles, independent of the direction of their velocity.  $|\bar{v}|$  is defined as

$$|\bar{v}|(\mathbf{r}) = \frac{1}{n(\mathbf{r})} \int_{\mathbf{v}} |\mathbf{v}(\mathbf{r})| f(\mathbf{v}) d^3v \quad (2)$$

The deflection angle from the Sun–comet line (usually simply referred to as deflection) is the angle between the bulk velocity and the antisunward direction. It is therefore within [0°, 180°].

In Fig. 1, this deflection is given in the two first panels, for solar wind protons and alpha particles. Results are displayed using the following method. Daily time series of proton deflection angles are computed, each value corresponding to a 192 s integration time (full field-of-view scan). These daily time series are then transformed into histograms of an arbitrary number of bins. One such histogram is given as a vertical set of circles in Fig. 1: The horizontal position is the date of this histogram, the vertical position is the value of the bin, i.e. deflection angle, and the radius of the circle gives the number of occurrences for that bin. Occurrences are normalized: the daily sum of occurrences is 1.0.

Two different proton speeds are given in the third panel from top, namely the norm of the bulk velocity  $|\bar{v}|$  and the mean speed  $\bar{v}$ . Each data point corresponds to a daily mean value. The accumulated integration time differs from one data point to the next, due to technical constraints.

The bottom panel gives heliocentric and cometocentric distances. For each full field-of-view scan, the integrated number of counts is compared to the count background level (for an equal integration time and an equal micro channel plate detector area), as a ratio. This signal-to-noise ratio is used to filter all calculated moments, before computing histograms and mean values. A threshold of 10 was used here.

Two periods are indicated with grey background. The first one, early in the mission, corresponds to a time when the Sun was obstructed by the spacecraft from the RPC-ICA field of view. This obstruction, together with the way it was dealt with on-board,



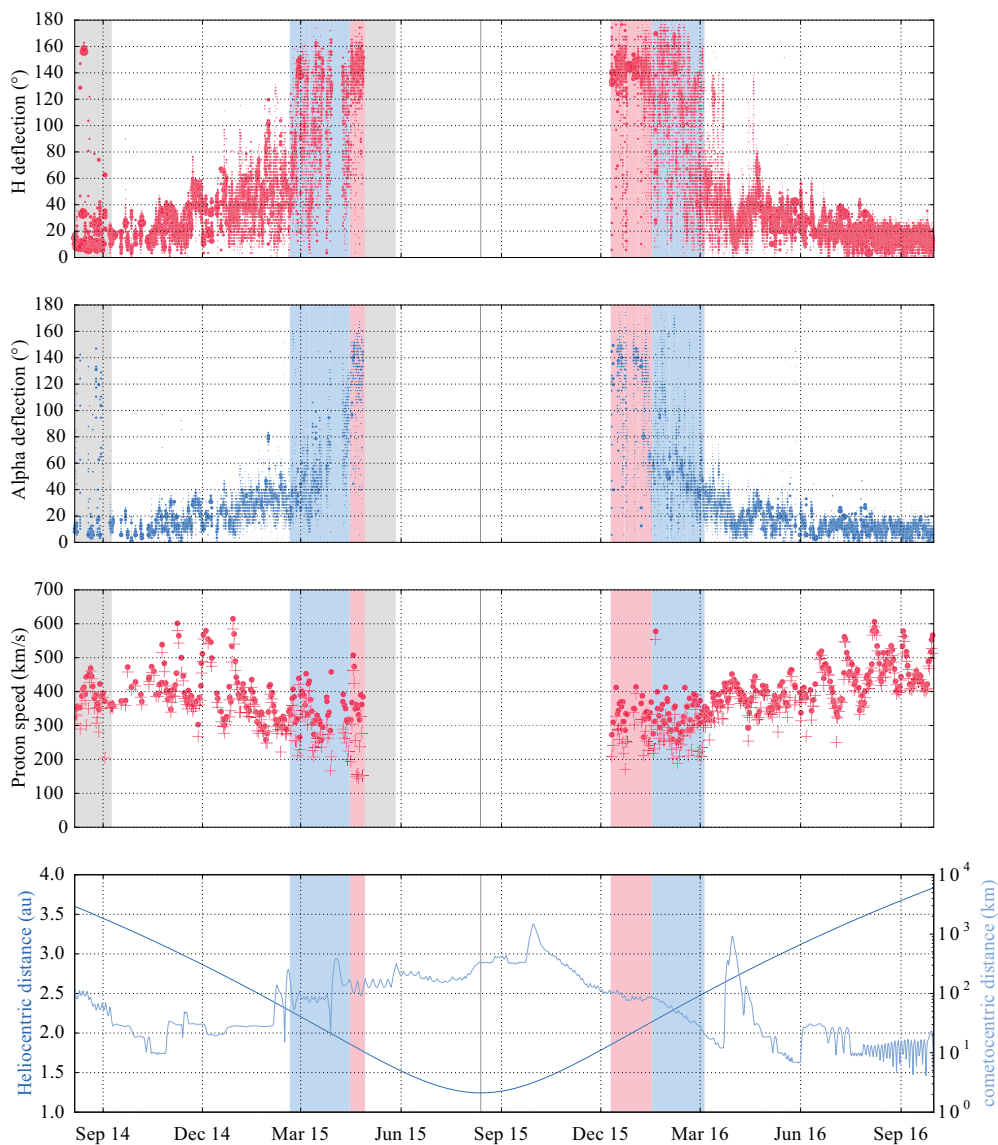


**Figure 1.** Proton and alpha particle bulk properties through the complete active mission.

results in poor quality moments, as seen in the figure. During the second period, because of technical issues, no data were produced.

Integrated ion velocity distributions are given in Fig. 2. The integration time was chosen to be 160 min (50 full-field-of-view scans) for each distribution, at the exception of the 6th of August 2014, first day of the active mission (21 scans available only). The

distributions are rotated from the instrument reference frame in which they are measured, to a right-handed frame with the  $x$ -axis pointing to the Sun and the  $z$ -axis direction given by the projection of the proton bulk velocity within the  $(y, z)$ -plane. With the assumption that solar wind proton flow remains in a plane while being deflected (assumption corresponding to the light mass-loading

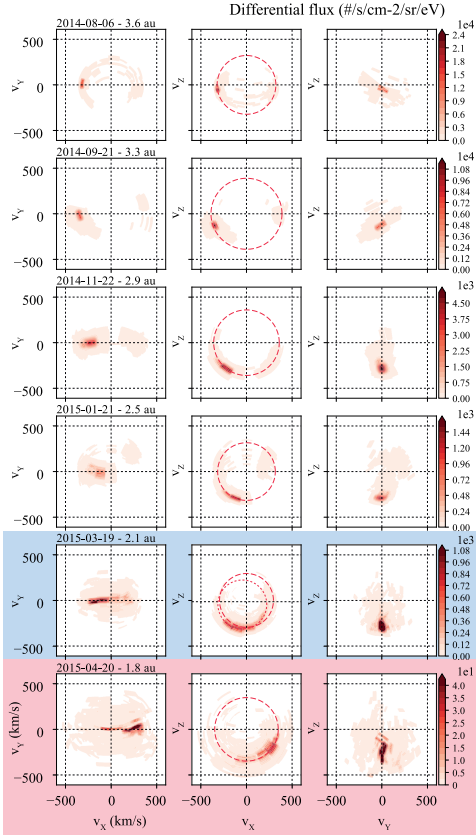


**Figure 2.** Velocity distributions of solar wind protons during the in-bound leg.

case; Behar et al. 2016b), this frame of reference is an estimation of the Comet–Sun–Electric field frame (CSE). The CSE frame has its  $x$ -axis pointing to the Sun, its  $z$ -axis along the upstream E-field and the upstream B-field lying in the  $(x, y)$ -plane. A similar frame is also used at other bodies, e.g. the Mars–Sun–Electric field frame of reference.

In Fig. 2, a red dashed circle of constant speed is given for each distribution in the  $(v_x, v_z)$  plane. The relevance of this plane is explained in the next section, and the radius of the circle corresponds to the mean energy of the observed protons. This mean energy is taken as the weighted mean of the integrated proton spectrum, and translated into a speed to be displayed in the velocity space.

### 3 RESULTS

The deflection of the solar wind was the first noticeable signature of its interaction with the tenuous ionized coma as activity was slowly increasing (cf. Broiles et al. 2015; Behar et al. 2016b). The flow

remained fairly mono-directional for heliocentric distances greater than 2.75 au (Behar et al. 2016a).

In Fig. 1, the spread of this observed deflection is seen to increase later on, closer to the Sun, with a maximum spread reached at distances between 1.9 and 2.5 au. During this period, highlighted in blue in the same figure, deflection spans from  $0^\circ$  to  $180^\circ$ . Note that data are given as daily histograms of plasma moments. Thus, a spread of  $180^\circ$  in one of the displayed histograms is not an indication of a broad shape of the local distribution function, but an indication of an extremely variable distribution, as observed by RPC-ICA. This variability is discussed later in Section 4.

During the two periods highlighted with light red background, at distances between 1.64 and 2.14 au, the flow deflection focuses again at  $\sim 140^\circ$ . During the entire mission, the Sun and the nucleus have been static in the instrument field of view the vast majority of the time, staying in their respective pixel. Therefore, during this refocusing of the deflection, a lack of low deflection values can most likely not be explained as an instrumental effect: we in fact observe a less variable distribution closer to the Sun.

In-between these two periods, from 2015 April 28 (1.76 au), the solar wind is not detected anymore by RPC-ICA, and reappears after perihelion at 1.64 au on 2015 December 11. We remind the reader that no data are available from 2015 28 April to 13 May. Protons have been observed during very few events in this time period. These detections are not included in the present results, mostly because of the very low statistics, but such events exist and further case studies should be conducted. One example is given by Edberg et al. (2016), in which authors present a case of a CME hitting the coma, pushing the surface of the solar wind cavity far enough for RPC-ICA to detect protons for a few hours. The spacecraft was then on the way back from a day-side excursion, 800 km away from the nucleus. We also note that alpha particles  $\text{He}^{++}$  are not observed on the same period (see also Nilsson et al. 2017), which is why we refer to the discussed cavity simply as the solar wind cavity.

The alpha particle deflection in the second panel shows a similar behaviour, with noticeably less spread. The value of the deflection is also systematically lower, with the exception of the two red highlighted areas where, just as for protons, alpha particle deflection shows a maximum around the same value,  $\sim 140^\circ$ .

In-between the two red periods, the spacecraft is not in the solar wind anymore, a solar wind cavity has been created around the nucleus. The most important observation presented in this study might be the following: close to the surface of this cavity, in the terminator plane, the solar wind is flowing almost sunward.

The second main expectation for mass loading is the deceleration of the solar wind, which to first order loses the energy gained by the new born cometary ions, in the comet reference frame. Behar et al. (2016a) reported small deceleration during the regime of light mass loading, with a maximum difference with the estimated upstream speed of  $40 \text{ km s}^{-1}$ . Because of the lack of direct upstream solar wind parameter measurements, solar wind moments measured at Mars were propagated to 67P/CG, which at that time was lying almost on the same Parker spiral as Mars. Therefore, the uncertainty of this deceleration is rather large and hardly quantifiable. Here, the period of interest spans over more than two years, thus this technique for upstream speed estimation is not applicable.

However, the ion velocity distribution functions can provide some information about deceleration. The choice of frame is motivated by the plasma dynamics described in Behar et al. (2016b), where data show that in the CSE frame and at low activity, neither the solar wind protons nor the cometary ion flow have a  $v_y$ -component. When actively rotating the distribution to cancel this  $v_y$ -component for

each measurement (each full field of view), the resulting integrated distribution functions remain very well focused. In Fig. 2, the four first rows correspond to the light-to-medium mass-loading regime, with deflection of the solar wind rising from  $0^\circ$  to  $90^\circ$ . In these distributions, the integrated solar wind signal is perfectly focused, a clear peak is observed. The last two distributions, highlighted with a blue and a red background, respectively, were chosen to illustrate the previously mentioned blue and red periods in Fig. 1. In these two cases, a spread of the distribution is observed along the  $v_x$ - and  $v_z$ -axis, the distributions remaining very focused along the  $v_y$ -axis. In the distribution highlighted with the blue background, a clear partial ring distribution is observed in this plane, and is discussed in the next section.

One thing is important to stress concerning these distributions. Resulting from an integration time of maximum 160 min, and with a total number of six, they are not meant to be representative of the complete solar wind dynamics and its details. In other words they don't give the whole story, these distributions are chosen to highlight one of the main and simple aspects of these flow dynamics and their evolution with heliocentric distance. And this aspect – the solar wind gyrating in the inner coma – is believed to correspond to the most simple configuration of this interaction.

## 4 DISCUSSION

### 4.1 Time variability of the measurements

The data show large time variability in the deflection of the solar wind, at the 192 s integration time-scale, and especially during the blue highlighted period. In other words, during this period, the direction of the solar wind and its density can change drastically from one scan to another. Fundamentally, only two cases are to be considered: first, the plasma dynamics are not in steady state at this time-scale (around 3 min) and are very turbulent, and secondly, the system used for the measurements (the instrument together with the spacecraft) is introducing time dependent effects convolved with the physical signal to be measured. Of course, both cases could be at work at the same time.

A few obvious illustrations for the time variability of the observed system can be listed. In Behar et al. (2016b), we see for example, how the inter-planetary magnetic field can change drastically its direction in less than a minute, and how such changes greatly affect the solar wind direction within the coma. This result indicates that at low activity, the plasma environment around the nucleus is asymmetric, and as the upstream magnetic field changes direction, the spacecraft itself will probe a different region of this asymmetric environment. In such a case, we learn that the system is highly sensitive to upstream conditions.

Another possibility for such a variable solar wind is the intrinsic instability of the interaction. It might be that even for steady upstream conditions, the system itself results in the solar wind never reaching steady state inside the coma. The particle-wave interactions, not taken into account in this work, could not be ignored for a dedicated study of the short time-scale variability of the particle dynamics. Large amplitude, low frequency magnetic waves were detected at 67P/CG, with a period of around 25 s (Richter et al. 2015), as well as at previously visited comets (Brinca & Tsurutani 1989; Tsurutani, Glassmeier & Neubauer 1995).

Finally, the structure of the coma and its time variation are obviously to be taken into account. Anisotropic outgassing was observed far from the Sun (more than 3 au heliocentric distance, cf. Biver et al. 2015; Lee et al. 2015) and closer (1.9 au; Migliorini

et al. 2016), and a heterogeneous plasma environment is observed in hybrid simulations of the coma-solar wind interaction (Koenders et al. 2015).

In contrast, not many effects or limitations of the system of measurement can be listed. In fact, the only one which was diagnosed is the limitations of the field of view of the instrument. With a partial coverage of the (azimuth, elevation) space of ( $360^\circ \times 90^\circ$ ) and a significant portion of this field of view being obstructed by the spacecraft body and solar arrays, distributions will be necessarily only partially observed, or even completely missed, at times. One could argue that this effect could and should be taken into consideration in the analysis, by identifying manually or systematically this type of observations, to then discard them. This could be in fact done for low activity when the deflection and the size of the velocity distribution are still small. But as soon as the distribution functions become much larger and more complex, one simply cannot say whether or not the solar wind signal is completely in the instrument field of view. In that sense, RPC-ICA together with *Rosetta* is not the ideal system for the observation of the solar wind at higher mass loading, and this limitation is for now not possible to overcome.

On the topic of the observed variability of the solar wind parameters during its interaction with the coma, a multi-instrument study could be conducted to identify properly the physical variations as opposed to instrumental effects. For this study, the influence of the field-of-view limitations on the results is considered acceptable, with around 53 per cent of the complete  $4\pi$  sr solid angle accessible by RPC-ICA.

### 4.2 Gyrating solar wind

In Fig. 1, the third panel from top, we see that the norm of the bulk velocity is systematically smaller than the mean speed, with a difference between the two growing with activity. As introduced in Behar et al. (2016a), this can be interpreted as the solar wind gyrating in the coma. In this interpretation, little energy is lost (i.e. the mean speed is almost conserved from upstream to within the coma), whereas the bulk velocity amplitude is significantly decreased. In Fig. 2, the proton distribution through the in-bound leg remains narrow in terms of speed, as seen in the ( $v_x$ ,  $v_z$ )-plane, despite the deflection getting larger with decreasing heliocentric distances.

The fifth distribution function from top gives us a perfect view of this gyration, with a partial ring distribution in a plane orthogonal to the perpendicular component of the magnetic field. If the loss of energy is small, it should still be expected that the longer a proton interacts with the coma, the larger this loss will be, to the point of being observable by RPC-ICA in this frame. In fact in the same distribution, particles with positive  $v_x$ -component are heavily deflected, which means they have been interacting with the coma for a longer time than particles with small deflection. Instead of a perfect circle centred on the origin, we should expect a decrease of the radius of this distribution (which directly corresponds to the speed) with an increase of the deflection. Such a trend is clearly visible in this integrated distribution, as in many other distributions during the mission.

Another interpretation for this characteristic distribution shape can be given, which does not oppose the previous one. In terms of a non-resistive hybrid description, the magnetic field flux tubes are convected at a velocity equal to the electron bulk velocity. In a frame moving with this velocity, the convective electric field disappears and the solar wind particles are seen gyrating without loss of kinetic energy. At low cometary plasma densities, this electron velocity

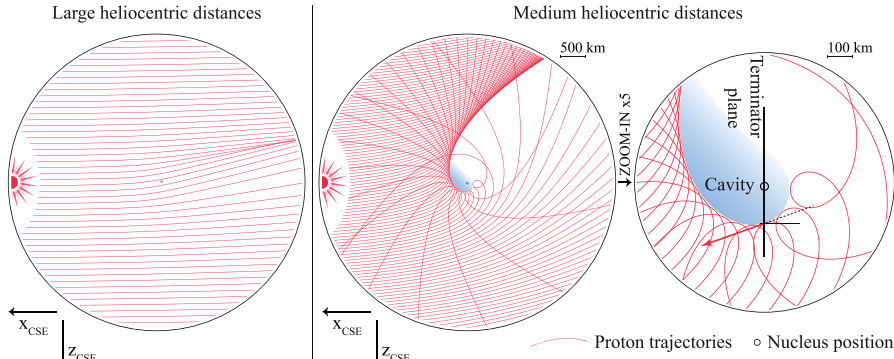


**Figure 3.** Geometric interpretation of the formation of the solar wind cavity, for the light mass-loading regime and the medium-to-heavy mass-loading regime.

will be dictated by the fast solar wind electrons, much denser than the cometary electrons. At high cometary plasma densities, i.e. for a dense coma, the opposite happens, and the electron velocity is given mostly by the relatively slow cometary electrons. Therefore, the difference between the body centred frame and the frame comoving with electrons will be small. In this precise case and with this interpretation, we would estimate the electron speed, and therefore the velocity of magnetic field convection, to be around  $50 \text{ km s}^{-1}$ , given by the centre of the second smaller circle. This offset has components both along the  $v_x$ - and the  $v_z$ -components, indicating that the magnetic field is convected not only antisunward along the comet-Sun line but also along the negative  $z$ -axis, a result also nicely highlighted by Koenders et al. (2016).

#### 4.3 A discontinuity

Through RPC-ICA data, we witness the formation of a solar wind cavity. This cavity can either have a sharp surface, which would be referred to as a discontinuity, or a not well-defined surface, in the case of a solar wind density only tending to zero with decreasing distance from the nucleus. The dynamics of the flow for both solar wind species we discuss might tell us something about this surface.

In the case of a well-defined discontinuity, on the very location of the discontinuity, the flow has to be tangential to the surface. This is a strong constraint on the distribution function: There can be no angular spread outside of the tangent plane. In addition to that, if we consider the solar wind ideally gyrating, the flow has to remain in a single plane normal to the upstream orthogonal component of the magnetic field, at least close to the ( $y_{\text{CSE}} = 0$ ) plane. These two simplistic considerations would lead to the expectation of a fairly unidirectional flow at the discontinuity, in the ( $x_{\text{CSE}}, z_{\text{CSE}}$ ) plane. In fact, the spacecraft can be considered to be very close to this plane, because of its small distance to the nucleus at any time. And we note that just before the solar wind disappearance, and just after its reappearance, the flow deflection is significantly refocused around one value, namely  $140^\circ$ . The chosen distribution highlighted in red in Fig. 2 illustrates the same phenomenon, with a refocusing of the distribution compared to the previous one highlighted in blue.

Motivated by this peculiar observation, we propose one geometrical illustration bringing these simple and ideal expectations together. We consider the same ( $x_{\text{CSE}}, z_{\text{CSE}}$ ) plane. We base this illustration on two very simple ideas: first, the solar wind is gyrating in the ionized coma, and secondly, the closer a proton gets to the nucleus, the shorter its gyroradius is (in other words, the more deflected it gets). This second point is naturally motivated by the fact that ion density, to the first order, is getting larger closer to the nucleus; and the denser the coma gets, the more the solar wind is deflected.

In Fig. 3, the Sun is on the left-hand side, the nucleus is in the middle of the schematics. Particles are flowing from the left-hand side, towards the right-hand side. As they get closer to the nucleus, they are more deflected. Every red line is one trajectory, or stream line, and the radius of curvature is a function of the distance to the centre. In this precise case, the radius of curvature is proportional to  $r^2$ . The first panel on the left-hand side gives the expectation for a low activity case, and summarizes nicely the observations made during this regime: limited deflection, antisunward and unidirectional flow. The two other panels give the same type of illustration for a higher activity case. The third panel (right-hand side) is simply a zoom-in of the central one. We see that the solutions of such a configuration can display complete loops along a trajectory, which is the major aspect of this illustration.

We find that an area in which no particle can enter appears around the nucleus: A cavity is formed. In order to give some scale to the picture, we find that with an initial speed of the particles (protons) of  $400 \text{ km s}^{-1}$  and a force deflecting the particles as  $F = 10^{-11}/r^2 \text{ N}$  (corresponding to the evolution of the radius of curvature discussed above), the extent of the cavity towards the  $+z$ -direction along the terminator line is of about 150 km, very close to the cometocentric distance at which the spacecraft was when crossing the boundary. What does the discontinuity look like on a terminator plane (i.e. at the vertical of the nucleus in this illustration, displayed with the solid black line in the lower second panel)? As pointed out above, the flow is in fact tangent to the discontinuity. But even more interesting, at the closest intersection between the terminator line and the discontinuity, this tangent flow (pictured by the red arrow in the third panel) is mostly sunward, with a deflection angle of around  $160^\circ$ .

Far from being a self-consistent model, this illustration is nothing more than an attempt to visualize the effect of one simple consideration: What does the simplified general picture look like if the solar wind gyrates in the coma, with a gyro-radius being smaller closer to the nucleus? We see that this results in an asymmetric cavity, generated by purely geometric – or kinetic – effects, and that on the terminator plane and at the discontinuity, particles are flowing with a very large deflection angle, almost sunward. Anywhere else in the flow, since different trajectories intersect at any point, the norm of the bulk velocity is smaller than the constant mean speed. Therefore, this illustration accounts for most of the main observations made previously.

In the scope of this interpretation, one observation of great interest was made at comet 26P/Grigg–Skjellerup and raised by Jones & Coates (1997). The authors reported solar wind protons deflected from the comet–Sun line, with a signal consisting of two different beams of similar energy (between 100 and 130 eV), both almost perpendicular to the B-field direction. One peak was reported coming almost from the undisturbed solar wind direction, while the other one was seen much more deflected. Despite a larger deceleration than what was observed at 67P/CG, the geometry of this observation display striking similarities with the present interpretation, in which two well-separated beams are seen in most of the area, corresponding to crossing trajectories. A thorough comparison with the observation at 26P/Grigg–Skjellerup would, however, require a greater modelling effort than presently done.

#### 4.4 The diamagnetic- and solar wind cavity surfaces separation

One of the experimental results brought by Rosetta is the marked difference between the solar wind cavity and the diamagnetic cavity, in contrast, with the classical view of the cometary plasma environment given by Biemann et al. (1967) (Fig. 1). Whereas diamagnetic cavity surface crossings have been detected at least 665 times (Goetz et al. 2016), we see that the observation of the solar wind cavity consists in one main period of solar wind void, spanning over more than seven months. From the observations, it is clear that during this period the spacecraft was most of the time outside the diamagnetic cavity but inside the solar wind cavity, with a total time spent in the diamagnetic cavity of 42h over around nine months (Goetz et al. 2016), compared to only a few proton detections during the similar period. This has a direct implication on the size of these cavities: The solar wind cavity is generally bigger than the diamagnetic cavity. The work of Goetz et al. (2016) and the data presented by Edberg et al. (2016) give both a feeling about these sizes, respectively, 400 km for the diamagnetic cavity (in the terminator plane) and 800 km for the solar wind cavity (in the day-side). These dimensions are only lower limits for cavities observed at different times and different places, close to perihelion.

Using a two-dimensional bi-ion fluid model, Sauer, Bogdanov & Baumgärtel (1994) nicely highlighted such a separation between the two boundaries. The authors named the surface of the solar wind cavity the protonopause, an ion composition boundary. On the experimental side, observations of solar wind ions presented in Johnstone et al. (1986), Ip (1989) and Fuselier et al. (1988) show strong decrease and disappearance of solar wind protons and alpha particles, as well as alpha particle deflection. However, it seems that due to the spacecraft speed and sensors' field-of-views limitations, the precise densities and the precise time of disappearance of these populations are not available for direct comparison with the detected diamagnetic cavity at 1P/Halley. Such a difference of size is

also seen in more recent simulation results from Rubin et al. (2014) (1P/Halley, fluid model) and Koenders et al. (2015) (67P/CG, hybrid model), both addressing the perihelion case. As demonstrated by Sauer et al. (1994), this configuration appears to be similar to the magnetic pile-up region at Venus, where the magnetic field is observed in the absence of solar wind ions (cf Luhmann 1986, 4.3.1).

A detailed analysis of the possible multiple crossings of the solar wind void surface (at disappearance and reappearance of the solar ions) would require a multi-instrument approach, since the detection relies greatly on the distribution of the solar wind, and therefore on the field of view of the instrument and its limitations.

## 5 CONCLUSION

As the nucleus gets closer to the Sun, the two plasma components – the solar wind and the ionized coma – tend to separate themselves. The interaction between the solar wind and the comet evolves from an asteroid-like interaction at aphelion, in which the solar wind impacts the surface of the atmosphere-less nucleus, to a Venus-like interaction at perihelion, in which both the solar wind and the diamagnetic cavities are formed. *Rosetta* allows us to characterize this evolution, and understand how and when the two cavities expand.

A very important aspect of the cavity formation appears to be the gyration of the solar wind: a macroscopic deceleration with limited energy loss, in the comet reference frame. Contrary to the classical fluid and macroscopic treatment of ionopauses, our description of the solar wind interacting with a growing coma does not involve pressure balance, but instead relies on the kinetic behaviour of the flow. We do not describe a thermalization and a deceleration of the solar wind, but instead a macroscopic deceleration together with a conservation of kinetic energy at the single particle scale.

At various scales in the universe, plasma stream cavities are to be observed (Marcowith et al. 2016). But comets might be the only natural laboratory within our reach for *in situ* study where such cavities are forming and vanishing periodically, not because of the change in the incoming flow, but because of the change in the obstacle itself.

## ACKNOWLEDGEMENTS

We wish to thank the referee for her/his detailed comments and constructive indications.

The work on RPC-ICA, as well as this PhD project, is supported by the Swedish National Space Board (SNSB) through grants 108/12, 112/13, 96/15 and 94/11.

The work on RPC-MAG was financially supported by the German Ministerium für Wirtschaft und Energie and the Deutsches Zentrum für Luft- und Raumfahrt under contract 50QP 1401.

We acknowledge the staff of CDDP and IC for the use of AMDA and the RPC Quicklook data base [provided by a collaboration between the Centre de Données de la Physique des Plasmas (CDDP) supported by CNRS, CNES, Observatoire de Paris and Université Paul Sabatier, Toulouse and Imperial College London, supported by the UK Science and Technology Facilities Council]. We are indebted to the whole *Rosetta* mission team, Science Ground Segment and Rosetta Mission Operation Control for their hard work making this mission possible.

Portions of this work was done at the Jet Propulsion Laboratory, California Institute of Technology, under contract with NASA.

The SPICE toolkit from NASA's Navigation and Ancillary Information Facility is heavily used in this study, and made accessible through PYTHON by the SpicePy wrapper.

## REFERENCES

- Behar E., Nilsson H., Stenberg Wieser G., Ramstad R., Götz C., 2016a, *A&A*, 596, 42
- Behar E., Nilsson H., Stenberg Wieser G., Nemeth Z., Broiles T. W., Richter I., 2016b, *Geophys. Res. Lett.*, 43, 1411
- Biermann L., Brosowski B., Schmidt H. U., 1967, *Solar Physics*, 1, 254
- Biver N. et al., 2015, *A&A*, 583, A3
- Brinca A. L., Tsurutani B. T., 1989, *J. Geophys. Res: Space Phys.*, 94, 5467
- Broiles T. W. et al., 2015, *A&A*, 583, A21
- Edberg N. J. T. et al., 2016, *MNRAS*, 462, S45
- Formisano V., Amata E., Cattaneo M. B., Torrente P., Johnstone A., 1990, *A&A*, 238, 401
- Fuselier S. A., Shelley E. G., Balsiger H., Geiss J., Goldstein B. E., Goldstein R., Ip W. H., 1988, *Geophys. Res. Lett.*, 15, 549
- Goetz C. et al., 2016, *MNRAS*, 462, S459
- Goetz C. et al., 2016, *A&A*, 588, A24
- Haerendel G., Paschmann G., Baumjohann W., Carlson C. W., 1986, *Nature*, 320, 720
- Ip W.-H., 1989, *ApJ*, 343, 946
- Johnstone A. et al., 1986, *Nature*, 321, 344
- Johnstone A. et al., 1993, *A&A*, 273, L1
- Jones G., Coates A., 1997, *Advances in Space Research*, 20, 271
- Koenders C., Glassmeier K.-H., Richter I., Ranocha H., Motschmann U., 2015, *Planet. Space Sci.*, 105, 101
- Koenders C., Goetz C., Richter I., Motschmann U., Glassmeier K.-H., 2016, *MNRAS*, 462, S235
- Lee S. et al., 2015, *A&A*, 583, A5
- Luhmann J. G., 1986, *Space Sci. Rev.*, 44, 241
- Marcowith A. et al., 2016, *Rep. Prog. Phys.*, 79, 046901
- Migliorini A. et al., 2016, *A&A*, 589, A45
- Neubauer F. M. et al., 1986, *Nature*, 321, 352
- Neugebauer M., 1990, *Rev. Geophys.*, 28, 231
- Nilsson H. et al., 2007, *Space Sci. Rev.*, 128, 671
- Nilsson H., Stenberg Wieser G., Behar E., Gunell H., Wieser M., 2017, *MNRAS*, 469, S252
- Richter I. et al., 2015, *Annales Geophysicae*, 33, 1031
- Rubin M. et al., 2014, *ApJ*, 781, 86
- Sauer K., Bogdanov A., Baumgärtel K., 1994, *Geophys. Res. Lett.*, 21, 2255
- Smith E. J., Tsurutani B. T., Slavin J. A., Jones D. E., Siscoe G. L., Mendis D. A., 1986, *Science*, 232, 382
- Tsurutani B. T., Glassmeier K. H., Neubauer F. M., 1995, *Geophys. Res. Lett.*, 22, 1149
- Young D. et al., 2004, *Icarus*, 167, 80

This paper has been typeset from a  $\text{\LaTeX}$  file prepared by the author.

D

PUBLICATION IV

---





# The root of a comet tail: Rosetta ion observations at comet 67P/Churyumov–Gerasimenko

E. Behar<sup>1,2</sup>, H. Nilsson<sup>1,2</sup>, P. Henri<sup>5</sup>, L. Berčič<sup>1,2</sup>, G. Nicolaou<sup>1,4</sup>, G. Stenberg Wieser<sup>1</sup>, M. Wieser<sup>1</sup>, B. Tabone<sup>7</sup>, M. Saillenfest<sup>6</sup>, and C. Goetz<sup>3</sup>

<sup>1</sup> Swedish Institute of Space Physics, Kiruna, Sweden

e-mail: [etienne.bekar@irf.se](mailto:etienne.bekar@irf.se)

<sup>2</sup> Luleå University of Technology, Department of Computer Science, Electrical and Space Engineering, Kiruna, Sweden

<sup>3</sup> Technische Universität Braunschweig Institute for Geophysics and Extraterrestrial Physics, Mendelssohnstraße 3, 38106 Braunschweig, Germany

<sup>4</sup> Mullard Space Science Laboratory, University College London, Dorking, UK

<sup>5</sup> LPC2E, CNRS, Orléans, 45071, France

<sup>6</sup> IMCCE, Observatoire de Paris, PSL Research University, CNRS, Sorbonne Université, UPMC Univ. Paris 06, LAL, Université de Lille, 75014 Paris, France

<sup>7</sup> LERMA, Observatoire de Paris, PSL Research University, CNRS, Sorbonne Université, UPMC Univ. Paris 06, 75014 Paris, France

Received 16 February 2018 / Accepted 19 April 2018

## ABSTRACT

**Context.** The first 1000 km of the ion tail of comet 67P/Churyumov–Gerasimenko were explored by the European Rosetta spacecraft, 2.7 au away from the Sun.

**Aims.** We characterised the dynamics of both the solar wind and the cometary ions on the night-side of the comet’s atmosphere.

**Methods.** We analysed in situ ion and magnetic field measurements and compared the data to a semi-analytical model.

**Results.** The cometary ions are observed flowing close to radially away from the nucleus during the entire excursion. The solar wind is deflected by its interaction with the new-born cometary ions. Two concentric regions appear, an inner region dominated by the expanding cometary ions and an outer region dominated by the solar wind particles.

**Conclusions.** The single night-side excursion operated by Rosetta revealed that the near radial flow of the cometary ions can be explained by the combined action of three different electric field components, resulting from the ion motion, the electron pressure gradients, and the magnetic field draping. The observed solar wind deflection is governed mostly by the motional electric field  $-u_{\text{ion}} \times B$ .

**Key words.** comets: general – comets: individual: 67P – plasmas – methods: observational – space vehicles: instruments

## 1. Introduction

All particles originating from a comet’s nucleus and subsequently ionised by solar radiation or electron impact eventually escape the comet, reaching on average the velocity of the solar wind. Because of the fast relative speed between the comet and the solar wind, the escaping ions are collimated into a narrow tail, known as the ion tail or gas tail. Contrary to the dust tail, this plasma structure can emit light by fluorescence, and depending on the conditions can be seen from Earth. The shape of these visible ion tails gives a major clue to the existence of both the solar wind and the interplanetary magnetic field (IMF), as for instance elaborated by [Alfvén \(1957\)](#). To that extent, the ion tail is one of the major aspects of the interaction between the solar wind and the comet’s atmosphere (coma).

During the first part of the 20th century, comets played an important role in the development of space physics. The first suggestion of the existence of a steady stream of charged particles flowing away from the Sun can be attributed to Arthur Eddington ([Durham 2006; Eddington 1910](#)), based on observations of comet Morehouse and the analysis of the shapes of the envelopes seen in the atmosphere and in the ion tail. Another model presented by [Biermann \(1951\)](#) describes the tail of comets

being dragged by a corpuscular radiation emitted by the Sun. In this description, the momentum is transferred from the wind to the tail by Coulomb collisions. During the same decade, another major model was proposed by [Alfvén \(1957\)](#) where the magnetic field of the Sun is ‘frozen’ in a similar flow of solar particles. The local addition of a cold and slow cometary ion population would correspond to a significant decrease of the total plasma velocity, and the frozen-in magnetic field piles up and drapes itself around the dense coma. This draping pattern was given as an interpretation of the typical pattern of streamers in a comet tail. Comets have acted as natural solar wind probes before the first in situ measurements and the space exploration era because of their high production rate (with values ranging from  $10^{25}$  to several  $10^{30} \text{ s}^{-1}$ ) and their very low gravity: they were the perfect tracers to make the solar wind ‘visible’ from Earth.

The first in situ investigation of the interaction between the solar wind and a coma was conducted by the International Cometary Explorer (ICE, launched as ISEE-3, see e.g. [Smith et al. 1986](#)) which encountered comet 21P/Giacobini–Zinner in September 1985. Since that date, ten other probes have visited eight different comets. ICE, Deep Space 1, and probably *Giotto* for its second encounter actually flew through the tails of their respective comets, 21P/Giacobini–Zinner, 19P/Borelli, and

26P/Grigg-Skjellerup, validating some of the theoretical results such as the draping of the IMF remarkably observed by ICE and presented in Slavín et al. (1986). Another noteworthy in situ result is the observation of the tail of comet Hyakutake (C/1996 B2) by the *Ulysses* spacecraft, 3.8 astronomical units (au) away from the comet's nucleus, reported by Jones et al. (2000). However, these few events are tail crossings; in other words, they only gave a snapshot of the tail structures along one straight line along the spacecraft trajectory. If the coverage along this line is optimum (from outside of the tail to inside to outside again), the spatial coverage along the radial dimension for instance is almost non-existent. The situation for one of the AMPTE mission experiments, the so-called artificial comet, was quite different to these fast passages, and allowed for a more thorough study of how momentum and energy were exchanged between the background incident plasma and the injected heavy ions (Valenzuela et al. 1986; Haerendel et al. 1986; Coates et al. 2015).

At the end of the 22 March 2016, as comet 67P/Churyumov–Gerasimenko (67P) was 2.64 au from the Sun and orbiting away from it, the European probe Rosetta operated the first manoeuvre that would bring it on an excursion within the previously unexplored night-side of the coma. The excursion lasted for more than 14 days, during which the spacecraft reached a maximum cometocentric distance of 1000 km, along a complex trajectory (see Fig. 1, upper panel). This was the second and last excursion operated by Rosetta; the first was a day-side exploration conducted in October 2015 during a different activity level and closer to the Sun. An overview of the ion data during the entire mission is shown in Nilsson et al. (2017), where it can also be seen how the ion data from the tail excursion stands out in relation to all the other data.

Contrasting with the otherwise low altitude terminator orbit, this tail excursion allowed the study of the root of the comet's ion tail, and specifically in our case, the study of the plasma dynamics of this region. 67P is less active than most of the previously visited or observed comets (the activity is typically quantified by the production rate of neutral elements). As pointed out by Snodgrass et al. (2017), its ion tail was actually never observed from the ground. To that extent, the interaction between the solar wind and the coma is remarkably different to what is usually described for more active comets closer to the Sun. Instead of the solar wind being deflected symmetrically around the coma and not flowing in the inner region close to the nucleus, we see a coma entirely permeated by the solar particles. By characterising the phase space distribution functions of both the cometary ions and the solar wind, we can understand how the two populations interact in this region, and to what extent this interaction takes part in the escape of cometary ions through the tail, for such a low activity comet far from the Sun. In a statistical study, Berčič et al. (2018) recently described the cometary ion dynamics at the same heliocentric distance, close to the nucleus and in the terminator plane. Two different cometary ion populations were reported, one which gained its energy mostly through its interaction with the solar wind upstream of the nucleus, and one that was accelerated in a region they dominate. That study is put into the perspective of this excursion, completing the larger picture of the interaction. Additionally, Volwerk et al. (2018) present an extensive analysis of the magnetic field observed during the same excursion. The authors found that the magnetic field was not draped around the nucleus in a classical sense; instead, the magnetic field direction was mostly aligned with the IMF direction expected from a Parker spiral model. However, the tail clearly showed a two-lobed structure with regard to the wave activity: directly behind the nucleus the so-called singing comet

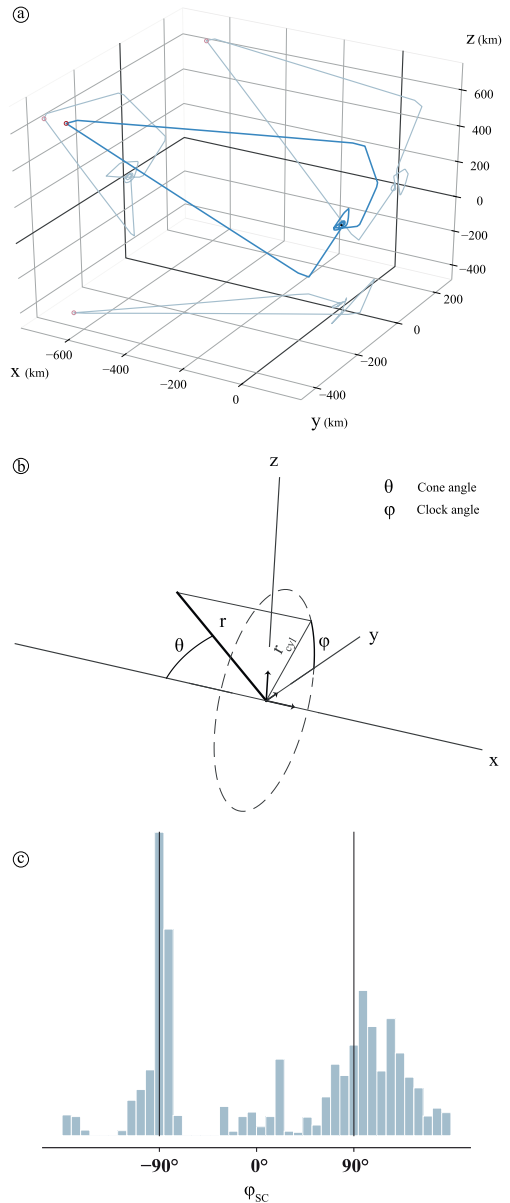


**Fig. 1.** Panel a: the trajectory of the spacecraft in the CSEQ reference frame (blue) and its projections (grey). Panel b: the cartesian and spherical sets of coordinates. Panel c: the distribution of spacecraft clock angle during the period of interest, in the CSEQ frame.

waves (Richter et al. 2015) were very prominent, whereas to the sides their contribution to the power spectral density becomes negligible.

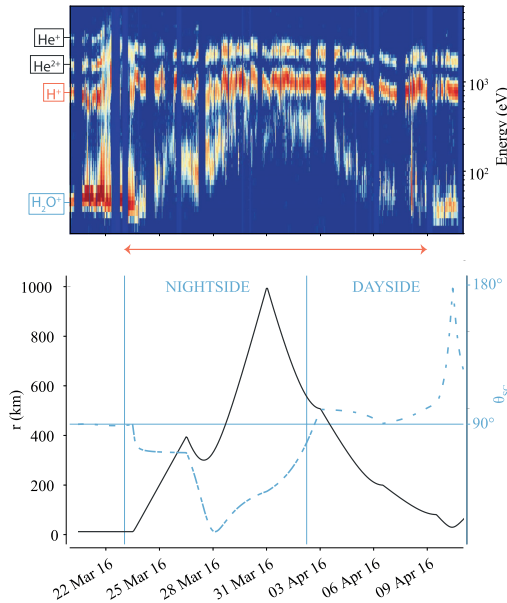


**Fig. 2.** Upper panel: spectrogram of the period, with the considered period displayed by the red arrow. Lower panel: corresponding comocentric distance  $r$  together with the cone angle  $\theta$  of the spacecraft.

## 2. Instrument and methods

### 2.1. Instrument

The particle data used in this work were produced by the Ion Composition Analyzer (ICA), part of the Rosetta Plasma Consortium (RPC; Nilsson et al. 2007; Carr et al. 2007). This instrument is an ion mass-energy spectrometer and imager, aimed at studying the interaction between the solar wind and positive cometary ions at comet 67P. The RPC-ICA data consist of count rates given in five dimensions, namely time, energy per charge, mass per charge, and incoming direction (two angles). Full energy scans are produced every 12 s and full angular scans (corresponding to the full velocity space coverage of the instrument) are produced every 192 s. The energy spans from a few electronvolts up to 40 keV in 96 steps with a resolution  $\frac{\delta E}{E} = 0.07$ . The instrument field of view is  $360^\circ \times 90^\circ$  (azimuth  $\times$  elevation), with a resolution of  $22.5^\circ \times 5.0^\circ$ . Mass is characterised through an assembly of permanent magnets and a position detection system consisting of 32 anodes, which we will refer to as mass channels. The radial position of ions on the detector plate is a function of both the mass and the energy.

### 2.2. Distribution functions & plasma parameters

Solar wind ions and cometary ions are well separated in velocity space (i.e. in both energy and direction) and in terms of mass. This is partly illustrated in Fig. 2, which presents a spectrogram (energy versus time) where the different species are identified on the left side of the panel. When the energy separation is poorer, the direction and the mass information allow further identification (see e.g. Nilsson et al. 2015; Berčič et al. 2018). For this

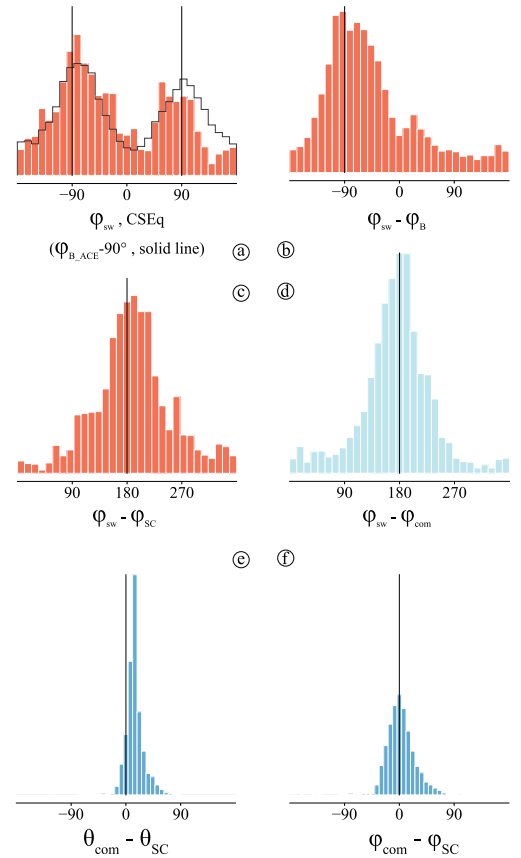


**Fig. 3.** Panel a: clock angle of the solar wind protons and the estimated upstream magnetic field in the CSEQ frame. Panel b: angular difference (clock angle) between the observed magnetic field and the solar wind protons. Panels c and d: angular difference between the solar wind protons and the spacecraft, and the protons and the cometary ions, respectively. Panels e and f: departure of the cometary ion flow direction from the purely radial direction for the cone and clock angle, respectively.

study, the species were therefore manually selected on daily time intervals.

Using these manual selections, we were able to analyse the velocity distribution functions for each species separately. By integrating the distributions, the plasma moments of order 0 and 1 were calculated, providing the density and the bulk velocity for the different species (Figs. 3 and 5). The distribution functions can be seen in Fig. 4, where red tones are used to represent solar wind protons, and blue tones for cometary ions.

### 2.3. Reference frames and coordinate systems

The bulk velocities were initially calculated in the Comet-centred Solar Equatorial (CSEQ) frame: the  $x$ -axis points towards the Sun, and the  $z$ -axis is oriented by the Sun's north

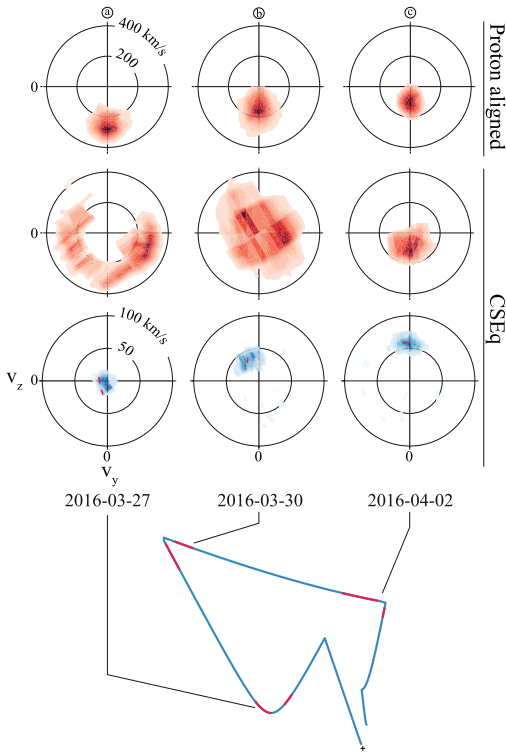


**Fig. 4.** Distribution functions of cometary ions (blue) and solar wind protons (red) for three different dates.

pole direction. For geometric considerations presented later on, a particular coordinate system is used to represent most of the results, namely the spherical system  $(r, \theta, \varphi)$  (see Fig. 1, middle row):  $r$  is the distance between the observation point (the spacecraft position) and the nucleus, or cometocentric distance;  $\theta$  and  $\varphi$  are respectively the cone angle and the clock angle. They can be used to describe the spacecraft's position as well as the orientation of vectors. In this system, the corresponding set of coordinates in velocity space is denoted  $(r_{sw}, \theta_{sw}, \varphi_{sw})$  for protons and  $(r_{com}, \theta_{com}, \varphi_{com})$  for cometary ions. In Figs. 4 and 5, the projection in the plane  $(r, \theta)$  of the spacecraft position is given.

More relevant when it comes to the plasma environment around the comet, the comet-Sun-electric field frame (CSE) also has its  $x$ -axis pointing towards the Sun and the  $z$ -axis is along the upstream electric field. However, since defined by unmeasured upstream parameters, this frame of reference is not directly available, and we can only give an estimation of the frame orientation.

Another reference frame is used in the following when working on the solar wind proton distribution functions. For each scan of the velocity space (every 192 s), a rotation around the comet-Sun line is done in order to cancel the  $v_y$ -component of the proton bulk velocity before integrating all distributions together, exactly as was done by Behar et al. (2017) and Berčić et al. (2018). With the assumption that protons are deflected in a plane

containing the comet-Sun line and the upstream electric field (as observed close to the nucleus in Behar et al. 2016), this rotation leaves the upstream electric field along the  $+z$ -axis and the upstream magnetic field along the  $+y$ -axis, in which case this particular frame corresponds to the CSE frame. In the present case, however, this assumption might not be verified, as we discuss below, and this frame can simply be considered a proton-aligned frame.

#### 2.4. Magnetic fields

An estimation of the upstream magnetic field is used in the next sections. It corresponds to ACE measurements at the Earth, propagated in time using a ballistic approach accounting for the radial and longitude differences between Earth and 67P, and using the solar wind velocity measured at the Earth. Magnetic field measurements at the spacecraft location are also used, and are provided by the RPC-MAG instrument. A comprehensive description is given in Glassmeier et al. (2007), and a study of the night-side excursion focusing on RPC-MAG results is given by Volwerk et al. (2018).

### 3. Results

#### 3.1. Overview

The goal of this study is to characterise and compare the flow of two ion populations in the close tail environment of a comet. This requires the use of numerous combinations of coordinates in order to describe their density, their average direction and average speed, the distribution of these values, and their evolution through time and space as the spacecraft moves along the excursion trajectory. As seen in Fig. 1, part of the excursion is actually on the day-side of the coma, for distances below 500 km. In order to report the entire excursion, this arc is included in the analysis for distances greater than 100 km, adding up to the purely night-side region. The period over which data were analysed in this work – from 23 March to 8 April inclusive – is given by the red arrow below the spectrogram in Fig. 2.

The first combination of parameters is given in Fig. 2, upper panel, and is the combination of time, energy, and number of detections of all ions. Four different species are identified on the left-hand side of the panel, a group of three solar wind species (protons  $H^+$ , alpha particles  $He^{2+}$ , and singly charged helium particles  $He^+$ , which result from charge exchange between the cometary neutral atmosphere and solar wind alpha particles, see Nilsson et al. 2015) and the cometary ions, assumed to be dominated by water molecules  $H_2O^+$ . The evolution of the spacecraft cometocentric distance is given in the lower panel, together with the cone angle of the spacecraft  $\theta_{sc}$ . One of the most striking results is already seen here, namely the correlation between the average energy of the cometary ions and the cometocentric distance. Their detection rate also seems to decrease with the cometocentric distance (as confirmed later on). In opposition, no obvious effect on the solar wind can be found in this figure (with variations in the average energy, the energy width, and the particle counts being in the usual range of fluctuations either of upstream origin or from the general interaction between the solar wind and the coma).

#### 3.2. Flow directions

The bulk velocity directions of solar wind and cometary ions are summarised in Fig. 3. The first three histograms a, b, and c

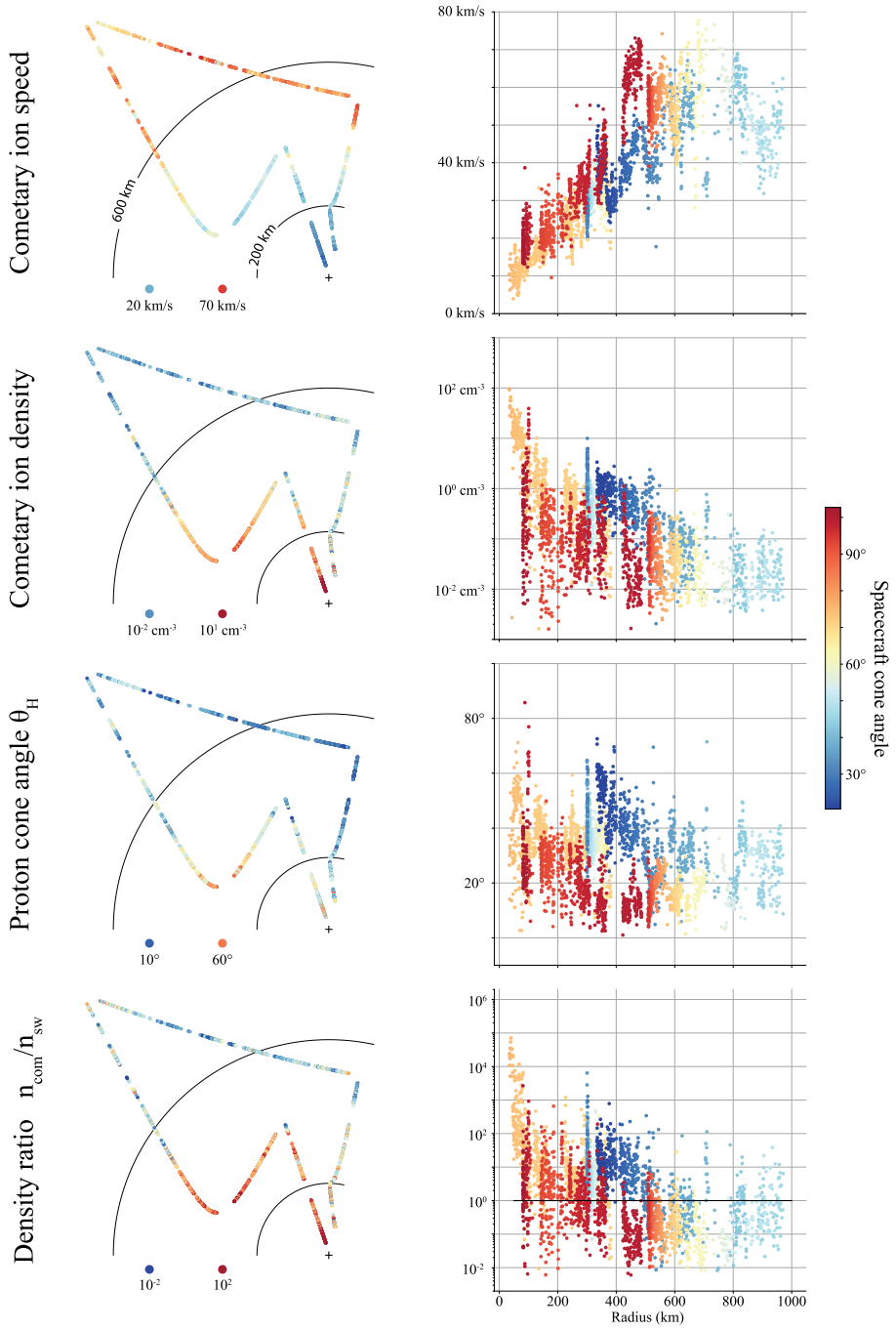


Fig. 5. Plasma parameters for cometary and solar wind ions.

describe the proton flow direction in terms of clock angle<sup>1</sup>. In (a) they are seen deflected away from the  $-x$ -direction with a corresponding clock angle peaking on average at either  $-90^\circ$  or  $+90^\circ$  in the CSEQ reference frame. The same clock angle is on average  $-90^\circ$  away from the magnetic field clock angle measured at the spacecraft, histogram b, even though all configurations were observed (breadth of the distributions). The spacecraft trajectory also presents two peaks in its clock angle distribution, at  $-90^\circ$  and  $+90^\circ$ , in Fig. 1 bottom histogram, similarly to protons. In turn, the difference of the two clock angles (Fig. 3c) shows a very clear trend centred on  $180^\circ$ , with 56% of the occurrences between  $135^\circ$  and  $225^\circ$ .

Next, we examine the departure of the cometary ion flow from the purely radial direction, i.e. the direction opposite to that of the nucleus seen from the spacecraft. The difference of cone and clock angles are given by the two histograms e and f, and display much narrower distributions than previously. The distribution of the cone angle difference peaks at a bit more than  $10^\circ$  (the particles are leaning from the radial to the anti-sunward direction), and the distribution of the clock angle difference has its maximum value at  $0^\circ$  on average, cometary ions were seen flowing more or less radially away from the nucleus.

The solar wind proton and cometary ion mean flow directions are compared in histogram d. They are seen on average flowing  $180^\circ$  apart from each other in terms of clock angle, with once again a very broad distribution presenting all configurations.

### 3.3. Distribution functions

To go further than the bulk direction of the flows and diagnose the actual spread of the populations in velocity space, the velocity distribution functions obtained during the three different days are shown in Fig. 4. The projection of the distributions in the plane ( $v_y, v_z$ ) is displayed for cometary ions (blue) and solar wind protons (red) in the CSEQ frame (middle and bottom rows), and in the proton-aligned frame (top row). Data were integrated over a period of about 15 h in each case, displayed on the orbit as the red segments (the orbit is projected in the  $(r, \theta)$ -plane). The three dates are chosen to illustrate the extreme cases: the first is taken from the inner region closest to the comet–Sun line, the second is taken from the farthest explored cometocentric distance, and the last corresponds to the region slightly day-side, close to the terminator plane, 500 km from the nucleus. These segments are cut in two parts because of data gaps matching spacecraft manoeuvres.

In the cometary ion distributions (bottom panels, blue), an indication of the radial velocity is given by the red lines: it is the velocity of particles that would flow purely radially away from the nucleus with the same average speed as the observed cometary ions. Because of the slow motion of the spacecraft, these lines are very limited.

The cometary population is well focused, beam like, in the CSEQ frame, even integrated over 15 hours. The distributions are also well focused along  $v_x$  (not shown here). In the same frame, the solar wind protons have much broader velocity distributions for the two first cases a and b. However, the last set of distributions (Fig. 4c) presents the average case seen in the histogram d of Fig. 3: two beams (cometary and solar wind) flowing  $180^\circ$  apart in the ( $v_y, v_z$ )-plane, with cometary ions purely radial.

<sup>1</sup> Only clock angles corresponding to a cone angle greater than  $10^\circ$  are considered to avoid poorly determined clock angles.

When aligning the bulk velocity of the solar wind protons with the  $v_y$ -axis for each 192 s scan, we get a well-focused beam for each day, which proves that the solar wind remains a beam at any time, only deflected and changing direction in the CSEQ frame, associated with rotations of the upstream magnetic field clock angle (Behar et al. 2016). It was verified that the rotation also focuses the proton distributions along the  $v_x$  dimension (not shown here).

### 3.4. Cometary ion speed

The cometary ion speed is given in Fig. 5a as the norm of the bulk velocity. The right-hand panel gives the evolution of the speed with the cometocentric distance  $r$ , and the spatial distribution measured along the spacecraft trajectory is given in the left-hand panel. The first obvious observation is that cometary ions gain speed until a distance to the nucleus of about 600 km. Further out, the observed speed is much more spread out, and no clear trend is found.

### 3.5. Cometary ion density

The density of particles originating from the nucleus is given in Fig. 5b, showing a reduction of around three orders of magnitude between closest and furthest point from the nucleus. Further away than 600 km from the nucleus, the density seems to flatten out with values between 1 and 0.1 particle  $\text{cm}^{-3}$ .

### 3.6. Solar wind proton deflection

Features of cometary origin in the solar wind speed and density could not be separated from the typical upstream variations in the observations during the excursion. However the solar wind deflection, i.e. the cone angle of the solar wind proton velocity  $\theta_{sw}$ , shows a clear spatial evolution. In Fig. 5c, we can see that for high cone angles and high radii, this deflection can be as low as  $10^\circ$ , whereas for spacecraft cone angles below  $45^\circ$  and radii below 600 km the deflection reaches  $50$ – $60^\circ$ . The distribution functions in Fig. 4 illustrate low and high deflection cases, and show how beam-like the distributions remain (in the proton-aligned frame). Such a value of  $50^\circ$  is well in line with the average deflection angles of that period, measured on the terminator plane close to the nucleus, before and after excursion. These average values can be seen in the data presented in Behar et al. (2017, Fig. 1) for both the alpha particles and the protons. In particular, the decrease corresponding to the night-side excursion can be easily recognised.

### 3.7. Solar wind ions versus cometary ions

The charge density ratio between the cometary ions and the solar wind is given in Fig. 5d as  $n_{com}/n_{sw}$ . The colour map displays a dominant cometary population as red tones and a dominant solar wind population as blue tones, whereas ratios close to 1 are displayed as pale yellow tones. Cometary ions dominate in terms of charge density 63% of the measurements.

The density ratio plotted against the radius (right-hand panel) shows a visible correlation with the cometary ion density and the solar wind deflection. The solar wind density variations are thus much smaller than those of the cometary ion density, and do not play an important role in the evolution of this ratio. The correlation with the solar wind deflection is discussed in the next section.



## 4. Discussion

### 4.1. Cometary ion origin

During the excursion, cometary ions are observed flowing mostly radially at all locations. It is fairly safe to believe that they originate from a region close to the nucleus. In Berčič et al. (2018), the authors made a statistical analysis of the cometary ion dynamics for typical orbit conditions, i.e. low cometocentric distance (about 30 km) and within the terminator plane. The heliocentric distance turns out to be the same for this statistical study (between 2.5 au and 2.7 au) and for the present excursion, which allows a direct comparison between the average cometary ion behaviour at the terminator plane, close to the nucleus, and their behaviour in the night-side region. The major result of Berčič et al. (2018) is the characterisation of two main cometary populations, namely the pick-up and the expanding populations. Whereas the pick-up ion population (average speed  $30 \text{ km s}^{-1}$ ) is well ordered by the upstream solar wind electric field and originates from the day-side of the coma, the expanding population (on average about  $6 \text{ km s}^{-1}$ ) presents a cylindrical symmetry around the comet–Sun line in terms of flow direction. However, as observed 30 km away from the nucleus, these expanding ions are not moving purely radially, and have an additional anti-sunward component. As presented by the same authors, the acceleration of this population could in part result from a radial ambipolar electric field, set up by charge separation between fast moving electrons and slower ions, due to pressure gradients of the spherically outflowing atmosphere. The cometary ions observed further out along the excursion, much faster than the expanding population, were once part of it. The extent of the region in which the ambipolar electric field may dominate has not been investigated yet, and does not appear as a sharp boundary in the present results. Far from trivial, this topic would most likely require the use of self-consistent fully kinetic numerical models.

### 4.2. Spacecraft position

On average and in the equatorial plane of the Sun, the IMF is twisted in a Parker spiral, pointing either outward or inward. This average configuration corresponds to an IMF clock angle of respectively  $0^\circ$  or  $180^\circ$  in the CSEQ reference frame, which is perfectly seen in the propagated ACE data, Fig. 3a. The corresponding upstream solar wind electric field is therefore on average along the  $z$ -axis, i.e. a clock angle of respectively  $-90^\circ$  and  $+90^\circ$ . The deflection of the solar wind was observed during the entire mission and has been shown to be the result of the mass-loading occurring upstream of the measurement point, in a region dominated by the solar wind: the new-born cometary ions, with almost no initial velocity, are accelerated by the local motional electric field. The momentum and energy they gain is taken from the solar wind, which in turn is necessarily deflected with a clock angle opposite to that of the cometary ions (see e.g. Behar et al. 2016; Berčič et al. 2018), therefore  $-90^\circ$  away from the magnetic field clock angle. In Fig. 3, histogram a, the propagated ACE data are shifted by  $-90^\circ$ , and overplotted (solid black line) with the proton clock angle in the same frame. A very nice match is found, in shape and even in the relative height of the two peaks. Measured at the spacecraft, the magnetic field is on average  $-90^\circ$  from the proton clock angle as well, as seen in histogram b. From histograms a, b, and d of Fig. 3, it appears that on average, the proton flow direction observed during the excursion is compatible with the effect of the mass-loading happening upstream of (and all the way to) the measurement point.

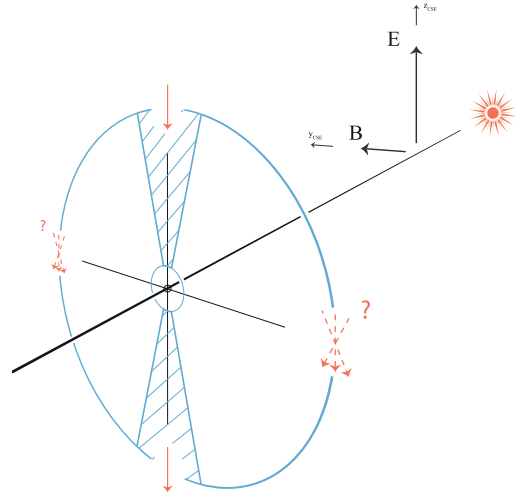


**Fig. 6.** Representation of the CSE frame, and the regions where the selected data are estimated to be measured (striped). The red arrows indicate the expected velocity of solar wind protons, projected in the plane ( $y_{\text{CSE}}, z_{\text{CSE}}$ ). The nucleus position is not shown as it is not fixed on this representation.

Assuming to first order that the solar wind protons are deflected with a clock angle of  $-90^\circ$  everywhere in the CSE frame of reference, then a clock angle difference of  $180^\circ$  between the protons and the spacecraft position in CSEQ implies that the spacecraft had no  $y$ -component and a positive  $z$ -component in CSE. For a difference of  $0^\circ$ , the spacecraft has no  $y$ -component and a negative  $z$ -component. This is illustrated in Fig. 6 by the two striped regions. This is the case most of the time during the excursion. However, the proton velocity can also gain a  $y$ -component, due to the total electron pressure gradients, magnetic field draping and upstream magnetic field cone angle (angle of the average Parker spiral). In this case, represented by dashed arrows in Fig. 6, the CSE and the proton aligned frames are no longer equivalent. However, in the plane  $y_{\text{CSE}} = 0$  this  $y$ -component is close to zero because of the general symmetry of the draping pattern and the pressure (see respectively Alfvén 1957 and Haser 1957). Additionally, the angle of the Parker spiral at this distance to the Sun is around  $70^\circ$  from the comet–Sun line, which is fairly close to  $90^\circ$ , a value for which the ideally draped field lines are perfectly symmetric. Therefore, in summary, a clock angle difference close to  $180^\circ$  or  $0^\circ$  is still a valid indication of the spacecraft position in the CSE frame. This is illustrated in the schematic in Fig. 7. As seen in the previous section, almost 60% of the observations are estimated to be within  $\pm 45^\circ$  of the ( $y = 0$ ) plane.

### 4.3. The interaction

This subsection is extensively based on the global 2D model of the interaction between the solar wind and the coma given in Behar et al. (2018), and the analysis of its dynamics given by Saillenfest et al. (2018). We summarise the main aspects of the model before comparing it to the observations.

In a cometary environment, all forces but the Lorentz force  $\mathbf{F} = e(\mathbf{E} + \mathbf{v} \times \mathbf{B})$  (with the electric field  $\mathbf{E}$ , the magnetic field  $\mathbf{B}$ , and the velocity  $\mathbf{v}$  and the single charge  $e$  of the considered particle), can be neglected. The alpha particles are also neglected, as well as pressure gradients, collisions, and electron inertia. Furthermore, considering spatial scales  $\ell$  much greater than the ion inertial length  $d_i$ , the total electric field is simplified to its ideal MHD form, hereafter referred to as  $\mathbf{E}_{\text{motional}}$ . Considering two plasma beams (one solar wind proton beam and one cometary ion beam), we have

$$\mathbf{E}_{\text{motional}} = -\mathbf{u}_{\text{ion}} \times \mathbf{B} = -\left(\frac{n_{\text{sw}}}{n_{\text{sw}} + n_{\text{com}}} \mathbf{u}_{\text{sw}} + \frac{n_{\text{com}}}{n_{\text{sw}} + n_{\text{com}}} \mathbf{u}_{\text{com}}\right) \times \mathbf{B}. \quad (1)$$

The corresponding Lorentz force on each species then reads

$$\begin{aligned} \mathbf{F}_{\text{sw}} &= e \frac{n_{\text{com}}}{n_{\text{sw}} + n_{\text{com}}} (\mathbf{u}_{\text{sw}} - \mathbf{u}_{\text{com}}) \times \mathbf{B} \\ \mathbf{F}_{\text{com}} &= -e \frac{n_{\text{sw}}}{n_{\text{sw}} + n_{\text{com}}} (\mathbf{u}_{\text{sw}} - \mathbf{u}_{\text{com}}) \times \mathbf{B}. \end{aligned} \quad (2)$$

The model then focuses on the plane ( $y_{\text{CSE}} = 0$ ). The symmetry of this ideal system (as mentioned in the previous section) gives in this plane  $\mathbf{B} = B_y \hat{\mathbf{y}}$ . Assuming that  $u_{\text{sw}} \gg u_{\text{com}}$ , we get

$$\begin{aligned} \mathbf{F}_{\text{sw}} &= eB \frac{n_{\text{com}}}{n_{\text{sw}} + n_{\text{com}}} \mathbf{u}_{\text{sw}} \times \hat{\mathbf{y}} \\ \mathbf{F}_{\text{com}} &= -eB \frac{n_{\text{sw}}}{n_{\text{sw}} + n_{\text{com}}} \mathbf{u}_{\text{sw}} \times \hat{\mathbf{y}}. \end{aligned} \quad (3)$$

By considering only new-born cometary ions flowing radially away from the nucleus at the speed  $u_0$ , and neglecting the accelerated (or pick-up) cometary ions, the dynamics of the protons is reduced to

$$\mathbf{F}_{\text{sw}} = \frac{m_{\text{sw}} \eta}{r^2} \mathbf{u}_{\text{sw}} \times \hat{\mathbf{y}}; \quad \eta = \frac{e v_i Q B_{\infty}}{4\pi v_{\text{ml}} n_{\text{sw}} m_{\text{sw}} u_0} \quad [\text{m}^2/\text{s}], \quad (4)$$

where  $Q$  is the production rate of neutral elements,  $v_i$  is the ionisation rate (taken to be constant through the coma),  $B_{\infty}$  is the amplitude of the upstream magnetic field, and  $n_{\text{sw}}$  the density of the solar wind, also assumed to be constant at zero order. The parameter  $v_{\text{ml}}$  is a non-physical destruction rate of cometary ions, which allows us to neglect the accelerated cometary ions in the analytical expression of the cometary ion density. All the previous values are taken from the literature, and  $v_{\text{ml}}$  is estimated to be about  $0.01 \text{ s}^{-1}$  based on the values found in Behar et al. (2016). When compared with the data of the excursion,  $v_{\text{ml}}$  is taken as a free parameter to allow a better fit to the data and to allow it to absorb the uncertainty of all other parameters. However, its final value is found to be in this precise range.

As seen in Eq.(4), the solar wind protons experience a force always orthogonal to their velocity and with an amplitude proportional to  $1/r^2$ . Protons are not decelerated and are only deflected. These dynamics have been thoroughly analysed by Saillenfest et al. (2018). The resulting proton trajectories are given in Fig. 7, bottom-left panel, as red lines. One characteristic of the dynamics is the formation of a caustic, along which proton trajectories intersect, a structure also observed in numerical models (see Behar et al. 2018 for a discussion of numerical models). In the resulting flow lines, two types of trajectories are to be considered with caution. After passing the caustic, the trajectories of protons are unphysical as they are not aligned with the local bulk velocity: they are expected to gyrate in a more complex manner. Additionally, the region downstream of the caustic for  $z_{\text{CSE}} < 0$  is poorly modelled, mostly because of the outflow

from the caustic (absent in this model), and the pile-up of the magnetic field is expected to be significantly more complex than modelled in this precise region (see Behar et al. 2018 for more details). Accordingly, these two types of trajectories are lightened in Fig. 7.

As previously discussed, many observations are estimated to be taken close to the ( $y_{\text{CSE}} = 0$ ) plane. From histogram c in Fig. 3, we have selected the data points lying in the interval  $[160^\circ, 200^\circ]$  (the peak of the distribution) and in the intervals  $[0^\circ, 20^\circ]$  and  $[340^\circ, 360^\circ]$ , the tips of the wings of the distribution. These data represent 33% of all the valid data. They are estimated to have been taken within  $\pm 20^\circ$  of the plane ( $y_{\text{CSE}} = 0$ ), which we illustrate with the two striped surfaces in the schematics of Fig. 6. The velocity vectors of the selected data are projected in the cartesian ( $x, z$ )-plane of the estimated CSE frame of reference. The proton velocity vectors are compared with the 2D model, and comparison for a value of  $v_{\text{ml}} = 0.01 \text{ s}^{-1}$  is given in Fig. 7, lower left panel, in the lower range of the interval estimated in Behar et al. (2018).

For  $z_{\text{CSE}} > 0$  and  $r > 200 \text{ km}$ , a very good agreement between the observed proton bulk velocity and the modelled proton flow direction is found. The data at  $z_{\text{CSE}} < 0$  lie in the region poorly constrained by the model, with all data points downstream of the caustic. We note that a higher value of the rate  $v_{\text{ml}}$  corresponding to an overall smaller deflection of the solar wind would give a better fit for data points for  $r < 200 \text{ km}$ . It appears that the model together with a value of  $v_{\text{ml}}$  of about  $0.01 \text{ s}^{-1}$  accounts for the general behaviour of the solar wind close to the plane ( $y_{\text{CSE}} = 0$ ) as seen during the night-side excursion.

The model does not solve the dynamics of the cometary ions. However, it gives us a valuable hint through the expression of the force they experience:

$$\mathbf{F}_{\text{com}} = -e \frac{n_{\text{sw}}}{n_{\text{sw}} + n_{\text{com}}} (\mathbf{u}_{\text{sw}} - \mathbf{u}_{\text{com}}) \times \mathbf{B}$$

For 54% of the selected observations, cometary ions are at least one order of magnitude slower than the solar wind protons. Therefore,  $\mathbf{F}_{\text{com}}$  is fairly orthogonal to the proton velocity. But we can go further, and can calculate either the motional electric field or the force experienced by the cometary ions since all quantities are actually measured by RPC-ICA and RPC-MAG. The result for  $\mathbf{E}_{\text{motional}}$  is given in Fig. 7 in the upper right panel. It represents the indirect measurement of that field, independent of any assumptions. The norm of the vectors depends on the density and velocity of particles and on the magnetic field amplitude, but the direction of the vectors only depends on the velocity vectors direction and the magnetic field direction. The RPC-ICA sensor is better at measuring the velocity of particles than their density; therefore, the direction of the vectors is better constrained than their norm. It should also be noted, however, that magnetic field data are not ideally constrained for most of the time interval, as explained in Volwerk et al. (2018). Based on Fig. 3b, we assumed the magnetic field to be orthogonal to the protons, which makes the computed electric field amplitude an upper limit.

The motional electric field results in a higher cometary ion acceleration further away from the nucleus in a region where the solar wind tends to dominate (Fig. 5, bottom panel). The corresponding force is aligned with the flow direction in the  $z > 0$  region for small  $x$ -coordinates. Going down in the inner tail region, the cometary ions are seen gradually departing from the field direction, to end up being completely misaligned for  $z < 0$ . Obviously, other sources of electric field are at work there. It is noteworthy that in this region, the singing comet waves in the



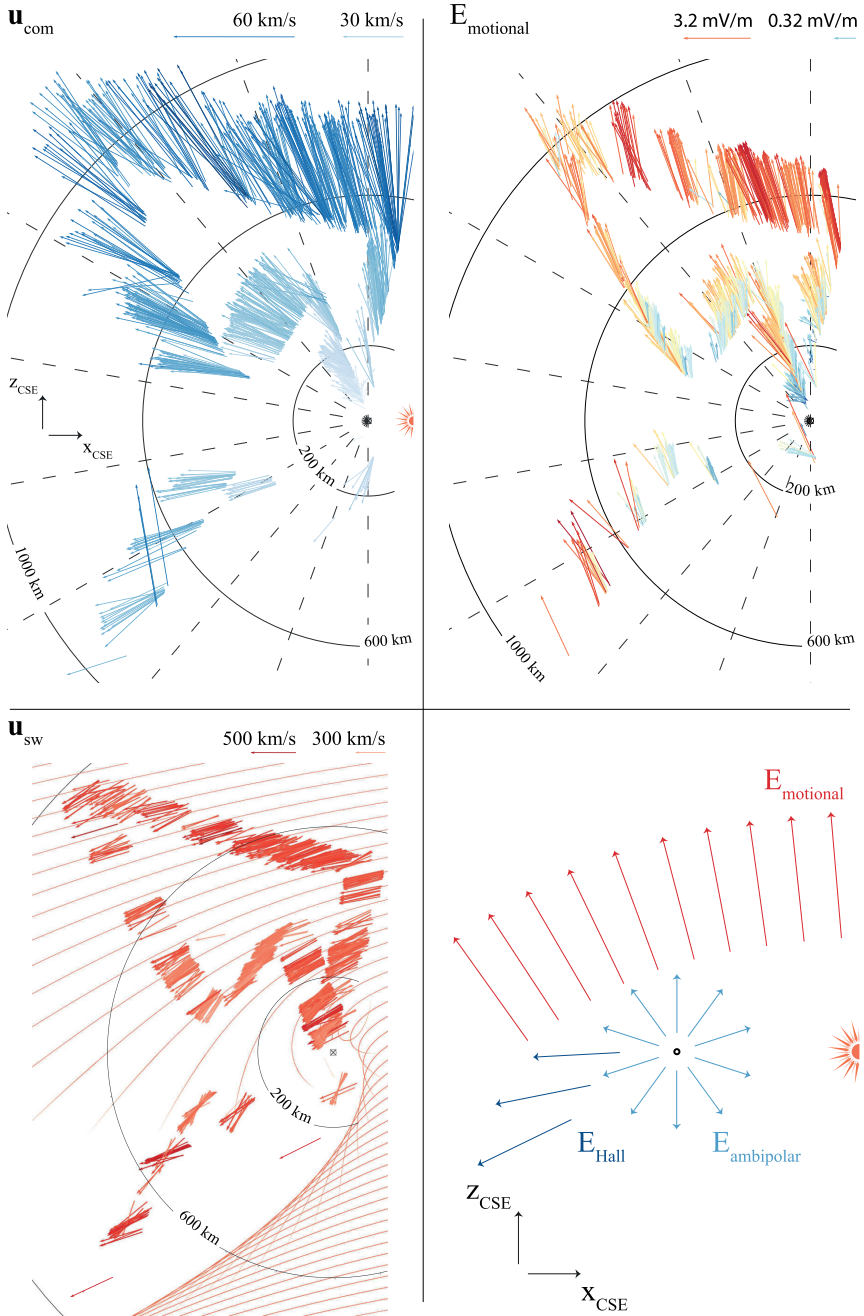


**Fig. 7.** Upper left: observed cometary ion bulk velocities in CSE. Lower left: observed solar wind proton bulk velocities in CSE, with their theoretical trajectories. Upper right: indirectly observed motional electric field. Lower right: schematics of the three terms of the total electric field (interpretation).

magnetic field (Richter et al. 2015) were found to be stronger than further out on the night-side of the coma, as shown by Volwerk et al. (2018).

#### 4.4. Hall electric field & pressure gradients

The generalised Ohm's law, when neglecting collisions and neglecting the electron mass compared to the ion mass, is reduced to

$$\mathbf{E} = -\mathbf{u}_{\text{ion}} \times \mathbf{B} + \frac{1}{ne} \mathbf{j} \times \mathbf{B} - \frac{1}{ne} \nabla P_e \quad (5)$$

with  $\mathbf{j}$  the total current,  $\nabla P_e$  the electron pressure gradient, and  $n = n_{\text{sw}} + n_{\text{com}}$  the total ion density. We have previously investigated the first of the three terms on the right-hand side of the equation, namely the motional electric field  $\mathbf{E}_{\text{motional}}$ . Neglecting the displacement current  $\partial_t \mathbf{E}$  in the Ampère-Maxwell law, the second one – the Hall term – becomes  $\mathbf{E}_{\text{Hall}} = (\nabla \times \mathbf{B}) \times \mathbf{B} / (\mu_0 n e)$ . It can arise from the magnetic field draping around the coma, which is a source of curl for  $\mathbf{B}$ . Using Ampère's law, we can find an electric field along the axis of symmetry of the draping pattern, anti-sunward. Numerical models would be appropriate for investigating further this source of electric field, as was done for example by Huang et al. (2018) (though at a fairly different activity level). An additional source of pile-up for the magnetic field is the asymmetric Mach cone, the caustic of the model; therefore,  $\mathbf{E}_{\text{Hall}}$  is expected to play a role mostly in the downstream region of the caustic, tailward.

The third term, the ambipolar electric field  $\mathbf{E}_{\text{ambipolar}}$ , is expected to be significant close to the nucleus. At zero order, this electric field points radially outward from the nucleus. It might be one of the reasons why close to the nucleus the modelled proton trajectories in Fig. 7 depart from the observed velocity vectors. Another effect arising from the ambipolar term is a polarisation electric field due to the different motion of the cometary new-born electrons and ions. The gyroradius of the cometary ions can be much larger than the interaction region, itself larger than the cometary electron gyroradius, which induces a charge separation, and in turn a polarisation electric field. This electric field contribution is explored in the analytical work of Nilsson et al. (2018), and results in one additional acceleration of the cometary ions with an anti-sunward component.

The three electric field are summarised in the schematic of Fig. 7. Above the nucleus ( $z_{\text{CSE}} > 0$ ),  $\mathbf{E}_{\text{motional}}$  and  $\mathbf{E}_{\text{ambipolar}}$  are essentially aligned. Towards the inner tail region,  $\mathbf{E}_{\text{ambipolar}}$  gives a tailward component to the total field compared to  $\mathbf{E}_{\text{motional}}$  and eventually along the comet–Sun line,  $\mathbf{E}_{\text{Hall}}$  adds up to the tailward acceleration of the cometary ions. Overall, the cometary ion acceleration ends up being mostly radial from the combination of the three terms in the generalised Ohm's law.

We note, however, that the apparent absence of acceleration for  $r > 600$  km cannot be accounted for by this interpretation. Neither the ambipolar electric field nor the Hall term is expected to provide any significant acceleration there, but as this region is dominated by a barely perturbed solar wind the motional electric field is still about a few  $\text{mV m}^{-1}$ , as seen in the upper right panel in Fig. 7. An instrumental effect cannot be completely discarded, even though the energy and density ranges are nominal. The validation (or discussion) of this observation may require numerical modelling of the interaction, and we already note that the fully kinetic simulation presented by Deca et al. (2017) give a similar result, with the energy of the cometary ions increasing and reaching a plateau in the tail region (cf. Fig. 3 of Deca et al. 2017).

#### 4.5. Hybrid simulations

A qualitatively identical dynamic is seen in Koenders et al. (2016), Fig. 14, lower and upper left panels, where the same interaction is simulated for a smaller heliocentric distance of 2.3 au. The solar wind forms an asymmetrical and curved Mach cone similarly to the caustic given by the semi-analytical model, and the overall deflection is in great qualitative agreement with both the data and the semi-analytical model. The simulated cometary ions are seen accelerated radially away from the nucleus on the night-side of the coma as well.

In another relevant simulation work, Bagdonat & Motschmann (2002) describe a region of weak suppression of the magnetic field downstream of the nucleus and aligned with the comet–Sun line (Bagdonat & Motschmann 2002, Fig. 4). The authors report a broad cycloidal tail leaving the nucleus orthogonal to the comet–Sun line (corresponding to our observation at  $z > 0$ , above the nucleus), and a different cometary ion population accelerated tailward from the nucleus, corresponding to the observed cometary ion in the inner tail region.

### 5. Summary and conclusions

During the night-side excursion, the cometary ion flow and the solar wind remained very directional. The cometary beam appears quasi-radial, which is interpreted as the result of its acceleration by three different electric fields of different origins: the motion of the charge carriers, the electron pressure gradients, or the magnetic field line bending. The solar wind deflection is in agreement with the analytical expression of the the magnetic field pile-up and the motional electric field, with some possible influence of the two other electric field terms close to the nucleus and in the inner tail region.

A remaining open question is the apparent lack of acceleration of the cometary ions further than 700 km from the nucleus, which is not in agreement with the electric field components discussed previously.

The observed plasma dynamics on the night-side could enable better constraints in the comparisons between data and various models, as the area covered is much greater than usually available during the rest of the active mission. These better constraints would also allow us to direct more precisely the analysis of the simulation results as the range of parameters is significantly greater than has been explored in the present article. As an example, an obvious follow-up of this work would be the three-dimensional mapping of the different electric field terms in the result of a numerical simulation, which would enable the study of the interaction on the flanks of the coma away from the plane ( $y_{\text{CSE}} = 0$ ).

**Acknowledgements.** This work was supported by the Swedish National Space Board (SNSB) through grants 108/12, 112/13, and 96/15. The work at LPC2E/CNRS was supported by ESEP, CNES, and by ANR under the financial agreement ANR-15-CE31-0009-01. We acknowledge the staff of CDDP and IC for the use of AMDA and the RPC Quicklook database (provided by a collaboration between the Centre de Données de la Physique des Plasmas (CDPP) supported by CNRS, CNES, Observatoire de Paris and Université Paul Sabatier, Toulouse, and Imperial College, London, supported by the UK Science and Technology Facilities Council). We are indebted to the whole Rosetta mission team, Science Ground Segment, and Rosetta Mission Operation Control for their hard work making this mission possible.

### References

- Alfven, H. 1957, *Tellus*, IX, 92
- Bagdonat, T., & Motschmann, U. 2002, *J. Comput. Phys.*, 183

- Behar, E., Nilsson, H., Stenberg Wieser, G., et al. 2016, *Geophys. Res. Lett.*, **43**, 1411
- Behar, E., Nilsson, H., Alho, M., Goetz, C., & Tsurutani, B. 2017, *MNRAS*, **469**, S396
- Behar, E., Tabone, B., Saillenfest, M., et al. 2018, *A&A*, DOI: 10.1051/0004-6361/201832736
- Berčić, L., Behar, E., Nilsson, H., et al. 2018, *A&A*, **613**, A57
- Biermann, L. 1951, *Z. Astrophys.*, **29**, 274
- Carr, C., Cupido, E., Lee, C. G. Y., et al. 2007, *Space Sci. Rev.*, **128**, 629
- Coates, A., Burch, J., Goldstein, R., et al. 2015, *J. Phys. Conf. Ser.*, **642**, 012005
- Deca, J., Divin, A., Henri, P., et al. 2017, *Phys. Rev. Lett.*, **118**, 205101
- Durham, I. T. 2006, *Notes and Records*, **60**, 261
- Eddington, A. S. 1910, *MNRAS*, **70**, 442
- Glassmeier, K.-H., Boehnhardt, H., Koschny, D., Kührt, E., & Richter, I. 2007, *Space Sci. Rev.*, **128**, 1
- Haerendel, G., Paschmann, G., Baumjohann, W., & Carlson, C. W. 1986, *Nature*, **320**, 720
- Haser, L. 1957, *Bull. Cl. Sci. Acad. Roy. Belg.*, **43**, 740
- Huang, Z., Tóth, G., Gombosi, T. I., et al. 2018, *MNRAS*, **475**, 2835
- Jones, G. H., Balogh, A., & Horbury, T. S. 2000, *Nature*, **404**, 574
- Koenders, C., Perschke, C., Goetz, C., et al. 2016, *A&A*, **594**, A66
- Nilsson, H., Lundin, R., Lundin, K., et al. 2007, *Space Sci. Rev.*, **128**, 671
- Nilsson, H., Stenberg Wieser, G., Behar, E., et al. 2015, *Science*, **347**
- Nilsson, H., Wieser, G. S., Behar, E., et al. 2017, *MNRAS*, **469**, S252
- Nilsson, H., Gunell, H., Karlsson, T., et al. 2018, *A&A*, in press, DOI: 10.1051/0004-6361/201833199
- Richter, I., Koenders, C., Auster, H.-U., et al. 2015, *Annales Geophysicae*, **33**, 1031
- Saillenfest, M., Tabone, B., & Behar, E. 2018, *A&A*, in press, DOI: 10.1051/0004-6361/201832742
- Slavin, J. A., Smith, E. J., Tsurutani, B. T., et al. 1986, *Geophys. Res. Lett.*, **13**, 283
- Smith, E. J., Tsurutani, B. T., Slavin, J. A., et al. 1986, *Science*, **232**, 382
- Snodgrass, C., A'Hearn, M. F., Aceituno, F., et al. 2017, *Phil. Trans. R. Soc. London, Ser. A*, **375**, 20160249
- Valenzuela, A., Haerendel, G., Föppl, H., et al. 1986, *Nature*, **320**, 700
- Volwerk, M., Goetz, C., Richter, I., et al. 2018, *A&A*, **614**, A10









# Dawn–dusk asymmetry induced by the Parker spiral angle in the plasma dynamics around comet 67P/Churyumov–Gerasimenko

E. Behar,<sup>1,2★</sup> B. Tabone<sup>3</sup> and H. Nilsson<sup>1,2★</sup>

<sup>1</sup>Swedish Institute of Space Physics, Kiruna, Sweden

<sup>2</sup>Department of Computer Science, Electrical and Space Engineering, Luleå University of Technology, Kiruna, Sweden

<sup>3</sup>LERMA, Observatoire de Paris, PSL Research University, CNRS, Sorbonne Université, UPMC Univ. Paris 06, Paris F-75014, France

Accepted 2018 April 26. Received 2018 April 11; in original form 2018 February 16

## ABSTRACT

The solar wind and the ionized atmosphere of a comet, exchange energy and momentum on interacting. Our aim is to understand the influence of the average Parker spiral configuration of the solar wind magnetic field on this interaction. We compare the theoretical expectations of an analytical generalized gyromotion with *Rosetta* observations at comet 67P/Churyumov–Gerasimenko. A statistical approach allows one to overcome the lack of an upstream solar wind measurement. We find that in addition to their acceleration along (for cometary pick-up ions) or against (for solar wind ions) the upstream electric field orientation and sense, the cometary pick-up ions drift towards the dawn side of the coma, while the solar wind ions drift towards the dusk side of the coma, independent of the heliocentric distance. The dynamics of the interaction is not taking place in a plane, as often assumed in previous works.

**Key words:** acceleration of particles – plasmas – methods: data analysis – techniques: imaging spectroscopy.

## 1 INTRODUCTION

At comets, the sublimation of the volatiles embedded in the nucleus produces a radially expanding neutral atmosphere, which is not gravitationally bound to the body. These neutral molecules can be ionized through photoionisation, electron impact, or charge exchange, and new-born ions are added to the solar wind. From there, the new-born ions will be accelerated by the ambient electric and magnetic fields and in the absence of collisions, momentum and energy are exchanged through the fields between the solar wind and the partially ionized atmosphere. This phenomenon is known as the *mass-loading* of the solar wind by the new-born ions, as mass is added to the plasma (Szegő et al. 2000). On large scales, much larger than the scales of the ion gyromotion, the cometary ions are seen accelerated instantaneously at the average plasma velocity, a result of the ideal magnetohydrodynamics (see for example Flammer & Mendis 1991; Schmidt, Wegmann & Neubauer 1993). However, in order to understand how momentum and energy are exchanged between the two populations, one has to consider smaller scales, and thus resolve the gyromotion of the ions<sup>1</sup> [see for example the simulation works of Hansen et al. (2007), Rubin et al. (2014), and Koenders et al. (2016)]. *In situ* results were obtained on the cometary ion gyromotion at different comets (Halley, Giacobini–

Zinner, Grigg–Skjellerup, and Borelly) and reviewed by Coates (2004). The present work is based on *Rosetta* data taken in the close environment of comet 67P/Churyumov–Gerasimenko (67P/CG).

In the absence of gravity, the motion of charged particles in an electric field  $\mathbf{E}$  and a magnetic field  $\mathbf{B}$  is dictated by the Lorentz force,  $\mathbf{F}_L = q(\mathbf{E} + \mathbf{v} \times \mathbf{B})$ , with  $q$  the charge of the particle and  $\mathbf{v}$  its velocity. In some cases this motion may be very simple. In the undisturbed solar wind for instance, the effect of the electric field and magnetic field cancel each other, and the resulting acceleration on the solar wind particles is null. When considering the simplistic case of a single new-born ion added to the solar wind with no initial velocity, one finds the classical cycloidal motion with the Larmor radius  $\mathcal{R} = m v_{\perp} / (q |\mathbf{B}|)$ . In this case, the solar wind and the electric and magnetic fields are left unaffected by the addition of a single ion. If the source region of cometary ions is much larger than their gyroradius, gyrotropic (phase space) distribution functions can form. First, unstable ring distributions form, which become thickened shell distributions, to eventually transform into Maxwellian distributions. The theory and the observations of these gyrotropic distributions are reviewed by Coates (2004). The deceleration of the solar wind can then be tackled by a fluid approach.

At 67P/CG however, for heliocentric distances large enough, the cometary ion gyroradius was comparable or larger than their source region, and the cometary pick-up ion distribution functions are non-gyrotropic (Koenders et al. 2016; Behar et al. 2018a). We note that closer to the Sun, more complex distribution functions of cometary ions were observed on two cases and reported by Nicolaou

\* E-mail: etienne.besar@irf.se (EB) hans.nilsson@irf.se (HN)

<sup>1</sup>For most purposes, at comets, the hybrid approximation is relevant, and electrons can be considered as a massless and charge-neutralizing fluid.

et al. (2017). It was shown that in this context, as the cometary pickup ion density becomes comparable to the solar wind ion density, both populations gyrate, and the fluid description of the solar wind breaks down. From upstream of the coma to the close tail region, individual solar wind ions describe less than one period of their gyromotion (Behar et al. 2017, 2018a,b). Cometary ions are initially accelerated along the electric field, and the solar wind is accelerated (deflected) in the opposite direction, a clear result observed within the coma of 67P/CG (Behar et al. 2016; Berčič et al. 2018). In these studies, the dynamics of both populations were depicted to take place in a plane, containing the comet–Sun line and the upstream electric field. In a semi-analytical model of the solar wind dynamics proposed in Behar et al. (2018b), the same hypothesis is done by assuming that the upstream magnetic field is perpendicular to the upstream solar wind velocity. However, on an average, the magnetic field has an angle with the flow direction different than  $90^\circ$  because of the Parker spiral configuration of the interplanetary magnetic field (IMF; Koenders et al. 2016). The influence of the IMF angle on the interaction between the solar wind and different obstacles has been studied at other unmagnetised bodies, and often result in similar dawn–dusk asymmetries, as shown by the simulation work of Jarvinen, Kallio & Dyadechkin (2013) at Venus, or by *in situ* studies at Mars (Dubinin et al. 2008) and at the Moon (Harada et al. 2015).

In the present short article, we explore the effect of such an angle on the interaction between the solar wind and the cometary ions, with a straightforward statistical approach based on measurements at comet 67P/CG as well as IMF measurements at 1 au. Using statistics over a long period allows us to overcome the one-point-measurement limitations (i.e. the space coverage and the time coverage are always at a great cost of one another).

## 2 GENERALISED GYROMOTION

In Behar et al. (2018b), the dynamics of the interaction between two perfect beams of plasma (the solar wind and the cometary ions, of respective velocities and densities  $\mathbf{u}_{sw}$ ,  $n_{sw}$  and  $\mathbf{u}_{com}$ ,  $n_{com}$ ) is analytically obtained for length-scales over which the total electric field is reduced to

$$\mathbf{E} = -\mathbf{u}_i \times \mathbf{B}$$

$$\mathbf{u}_i = \frac{n_{com}\mathbf{u}_{com} + n_{sw}\mathbf{u}_{sw}}{n_{com} + n_{sw}} \quad (1)$$

Introducing the expression of the electric field in the Lorentz force, gives the following equation of motion for each beam, assuming  $q_{sw} = q_{com} = q$ :

$$\dot{\mathbf{u}}_{sw} = \frac{q n_{com}}{m_{sw}(n_{sw} + n_{com})}(\mathbf{u}_{sw} - \mathbf{u}_{com}) \times \mathbf{B}$$

$$\dot{\mathbf{u}}_{com} = -\frac{q n_{sw}}{m_{com}(n_{sw} + n_{com})}(\mathbf{u}_{sw} - \mathbf{u}_{com}) \times \mathbf{B}. \quad (2)$$

All ions of the same population experience the same force at the same time, and the single particle velocity is equal to the population average velocity: a beam remains a beam. Elements of the resolution of these equations are given in Behar et al. (2018b). One finds that in the most general configuration of the initial conditions, the two beams will evolve in velocity space along circles, with each circle contained in a plane orthogonal to the magnetic field: there is no acceleration along the magnetic field. Therefore, if initially the beams have different velocity components parallel to  $\mathbf{B}$ , the two circles are in different planes and the motion in physical space is not happening in a plane in any frame. The top plot of Fig. 1, purely

frame independent, shows the evolution of the beams in velocity space. If the magnetic field sense is flipped, the beams evolve along the same two circles, with the opposite rotations. As indicated by the + sign in the upper panel of Fig. 1 and in agreement with the classical single particle motion, these rotations are prograde given the sense of  $\mathbf{B}$ . The velocity of the centre of mass of the two beams  $\mathbf{v}_i$  is conserved through time,  $\dot{\mathbf{v}}_i = 0$ , as shown by the black crosses on the same plots. These dynamics generalize the classical single test-particle gyromotion to the case of two plasma beams in an electric and a magnetic field, with an arbitrary initial configuration.

We now put the exact same configuration in a reference frame, shown in the bottom plot of Fig. 1. Here, cometary ions in blue have no initial velocity and the beam is at the origin at  $t = 0$ . At the same time, the solar wind velocity is chosen to be along the  $x$ -axis, which points at the Sun. The  $z$ -axis completes this right-handed Cartesian frame, referred to as the comet frame. In this precise frame, the magnetic field has an angle  $\chi$  with the  $x$ -axis, and is within the  $(x, y)$ -plane. The  $v_z$ -component for each species is changing sign every half gyration period. More interestingly, we find that the solar wind beam has a  $v_y$ -component, which is always positive. Conversely, the cometary ions have a  $v_y$ -component always negative. The evolution of the  $v_y$ -component is the same irrespective of the sense of the magnetic field.

In the comet frame, one can easily derive the velocity of the guiding centres of each population (centres of the two circles) that correspond to the drift of the populations in physical space. In this frame, the cometary ions are drifting perpendicular to the magnetic field, similarly as in the illustration in Coates (2004), Fig. 2. When solar wind ions are largely dominating, this tends to the classical  $\mathbf{E} \times \mathbf{B}$  drift of a test particle. As the cometary ion density gets larger, the drift speed decreases.

The solar wind ions drift towards the  $+y$ -axis with an angle that depends on the density and mass ratios, which will therefore evolve through the coma, resulting in complex trajectories.

We note however that the problem cannot be reduced to the motion of guiding centres in the case of 67P/CG. Guiding centres are not relevant since ions are only following the early phase of a single gyro-period (Behar et al. 2017, 2018a,b). In other words, ions do not have time to drift.

## 3 OMNI DATA SET AND ROSETTA OBSERVATIONS

In the Sun’s equatorial plane, the magnetic field is on an average directed along an Archimedean spiral, lying in the same plane (the Parker spiral). The local angle of the spiral is determined by the Sun’s rotation, the speed of the radially expanding solar wind, and the distance to the Sun. The orbital planes of comet 67P/CG and of Earth are both inclined about  $7^\circ$  away from the Sun’s equatorial plane. In this study, the inclinations are neglected and we consider the average IMF upstream of the comet and upstream of the Earth given by the planar Parker spiral as illustrated in Fig. 3.

Within the coma of 67P/CG, the solar wind ions and the cometary ions were measured by the imaging spectrometer *Rosetta* Plasma Consortium–Ion Composition Analyser (Nilsson et al. (2007)). The instrument has a field of view of  $90^\circ \times 360^\circ$ , measures positive ions with energy from about 10 to 40 keV, and can discriminate their masses. The duration for a complete velocity space scan is 3 min. The limited field of view and its obstruction by the spacecraft are not expected to induce any systematic effect, considering the constant movement of the probe, the variability of the ion dynamics, and the integration over several months of data. Using daily manual



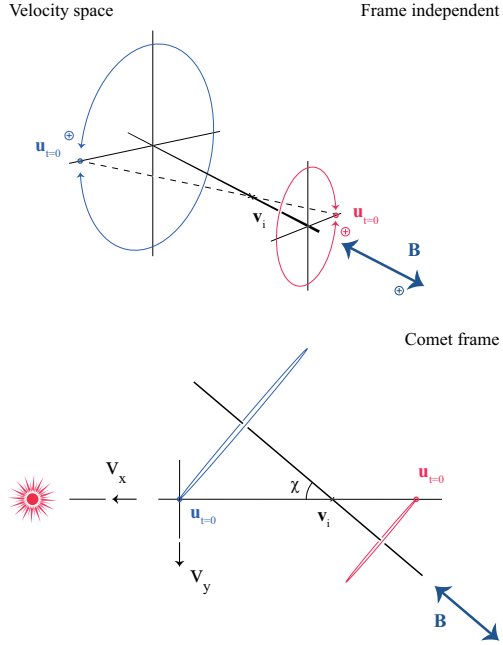


**Figure 1.** Evolution in velocity space of the two interacting plasma beams (generalized gyromotion), for two opposite senses of the magnetic field, frame independent (top) and within a chosen frame (bottom). In this frame, the magnetic field lies in the  $(x, y)$ -plane. Applied to the situation at the comet, blue is used for the cometary ions and red for the solar wind ions.

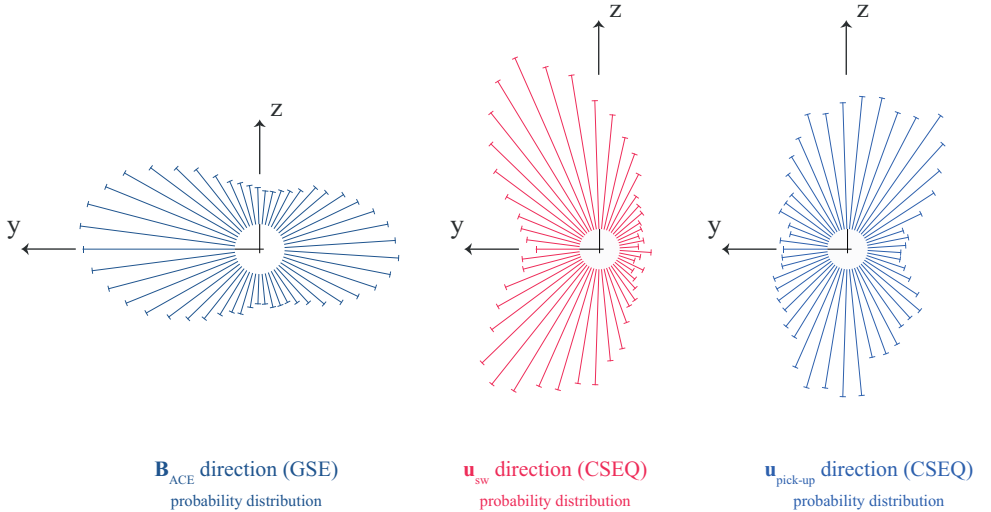


**Figure 2.** Probability distributions of the vector directions projected in the  $(y, z)$ -plane.

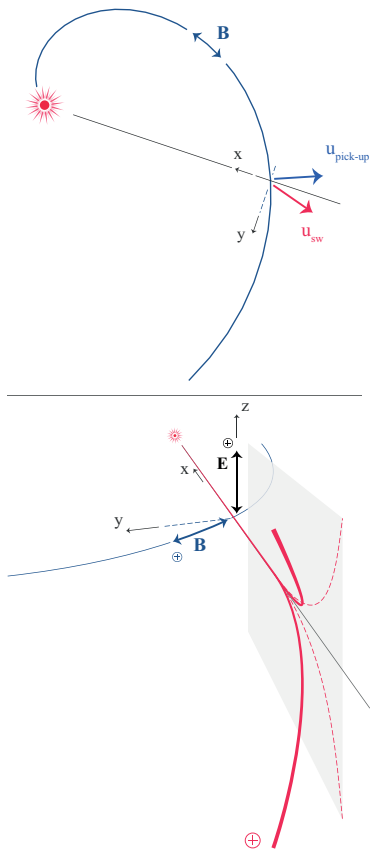


**Figure 3.** Schematics of the dynamics, for the solar wind ions (red) and the cometary pick-up ions (blue). Irrespective of the sense of the IMF along the Parker spiral, the solar wind proton velocity will gain a component along the  $+y$ -axis (dusk), while the cometary pick-up ions gain a negative  $-y$ -component (dawn).

selections of the energy- and mass-channel range where a significant signal is seen, as presented in Behar et al. (2016) and Berčič et al. (2018), one can separate solar wind protons and cometary pick-up ions through most of the mission. Another cometary ion population – the new-born ions – is observed, and is excluded from the cometary pick-up ions selection. Based on these selections, plasma moments are integrated. The aberration caused by the motion of the comet around the Sun is corrected, with barely any effect. We use here the bulk velocity of each of the two populations expressed in the body-centred solar equatorial (CSEQ) reference frame: the  $x$ -axis points to the Sun, the  $z$ -axis is perpendicular to the  $x$ -axis and oriented by the Sun’s north pole, the  $y$ -axis completes the right-handed triad. The  $(x, y)$ -plane and the Sun’s equatorial plane are thus close to parallel (separated by  $7^\circ$ , neglected here). As the rotation of the nucleus is prograde, the dusk is along the  $+y$ -axis and the dawn is along the  $-y$ -axis. The results shown in Fig. 2 were taken between

the beginning of the active mission, 2014 August 6 (3.6 au), and the end of the mission, 2016 September 30 (3.8 au). When the spacecraft is within the solar wind ion cavity (from early 2015 June to 2015 mid-December, see Behar et al. 2017), solar wind protons are not observed, and cometary pick-up ion data are also not considered. The resulting data set is about 21-monthlong.

Solar wind magnetic field data at 1 au, retrieved from the *OMNI-Web Plus* interface, have a time resolution of 5 min. For this precise time period, the data were obtained by the *ACE* probe (Smith et al. 1998) and the *WIND* probe (Lepping et al. 1995). The IMF direction is expressed in the Geocentric Solar Ecliptic (GSE) reference frame, with the  $x$ -axis pointing towards the Sun, the  $z$ -axis orthogonal to the  $x$ -axis and parallel to the ecliptic north pole ( $7.2^\circ$  away from the Sun’s rotation axis), and the  $y$ -axis completing the right-handed system. Based on these definitions, the IMF is expected to be on average in the  $(x, y)$  plane, both at Earth and 67P/CG. To that extent, the use of *ACE* data is more illustrative than necessary. It also quantifies how variable the IMF was over the same period.

The magnetic field measured at 1 au is projected in the  $(y, z)$ -plane of the GSE frame, and a probability distribution function of its direction is obtained for all data measured between 2014 August and 2016 September. The result is shown in Fig. 2, left-hand panel. In the context of this figure, the direction of a vector is given by its orientation and its sense. As expected, two peaks are found close to the  $y$ -axis due to the Parker spiral average configuration of the IMF. An apparent tilt in the distribution is found as well as an asymmetry in the maximum probability of the two peaks. The same analysis was done over a 2-month wide sliding window, verifying that these aspects result from the statistical fluctuations. The exact same procedure is done with the proton and pick-up cometary ion bulk velocities and shown in Fig. 2 centre and right-hand panels, respectively. All available bulk velocities (one per 3-min long scan) over the mission are filtered as following: only densities above  $10^{-3} \text{ cm}^{-3}$  and only vectors that are further than  $20^\circ$  away from the Sun–comet line are considered. These two thresholds, however arbitrary, allows to consider signals in the proper range of the instrument sensitivity and with a well-defined orientation in the  $(y, z)$ -plane. Considering all data, without filters on the density and the flow direction, gives the exact same results with less-pronounced features. About 62000 data points are binned for the solar wind protons, and about 56000 for the cometary pick-up ions. The protons display two peaks with either a positive or a negative  $z$ -component, both with a positive  $y$ -component (dusk). Similarly, the probability distribution of the cometary ion direction has two peaks along  $+z$  and  $-z$ , and the probability distribution has a general shift towards the  $-y$  direction (dawn). This general shift appears far away from the Sun as well, at the largest heliocentric distances *Rosetta* has probed, and is at zero-order constant with the heliocentric distance (not shown here).

The  $x$ -component of all the probability distributions of Fig. 2 depends on the heliocentric distance. The angle between the Sun–Earth line and the magnetic field orientation, measured to be of about  $45^\circ$  at 1 au, would increase and tend to  $90^\circ$  with increasing heliocentric distances. Therefore, the  $(x, y)$ -projection of the probability distribution of the magnetic field direction measured at Earth is not relevant for the comet. Concerning the ions measured at the comet, the angle between their bulk velocity and the Sun–comet line has shown strong evolution with heliocentric distances. For instance, the solar wind deflection has been observed from about  $10^\circ$  up to  $180^\circ$  (Behar et al. 2017). Therefore, the  $(x, y)$ -projection of their distribution integrated over the entire mission, does not provide a valuable information.

#### 4 PHASE SPACE DISTRIBUTION FUNCTION AND MOMENTUM EXCHANGE

The shift towards the  $-y$  direction (dawn) of the cometary pick-up ions is not as pronounced as for the solar wind protons (dusk). The reason for this may be instrumental, one possibility being that the selected pick-up ions may be contaminated by cold cometary ions (see Stenberg Wieser et al. (2017); Berčič et al. 2018). It may also be purely physical. The distribution function of cometary pick-up ions was observed to get more complex when close to the Sun, as reported by Nicolaou et al. (2017) in two case studies. In one of the cases, a partial ring distribution function is found for the cometary pick-up ions, compatible with their gyration in the coma. The average orientation of such a distribution function and its effects on the result of Fig. 2 is not obvious. However, these partial ring distributions are still rare in ICA observations, and their average shape in the CSEQ reference frame is thus not accessible. Further statistical investigation is needed to find out if and when the cometary ion distribution function at the spacecraft location turns from non-gyrotropic to gyrotropic.

We also note that additionally, the solar wind ions did not have perfect beam-like distribution functions at all time either, at the spacecraft position. In Behar et al. (2017), Fig. 2, partial ring distributions of solar wind protons are shown, observed at around 2 au, when the solar wind ion cavity was about to pass over the spacecraft location. The fact that only partial ring distributions were observed at 67P/CG stresses out that, as discussed previously, in the day side of the coma and close to the nucleus, solar and cometary ions have only followed part of one gyration, with a gyroradius following the evolution of the density ratio between the two populations (Behar et al. 2018b). This is most likely why the bulk velocities exhibit such a clear statistical behaviour.

It was verified that including or not heliocentric distances below 2.5 au does not change the result, qualitatively, therefore these more complex distributions do not change the observed asymmetry at a statistical level.

The two peaks of the probability distribution of the magnetic field direction indicate that, as expected, the solar wind electric field is mostly directed along either  $+z$  ( $B$  along  $+y$ ) or  $-z$  ( $B$  along  $-y$ , accordingly with equation 1). Thus, upstream of the measurement point where the solar wind first meets the new-born ions, the exchange of momentum between the solar wind and the thin coma happens along the  $z$ -axis. However, within the coma close to the nucleus, protons are seen with a positive  $y$ -component and cometary ions with a negative one, consistently with the generalized gyromotion presented here above, as in the case of a non-perpendicular magnetic field. Therefore, the motion of both populations is not contained in a single plane through the coma, as illustrated in the bottom panel of Fig. 3. In this schematic, the exchange of momentum initially takes place in the grey plane, but immediately the proton red trajectory will get a component along the  $y$ -axis and get out of the plane. Depending on the direction of the magnetic field, the trajectory will be deflected towards  $+z$  or  $-z$  but with a  $+y$ -component in both cases.

An obvious reason for the upstream magnetic field to not be perpendicular with the solar particle flow, and therefore along the  $y$ -axis, is the angle of its spiral configuration (Fig. 3).

Despite large heliocentric distances (with a maximum distance of 3.8 au), the IMF upstream of 67P/CG always had on an average an angle different than  $90^\circ$  with the  $x$ -axis (theoretically, the Parker angle spiral at 3.8 au is expected to be about  $75^\circ$  Cravens 2004). Thus as shown by the generalized gyromotion, on an average, the sense of the IMF along the spiral and additionally their deflection

towards the  $\pm z$ -axis does not matter, the protons will have a positive  $v_y$ -component at all heliocentric distances towards the dusk side of the coma, and the cometary pick-up ions will have a negative  $v_y$ -component at all heliocentric distances towards the dawn side of the coma.

#### 5 CONCLUSIONS

By generalizing the gyromotion of two populations interacting with each other and working in a precise reference frame, it was shown that the solar wind ions and the cometary pick-up ions are expected to drift sideways, with drifts of opposite signs, regardless of the magnetic field sense.

The statistical approach at comet 67P/CG over a period of 21 months allowed us to overcome the lack of measurement upstream of the interaction region. Based on data, it was demonstrated that indeed both populations have a velocity component contained in the IMF plane, misaligned with the Sun–comet line, irrespective of the heliocentric distance. Since ions move along less than a gyro-period, this velocity component does not strictly correspond to a drift. This additional velocity component is duskward for the solar wind protons, while cometary pick-up ions have a dawnward additional velocity component, irrespective of the outward or inward magnetic field in the Parker spiral.

In this article, we only describe an average configuration. An orientation of the IMF that would depart from the Parker spiral would obviously results in different orientations of the velocity vectors as well, which in fact corresponds to the breadth of the probability distributions in Fig. 2. Qualitatively, the configuration is only rotated around the Sun–comet line. In a plasma frame in which the upstream electric field would have the same orientation and sense at any time (the Comet–Sun Electric field frame for instance, in which the electric field is along the  $z$ -axis and the  $x$ -axis pointing towards the Sun), the probability distributions would be much narrower (and of different shape). However, this work demonstrates that such a plasma frame cannot be obtained properly, without monitoring the upstream solar wind parameters. In Behar et al. (2017) and Berčič et al. (2018), a proton-aligned reference frame, based on the observed solar wind proton direction, was used. We now see that such a proton-aligned frame is on an average rotated from the orientation of the upstream solar wind electric field. We note that this rotation has no impact on the results of these studies.

#### ACKNOWLEDGEMENTS

This work was supported by the Swedish National Space Board (SNSB) through grants 108/12, 112/13, and 96/15.

We are indebted to the whole *Rosetta* mission team, Science Ground Segment, and *Rosetta* Mission Operation Control for their hard work making this mission possible.

#### REFERENCES

- Behar E. et al., 2018a, A&A, submitted
- Behar E., Nilsson H., Alho M., Goetz C., Tsurutani B., 2017, *MNRAS*, 469, S396
- Behar E., Nilsson H., Stenberg Wieser G., Nemeth Z., Broiles T. W., Richter I., 2016, *Geophys. Res. Lett.*, 43, 1411
- Berčič L., Behar E., Nilsson H., Nicolau G., Stenberg Wieser G., Wieser M., Goetz C., 2018, A&A
- Behar E., Tabone B., Saillenfest M., Henri P., Deca J., Lindkvist J., Holmström M., Nilsson H., 2018b, A&A, submitted

- Coates A., 2004, *Adv. Space Res.*, 33, 1977
- Cravens T., 2004, *Physics of Solar System Plasmas*. Cambridge Univ. Press, Cambridge
- Dubinin E. et al., 2008, *Planet. Space Sci.*, 56, 832
- Flammer K. R., Mendis D. A., 1991, *Ap&SS*, 182, 155
- Hansen K. C. et al., 2007, *Space Sci. Rev.*, 128, 133
- Harada Y., Halekas J. S., Poppe A. R., Tsugawa Y., Kurita S., McFadden J. P., 2015, *J. Geophys. Res.*, 120, 4907
- Jarvinen R., Kallio E., Dyadechkin S., 2013, *J. Geophys. Res.*, 118, 4551
- Koenders C., Goetz C., Richter I., Motschmann U., Glassmeier K.-H., 2016, *MNRAS*, 462, S235
- Lepping R. P. et al., 1995, *Space Sci. Rev.*, 71, 207
- Nicolaou G., Behar E., Nilsson H., Wieser M., Yamauchi M., Berčič L., Wieser G. S., 2017, *MNRAS*, 469, S339
- Nilsson H. et al., 2007, *Space Sci. Rev.*, 128, 671
- Rubin M. et al., 2014, *Icarus*, 242, 38
- Schmidt H. U., Wegmann R., Neubauer F. M., 1993, *J. Geophys. Res.*, 98, 21009
- Smith C. W., L’Heureux J., Ness N. F., Acuña M. H., Burlaga L. F., Scheifele J., 1998, *The Ace Magnetic Fields Experiment*. Springer Netherlands, Dordrecht
- Stenberg Wieser G. et al., 2017, *MNRAS*, 469, S522
- Szegő K. et al., 2000, *Space Sci. Rev.*, 94, 429

This paper has been typeset from a  $\text{\LaTeX}$  file prepared by the author.





# Solar wind dynamics around a comet

## A 2D semi-analytical kinetic model

E. Behar<sup>1,2</sup>, B. Tabone<sup>3</sup>, M. Saillenfest<sup>4</sup>, P. Henri<sup>5</sup>, J. Deca<sup>6,7</sup>, J. Lindkvist<sup>8</sup>, M. Holmström<sup>1</sup>, H. Nilsson<sup>1</sup>

<sup>1</sup> Swedish Institute of Space Physics, Kiruna, Sweden.

<sup>2</sup> Luleå University of Technology, Department of Computer Science, Electrical and Space Engineering, Kiruna, Sweden

<sup>3</sup> LERMA, Observatoire de Paris, PSL Research University, CNRS, Sorbonne Université, UPMC Univ. Paris 06, 75014 Paris, France

<sup>4</sup> IMCCE, Observatoire de Paris, PSL Research University, CNRS, Sorbonne Université, UPMC Univ. Paris 06, LAL, Université de Lille, 75014 Paris, France

<sup>5</sup> LPC2E, CNRS, Orléans, France

<sup>6</sup> Laboratory for Atmospheric and Space Physics (LASP), University of Colorado Boulder, Boulder, Colorado 80303, USA

<sup>7</sup> Institute for Modeling Plasma, Atmospheres and Cosmic Dust (IMPACT), NASA/SSERVI, Boulder, Colorado 80303, USA

<sup>8</sup> Umeå University, Department of Physics, Umeå, Sweden

e-mail: etienne.bear@irf.se

Received 2018-01-31; accepted 2018-04-28

### ABSTRACT

**Aims.** We aim at analytically modelling the solar wind proton trajectories during their interaction with a partially ionised cometary atmosphere, not in terms of bulk properties of the flow but in terms of single particle dynamics.

**Methods.** We first derive a generalised gyromotion, in which the electric field is reduced to its motional component. Steady-state is assumed, and simplified models of the cometary density and of the electron fluid are used to express the force experienced by individual solar wind protons during the interaction.

**Results.** A three-dimensional (3D) analytical expression of the gyration of two interacting plasma beams is obtained. Applying it to a comet case, the force on protons is always perpendicular to their velocity and has an amplitude proportional to  $1/r^2$ . The solar wind deflection is obtained at any point in space. The resulting picture presents a caustic of intersecting trajectories, and a circular region is found that is completely free of particles. The particles do not lose any kinetic energy and this absence of deceleration, together with the solar wind deflection pattern and the presence of a solar wind ion cavity, is in good agreement with the general results of the *Rosetta* mission.

**Conclusions.** The qualitative match between the model and the *in situ* data highlights how dominant the motional electric field is throughout most of the interaction region for the solar wind proton dynamics. The model provides a simple general kinetic description of how momentum is transferred between these two collisionless plasmas. It also shows the potential of this semi-analytical model for a systematic quantitative comparison to the data.

**Key words.** Comets: general, Methods: analytical, Plasmas

## 1. A global model

The plasma interaction between the solar wind and a cometary atmosphere (coma) offers a unique situation in the solar system. The absence of an intrinsic magnetic field, the typical small size of the nucleus, and its negligible gravity combined with its highly elliptical orbit result in an ever changing interaction, in which the coma continuously and completely escapes the comet, dragged away by the magnetised stream of solar particles. These properties also result in one of the largest obstacles to the solar wind in the solar system. At comet Halley, the first cometary ions were detected 7.8 million kilometres away from the nucleus by the *Giotto* probe (Johnstone et al. 1986), a distance comparable to the day-side extent of the Jovian magnetosphere.

A major advance to comprehend this interaction was proposed by Alfvén (1957), who emphasised the role of the solar wind magnetic field in the formation of the cometary tails. Biermann et al. (1967) proposed a model of the day-side of a comet atmosphere in a hydrodynamical description of the interaction. These and all the previous efforts were tackling the features of

the comet's head and tails that were visible from Earth, naturally directing the scientific interest towards strongly outgassing comets close to their perihelion. In the next two decades, space probes were leaving Earth targeting such active comets, and at Giacobini-Zinner and Halley, what had previously been invisible became visible: a whole set of plasma structures came within the reach of scientists (Grewing et al. 1988; Cowley 1987; Gombosi 2015).

Between 2014 and 2016, the *Rosetta* spacecraft cohabited for more than two years with its host body, comet 67P/Churyumov-Gerasimenko (67P/CG), enabling for the first time observations at large heliocentric distances ( $> 3$  au). Scientists were given the opportunity to witness the early interaction between a young tenuous coma and the solar wind, far away from the Sun. The nature of such an interaction was entirely new. Indeed, whereas at previously visited comets the interaction region was much larger than the scale of the ion gyromotion, resulting in what one could call a "fluid comet", for which the classical fluid treatment of the plasmas applies, at 67P/CG and at large heliocentric distances, the ion transit timescale through the coma is shorter than its gy-

roperiod, resulting in a "kinetic comet" for which no analytical approach is available so far.

Using *in situ* measurements, the evolution of this interaction was followed carefully (Behar et al. 2016a; Nilsson et al. 2017) resulting in some surprising findings. Initially barely disturbed, the solar wind started displaying a peculiar behaviour as the nucleus was getting closer to the Sun. Its flow slowly diverged from the Sun-comet direction, to eventually be seen flowing almost back towards the Sun at speeds of hundreds of kilometres per second. Eventually, the flow vanished from the *in situ* measurements: a void of solar ions was formed around the nucleus, while no severe deceleration was observed (Behar et al. 2017). The same interaction – for large to intermediate heliocentric distances – was also tackled by several simulation efforts, using hybrid particle-in-cell models (Bagdonat & Motschmann 2002; Hansen et al. 2007; Koenders et al. 2016a; Behar et al. 2016a), as well as a fully kinetic model (Deca et al. 2017). At heliocentric distances down to less than 2 au, simulations result in a highly asymmetric plasma environment. In particular, the solar wind presents a structure of high ion density only seen in the hemisphere of the coma opposite to the direction of the upstream electric field, one of the typical signatures of such a kinetic comet. This structure is interpreted as a Mach cone by Bagdonat & Motschmann (2002), a term adopted in several of the cited simulation studies. However until now, this asymmetric structure was only found in numerical models with intricate physics, and generally lacks the physical interpretation which would elucidate the experimental results exposed above.

Our goal is to understand and analyse the mechanism which transfers momentum between the solar wind and the coma, leading to such a deflection of a barely decelerated flow, in the absence of collisions. Additionally, we aim at providing novel insight into the nature of this asymmetric solar wind structure, which may be considered as the very seed of a cometary magnetosphere.

The present attempt to model the interaction puts the emphasis on the role of the motional electric field by considering the parameter space region, in which currents orthogonal to the magnetic field and pressure gradients can be neglected. Under these conditions, any noticeable disturbances of the flow necessarily result from the integrated interaction with and through the smooth and extended obstacle. This is in contrast to the situation at more classical and massive solar system bodies with intrinsic magnetic fields, dense and limited atmospheres, or conductive cores inducing a magnetic feedback to the solar wind. There, contrasted plasma structures and boundaries are formed, such as bow shocks, magnetopauses, induced magnetospheric boundaries or ionopauses. The obstacle to the solar flow is therefore compact and localised. Similar plasma boundaries may also appear at comets. For example, weak bow shocks were observed at comets Halley, Giacobini-Zinner, Grigg-Skjellerup and Borrelly (Coates 2009). However, such boundaries are only formed close to the Sun, and even in that case, the neutral atmosphere extends further out (a weak bow shock was observed about a million kilometres away from comet Halley's nucleus, after the detection of the first cometary ions (Johnstone et al. 1986)), and mass-loading (the addition of new-born cometary ions to the solar wind) takes place, whether boundaries are formed closer to the nucleus or not. Therefore the present model should be representative and relevant for the region beyond the potential bow shock which forms when a comet gets closer to the Sun.

To infer the global behaviour of a system, whenever possible, an analytical model may overcome intrinsic limitations of *in situ* data (one-point measurement, instrumental errors and limitations) and simulation data (simulation of only a finite region of space, intricate physics, numerical limitations). While doing so, it allows to encapsulate one or a few of the driving mechanisms of a system in a reduced form, though at the cost of realism. In the present series of articles, the synergy between these three approaches – experimental data, numerical simulations, and theoretical models – is explored. This article focuses on the physical model and provides an expression for the force experienced by single solar wind protons, through the extended coma. The corresponding dynamics is thoroughly solved by Saillenfest et al. (2018), a solution widely used in the present work. The semi-analytical model we propose is computationally very cheap, and allows for a systematic comparison to each and every *in situ* data point. This extended comparison, together with the comparisons to numerical simulations, follows in subsequent articles of the series.

The model developed in the following sections requires several sub-models. One is a description of the ionised coma and its density distribution, following the same need for simplicity-to-relevancy ratio. The second is a description of the electric field and the magnetic field, which piles up due to the local decrease in the average velocity of the electrons, as slow new-born cometary ions are added to the flow. The motional electric field is completely dependent on the motion of the particles, which itself depends on the electric and magnetic fields. This inter-dependency is tackled in the following section as a generalised gyromotion, and results in a three-dimensional (3D) model of its own.

## 2. Generalised gyromotion

In this section, we derive the general dynamics of the interaction between two collisionless beams of plasma that are only subject to the Lorentz force. The subscripts *sw* and *com* are used for parameters and values of the solar wind and the cometary ion populations, respectively. The characteristic length, time, and velocity of the system are  $\ell$ ,  $t$  and  $u$ .  $\mathbf{E}$  and  $\mathbf{B}$  are the electric and the magnetic field,  $\mathbf{u}_i$  is the average velocity of all charges carried by ions,  $n$  is the plasma number density,  $e$  is the elementary charge,  $\mathbf{j}$  is the electric current and  $\mathbf{P}_e$  is the electron pressure.

Our starting point is the simplified Ohm's law, in which the electron inertial and the resistivity/collisional terms are neglected (see, e.g. Valentini et al. (2007)). The plasma is weakly magnetised and quasi-neutral. The system is considered to be at steady state:  $\partial_t \cdot \equiv 0$ .

$$\mathbf{E} = -\mathbf{u}_i \times \mathbf{B} + \frac{1}{ne} \mathbf{j} \times \mathbf{B} - \frac{1}{ne} \nabla \mathbf{P}_e. \quad (1)$$

The total electric field exhibits three distinct components: the motional electric field, the Hall term, and the pressure gradient term. Analysing orders of magnitude in these three terms, as well as in the Ampère's law, the Faraday's law, and the Lorentz force, the following orderings can be found.

$$\begin{aligned} \ell \gg d_i &\Rightarrow |\mathbf{u}_i \times \mathbf{B}| \gg 1/ne |\mathbf{j} \times \mathbf{B}| \\ \ell_P \gg r_{ge} v_{the}/u &\Rightarrow |\mathbf{u}_i \times \mathbf{B}| \gg 1/ne |\nabla \mathbf{P}_e| \end{aligned} \quad (2)$$

In these expressions,  $d_i$  is the ion inertial length, and  $\ell_P$  is the characteristic length of the pressure gradient.  $r_{ge} = m_e u_e / (eB)$  is



the electron gyroradius and  $v_{the} = \sqrt{2kT_e/m_e}$  the electron thermal speed. At these scales (Eq. (2)), the electric field is reduced to

$$\mathbf{E} = -\mathbf{u}_i \times \mathbf{B}. \quad (3)$$

This directly implies that the currents perpendicular to the magnetic field are negligible for scales  $\ell \gg d_i$ . The average velocity  $\mathbf{u}_i$  in the case of our two beams can be reduced to only two terms:

$$\begin{aligned} \mathbf{u}_i &= \xi_{sw} \mathbf{u}_{sw} + \xi_{com} \mathbf{u}_{com} \\ \xi_{sw} &= \frac{n_{sw} q_{sw}}{n_{sw} q_{sw} + n_{com} q_{com}}; \xi_{com} = \frac{n_{com} q_{com}}{n_{sw} q_{sw} + n_{com} q_{com}}. \end{aligned} \quad (4)$$

In the absence of any force other than the Lorentz force, the dynamics of a single particle in either of the two populations is described by the following system of ordinary differential equations:

$$\begin{cases} \dot{\mathbf{u}}_{sw} = q_{sw}/m_{sw} (\mathbf{E} + \mathbf{u}_{sw} \times \mathbf{B}) \\ \dot{\mathbf{u}}_{com} = q_{com}/m_{com} (\mathbf{E} + \mathbf{u}_{com} \times \mathbf{B}) \end{cases} \quad (5)$$

Considering two initially perfect beams in velocity space, we have  $\mathbf{u}_{com} = \mathbf{u}_{com}$  and  $\mathbf{u}_{sw} = \mathbf{u}_{sw}$ : all particles of the population experience the same acceleration at the same time. The temperature is not defined.

Without loss of generality, one can choose a frame in which the magnetic field is directed along the y-axis. With (3), (4), (5), and  $q_{sw} = q_{com} = q$ :

$$\begin{cases} \dot{\mathbf{u}}_{sw} = \frac{q \xi_{com} B}{m_{sw}} (\mathbf{u}_{sw} - \mathbf{u}_{com}) \times \hat{\mathbf{y}} \\ \dot{\mathbf{u}}_{com} = -\frac{q \xi_{sw} B}{m_{com}} (\mathbf{u}_{sw} - \mathbf{u}_{com}) \times \hat{\mathbf{y}} \end{cases} \quad (6)$$

A first important result is that there can be no particle acceleration along the magnetic field.

A second noteworthy result is that the velocity of the centre of mass, defined as

$$\mathbf{v}_i = \frac{n_{sw} m_{sw}}{n_{sw} m_{sw} + n_{com} m_{com}} \mathbf{u}_{sw} + \frac{n_{com} m_{com}}{n_{sw} m_{sw} + n_{com} m_{com}} \mathbf{u}_{com} \quad (7)$$

is conserved through time,  $\dot{\mathbf{v}}_i = \mathbf{0}$ . This holds over spatial scales shorter than  $\ell$  and  $\ell_p$ , and if no mass is added. The equations of motion have the general form  $\dot{\mathbf{u}} = \omega \mathbf{u} \times \hat{\mathbf{y}}$ . In velocity space, the two beams move along circles perpendicular to the magnetic field (no acceleration along the magnetic field), as shown in Fig. 1.

If the two beams have initially the same parallel velocity (velocity component along the magnetic field), the two circles are in one and the same plane, centred on  $\mathbf{v}_i$ , independent of any change of inertial frame. This can easily be seen in Fig. 1. Then in the frame in which  $\mathbf{v}_i = \mathbf{0}$ , the two populations describe

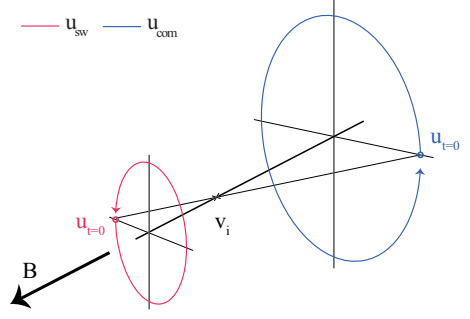


Fig. 1. Evolution in velocity space of two interacting beams of plasma, for the most general configuration.

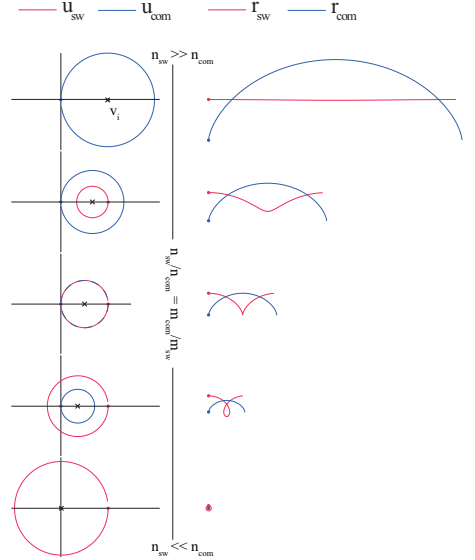


Fig. 2. Evolution of both populations in velocity and physical space (left and right columns, respectively), projected in the plane perpendicular to the magnetic field in the comet frame for different density ratios (top to bottom).  $\mathbf{v}_i$  is shown with a black cross in the left column.

circles in velocity and physical space. The generalised gyrofrequency and gyroradii are then:

$$\begin{aligned} \mathcal{R}_{sw} &= |\mathbf{u}_{sw}|/\omega \\ \mathcal{R}_{com} &= |\mathbf{u}_{com}|/\omega \\ \omega &= eB \frac{n_{sw} m_{sw} + n_{com} m_{com}}{(n_{sw} + n_{com}) m_{sw} m_{com}} \end{aligned} \quad (8)$$

Still considering the case where both populations have the same initial parallel velocity, one can also always choose an inertial Cartesian frame in which  $\mathbf{u}_{sw}$  is along the x-axis, and  $\mathbf{u}_{com} = \mathbf{0}$ . This frame is referred to as the comet frame,

and is used in Fig. 2. Both beams describe circles in velocity space with the same angular speed and the same centre  $\mathbf{v}_i$ . The corresponding motion of the ions in physical space is a trochoid, the most general two-dimensional (2D) gyromotion. In the comet frame, the particles belonging to the cometary population (*com*) describe a more classical cycloid, as they periodically reach a velocity equal to  $\mathbf{0}$ . In Fig. 2, one can see that as the density ratio increases,  $|\mathbf{v}_i|$  becomes closer to the origin. This can be interpreted as the corresponding slowing down of the plasma fluid for spatial scales much larger than the generalised gyroradius.

We note that if neither the ions nor the electrons have a velocity component parallel to the magnetic field, and they will not gain such a component during the interaction. We therefore obtain  $\mathbf{u}_i = \mathbf{u}_e$ . More generally, this equality is only verified if at any point in time, electrons and ions have the same parallel velocity, independent of the reference frame.

The dynamics depends greatly on the density ratio. If  $n_{sw} \gg n_{com}$ , then  $\mathbf{v}_i \sim \mathbf{u}_{sw}$  (top-part in Fig. 2), and the seldom cometary ions behave as test particles in the almost undisturbed flow of the population *sw*. The cycloid has then a radius equal to the cometary ion Larmor radius. As the density ratio  $n_{com}/n_{sw}$  increases, particles of the cometary population still describe a cycloid, though the corresponding radius decreases. When the density ratio is equal to the inverse of the mass ratio, both populations move along cycloids of equal radius, as seen in the middle panel of Fig. 2.

If the beams do not have the same initial parallel velocity, independent of the choice of frame, at least one of the populations will drift along the  $y$ -axis at a constant speed. This is the case in the comet frame, when accounting for the Parker spiral angle: both populations present an additional drift perpendicular to the  $x$ -axis, with opposite directions. Flipping the sense of the magnetic field does not change the direction of the drift, and the average Parker spiral configuration of the interplanetary magnetic field induces a dawn-dusk asymmetry in the ion dynamics around the comet. This topic is tackled in Behar et al. (2018 (Under revision), based on statistics over the entire mission, and is based on this generalised gyromotion.

This generalised gyromotion is a collisionless 3D description of such a beam-beam interaction, much broader than the following 2D application for a comet.

### 3. Generalised gyromotion in a cometary atmosphere

We will now see to what extent this generalised gyromotion can describe the dynamics of the solar wind during its interaction with a comet. In order to resolve the equation of motion for the solar wind protons in Eq. (6), we need to express three main parameters, namely the cometary ion density and velocity, and the magnetic field.

#### 3.1. Cometary ion density

The spatial distribution of the cometary ions is a major ingredient of the model, as it defines what obstacle is presented to the solar wind. The cometary atmosphere is assumed to have a spherical symmetry. For this exercise, the size of the nucleus is negligible,

and so is its mass: the neutral elements, produced at a rate  $Q$ , are expanding radially in all directions with a constant speed  $u_0$ . We assume these particles to be water molecules,  $H_2O$ . They are ionised or photo-dissociated at a rate  $\nu_d$ . By writing the equation of continuity with source terms on the cometary neutral density  $n_0$ , we obtain, in this spherical symmetry,

$$\frac{1}{r^2} \frac{d(r^2 n_0 u_0)}{dr} = -\nu_d n_0, \quad (9)$$

with the following solution established and used by Haser (1957):

$$n_0(r) = \frac{Q}{4\pi u_0 r^2} \cdot e^{-r/R_d} \quad ; \quad R_d = u_0/\nu_d. \quad (10)$$

The cometary ions are created by ionisation of the neutral particles with a rate  $\nu_i$ . They have the initial radial velocity  $\mathbf{u}_0$  but will immediately be accelerated by the local electric and magnetic fields, to eventually escape the region of the denser coma. We separate the ionised coma into two different cometary ion components: the new-born cometary ions first, which are the main obstacle to the solar wind, and second the accelerated (or pick-up) cometary ions. The dynamics of the first population is assumed to be trivial: the new-born cometary ions move radially away from the nucleus with the same speed as the neutral molecules. The dynamics of the second, however, is much more complex, driven mostly by the mass-loading mechanism, meaning that the pick-up cometary ions leave the system quicker than they would have ballistically. New born ions become pick-up ions at a rate of  $\nu_{ml}$ . Accordingly, a destruction term appears in the continuity equation of the new-born cometary ions:

$$\frac{1}{r^2} \frac{d(r^2 n_{com} u_0)}{dr} = \nu_i n_0 - \nu_{ml} n_{com}. \quad (11)$$

With  $R_i = u_0/\nu_i$  and  $R_{ml} = u_0/\nu_{ml}$

$$n_{com}(r) = \frac{1}{R_i R_d - R_{ml}} \left( 1 - e^{-r \left( \frac{1}{R_{ml}} - \frac{1}{R_d} \right)} \right) \cdot n_0(r). \quad (12)$$

Three characteristic radii are found in the density profile. In Sect. 3.5, we see that  $R_{ml} \ll R_d < R_i$ . For  $r < R_{ml}$ , that is, before the new born ions are accelerated and neglected,  $n_{com}(r < R_{ml}) \propto 1/r$ , a result observed by the *Rosetta* mission at comet 67P/CG in the first  $\sim 200$  km from the nucleus, and discussed by Edberg et al. (2015). At the larger scales that we are interested in,  $R_{ml} \ll \ell \ll R_d$ , the neutral and the ion densities are proportional, while the exponential term is still negligible. Subsequently, we obtain

$$n_{com}(R_{ml} \ll r \ll R_d) = \frac{\nu_i}{\nu_{ml}} \frac{Q}{4\pi u_0} \cdot \frac{1}{r^2} \quad [m^{-3}]. \quad (13)$$

In this description, we have a steady creation and disappearance of the slow, new-born cometary ions that are constituting the bulk mass of the ionised coma, which interacts electromagnetically with the solar wind.

#### 3.2. Two-dimensional magnetic pile-up

Another important term to model in the equation of motion of the protons is the magnetic field  $\mathbf{B}$  within the coma. We first need to express  $\mathbf{u}_i$ , the total velocity of the ion fluid, in which the B-field is considered to remain frozen-in:

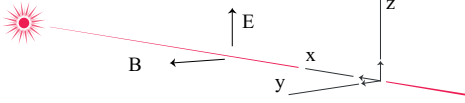


**Fig. 3.** Comet-Sun-Electric field frame of reference. The solar wind dynamics is considered in the plane  $y = 0$  only.

$$\mathbf{u}_i = \mathbf{u}_e = \frac{n_{sw}}{n_{sw} + n_{com}} \mathbf{u}_{sw} + \frac{n_{com}}{n_{sw} + n_{com}} \mathbf{u}_{com}. \quad (14)$$

Our goal is to solve for  $\mathbf{u}_{sw}$ , therefore necessarily some more assumptions have to be made in order to simplify the total ion velocity and remove degrees of freedom in the system.

We first define the Comet-Sun-Electric field reference frame, illustrated in Fig. 3, as follows: the upstream solar wind magnetic field is directed purely along the  $y$ -axis, with an amplitude  $B_{\infty}$ . The corresponding electric field according to Eq. (3) is along the  $z$ -axis with an amplitude  $E_{\infty} = u_{\infty} B_{\infty}$ . In this precise frame (comet-centred CSE),  $\mathbf{u}_{com} \ll \mathbf{u}_{sw}$ , and it can be shown with the help of Eq. (13) that in most of the interaction region,  $\mathbf{u}_i \sim \xi_{sw} \mathbf{u}_{sw}$ . The latter is in agreement with fully kinetic simulations of the interaction (e.g. Fig. 2 of Deca et al. 2017). In the generalised gyromotion, the asymmetry in the total ion velocity appears only because of the different masses of the two populations, as for identical masses  $\mathbf{u}_i = \mathbf{v}_i$  (see Sect. 2), that is, both not accelerated and remaining along the  $x$ -axis only.

As  $\mathbf{B}_{\infty}$  is along the  $y$ -axis (i.e. no Parker spiral angle),  $\mathbf{u}_{\infty}$  is along the  $x$ -axis and as the cometary outflow is spherical, the plane  $y = 0$  is a plane of symmetry of the system. Therefore, within  $y = 0$ , neither  $\mathbf{v}_i$  nor  $\mathbf{u}_i$  can have a component along  $\hat{\mathbf{y}}$  (corresponding to the fact that no particle acceleration happens along  $\mathbf{B}$ ). One more simplification is needed to be able to express the magnetic field. We assume that the total ion velocity remains along the  $x$ -axis and follows:

$$\mathbf{u}_i = -\xi_{sw} u_{\infty} \hat{\mathbf{x}}, \quad (15)$$

with  $\xi_{sw} > 0$  and  $u_{\infty} > 0$ . From Eq.(15) of the total ion velocity and Eq.(3) of the electric field, one finds that  $\mathbf{E} = (0, -u_i B_z, u_i B_y)$  with  $u_i = |\mathbf{u}_i| > 0$ . Additionally, the steady state Faraday's law  $\nabla \times \mathbf{E} = \mathbf{0}$  states that neither  $E_y$  nor  $E_z$  vary along  $x$ . Finally, in the plane of interest ( $y = 0$ ):

$$\mathbf{B} = \frac{B_{\infty}}{\xi_{sw}} \hat{\mathbf{y}}. \quad (16)$$

The magnetic field frozen in the ion fluid should – in the absence of a Hall term – depend on the motion of both the solar wind and cometary ions. Since the advection of the cometary ions is not solved, the total ion velocity cannot be consistently derived.

### 3.3. Solar wind proton dynamics

Considering the new-born cometary ion population, one can assume in the cometary frame that  $u_{com} \ll u_{sw}$ . Therefore, using (6), (15) and (16), we have

$$\begin{aligned} \mathbf{u}_{sw} &= \frac{e \xi_{com} B}{m_{sw}} \cdot \mathbf{u}_{sw} \times \hat{\mathbf{y}} \\ &= \frac{e v_i Q B_{\infty}}{4\pi m_{sw} n_{sw} v_{ml} u_0} \cdot \frac{1}{r^2} \cdot \mathbf{u}_{sw} \times \hat{\mathbf{y}} \quad [\text{m/s}] \end{aligned} \quad (17)$$

The force experienced by an individual solar wind proton is therefore of the form

$$\mathbf{F} = \frac{m_{sw} \eta}{r^2} \mathbf{u}_{sw} \times \hat{\mathbf{y}}. \quad (18)$$

The force is always perpendicular to the proton velocity, with a strength proportional to the inverse of the square distance  $1/r^2$ . The equation of motion for protons is then

$$\ddot{\mathbf{r}} = \frac{\eta}{r^2} \dot{\mathbf{r}} \times \hat{\mathbf{y}} \quad ; \quad \eta = \frac{e v_i Q B_{\infty}}{4\pi v_{ml} n_{sw} m_{sw} u_0} \quad [\text{m}^2/\text{s}]. \quad (19)$$

In this description, the solar wind protons do not lose energy and are only gyrating, with a gyroradius function of their distance to the nucleus only. This can also be seen as the motion of charged particles in an effective magnetic field always perpendicular to the plane of the motion, with an amplitude proportional to  $1/r^2$ . This is the core of the model, the reduced form of the solar wind proton interaction with a coma.

The dynamical system defined by (19) for solar wind protons is integrable. Its solutions are thoroughly studied in Saillenfest et al. (2018); here, we recall their main features. Let us introduce the polar coordinates  $(r, \theta)$  in the  $(x, z)$  plane of motion. The dynamical equations rewrite<sup>1</sup>:

$$\begin{cases} \ddot{r} - r\dot{\theta}^2 = -\frac{\eta}{r} \dot{\theta} \\ r\ddot{\theta} + 2\dot{r}\dot{\theta} = \frac{\eta}{r^2} \dot{r} \end{cases}, \quad (20)$$

where the dot means derivative with respect to time  $t$ . These coupled differential equations imply the conservation of kinetic energy  $E$  and a generalised angular momentum  $C$  that can be expressed as two characteristic radii:

$$\begin{cases} r_E = \frac{|\eta|}{u} \quad \text{where} \quad u = \sqrt{\dot{r}^2 + r^2 \dot{\theta}^2} \\ r_C = r \exp(1 - r^2 \dot{\theta} / \eta) \end{cases}. \quad (21)$$

Their respective values fully determine the trajectory, with a bifurcation occurring at  $r_C = r_E$ . As for  $1/r^3$  magnetic fields (Graef & Kusaka 1938), the solution  $(\theta, t)$  can be written as a function of  $r$  defined by an integral.

The solar wind particles can be considered as originating from infinity on initially parallel trajectories. Since they all have the same conserved velocity  $u = u_{sw}$ , the characteristic radius  $r_E$  acts only as a scaling parameter (whereas the particles of the solar wind span all the possible values of  $r_C$ ). With this setting, Saillenfest et al. (2018) show that around the nucleus at the origin, a circular cavity totally free of particles is created with radius<sup>2</sup>  $r_{cav} \approx 0.28 r_E$ .

<sup>1</sup> The coefficient  $k$  used by Saillenfest et al. (2018) is equal to  $-\eta$ .

<sup>2</sup> The exact radius of the cavity is  $r_{cav}/r_E = W_0(1/e)$ , where  $e = \exp(1)$  and  $W_0$  is the positive branch of the Lambert  $W$  function. Its first decimals are  $W_0(1/e) = 0.2784645427610738...$

**Table 1.** Nominal parameters used to get the value of  $\eta$ .

	1 au	4 au	law
$Q_i$	$2.6 \cdot 10^{28} \text{ s}^{-1}$	$2.2 \cdot 10^{25} \text{ s}^{-1}$	$\propto R^{-5.10}$
$Q_o$	$1.6 \cdot 10^{29} \text{ s}^{-1}$	$7.8 \cdot 10^{24} \text{ s}^{-1}$	$\propto R^{-7.15}$
$v_i$	$6.5 \cdot 10^{-7} \text{ s}^{-1}$	$1.8 \cdot 10^{-8} \text{ s}^{-1}$	$\propto R^{-2}$
$v_d$	$1.8 \cdot 10^{-5} \text{ s}^{-1}$	$1.1 \cdot 10^{-6} \text{ s}^{-1}$	$\propto R^{-2}$
$n_\infty$	$5.0 \text{ cm}^{-3}$	$0.3 \text{ cm}^{-3}$	$\propto R^{-2}$
$ \mathbf{B} $	4.6 nT	1.2 nT	$\propto (R - \alpha)/R$
$u_0$	0.7 km/s	0.7 km/s	-
$v_{ml}$	$0.01 \text{ s}^{-1}$	$0.01 \text{ s}^{-1}$	-
$\eta$	$1.7 \cdot 10^{13} \text{ m}^2 \text{ s}^{-1}$	$3.7 \cdot 10^9 \text{ m}^2 \text{ s}^{-1}$	-
$u_\infty$	400 km/s	400 km/s	-

The resulting trajectories are shown in Fig. 4. A portion of the incoming flux of particles is temporarily focussed along a very specific curve, defined as the crossing points of infinitely close neighbour trajectories. By analogy to light rays, we call it a “caustic”, resulting in an overdensity of particles. This caustic has a well-defined shape, which can be expressed as the root of the variational vector. It is plotted in Fig. 4 for different values of the scaling parameter  $r_E$ , which rescales according to the comet activity and the heliocentric distance. A similar overdensity curve can be observed in other contexts, such as a flux of charged particles in the equatorial plane of a magnetic dipole (Störmer 1930; Shaikhislamov et al. 2015), or the deflection of solar particles around the thin atmosphere of Pluto (McComas et al. 2008). This could indicate that analogous processes are at play. Further discussions regarding a general  $1/r^4$  law are given by Saillenfest et al. (2018).

We note that the notion of “impact parameter”,  $z_\infty = z(x \rightarrow \infty)$ , has no clear meaning for a  $1/r^2$  effective magnetic field (it is infinite for every particle). We should therefore express the problem in another way: we simply deal here with a far-enough starting distance for the particles, such that we can safely assume that their trajectories are parallel.

### 3.4. Third dimension

Outside of the plane ( $y = 0$ ), the magnetic field draping introduces an angle between the magnetic field and the normal to the Comet-Sun line. As previously mentioned, such an angle would result in an additional acceleration of the solar wind along the  $y$ -axis, and the dynamics out of the ( $y = 0$ )-plane would not be planar. Just as its pile-up, the draping of the magnetic field is also given by the bulk velocity of the ions, assuming the field is frozen in the ion flow. Therefore a generalisation of the model to the third spatial dimension would result in the same physics as this 2D approach in the ( $y = 0$ )-plane.

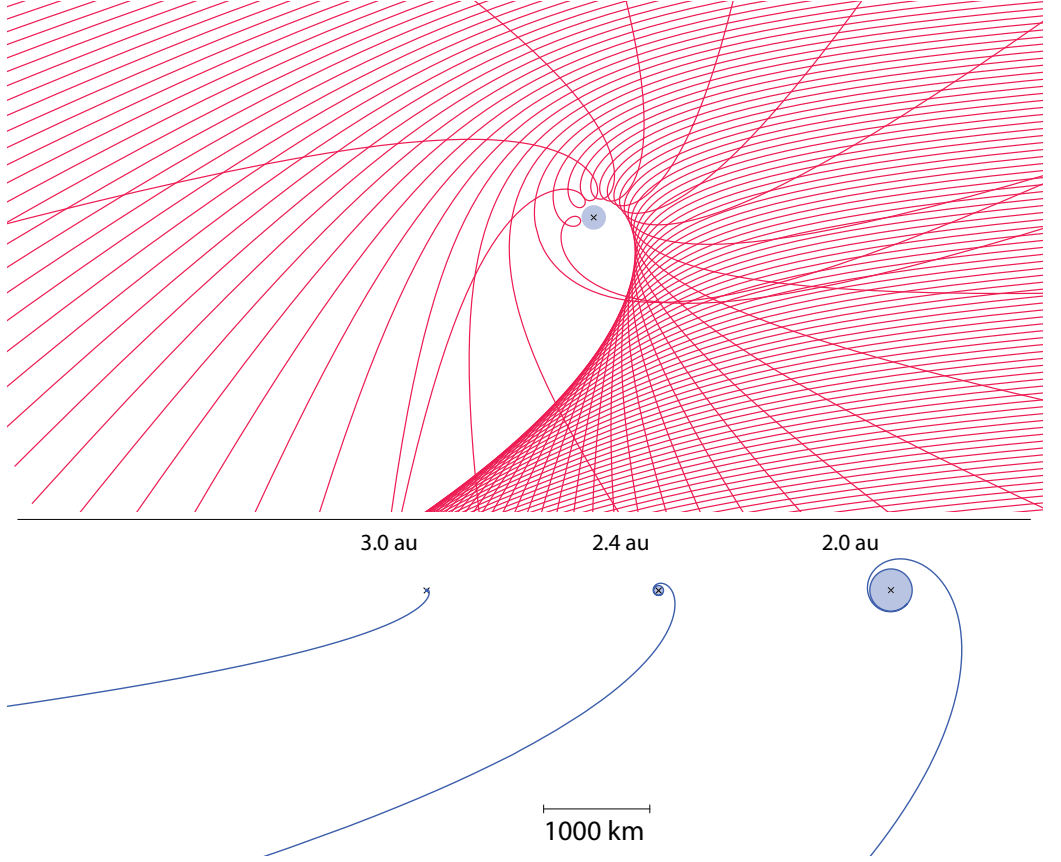
### 3.5. Parameters and scales

Table 1 gives the physical quantities in the factor  $\eta$  together with their evolution with the heliocentric distance  $R$ . At comet 67P/CG, the creation rate of neutral volatiles  $Q$  was found to be asymmetric around perihelion, with a higher activity after perihelion. A multi-instrument analysis can be found in Hansen

et al. (2016), resulting in an empirical analytical fit given in Table 1. When necessary, we use the notation  $Q_i$  for the pre-perihelion in-bound leg of the *Rosetta* mission, and  $Q_o$  for the post-perihelion out-bound leg. The drawback of this empirical model is a discontinuity in the value of  $Q$  at perihelion. The value of the destruction rate  $v_d$  and the ionisation rate  $v_i$  and their dependence on the heliocentric distance is taken from Crovisier (1989). The magnetic field function of the heliocentric distance can be found in Cravens (2004).

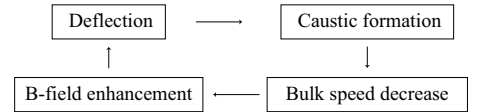
The rate  $v_{ml}$  at which new-born cometary ions are considered to turn into accelerated pick-up ions is arbitrary, but plays an important role in various parameters and scales of the model. It should be much larger than  $v_i$  and  $u_0/\ell$ , with  $\ell$  being the characteristic length scale of the system. A proxy of its value can be obtained from *in situ* data. In a mission overview, using the imaging spectrometer RPC-ICA onboard *Rosetta*, Nilsson et al. (2017) show that a large majority of cometary ions observed at the spacecraft are rather slow, typically below a few tenths of an electron Volt. Detaching from this cold population, accelerated cometary ions are observed with fluxes two to three orders of magnitude lower. In the case study of Behar et al. (2016b), which used data from the RPC-ICA instrument as well, most of the values needed for estimating  $v_{ml}$  can be found, with the exception of the proton and the cold cometary ion densities. Both densities are given here as the integrated plasma moment of order zero, on the same day. The data were taken on 2014-11-28, a day representative of the general cometary ion spectrum during the mission. An integrated spectrum (differential flux function of the energy per charge of the ions) is given in Fig. 5. The probe was 2.88 au from the Sun, 30 km away from the nucleus on a terminator orbit.

The cold ions reach energies up to 45 eV ( $22 \text{ km.s}^{-1}$ ), and have an average density of  $16.7 \text{ cm}^{-3}$ . The spacecraft potential, observed to be negative, on average, and often below  $-10 \text{ eV}$  (Odelstad et al. 2017), accelerates the positive ions towards the spacecraft, so that the ions collected by the instrument appear more energetic than they actually are in the cometary plasma. The peak in the flux of the cometary new-born ions at about 20 eV corresponds to much lower energies, closer to 0 eV: the population modelled by cometary ions at rest in the analytical model, disappearing with rate  $v_{ml}$ . Unfortunately, no spacecraft potential measurement is available on that day. The solar wind protons have an average speed of  $376 \text{ km.s}^{-1}$  (734 eV), with an average density of  $0.14 \text{ cm}^{-3}$ . One obtains a total ion fluid velocity of  $\xi_{sw} u_{sw} \sim 3.13 \text{ km.s}^{-1}$ . With an average magnetic field of about 15 nT as measured by RPC-MAG that day, the motional electric field is about  $0.05 \text{ mV.m}^{-1}$ . Assuming a constant acceleration, we get a very coarse duration of 77 s for the cometary ions to reach 45 eV. In summary, after about 77 seconds, slow new-born cometary ions surpass the kinetic energy of 45 eV ( $22 \text{ km.s}^{-1}$ ) and become ‘accelerated’ cometary ions, or pick-up cometary ions that have a density of  $0.28 \text{ cm}^{-3}$ . The corresponding rate  $v_{ml}$  is  $0.011 \text{ s}^{-1}$  (corresponding at this heliocentric distance to a value of  $r_E = 77.5 \text{ km}$ ). Moreover, on that precise day, it is fair to neglect the accelerated cometary ions, 60 times less dense than the cold ions. For the rest of the study, we consider  $v_{ml}$  to be on the order of  $0.01 \text{ s}^{-1}$  in magnitude: new-born cometary ions are neglected after being accelerated for 100 s.



**Fig. 4.** Top row: examples of solar proton trajectories, dimensionless, initially flowing from the right to the left. No particle can enter into the cavity, the central disk of radius  $r_{\text{cav}} \approx 0.28 r_E$ . Bottom row: the shape of the caustic created by particles coming from infinity, using the same spatial scale for three different heliocentric distances, as developed by Saillenfest et al. (2018). The corresponding values of  $r_E$  are, from left to right: 27, 165 and 714 km. Near the origin, the caustic wraps around the cavity. The nucleus position is displayed by a black cross in all plots.

### 3.6. Particle-field feedback



The steady-state assumption together with the scales that are considered in the problem result in extremely simplified Faraday's and Ampère's laws. Close to the caustic, two beams are seen, one incident and one emerging from it. These two beams of identical speed but different direction have the effect of decreasing the local bulk speed. The magnetic field should also be affected, slightly increasing along this structure. In turn, particle trajectories will be corrected by this magnetic feedback. Particles and fields will affect each other until steady state is reached. The model however cannot go further than the third step – the bulk speed decrease – in the following sequence.

Yet another source of magnetic field pile-up is missing: pick-up cometary ions that gained energy from the interaction are neglected. Even though these ions are present everywhere, they will more significantly increase the total cometary ion density in the  $+z$ -hemisphere of the coma. The magnetic field will pile-up slightly more in this hemisphere and the proton deflection is expected to be somewhat higher for positive  $z$  values, close to the nucleus. An example of such effects can be found in the data and simulation analyses of Koenders et al. (2016a).

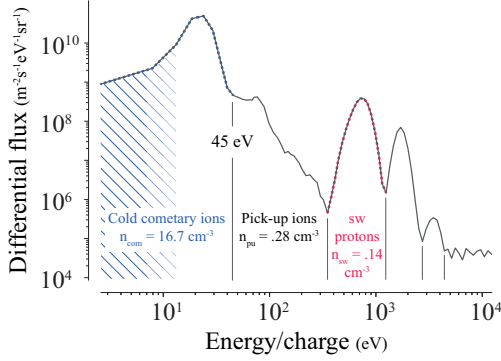


**Fig. 5.** Ion spectrum (differential flux vs. energy per charge of the ions) taken on 2014-11-28 at 2.88 au, integrated for 3 hours. The stripped region for low energies indicates measurements affected by the spacecraft potential.

### 3.7. Consistency of the model & Summary

We gather the main assumptions and orderings we have been working with below. We remind that  $\ell$  is the characteristic length of this steady-state system,  $u$  is its characteristic velocity, and  $\ell_P$  is the characteristic length of the electron pressure gradient.

- i  $\ell \gg d_i$
- ii  $\ell_P \gg r_{ge} v_{the}/u$
- iii  $\partial_t \cdot \equiv 0$
- iv  $\mathbf{u}_{com} = \mathbf{u}_{com}$  and  $\mathbf{u}_{sw} = \mathbf{u}_{sw}$
- v  $\mathbf{B} \perp \mathbf{u}_{sw}$
- vi  $R_{ml} \ll \ell \ll R_d < R_i$
- vii  $n_{com} \sim n_{new-born}$
- viii  $\mathbf{u}_{com} \ll \mathbf{u}_{sw}$
- ix  $\underline{\mathbf{u}}_i = \xi_{sw} \mathbf{u}_{sw} \hat{\mathbf{x}}$

Since the phenomenon we model is the deflection of the solar wind, the characteristic length  $\ell$  can be considered as the distance over which a particle is deflected by some amount. In other words, the characteristic length is a fraction of the radius of curvature of the trajectories, which in our case has the simple and convenient expression  $\rho = -u_{\infty}^2/\eta$ . We choose the definition  $\ell \equiv \rho$ , corresponding to the distance over which a particle is deflected by 1 radian. The smallest radius being modelled is the radius of the cavity,  $r_{cav} \sim 0.28 |\eta|/u_{\infty}$ , and therefore the assumptions are not verified closer to the nucleus.

We now review these assumptions.

i  $\ell \gg d_i$  — We compared the values of  $\ell$  and  $d_i = c/e\sqrt{\epsilon_0} * m/n$  depending on the heliocentric distance, at the cavity radius (the most constraining cometocentric distance). For large heliocentric distances and at the cavity, both terms become of the same order of magnitude. Farther away from the nucleus, the ordering is verified.

ii  $\ell_P \gg r_{ge} v_{the}/u$  — Assuming an isothermal and spherically symmetric coma, the typical length scale of the electronic pressure gradient is  $\ell_P = P_e/\partial_r P_e = r(n_{com} + n_{sw})/2n_{com} \cdot r_{ge} = m_e v_{the}/(B e)$  is the electron gyroradius,  $v_{the} = \sqrt{(2 e E_e/m_e)}$  is the electron thermal speed, with  $E_e \sim 7.5 eV$  being the electron thermal

energy taken from Eriksson, A. I. et al. (2017). The thermal speed for both the solar wind electrons and the cometary electrons are of the same order of magnitude, which is greater than the average speed of each electron population. Similarly to the Hall term of the electric field, condition ii is not fulfilled at large heliocentric distances and close to the nucleus.

iii  $\partial_t \cdot \equiv 0$  — Dynamic phenomenons are not modelled, and the system can only reach another state adiabatically, with changing upstream conditions.

iv  $\mathbf{u}_{com} = \mathbf{u}_{com}$  and  $\mathbf{u}_{sw} = \mathbf{u}_{sw}$  — This is one of the strongest assumptions made in the model, that actually allows one to consider protons as single particles: the trajectories can only be relevant if they are not crossing each other. In the flow presented in Fig. 4, as long as protons do not reach the caustic, neighbouring trajectories are never intersecting: only the density and the bulk velocity change, but the assumed beam distribution is not deformed. We note that this is still true on the caustic itself, where, by definition, all trajectories are aligned. However, immediately after the caustic, two beams of comparable density appear in velocity space. This is a very interesting situation that is not accounted for in the present model. After the caustic, the beam quickly loses density and its particles will experience electric and magnetic fields dictated by the ‘upstream’ beam: they will have a general gyromotion which is not modelled here.

v  $\mathbf{B} \perp \mathbf{u}_{sw}$  — For an upstream magnetic field along the y-axis, the symmetry of the system guarantees this configuration everywhere in the plane ( $y = 0$ ). The average Parker spiral angle will break this symmetry, and the two populations will have an additional drift along the y-axis. In a purely parallel case,  $\mathbf{B} = B \hat{\mathbf{x}}$  and no solar wind deflection nor cometary ion acceleration can happen. At heliocentric distances above 1 au,  $\mathbf{B}$  becomes closer to  $90^\circ$  from the y-axis on average, and projected in the plane of interest we expect the dynamics to be qualitatively identical to the one depicted here-above.

vi  $R_{ml} \ll \ell \ll R_d < R_i$  — In Sect. 3.5, we have found that  $R_{ml} \sim 10^2$  km,  $R_d \sim 10^6$  km and  $R_i \sim 10^8$  km, verifying  $R_{ml} \ll R_d < R_i$ . For  $r \sim R_d$  and beyond, the cometary ion density is already negligible compared to the solar wind density. We remind that only the ratio of the densities matters in the dynamics, and therefore the change of slope in the density profile at these scales barely has any impact on the solar wind dynamics.

vii  $n_{com} \sim n_{new-born}$  — (Discussed with viii)

viii  $\mathbf{u}_{com} \ll \mathbf{u}_{sw}$  — The observations presented by Nilsson et al. (2017) show that over the mission duration and as seen by the spacecraft, these two assumptions are sound. The flux of pick-up cometary ions is always two to three orders of magnitude above the flux of low-energy cometary ions, a difference that cannot be evened out by the difference of speeds (see also Fig. 5). The solar wind energy was also never close to the cold cometary ions’ energy.

ix  $\underline{\mathbf{u}}_i = \xi_{sw} \mathbf{u}_{sw} \hat{\mathbf{x}}$  — This is actually inconsistent with the generalised gyromotion, as the ion bulk velocity is seen to change its direction (precisely the interest of the model). But as of now, this simplification seems necessary, and allows us to reduce the proton dynamics to the simple object of Eq. (19). We also mentioned that for most cometocentric distances,  $\underline{\mathbf{u}}_i \sim \xi_{sw} \mathbf{u}_{sw}$ , so as long as the deflection of the protons is not



too high, the resulting pile-up is relevantly modelled (within the limits of our description of the coma density).

In summary, different aspects of the flow in Fig. 4 are to be considered lightly, and these are:

- Trajectories of protons some time after they passed the caustic are non-physical (see iv). The local density is however only slightly disturbed.
- The magnetic pile-up will be affected in areas where protons have experienced significant deflection (see ix), typically the region downstream of the caustic, that is, the lower-left quadrant of the top graph in Fig. 4. For these two reasons, the solar wind ion cavity should most likely not be circular.
- In the region closest to the nucleus at large heliocentric distances, electrons and ions are expected to decouple and pressure gradients will be at work (see i and ii), which is not accounted for by the model.

Finally, the entire subject of waves and instabilities has been voluntarily neglected in the pursuit of simplicity, and it is believable that close to the nucleus and close to the Sun, these phenomena begin to play a major role. We refer to the work of Sauer et al. (1996), in which the authors study magneto-acoustic waves propagating transverse to the magnetic field in the frame of the bi-ion fluid theory, in a similar system (the artificial comet experiment conducted by the *AMPTE* mission).

#### 4. Rosetta data & self-consistent models in the literature

We now have a 2D model to describe the velocity of individual solar wind protons around a comet. The dynamics is governed by a simple force acting on protons that is always perpendicular to their velocity and has an amplitude proportional to  $1/r^2$ . The resulting flow in Fig. 4 is highly asymmetric and is only scaled with varying heliocentric distances. We now briefly review a selection of studies and results that support the model, both from *in situ* data and from numerical simulations.

##### 4.1. Rosetta

A force always orthogonal to the solar wind protons and proportional to  $1/r^2$  in strength was initially proposed as an empirical model in Behar et al. (2017) to account for high solar wind deflection close to the nucleus together with very low deceleration, which eventually lead to the creation of a solar wind ion cavity. The ion cavity and the diamagnetic cavity observed at 67P/CG and reported by Goetz et al. (2016b,a) are different, the former being much larger than the latter. More detailed and physical differences are discussed by Sauer et al. (1994) and Behar et al. (2017). It was also pointed out that just before the expanding cavity passed the spacecraft position<sup>3</sup>, the deflection was focusing on a value of around  $140^\circ$ , with proton velocity distributions more stable for a time. This would correspond to the crossing of the caustic, at the vertical ( $x = y = 0$  and  $z > 0$  in the CSE frame, Fig. 3) of the nucleus.

The orbit of the spacecraft over the two years of active mission provided two opportunities to map the solar wind flow over an extended region. The first was a day-side excursion, which ended up being almost entirely within the solar wind ion cavity

and therefore of little interest here. During the second excursion, which was conducted at lower activity and in the night-side of the coma, the spacecraft reached distances up to almost 1000 km, and the solar wind was observed during the entire excursion. In Behar et al. (2018), it is shown that a combination of the spacecraft position and of the upstream electric field orientation results in the spacecraft being fairly close to the plane of the model ( $y = 0$  in the CSE frame) during most of the excursion. Ion data present an excellent match with the modelled flow, especially in the  $+z_{CSE}$ -hemisphere. The value of  $v_{ml}$  giving the best fit with the data is  $0.01 \text{ s}^{-1}$  (with all other parameters taken from other studies), surprisingly close to the value found above,  $v_{ml} = 0.011 \text{ s}^{-1}$ . We note that two independent methods based on different ion populations give the same value of  $v_{ml}$ .

Additionally, no significant deceleration in the night-side of the coma was seen to correlate with the deflection, itself observed from just a few degrees up to  $70^\circ$ . As described by Eq. (19) and by the overall mission analysis of Behar et al. (2017) and Nilsson et al. (2017), the solar wind mostly gives momentum to the coma, without significant loss of kinetic energy. The present work provides a physical explanation for this important observation, and shows under which assumptions the solar wind can indeed be deflected by any angle, with negligible loss of kinetic energy.

##### 4.2. Numerical models

The analytical expressions of the generalised gyromotion were verified with the hybrid simulation results, found in Lidström (2017).

The solar wind deflection pattern and the corresponding caustic (an over-density structure in the solar wind) can be seen in the results of numerical simulations, in several publications. In the context of comet 67P/CG, this curved over-density in the solar wind can clearly be seen in the results of Wiehle et al. (2011) (Fig. 3-a), Koenders et al. (2016b) (Fig. 14-a), Koenders et al. (2016a) (Fig. 3-b), Behar et al. (2016a) (Fig. 6), and Deca et al. (2017) (Fig. 4-c). Many of these results also show the general deflection of the solar wind, in qualitative agreement with the present model.

Such an asymmetric density structure in the solar particle flow can also be spotted in the simulation of the plasma environment at other solar system bodies. A first example is the solar wind dynamics modelled by Delamere (2009) at Pluto; see their Fig. 4. There, for two neutral production rate cases, the flow is highly asymmetric and develops a similar structure along which proton trajectories intersect. An even more familiar result can be found in Kallio & Jarvinen (2012), with the simulation of the solar wind interaction with unmagnetised bodies like Mars or Venus. Figure 3 presents the effect of mass-loading on the solar wind, in a test run where the body has no physical extent, and newborn ions are created according to a  $1/r^2$  law, with a total production rate of  $10^{26} \text{ s}^{-1}$ . This is virtually the same system as treated here, and therefore the strong agreement between the flow line of Fig. 3-b in Kallio & Jarvinen (2012) and the proton trajectories modelled here-above is natural.

However, all these results present only the bulk velocity of the flow, with the exception of Delamere (2009). This makes it impossible to judge how single particles behave in the structure itself. In Fig. 6, trajectories of single solar wind protons taken from a self-consistent numerical model are given as a first illus-

<sup>3</sup> The spacecraft can be considered as standing still, close to the nucleus.

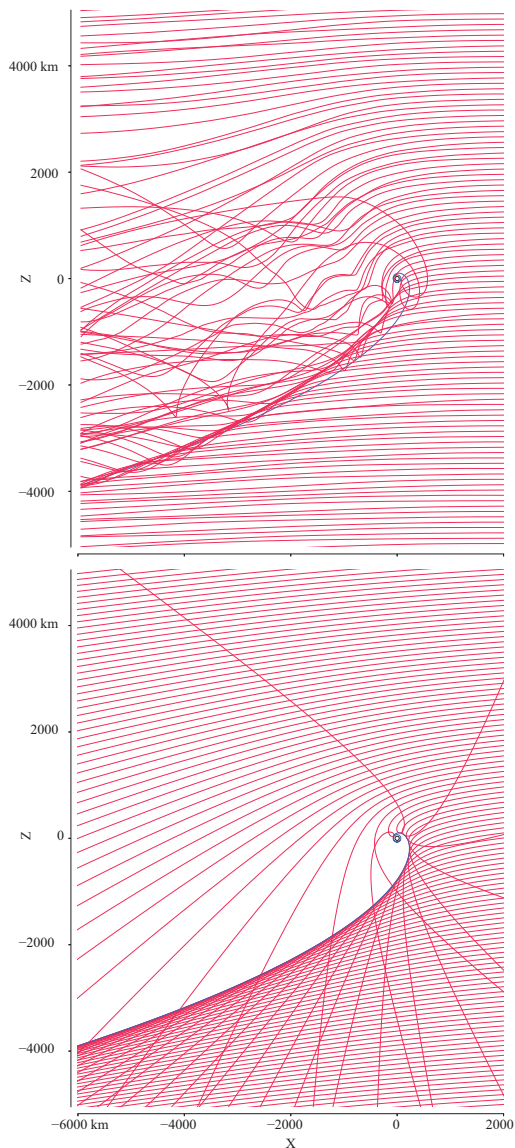


**Fig. 6.** Solar wind proton trajectories (red lines) simulated using hybrid FLASH, a self-consistent numerical model (upper panel) and the trajectories of the 2D semi-analytical model (lower panel). The theoretical position of the caustic is given by the blue line.

trative overview. The hybrid-FLASH model is a hybrid particle-in-cell solver<sup>4</sup> developed by Holmström (2010, 2013), and used

<sup>4</sup> Ions are treated as massive particles and electrons as a massless charge-neutralising fluid.

in the context of 67P/CG in Behar et al. (2016a) and Lindkvist et al. (2018). The model of the comet was purposefully kept simple, with a spherically symmetrical outgassing (Haser model), two ion populations (solar wind protons and cometary water ions), no charge exchange between neutral particles and ions, and in this particular simulation,  $\mathbf{B}_\infty$  is along the y-axis. The cell size is constant and equal to 50 km. The heliocentric distance is 2 au, the production rate is  $Q = 7.52 \cdot 10^{26} \text{ s}^{-1}$ , the ionisation rate is  $\nu_i = 1.63 \cdot 10^{-7} \text{ s}^{-1}$ , and the speed of neutral molecules is 700 m/s. The upstream magnetic field of the solar wind is along the y-axis,  $B = 2.53 \text{ nT}$ , its upstream speed is  $u_\infty = 430 \text{ km/s}$  and its upstream density is  $n_\infty = 1.25 \text{ cm}^{-3}$ .

The value of  $v_{ml}$  that gives the best match between the caustics, especially at large distances, is found to be  $v_{ml} = 0.025 \text{ s}^{-1}$ , which is larger than the previous experimental estimates. We find that similarly to in the semi-analytical model, proton trajectories are slowly deflected, and intersect each other in the  $(-x, -z)$  quadrant, forming a caustic. Immediately after passing the caustic, the protons are now experiencing the electric field mostly dictated by the denser incoming beam, and therefore starts a more complex gyromotion not accounted for by the analytical model. These protons are accelerated upward and cross the caustic. In both the simulation and the analytical model, immediately below the caustic, the phase space distribution function of the solar wind protons presents two beams (which might be similar to the observations of two proton beams reported by Jones & Coates (1997) at comet Grigg-Skjellerup). One can also note that the presence of the pick-up ions, denser in the  $+z$  hemisphere, can be seen in the locally higher deflection of the solar wind protons. We do not discuss the situation for cometocentric distances below 500 km, as with too few cells, one cannot properly resolve the smaller scales in this inner region, where charge exchange is also expected to play a role. A noteworthy observation is that in the simulation, the finite size of the box leads to an underestimation of the deflection, as can be seen at the boundary 2000 km upstream of the nucleus. This is due to an injection of solar wind protons at the upstream boundary with an initial velocity along the x-axis, whereas in the analytical model, protons have already experienced a significant deflection at this cometocentric distance. This issue is pointed out and quantified in Saillenfest et al. (2018) (cf. Sect. 3.2). It is also probably one of the reasons why the best-fit value of  $v_{ml}$  is larger here, since it must compensate for the distortion induced by the finite size of the simulation box.

Downstream of the caustic, the proton density drops in both panels, and accordingly to Eqs. (3) and (4), so does the electric field. In turn, the newborn cometary ions will be less accelerated than immediately upstream from the caustic, and will accumulate: the caustic shields the newborn cometary ions, and in turn a discontinuity in their density is expected to form along the caustic. This issue goes beyond the scope of this article, and is left for further studies.

Finally, the nature of this structure may now be discussed under a new light. Bagdonat & Motschmann (2002) describe the structure (the caustic in our description) as one side of an asymmetric Mach cone formed by the front wave of propagating density and magnetic field disturbances, induced by the obstacle – the newborn cometary ions in this case – in the incident flow. The complete asymmetry of the cone is however not further discussed. It is extremely interesting to note that the present model does not consider the super-magnetosonic character of the solar wind, nor does it propagate any type of disturbance. Based on this 2D approach, this asymmetric structure is not formed by a propagating perturbation, and therefore is not a Mach cone. Fur-



thermore, the cometary newborn ions are only indirectly the obstacle in this picture, as the over-density (the caustic) is formed purely by the geometry of the deflected flow. The solar wind is forming an obstacle to itself, an obstacle with a shape independent of the magnetosonic Mach number. Developing the model to a third dimension, comparing it more thoroughly to self-consistent numerical models, and studying the effect of the plasma pressure on this structure is however necessary to conclude on this topic.

## 5. Concluding remarks

We have shown how momentum and energy are transferred between two collisionless plasma beams for spatial scales that are large compared to the ion inertial length and in the case of negligible electron pressure gradients. This so-called generalised gyromotion applies to the most general, or arbitrary, 3D configuration of two plasma beams.

There are two possible ways to consider the exchange of energy between the solar wind and the coma. The first way states that at scales that are large compared to the gyroradius, and based on classical fluid concepts, there is necessarily a loss of kinetic energy in the solar wind. The second way considers individual particles of the solar wind, and the present model shows how and under which conditions and assumptions these particles do not lose kinetic energy, at zero order. However, part of the plasma is accelerated in this interaction (pick-up ions); therefore at a higher order, also the solar wind loses kinetic energy. We further note that translated into bulk properties, this model also displays a deceleration of the fluid.

In the plane of symmetry of the classical magnetic field draping at comets, the exchange of momentum through the fields between the solar wind and a comet atmosphere results in a very simple expression of the force applied to the protons: this force is perpendicular to their velocity, with an amplitude proportional to  $1/r^2$ . The solar particle flow is reduced to a peculiar and highly asymmetric pattern, exhibiting a caustic, which is also seen in numerical models. *In situ* data from the *Rosetta* mission show strong support to the semi-analytical model, in terms of deflection and speed, and with the observation of a solar wind ion cavity. We note that these results can be straightforwardly extended to solar wind alpha particles.

The cheapness of the model will allow for an extended and systematic comparison with *in situ* data, allowing us to distinguish how dominant the motional electric field is during a given activity level. The model may also point to previously unnoticed structures, such as the peculiar distribution function of the solar wind proton close to the caustic. Furthermore, the model should also greatly ease the understanding of complex mass-loaded solar wind kinetic simulations.

Finally, the validity of the model close to the nucleus is expected to crumble closer to the Sun, as a bow shock might form, at least for strong-enough cometary outgassing. There, waves and instabilities will provide additional ways to transfer energy and momentum, and these phenomena will most likely act to transform the described caustic into a bow shock, beyond the domain of validity of this model. Pinning down the conditions for which this transition happens, together with the micro-physics involved, is an obvious direction to explore. However, further out than the potential bow shock, at comets and at unmagnetised

bodies as well, the mass-loading is affecting the solar wind flow, and the present model remains relevant.

**Acknowledgements.** This work was supported by the Swedish National Space Board (SNSB) through grants 108/12, 112/13, 96/15 and 201/15. The work at LPC2E/CNRS was supported by ESEP, CNES and by ANR under the financial agreement ANR-15-CE31-0009-01. This work was supported in part by NASA's Solar System Exploration Research Virtual Institute (SSERVI): Institute for Modelling Plasmas, Atmosphere, and Cosmic Dust (IMPACT). Partial support is also acknowledged by Contract No. JPL-1502225 at the University of Colorado from Rosetta, which is an European Space Agency (ESA) mission with contributions from its member states and NASA. The hybrid solver is part of the openly available FLASH code and can be downloaded from <http://flash.uchicago.edu/> developed by the DOE NNSA-ASC OASCR Flash Center at the University of Chicago. The hybrid simulations were conducted using resources provided by the Swedish National Infrastructure for Computing (SNIC) at the High Performance Computing Center North (HPC2N), Umeå University, Sweden. Part of this work was inspired by discussions within International Teams 336: "Plasma Surface Interactions with Airless Bodies in Space and the Laboratory" and 402: "Plasma Environment of Comet 67P after Rosetta" at the International Space Science Institute, Bern, Switzerland.

## References

- Alfvén, H. 1957, *Tellus*, IX, 92
- Bagdonat, T. & Motschmann, U. 2002, *Earth, Moon, and Planets*, 90, 305
- Behar, E., Lindkvist, J., Nilsson, H., et al. 2016a, *Astronomy & Astrophysics*, 596, A42
- Behar, E., Nilsson, H., Alho, M., Goetz, C., & Tsurutani, B. 2017, *Monthly Notices of the Royal Astronomical Society*, 469, S396
- Behar, E., Nilsson, H., Henri, P., et al. 2018, *Astronomy & Astrophysics*, (submitted)
- Behar, E., Nilsson, H., Stenberg Wieser, G., et al. 2016b, *Geophysical Research Letters*, 43, 1411, 2015GL067436
- Behar, E., Tabone, B., & Nilsson, H. 2018 (Under revision), *Monthly Notices of the Royal Astronomical Society*
- Biermann, L., Brosowski, B., & Schmidt, H. U. 1967, *Solar Physics*, 1, 254
- Coates, A. J. 2009, *AIP Conference Proceedings*, 1183, 121
- Cowley, S. W. H. 1987, *Philosophical Transactions of the Royal Society of London A: Mathematical, Physical and Engineering Sciences*, 323, 405
- Cravens, T. 2004, *Physics of Solar System Plasmas*, Cambridge Atmospheric and Space Science Series (Cambridge)
- Crovisier, J. 1989, *Astronomy & Astrophysics*, 213, 459
- Deca, J., Divin, A., Henri, P., et al. 2017, *Phys. Rev. Lett.*, 118, 205101
- Delamere, P. A. 2009, *Journal of Geophysical Research: Space Physics*, 114, n/a, a03220
- Edberg, N. J. T., Eriksson, A. I., Odelstad, E., et al. 2015, *Geophysical Research Letters*, 42, 4263, 2015GL064233
- Eriksson, A. I., Engelhardt, I. A. D., André, M., et al. 2017, *Astronomy & Astrophysics*, 605, A15
- Goetz, C., Koenders, C., Hansen, K. C., et al. 2016a, *Monthly Notices of the Royal Astronomical Society*, 462, S459
- Goetz, C., Koenders, C., Richter, I., et al. 2016b, *Astronomy & Astrophysics*, 588, A24
- Gombosi, T. I. 2015, *Physics of Cometary Magnetospheres* (John Wiley & Sons, Inc), 169–188
- Graef, C. & Kusaka, S. 1938, *Journal of Mathematical Physics*, 17, 43
- Grewing, M., Praderie, F., & Reinhard, R., eds. 1988, *Exploration of Halley's Comet*, Vol. 10.1007/978-3-642-82971-0 (Springer)
- Hansen, K. C., Altwegg, K., Berthelier, J.-J., et al. 2016, *Monthly Notices of the Royal Astronomical Society*, 462, S491
- Hansen, K. C., Bagdonat, T., Motschmann, U., et al. 2007, *Space Science Reviews*, 128, 133
- Haser, L. 1957, *Bulletin de la Classe des Sciences de l'Académie Royale de Belgique*, 43, 740
- Holmström, M. 2010, in *Numerical Mathematics and Advanced Applications 2009: Proceedings of ENUMATH 2009, the 8th European Conference on Numerical Mathematics and Advanced Applications*, Uppsala, July 2009, ed. G. Kreiss, P. Lötstedt, A. Målqvist, & M. Neytcheva (Berlin, Heidelberg: Springer Berlin Heidelberg), 451–458
- Holmström, M. 2013, *ASP Conference series*, 474, 202
- Johnstone, A., Coates, A., Kellock, S., et al. 1986, *Nature*, 321, 344
- Jones, G. & Coates, A. 1997, *Advances in Space Research*, 20, 271, planetary Ionospheres and Magnetospheres
- Kallio, E. & Jarvinen, R. 2012, *Earth, Planets and Space*, 64, 11
- Koenders, C., Goetz, C., Richter, I., Motschmann, U., & Glaesmeier, K.-H. 2016a, *Monthly Notices of the Royal Astronomical Society*, 462, S235

- Koenders, C., Perschke, C., Goetz, C., et al. 2016b, *Astronomy & Astrophysics*, 594, A66
- Lidström, V. 2017, Master's thesis, Luleå University of Technology, Space Technology
- Lindkvist, J., Hamrin, M., Gunell, H., et al. 2018, *Astronomy & Astrophysics*, Submitted
- McComas, D., Allegrini, F., Bagenal, F., et al. 2008, *Space Science Reviews*, 140, 261
- Nilsson, H., Wieser, G. S., Behar, E., et al. 2017, *Monthly Notices of the Royal Astronomical Society*, 469, S252
- Odelstad, E., Stenberg-Wieser, G., Wieser, M., et al. 2017, *Monthly Notices of the Royal Astronomical Society*, 469, S568
- Saillenfest, M., Tabone, B., & Behar, E. 2018, *Astronomy & Astrophysics*, submitted
- Sauer, K., Bogdanov, A., & Baumgärtel, K. 1994, *Geophysical Research Letters*, 21, 2255
- Sauer, K., Bogdanov, A., Baumgärtel, K., & Dubinin, E. 1996, *Physica Scripta*, 1996, 111
- Shaikhislamov, I. F., Posukh, V. G., Melekhov, A. V., et al. 2015, *Plasma Physics and Controlled Fusion*, 57, 075007
- Störmer, C. 1930, *Zeitschrift für Astrophysik*, 1, 237
- Valentini, F., Trávníček, P., Califano, F., Hellinger, P., & Mangeney, A. 2007, *Journal of Computational Physics*, 225, 753
- Wiehle, S., Motschmann, U., Gortsas, N., et al. 2011, *Advances in Space Research*, 48, 1108



